April 2023

Structure-Function Relationships of Bighorn Sheep Horncore Bone and Horn-Horncore Interface Materials for Energy Absorption Applications

University of Massachusetts Amherst

Structure-function relationships of bighorn sheep horncore bone and horn-horncore interface materials for energy absorption applications

A Dissertation Presented

by

Luca H. Fuller

Submitted to the Graduate School of the
University of Massachusetts Amherst in partial fulfillment
of the requirements for the degree of

Doctor of Philosophy

February 2023

Biomedical Engineering

Structure-function relationships of bighorn sheep horncore bone and horn-horncore interface materials for energy absorption applications

A Dissertation Presented

by

Luca H. Fuller

Approved as to style and content by:

Seth W. Donahue, Chair

Alfred J. Crosby, Member

Duncan J. Irschick, Member

Simos Gerasimidis, Member

S. Thai Thayumanavan, Department Head
Biomedical Engineering Department

ACKNOWLEDGEMENTS

I would first like to thank my advisor, Dr. Seth Donahue, for his many years of continued guidance and support. His leadership has undoubtedly helped me develop my skills as a researcher, engineer, and teacher, and will be instrumental in any professional success I achieve moving forward. He holds his students to a high standard, but also understands the importance of a life-work balance, which made the long and windy road of graduate school much more enjoyable. Thank you for being an exceptional mentor and friend over the past five years.

Additional thanks are due to my committee, Dr. Al Crosby, Dr. Duncan Irschick, and Dr. Simos Gerasimidis. I have learned a great deal from each of them, and appreciate the time and knowledge they so generously shared with me throughout my time in graduate school. Their advice and feedback over the years have challenged me to think critically about complex research questions, and certainly improved my abilities as a young scientist.

I also need to thank the entire Donahue Research Lab. Thank you first to Dr. Sam Wojda – long time member of the lab – who was always willing to share her expertise and offer feedback on many different aspects of the work presented in this manuscript. I also had the privilege of working with many exceptional graduate researchers, specifically, Tim Seek, Dr. Trevor Aguirre, Emily Cravens, Cole Ferreira, and Auden Balouch. Each of them made it enjoyable to come to the lab each day and frequently offered valuable feedback and support. Beyond my fellow graduate researchers, I was lucky enough to work with many gifted undergraduate researchers. Much of the work presented in this manuscript would not have been possible if not for the dedication of Cyrus Karimy, Paige Ruschke, Laura Agarkov, Evan Marcet, and Prisha Singh.

Outside of the Donahue Research Lab, I would also like to thank the entire UMass Biomedical Engineering Department. It has been a pleasure being a member of such a supportive community, and seeing how far the department has come since starting in 2018. I know the department will continue to thrive in the years to come.

Finally, I would like to thank Steve Johnson, Walter Pollard, Meredith Tagon, and Vernon Lamb, for helping with various aspects of mechanical testing including test fixture design and manufacturing and machine operation.

ABSTRACT

STRUCTURE-FUNCTION RELATIONSHIPS OF BIGHORN SHEEP HORNCORE BONE AND HORN-HORNCORE INTERFACE MATERIALS FOR ENERGY ABSORPTION APPLICATIONS

FEBRUARY 2023

LUCA H. FULLER, B.S., CALIFORNIA POLYTECHNIC STATE UNIVERSITY

PH.D., UNIVERSITY OF MASSACHUSETTS AMHERST

Directed by: Professor Seth W. Donahue

Bighorn sheep rams do not show overt signs of traumatic brain injury from head impacts experienced during intraspecific combat. Rams' cranial appendages bear the brunt of ramming impacts and are composed of a keratin-rich horn anchored to a bony horncore via a soft connective tissue interface. The horncore is filled with velar bone which has a unique porous architecture with a comparable bone volume fraction, but larger strut thickness and separation than typical mammalian trabecular bone. Velar bone absorbs more energy than the horn and substantially reduces post-impact brain cavity accelerations in computational models of bighorn sheep ramming. These findings have implications for brain injury mitigation, but are limited by assumed material properties of the horncore bone and horn-horncore interfacial tissue as these were previously unknown. Since bone adapts to mechanical stimuli, and the horncore is exposed to a high impact environment, horncore bone material and the velar bone architecture are expected to have superior energy absorption than other mammalian bone tissues. Furthermore, the horn-horncore interface is expected to have an interdigitated microstructure like other dermo-epidermal junctions

(e.g., the equine hoof-bone interface) to facilitate load transfer between the impacted horn and energy absorbing horncore. This dissertation explored these possibilities by quantifying the composition, microstructure, and mechanical properties of horncore bone and the horn-horncore interface tissue. In addition, computational modeling was used to provide a preliminary comparison between velar and trabecular bone architectures under compressive loading. Horncore bone materials and the velar bone architecture were not shown to increase energy absorption compared to other mammalian bone tissues or trabecular bone architectures. Interestingly, velae had osteons which are rare in trabeculae. Velar osteons may provide crack arrest and deflection to increase microdamage accumulation (i.e., microcrack toughening) and increase the energy absorption of the entire horncore compared to a similar volume of trabecular bone. Furthermore, the horn-horncore interface displayed a 4-fold increase in microscopic contact area, but did so with a morphology unlike other dermo-epidermal junctions. Despite morphological differences, lap-shear properties were comparable to the equine hoof-bone interface and were positively correlated with the microscopic contact area.

TABLE OF CONTENTS

Page

ACKNOWLEDGEMENTS iv

ABSTRACT vi

LIST OF TABLES xiv

LIST OF FIGURES xvi

Chapter

1. INTRODUCTION 1

1.1. Traumatic Brain Injury 1

1.2. Animal Models for Concussion Prevention 2

1.3. Bighorn Sheep Cranial Appendages 4

1.3.1. Horn 5

1.4. Finite Element Modeling of Bighorn Sheep Ramming 8

1.5. Bone Tissue 10

1.5.1. Bone Tissue Structure and Composition 10

1.5.2. Bone Remodeling and Functional Adaptation 14

1.5.3. Bone Mechanical Behavior 16

1.6. Horn-Bone Interfaces 21

1.6.1. Equine Hooves and the Laminar Junction 21

1.6.2. Avian Beaks 23

1.7. Rationale for Dissertation Research 24

1.7.1. Specific Aims 1-2: Quantifying the composition, microstructure, and mechanical properties of bighorn sheep horncore cortical and velar bone. 25

1.7.2. Specific Aim 3: Quantifying the composition, microstructure, and mechanical properties of bighorn sheep horn-horncore interfacial tissue. 26

1.7.3. Specific Aim 4: Investigating the role of velar bone architecture in impact energy absorption. 29

1.8. Hypotheses and Specific Aims 31

1.9. References 35

2. HORNCORE CORTICAL BONE CHARACTERIZATION 43

2.1. Abstract 43

2.2. Introduction 44

2.3. Materials and Methods 47

2.3.1. Samples 47

2.3.2. Mechanical Testing 48

2.3.4. Composition 50

2.3.5. Histology 50

2.3.6. Statistics 52

2.4. Results 53

2.4.1. Mechanical Properties 53

2.4.2. Composition 54
2.4.3. Histomorphometry 54
2.5 Discussion 58
2.6. Acknowledgements 62
2.7. References 64
3. CHARACTERIZATION OF HORNCORE VELAR BONE 70
3.1. Introduction 70
3.2. Materials and Methods 73
3.2.1. Samples 73
3.2.2. Mechanical Testing 75
3.2.2.1. Specimen Prep 75
3.2.2.2. Dynamic Mechanical Analysis 77
3.2.2.3. Three-point Bending 78
3.2.3. Histomorphometry 81
3.2.4. Composition Analysis 83
3.2.5. Statistics 84
3.3. Results 85
3.3.1. Mechanical Testing 85
3.3.1.1. Specimen Prep 85
3.3.1.2. Dynamic Mechanical Analysis 88

3.3.1.3. Three-point Bending 92
3.3.2. Histomorphometry 96
3.3.3. Composition 98
3.3.4. Regression Analyses 98
3.3.5. Horncore Velar vs. Cortical Bone 103
3.4. Discussion 105
3.5. References 115
4. CHARACTERIZATION OF THE HORN-HORNCORE INTERFACE 120
4.1. Introduction 120
4.2. Methods 123
4.2.1. Samples 123
4.2.2. Mechanical Testing 125
4.2.2.1. Lap-shear specimen preparation 125
4.2.2.2. Lap-shear testing 129
4.2.3. Histology 131
4.2.4. Image Analysis 133
4.2.5. Statistics 136
4.3. Results 138
4.3.1. Lap-shear Testing 138
4.3.2. Histology 141

4.3.3. Regression Analysis 147

4.4. Discussion 149

4.5. References 156

5. COMPUTATIONAL MODELING OF VELAR BONE ARCHITECTURES 159

5.1. Introduction 159

5.2. Materials and Methods 161

5.2.1. Samples 161

5.2.2. Representative Volume Elements 162

5.2.2.1. Velar Bone 162

5.2.2.2. Trabecular Bone 165

5.2.3. Finite Element Modeling 166

5.2.3.1. Volume Meshing, Constraints, and Boundary Conditions 166

5.2.3.2. Uniaxial Compression Models 168

5.2.3.3. Buckling Models 169

5.2.4. Model Architectural Indices 171

5.3. Results 172

5.3.1. Mesh Convergence 172

5.3.2. Size Effects 173

5.3.3. Strain Energy Density 174

5.3.4. Buckling 175

5.4. Discussion 177

5.5. References 183

6. CONCLUSIONS AND FUTURE DIRECTIONS 185

6.1. Summary 185

6.2. Key Findings 187

6.3. Future Research Directions 188

6.3.1. Strain rate sensitivity of horncore bone tissue 188

6.3.2. Horncore microdamage and bone remodeling activity 189

6.3.3. Horn-horncore interface attachment 190

6.3.4. Computational modeling 190

6.4. References 192

BIBLIOGRAPHY 195

LIST OF TABLES

Table Page

Table 2-1. Tabulated experimental results for individual compressive (C) and tensile (T) samples along with summary data from each cortex expressed as Mean ± SE. Results from paired t-tests are expressed as p-values below the summary data with **bold** values indicating significant differences between cortices ($p < .05$). Measured parameters include horn curl length (CL), the bending modulus (E), modulus of toughness (u_t), bone mineral content (BMC), porosity, osteon population density (OPD), and mean secondary osteon area (MSOA). 55

Table 3-1. Final dimensions of velar bone mechanical test specimens For each ram, values are presented as the average ± standard deviation of all specimens. Note: width and thickness of each specimen were determined by averaging three measurements taken along specimen length. 88

Table 3-2. Storage modulus (E'), loss modulus (E"), and damping factor (tan□) measured via dynamic mechanical analysis (DMA) at 0.1, 1.0, 10, and 50 Hz. Values presented as Mean ± Standard Deviation for all specimens. 90

Table 3-3. P-values from mixed model analyses of storage modulus, loss modulus, and damping factor measured via dynamic mechanical analysis at 0.1, 1.0, 10, and 50 Hz. Significant values ($p < 0.05$) shown in **bold**. 91

Table 3-4. P-values from linear mixed model analyses of mechanical properties measured via three-point bending including bending modulus (E), yield strength (σ_y), yield strain (ε_y), modulus of resilience (u_r), ultimate strength (σ_{ult}), ultimate strain (ε_{ult}), modulus of toughness (u_t), and fracture energy (W). Significant values ($p < 0.05$) indicated in **bold**.94

Table 3-5. Results from three-point bending showing bending modulus (E), yield strength (σ_y), yield strain (ε_y), modulus of resilience (u_r), ultimate strength (σ_{ult}), ultimate strain (ε_{ult}), modulus of toughness (u_t), and fracture energy (W). Values presented as Mean ± Standard Deviation for each ram (BHS 3-6), and means for all rams (Mean) 94

Table 3-6. Results from histomorphometry and composition analysis showing velar bone porosity (φ), osteon population density (OPD), bone mineral content (BMC), and bone water content (H_2O). Data presented as mean ± standard deviation for individual rams (BHS 3-6) and the means from all rams (Mean). 97

Table 3-7. P-values from linear mixed model analyses of results from histomorphometry and composition analyses. No significant ($p < 0.05$) sources of variation were identified. 97

Table 3-8. Estimated regression coefficients for predictive models of viscoelastic properties measured using DMA including storage modulus (E'), loss modulus (E"), and loss factor (tan δ). 100

Table 3-9. Estimated regression coefficients for predictive models for elastic properties measured via three-point bending including bending modulus (E), yield strength (σ_y), yield strain (ε_y), ultimate strength (σ_{ult}), and ultimate strain (ε_{ult}). 102

Table 4-1. Final lap-shear specimen dimensions including keratin adherend length ($l_{keratin}$) and thickness ($t_{keratin}$), bone adherend length (l_{bone}) and thickness (t_{bone}) as well as the width, length, and thickness ($w_{int,LS}$, $l_{int,LS}$, and $t_{int,LS}$, respectively) of the intact interface used in calculations of stress and strain to determine mechanical properties. Values shown as mean ± standard deviation for each ram (BHS 3-6), and all specimens combined (mean). 139

Table 4-2. Distribution of the anatomical position of lap-shear specimens included in statistical analyses (grey boxes) for each ram. The triple asterisks (***) indicates the two samples that failed due to bone adherend fracture which were excluded from statistical analysis of failure properties (τ_{ult}, γ_{ult}, and SED). 139

Table 4-3. Summary of mechanical testing results including ultimate apparent shear strength (τ_{ult}), ultimate apparent shear strain (γ_{ult}), low-strain modulus ($G_{low\text{-}strain}$), high-strain modulus ($G_{high\text{-}strain}$), and total strain energy density (SED) for each ram and all mechanical tests combined (total). All values shown as Mean ± Standard Deviation. .. 141

Table 4-4. P-values from mixed model analysis results showing significance of fixed effects on calculated mechanical properties including ultimate apparent shear strength (τ_{ult}), ultimate apparent shear strain (γ_{ult}), low-strain modulus ($G_{low\text{-}strain}$), high-strain modulus ($G_{high\text{-}strain}$), and total strain energy density (SED). Significant p-values ($p < .05$) are shown in **bold**..... 141

Table 4-5. Distribution of the anatomical positions of longitudinal (L) and transverse (T) histological sections included in statistical analyses (grey boxes) for each ram. 142

Table 4-6. Summarized histology data for longitudinal and transverse sections including interface thickness (t_{int}), the length ratio (LR), and the area fractions of collagen ($A_{f,col}$) and keratin ($A_{f,ker}$). Data shown as mean ± standard deviation for each ram (BHS 3-6) and all rams combined (mean). P-values from paired t-tests between morphologic parameters quantified in longitudinal and transverse sections from the same samples shown in the bottom row. 146

Table 4-7. P-values from mixed model analysis of histomorphometric results for each orientation (transverse and longitudinal sections) including interface thickness (t_{int}), the length ratio (LR), and the area fractions of collagen ($A_{f,col}$) and keratin ($A_{f,ker}$). Significant values ($p < .05$) shown in **bold**. 147

Table 4-8. Parameter estimates for regression models used to predict mechanical properties. Independent variables included in the final models included the curl length (CL) along with the interface thickness and length ratio measured in transverse histology sections ($t_{int,T}$ and LR_T, respectively). Equations presented in the bottom row of each mechanical property. 148

LIST OF FIGURES

Figure Page

Figure 1-1. Longitudinal section of the proximal region of bighorn sheep horn showing various components including the horn, horncore cortical and velar bone, and the horn-horncore interface. 5

Figure 1-2. Illustration of the hierarchical structure of the bighorn sheep horn from the gross structure of the tapered-spiral horn (left) to the molecular structure of the keratin α-helices (right). At intermediate length scales, disk shaped cells with randomly oriented macrofibrils form a laminar structure around microscopic tubules that run along the horn length. Reprinted with permissions from [23]. 7

Figure 1-3. Hierarchical structure of bone tissue. (from left to right) Collagen molecules combine to form the tropocollagen triple helices which are arranged into microfibirils. Hydroxyapatite nanocrystals nucleate and grow in small gaps within microfibrils. Microfibrils aggregate to form mineralized collagen fibrils, which are bundled together to form mineralized collagen fibers with diameters ranging from hundreds of nanometers to one micrometer. Mineralized collagen fibers serve as the basic building block of lamellar bone observed in cortical (dense) and trabecular (porous) bone tissues that make up whole bones. Reproduced with permission from [99]. 11

Figure 2-1. A longitudinal section of the proximal region of the horn showing the organization of bone and horn materials. 45

Figure 2-2. (a) Longitudinal sections of bighorn sheep horns were cut to expose tensile and compressive stress cortices of the horncore. (b) Sections of cortical bone 60 mm long (between the dashed lines) were removed from tensile and compressive cortices using a bandsaw and separated from the horn using a scalpel. (c) Histology slides were prepared from the distal portion of cortical bone sections. (d) Cortical bone mechanical test coupons (30 mm long) were prepared from the proximal portion of cortical bone sections and loaded to failure in three-point bending. (e) The distal half of the fractured coupon was used for mineral content quantification. 48

Figure 2-3. Histological images of bighorn sheep horncore cortical bone stained with toluidine blue. (a) Intact secondary osteons were distinguishable by peripheral cement lines (arrows). Examples of pore spaces (P) and secondary osteon fragments (F) are also visible. (b) Secondary osteons were not present in samples from the two younger rams which displayed extreme cortical porosity due to large pore spaces (P). 52

Figure 2-4. Curl length regressions for: (a) the bending modulus, (b) modulus of toughness, (c) bone mineral content, and (d) porosity of bighorn sheep horncore cortical bone tissue. Data points represented with a 'C' and 'T' are from compressive and tensile cortices, respectively. Regression lines shown for significant correlations ($p < .05$). 56

Figure 2-5. Comparisons between cortical bone properties of bighorn sheep horncores, black bear tibias [37], and red deer antlers from two populations: free-ranging (free) and farm raised (farm) [46]. Comparisons include (a) bending modulus, (b) modulus of toughness, (c) bone mineral content, and (d) porosity. Error bars represent standard error. 57

Figure 2-6. Porosity was the best predictor variable for bending modulus (E) and modulus of toughness (u_t). Data points represented with a 'C' and 'T' are from compressive and tensile cortices, respectively. Regression lines shown for significant correlations ($p < .05$). 57

Figure 3-1. (a) Velar bone in the horncore of a bighorn sheep ram illustrating the sail-like morphology of this unique porous bone architecture. (b) Trabecular bone typically displays a more rod-like strut morphology with a much smaller size scale compared to velar bone. 71

Figure 3-2. (a) Anterior/posterior and proximal/distal locations of velar extraction. (b) Schematic illustration of approximate orientation of longitudinal and transverse mechanical test specimens. 75

Figure 3-3. Sample preparation procedure. (a-b) 12 velar bone sails were cut from each horncore using an oscillating dremmel. (c-d) Sails were gripped in a vice to cut a strip with uniform width (w = ~1.05 mm) using a precision saw. (e) Cut strips were held in slotted plastic blocks and ground to final specimen thickness on rotating SiC polishing pads. A series of slotted plastic blocks with constant slot wdith (equal to specimen width ~1.05 mm) and decreasing slot depth (d = 2 to 0.6 mm) were used to maintain perpindicularity between adjacent walls as thickness was reduced during grinding process. (f) Final mechanical test specimens were ~14.5 mm long, 1.05 mm wide, and 0.6 mm thick. 77

Figure 3-4. Histological cross-sections of velar bone mechanical test coupons. (a) Cross-section with secondary osteons (white arrows) that are mostly circular in shape and aligned with the long axis of the mechanical test coupon as indicated in the schematic below (schematic not to scale). These osteons were included in the calculation of OPD. A representative selection of pores (white triangles) that contributed to the calculated pore area are also shown. Scale bar = 100 μm. (b) Cross-section with elongated Haversian canals (black arrows) indicative of osteons aligned perpendicularly or obliquely to the long axis of the mechanical test coupon as illustrated in the schematic below (schematic not to scale). These osteons were not included in the calculation of OPD since it was difficult to reliably identify cement lines in this orientation. Secondary osteons aligned with the long axis of the mechanical test specimen (white arrow) and representative pores (white triangles) are also shown. Scale bar = 100 μm. 83

Figure 3-5. Specimen distribution for each ram in terms of anterior-posterior position. . 86

Figure 3-6. Specimen distribution for each ram in terms of proximo-distal position..... 87

Figure 3-7. Specimen distribution for each ram in terms of orientation. 87

Figure 3-8. Storage modulus of velar bone specimens from 0.1-50 Hz separated by orientation. Storage modulus increased with increasing frequency in both orientations. Data shown as means ± standard deviation. 89

Figure 3-9. Loss modulus of velar bone specimens from 0.1-50 Hz separated by orientation. Loss modulus decreased with increasing frequency in both orientations. 89

Figure 3-10. Damping factor of velar bone specimens from 0.1-50 Hz separated by orientation. Damping factor decreased with increasing frequency in both orientations... 90

Figure 3-11. Interaction between anterior-posterior position and orientation on measured storage modulus at each investigated frequency. Values presented as mean ± standard deviation. Longitudinal samples tend to have higher storage modulus in the anterior region while transverse specimens have a higher storage modulus in the posterior region. Pairwise comparison at each frequency using Tukey HSD with Tukey-Kramer adjustment found no significant differences between individual pairs..... 92

Figure 3-12. Pairwise comparisons of (a) bending modulus, (b) yield strength, (c) yield strain, and (d) bending strength based on anterior-posterior position and orientation of each sample. Data presented as mean ± standard deviation in all plots. Results from mixed model analyses indicated that the interaction term between anterior-posterior position and orientation significantly influenced the bending modulus, yield strength, and ultimate strength (Table 5). Longitudinal samples tended to have higher bending modulus and strength in the anterior region, while transverse samples had increased elastic modulus and strength in the posterior region (a, b, d). In the posterior region of the horncore, transverse samples had significantly higher yield strength ($p = .0475$) and marginally higher bending strength ($p = .0763$) than longitudinal samples. Other pairwise comparisons for bending modulus, yield strength and ultimate strength were insignificant. Meanwhile, yield strain was significantly higher in transverse samples compared to longitudinal samples regardless of other factors ($p = .0070$). 95

Figure 3-13. Pairwise comparisons of modulus of resilience (a) and modulus of toughness (b) based on anterior-posterior position and orientation of each sample. Data presented as mean ± standard deviation in both plots. Results from mixed model analyses indicated that transverse samples had significantly higher modulus of resilience ($p = .0291$) and modulus of toughness ($p = .0371$) than longitudinal samples. Additionally, the interaction term between anterior-posterior position and orientation significantly influenced the each of these properties (Table 5). For longitudinal samples, energy storage and absorption were greater in the anterior region but transverse samples demonstrated greater energy storage and absorption in the posterior region. However, pairwise comparisons indicated that the only significant differences in these values were found in the posterior region of the horncore, where transverse samples had significantly higher modulus of resilience ($p = .0127$) and modulus of toughness ($p = .0222$) than longitudinal samples. The fracture

energy demonstrated identical trends to the modulus of toughness and is therefore not presented for brevity. 96

Figure 3-14. Pairwise comparisons of osteon population density (OPD) (a), and porosity (b) based on anterior-posterior position and orientation. Data presented as least-square (LS) means ± standard error. Transverse samples had similar values of OPD and porosity in both regions (anterior and posterior) of the horncore. However, longitudinal samples from the anterior region tended to have higher OPD (marginally significant, p = .0609) and significantly lower porosity (p = .0293) compared to longitudinal samples from the posterior region. Additionally, velar bone porosity was significantly higher in longitudinal samples from the posterior region than transverse samples from the anterior region (p = .0355). 98

Figure 3-15. Bone mineral content had a significant but weak positive correlation with curl length (p = .0203, r^2 = 0.119). 99

Figure 3-16. Storage modulus was positively correlated with osteon population density at 0.1 Hz (a), 1.0 Hz (b), 10 Hz (c) and 50 Hz (d). Loss factor was negatively correlated with osteon population density at 0.1 Hz (e), 1.0 Hz (f), 10 Hz (g) and 50 Hz (h). Regression model parameter estimates are presented in Table 8. 101

Figure 3-17. Bending modulus (a), yield strength (b), yield strain (c), modulus of resilience (d), and ultimate strength (e) were positively correlated with osteon population density. Ultimate strain was negatively correlated with curl length (f). Estimated regression coefficients for each regression model are shown in Table 9. 103

Figure 3-18. Comparison of horncore bone properties between cortical and velar bone tissues. Velar bone had significantly lower porosity (a), bending modulus (b), yield strength (c), ultimate strength (d), modulus of resilience (e), and fracture energy (f) than cortical bone based on a linear mixed model including tissue type (velar or cortical) as a fixed effect and ram ID as a random effect. 104

Figure 3-19. Storage modulus measured from 0.1 – 100 Hz for samples of bovine cortical bone taken from the medial, lateral, anterior, and posterior quadrants of the femoral diaphysis. Reproduced with permissions from [57]. 109

Figure 3-20. Loss factor (i.e., damping factor) measured from 0.1 – 100 Hz for samples of bovine cortical bone taken from the medial, lateral, anterior, and posterior quadrants of the femoral diaphysis. Reproduced with permissions from [57]. 110

Figure 4-1. Sample extraction and processing. (a) Full skull and horn indicating the measured curl length and location of the proximal transverse section (gray dashed lines) cut from the horn. (b) Longitudinal section of proximal transverse section of horn. (c) The anatomical locations of extracted samples and the longitudinal axis defined in the quasi-cylindrical coordinate system. (d) Interface sections were segmented to prepare lap-shear specimens for mechanical testing and histological sections with transverse (blue plane) and

longitudinal (green plane) orientations. The coordinate system shown indicates the longitudinal (l), circumferential (θ), and radial (r) axes of each interface sample. 125

Figure 4-2. Lap-shear specimen milling procedue. (a) Sample secured in vice and top material milled to final adherend thickness of 2 mm. (b) Sample flipped over, and milled surface from (a) positioned on parallels to mill second material to final adherend thickness of 2 mm. (c) Sample secured in custom fixture with stepped jaws and exposed material on free end milled completely to bottom material to finalize first adherend length of ~15 mm. (d) Sample flipped over to repeat (c) on opposite side to obtain second adherend length (~15 mm) and finalize lap-shear specimen. 128

Figure 4-3. Reflected light stereoscope image used to measure lap-shear interface length ($l_{int, LS}$) and lap-shear interface thickness ($t_{int, LS}$) of final lap-shear specimens. Images were loaded into BioQuant, and the horn surface (white curved line) and bone surface (black curved line) adjacent to the soft-tissue interface were manually traced. The double labeled surface measurement was used to calculate the average length of these two surfaces ($l_{int, LS}$) as well as the average distance between these two surfaces from individual measurements made in 5 μm increments ($t_{int, LS}$). 129

Figure 4-4. Representative stress-strain curve from lap-shear testing illustrating the low-strain shear moduli ($G_{low\text{-}strain}$, red line), high-strain shear moduli ($G_{high\text{-}strain}$, blue line), ultimate apparent shear strength (τ_{ult}), ultimate apparent shear strain (γ_{ult}), and strain energy density (SED, grey area under the stress-strain curve). 131

Figure 4-5. Representative image of interface histology section. (a) Entire section with mature bone (red) on the left, dense horn (yellow) on the right, and interfacial tissue with a mix of collagen (blue) and keratin (red) fibers. (b) Bone side of the interface showing unmineralized collagen fibers stained blue on the right side of the image. (c) Horn side of the interface showing the unorganized network of keratin fibers (red) and collagen fibers (blue) on the left and horn on the right. Within the horn, a region of keratinized tissue adjacent to the interfacial tissue is stained red, but the horn tissue eventually transitions to yellow staining as the keratinocytes become squamous and more densely packed. 133

Figure 4-6. Example measurements of interface histology images. (a) Representative region of interest (ROI) used to calculate area fractions of collagen (blue) and keratin (red) observed in the interface. Average interface thickness (t_{int}) was measured in the radial direction by averaging incremental measurements between manually traced bone and horn surfaces using the double labeled surface measurement in BioQuant. Nominal contact length (l_{nom}) was measured as the straight-line edge-to-edge distance parallel to the horn surface. (b) Magnified view of histology section illustrating the undulated horn surface and horn pore perimeters used to calculate the contact length (l_{cont}) using Equation 4.5. Pores along the inner horn surface were included if they were contained within the red-stained region that precluded the yellow-stained horn. 136

Figure 4-7. Failure modes of lap-shear specimens. (a) Interface failure along horn surface with interfacial tissue still attached to bone (black arrow). (b) Cohesive interface failure

with remnants of interfacial tissue still attached to bone (black arrow) and horn (white arrow). (c) Failure due to fractured bone adherend (white arrow). 139

Figure 4-8. Comparison of ultimate apparent shear strength calculated from samples in each quadrant. Results from the linear mixed model showed that quadrant was a significant fixed effect ($p = .0319$). Post-hoc pairwise comparisons showed that the posterior quadrant had marginally lower ultimate apparent shear strength than the medial ($p = .0533$) quadrant. 140

Figure 4-9. (a) Longitudinal and (b) transverse horn-horncore interface sections from the same sample. Sections were stained with Masson's trichrome. The interfacial tissue between horn (yellow) and bone (red) was an unorganized network of collagen fibers (blue) and keratin fibers (red). Longitudinal and transverse section morphologies were not different ($p \geq .1242$). Scale bars = 500 µm. 142

Figure 4-10. Histology sections stained with Masson's Trichrome. Dense horn is stained yellow, bone is stained red, and the interfacial tissue is an unorganized matrix of collagen fibers (blue) and keratin fibers (red). (a) Full histology cross section showing horn surface undulation and porosity where collagen attaches to horn. (b) Increased magnification of black box region in (a), showing unorganized matrix of collagen (blue) and keratin (red) fibers. (c) Black box in (b) showing Sharpey's fibers (black arrows) penetrating bone. (d) Collagen fiber bundle (black arrow) penetrating several millimeters into horncore cortical bone. 144

Figure 4-11. Histology sections stained with Masson's trichrome. Dense horn is stained yellow, mature bone is stained red, and the interfacial tissue is an unorganized matrix of collagen fibers (blue) and keratin fibers (red). (a) Sectioning tearing artifacts (black arrows) visible in the horn. (b) Black box labeled 'b' in (a) showing keratinized tissue forming the walls of pores (P) filled with collagen (blue) and trace amounts of keratin (red) (c) Black box 'c' in (a) showing keratinized tissue extensions forming branched structures (black arrows) within the surrounding interface tissue. Additional pores (P) can also be seen. (d) Dense network of collagen fibers arranged circumferentially to form a tubular structure in the bone. 145

Figure 4-12. Linear mixed model analysis demonstrated that transverse interface thickness was higher in proximal samples than distal samples ($p = .0316$). Data shown as mean ± standard deviation. 146

Figure 4-13. Regression model demonstrating negative correlation between ultimate shear strain and transverse interface thickness. 148

Figure 5-1. Isolated 45 mm representative volume element (RVE) cropped from the left horncore. 162

Figure 5-2. Thresholding and segmentation layer repair process. (a) Raw CT scan image. (b) Automatic thresholding adjusted so the included bone tissue (blue) closely matches the

bone tissue visible in the raw images. (c) Regions of bone tissue missed by automatic thresholding (white arrows) (d) Repaired segmentation layer with pixel values added to regions missed by automatic thresholding. 163

Figure 5-3. The original 45 mm cubic RVE and 40, 35, 30, and 25 mm RVEs cropped from the 45 mm geometry. 164

Figure 5-4. Mirrored representative volume element (MRVE) with eight 45 mm RVEs making up the 90 mm MRVE. 165

Figure 5-5. Nodes of distal surface (red points) were tied to the distal surface reference point (white point) with a rigid body boundary condition. Loads/displacement boundary conditions were applied to the distal surface reference point (white point) to impose compression in the proximodistal direction (grey arrow). 167

Figure 5-6. Dilation procedure to increase BV/TV of velar and trabecular bone models that demonstrate non-local buckling. 40 mm velar bone RVE shown. Top row shows layer segmentation with progressive dilation from left to right. Bottom row shows isosurfaces computed and exported from Seg3D. 170

Figure 5-7. Results from the mesh convergence study for (a) velar bone and (b) trabecular bone. 173

Figure 5-8. Influence of the RVE size on (a) apparent stress and (b) strain energy density. Both variables increase with increasing cube side length. Some evidence of convergence is demonstrated by larger MRVEs. 174

Figure 5-9. (a) Stress-strain behavior of the porous bone architectures demonstrated that the 45 mm velar bone RVE was slightly stiffer than the original trabecular bone architecture under compressive loading. (b) The original trabecular bone architecture stored greater total strain energy density than the 45 mm velar bone RVE under the applied apparent compressive strain. 175

Figure 5-10. Local (left) and non-local (right) buckling modes demonstrated by 40 mm velar bone RVE. Colored gradient illustrating deformation magnitudes which have been visually scaled up by a factor of 4x. 176

Figure 5-11. (a) Apparent critical buckling stress increased with increasing bone volume fraction (BV/TV) for velar and trabecular bone architectures. (b) Apparent critical buckling stress decreased with increasing slenderness ratio for velar and trabecular bone architectures. 177

CHAPTER 1

1. INTRODUCTION

1.1. Traumatic Brain Injury

Traumatic brain injury (TBI) is a disruption in brain function induced by jostling of the skull due to direct head impact, whip-lash, or blast exposure [1]. It has been estimated that TBI costs the United States $17 billion annually [2]. Severe TBI can result in extended periods of unconsciousness and even death. However, most cases (70 – 90% [3]) cause only brief changes in consciousness at the time of injury and are referred to as mild TBIs or concussions. While the initial consequences of concussions are relatively minor, there is growing evidence that repeated concussions can lead to chronic neurological consequences. For example, some studies have demonstrated a connection between repeated concussions and chronic traumatic encephalopathy, a progressive condition of neurodegeneration [4,5]. Other studies have associated repeated concussions to depression [6,7], early onset dementia [8], and Parkinsonism [9], though the long-term effects of concussive injuries remain under active investigation and debate. Regardless, heightened awareness about the dangers associated with brain injuries has motivated efforts to mitigate or prevent concussions in at risk populations such as athletes and military personnel.

An incomplete understanding of concussion etiology makes injury prevention difficult. However, substantial evidence suggests inertial forces experienced by the brain are responsible for concussive injury [10]. Inertial forces arise as a result of direct impact to the head or from impulsive head movements (i.e. whiplash), and can be in the form of translational or rotational accelerations. Linear accelerations of the head cause pressure

gradients to develop in the brain, and transient increases in brain pressure have been shown to cause neurological dysfunction. Conversely, rotational accelerations of the head can result in shear-induced brain tissue damage. Since brain tissue is more compliant under shear-loading than transient pressure changes, it is generally agreed that rotational accelerations of the head are the primary mechanism of concussive injury [10]. Consequently, efforts to mitigate concussion occurrence focus on reducing the risk of high magnitude head accelerations following an impact. Current helmet technologies such as the multidirectional impact protection system (MIPS) can greatly reduce rotational accelerations of the head under oblique impact [11,12], but further improvement is needed. Studying injury mitigation mechanisms employed by animal species exposed to frequent head trauma may inspire novel advancements to helmet technology that provides even greater protection against brain injuries.

1.2. Animal Models for Concussion Prevention

Several extant animal species display unique behaviors resulting in frequent exposure to high-impact head trauma. For example, bighorn sheep participate in seasonal bouts of head-butting to assert dominance and establish mating rights within a herd. In computational studies of ramming impacts, translational brain cavity accelerations have been estimated around 400 g [13]. Woodpeckers also experience repetitive head trauma during routine pecking behavior. High-impact pecking has been shown to produce translational head accelerations as high as 1000 g [14,15]. Comparatively, concussive injury in collegiate football players have been associated with impacts producing acceleration magnitudes as low as 60 g but averaging 100 g [16]. Historically, bighorn sheep and woodpeckers were believed to be resistant to brain injury due to the absence of

overt concussion symptoms. However, recent evidence of tau accumulations in the brains of woodpeckers and headbutting bovids suggests they may experience some level of brain injury after all [17,18]. With that said, the thicker skulls and larger horns of male bovids may offer some protection considering tauopathies were more prevenlant in female samples of muskoxen and bighorn sheep [18]. Furthermore, the lack of observable signs of brain injury (i.e. unconsciousness) following head trauma in these species suggest that some level of brain injury mitigation is achieved.

Several mechanisms of injury prevention have been proposed for woodpeckers. In some studies, injury mitigation has been attributed to linear pecking motion resulting primarily in translational accelerations which are less likely to cause brain injury than rotational accelerations of the head [15]. Other groups have suggested that the hyoid apparatus of woodpeckers plays a protective role during pecking by securing and cushioning the brain within the skull [19]. Ultimately, it seems likely that several mechanisms work together to protect woodpeckers from brain injury during impact.

To date, less research has been done to elucidate any injury mitigation mechanisms active in bighorn sheep during ramming. However, there is growing interest in investigating the protective role of their helmet-like cranial appendages that bear the brunt of the impact during combat. Initial efforts on this frontier have focused largely on characterizing the horn material. Computational modeling has also provided a valuable tool for investigating how horn and horncore structures contribute to energy absorption and injury mitigation during ramming. Determining how materials and structures of these cranial appendages interact to provide injury mitigation during ramming may inspire novel

designs of head protection systems that can effectively reduce concussion occurrence in humans.

1.3. Bighorn Sheep Cranial Appendages

Rams have permanent cranial appendages that grow continuously into large, tapered spiral structures. Unlike antlers, these cranial appendages are not shed and regrown seasonally, and are generally representative of animal age and size. A bony horncore projects from the skull and is encased in a keratinized horn (Figure 1). The horn is anchored to the horncore via a soft, connective tissue interface. The horncore is further discretized into a dense, cortical bone shell filled with a porous bone architecture. The porous architecture of the horncore has a bone volume fraction that falls within the range of typical mammalian trabecular bone (~20%) but different strut geometry. The strut thickness (2.87 ± 0.78 mm) and separation (11.91 ± 0.88 mm) measured for porous horncore bone are several orders of magnitude larger than trabecular thickness (0.12 ± 0.02 mm) and separation (0.57 ± 0.08 mm) measured for trabecular bone samples from the proximal tibia of grizzly bears [20]. Additionally, the struts in the horncore are generally wide and flat plates instead of the long and narrow rods observed in trabecular bone. Accordingly, this unique bone architecture is referred to as “velar” bone (from the latin *velum* for sail) [20].

Since the horn and horncore are not shed and regrown annually like antlers they must be exceptionally resistant to damage accumulation and flaw propagation. However, the horn and horncore must also maintain low weight to minimize the metabolic cost of locomotion. Since similar mechanical efficiency is desirable in many engineering applications there is motivation to understand the structure-function relationships of

bighorn sheep horn materials. Research to date has been limited to characterizing the horn, neglecting the horncore and connective tissue interface.

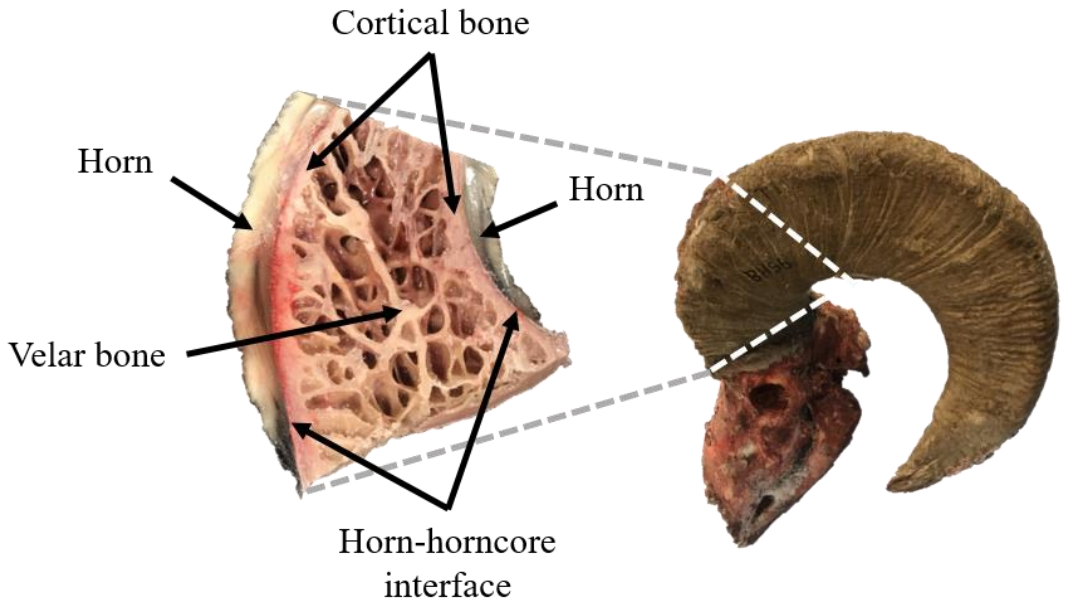

Figure 1-1. Longitudinal section of the proximal region of bighorn sheep horn showing various components including the horn, horncore cortical and velar bone, and the horn-horncore interface.

1.3.1. Horn

Keratin is a structural protein found abundantly in biological materials including horns, hooves, hair, and beaks. Like many natural materials, the exceptional material properties of ram horn are attributed to its hierarchical structure (illustrated in Figure 2). Starting at the molecular level, keratin α-helices are joined by disulfide and hydrogen bonds to form intermediate filaments approximately 12 nm in diameter [21–23]. Intermediate filaments are embedded in an amorphous keratin matrix to form macrofibrils with diameters around 200 nm [21–23]. Microscopically, randomly oriented macrofibrils aggregate within a plane to form disk shaped cells approximately 1 – 2 μm thick and 20 – 30 μm in diameter [23]. These keratinized cells form a lamellar structure that encapsulates

elliptical tubules running along the length of the horn. The lamina surrounding these tubules form an angle of ~30° with respect to the tubule direction [23]. Tubule cross sections are organized with the major axis (~59 – 100 μm) and minor axis (~25 – 40 μm) oriented circumferentially and radially, respectively [23,24]. Furthermore, tubules are distributed such that there is a radial porosity gradient that decreases from 8 – 12% porosity near the outer horn surface to completely solid (0% porosity) at the inner horn surface [24]. Although a porosity gradient in the opposite direction would more effectively resist bending, deformation of the porous tubules near the outer surface of the horn is likely beneficial for absorbing energy and reducing impact forces [24]. This porous microstructure allows the horn to maintain relatively low weight while providing adequate mechanical competence to survive frequent ramming impacts during intraspecific combat.

The mechanical behavior of the ram horn has been quantified under a multitude of conditions including varying states of tissue hydration, loading modes, and loading rates. Generally, horn displays anisotropic behavior due to the preferential orientation of tubules. Horn is stiffest and strongest when loaded in the longitudinal direction (parallel to tubule length) but absorbs more energy when loaded radially (in the direction of ramming impact) [23–25]. Additionally, horn displays different mechanisms of deformation and failure depending on the applied loading mode and is most compliant and ductile under compressive loading. Compressive loading results in microbuckling, shear band failure, and delamination while failure under tensile loading typically occurs from matrix failure,

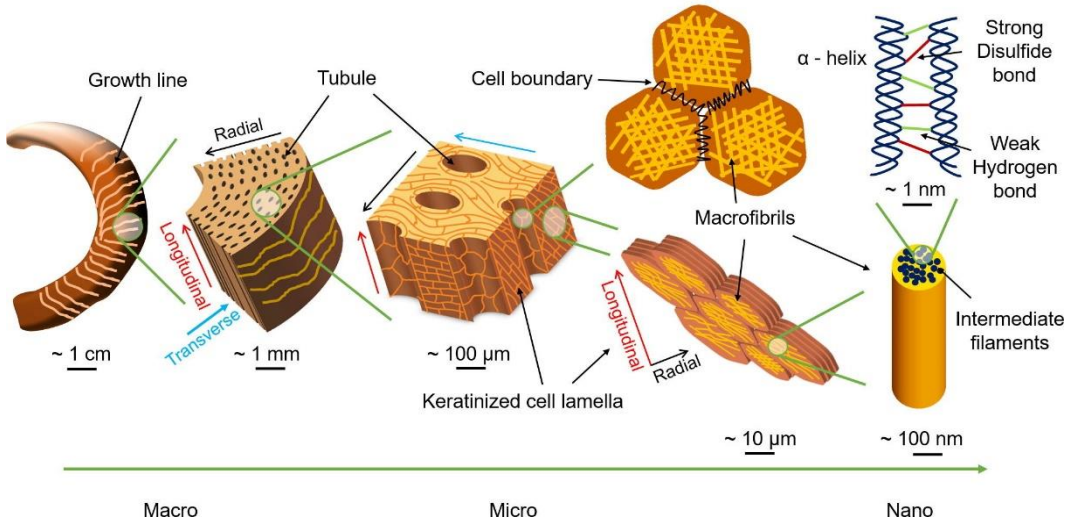

Figure 1-2. Illustration of the hierarchical structure of the bighorn sheep horn from the gross structure of the tapered-spiral horn (left) to the molecular structure of the keratin α-helices (right). At intermediate length scales, disk shaped cells with randomly oriented macrofibrils form a laminar structure around microscopic tubules that run along the horn length. Reprinted with permissions from [23].

fiber pull-out, and tubule fracture [23–26]. Additionally, horn demonstrates viscoelasticity in the form of strain-rate sensitivity similar to many other natural materials, with increased strength, stiffness, and energy absorption at higher loading rates. These characteristics are true for both wet and dry horn but are more pronounced for dry horn (~10 wt% water) compared to rehydrated conditions (~35 wt% water). The elastic modulus reported for dry horn ranges from 0.96 GPa (0.001 s^{-1}, radial direction) to 3.66 GPa (4000 s^{-1}, longitudinal direction) while elastic modulus values for wet horn range from 0.13 – 1.525 GPa under similar conditions [23]. Compressive strength of horn loaded at 1000 s^{-1} ranges from 109 – 165 MPa for dry horn and 27 – 28 MPa for wet horn [26]. Meanwhile, the tensile strength of horn loaded at 1000 s^{-1} ranges from 48 – 117 MPa for dry horn and 34 – 49 MPa for wet horn [26]. The results indicate the important role moisture content plays in determining the mechanical properties of the horn during ramming.

Perhaps most notably, hydrated horn has demonstrated a remarkable ability to undergo extreme deformation without damage. In one study, horn samples impacted to compressive strains as high as 30% recovered their initial length upon unloading [23]. This finding suggests that the horn is capable of storing significant amounts of energy without damage and may play a critical role in reducing energy transfer to the brain during ramming. While these findings provide insight into the potential role of the horn in brain injury mitigation, similar characterization studies on the horncore and horn-horncore interface are lacking. With that said, computational modeling of bighorn sheep ramming has demonstrated the importance of velar bone for impact energy absorption.

1.4. Finite Element Modeling of Bighorn Sheep Ramming

Simulations of bighorn sheep ramming have offered valuable insight into the role of the horn and horncore in post-impact injury mitigation [13,27]. One computational study demonstrated that the porous architecture and elastic modulus of horncore bone are important for distributing stresses over large volumes and increasing the total strain energy storage capacity of the entire structure [27]. However, this study used quasi-static loading to model the peak impact force produced during ramming which limits the utility of these results.

In a more sophisticated computational study, varying skull and horn geometry were impacted against a deformable plate to simulate idealized ramming collisions [13]. Three model geometries were compared to investigate how various structures influence energy storage, stress/strain distributions, and brain cavity accelerations during and post-impact. In the *full model,* an anatomically accurate model of the skull/horn geometry was built from

computed tomography scans. The horn and horncore were segmented based on differing bone and keratin densities, and assigned mechanical properties assumed to be linear elastic, isotropic, and homogenous. Horn was assigned a density of 1.3 g/cm^3, elastic modulus of 2 GPa, and a poisson's ratio of 0.3 based on values available in the literature [24,25]. Horncore bone was given a density of 1.725 g/cm^3, elastic modulus of 15 GPa, and a poisson's ratio of 0.28 based on values reported for primate cranial bone since values for ram skull bone had not yet been reported [28]. A point mass and spring-dashpot system were used to model the remaining animal mass (not including the skull/horns) and spinal stiffness, respectively. Furthermore, symmetry about the sagittal plane justified using one half of the skull and applying symmetric boundary conditions to reduce computational cost. Next, the *half horn model* was created by removing the distal half of the horn and the *bone removed model* was created by removing the porous velar bone architecture from the horncore.

Comparing the relative outputs of the three different models led to two major conclusions. First, it was shown that the horncore stored a greater fraction of the total model energy than the horn (24% and 8%, respectively). Additionally, removing the velar bone from the horncore produced a 442% increase in peak rotational accelerations during impact. These findings indicate that the horncore architecture plays a critical role in injury mitigation during impact based on our current understanding of traumatic brain injury. However, it remains unclear what specific features of horncore bone – material and/or structural – are important for injury mitigation during impact. Additionally, the connective tissue interface may be important for efficient load transfer between the impacted horn and energy absorbing horncore. Therefore, a better understanding of the structure-function

relationships of horncore bone and the connective tissue interface are necessary to gain further insight into mechanisms of brain injury mitigation in head-butting rams.

1.5. Bone Tissue

1.5.1. Bone Tissue Structure and Composition

Although horncore bone appears to play an important role in energy absorption and brain injury mitigation during ramming, horncore bone properties have not yet been quantified. However, other mammalian bone tissues have demonstrated exceptional mechanical efficiency and toughening mechanisms attributed to the underlying composition and structural hierarchy. More importantly, bone tissue is known to adapt to mechanical stimuli and demonstrates damage repair mechanisms unavailable to avascular horn. These unique features of bone tissue may make it advantageous for the horncore to be the primary energy absorber during ramming. Additionally, due to the extreme impact loading environment of the horncore, it is possible that this tissue has adapted unique properties compared to other mammalian bone tissues. In order to explore these possibilities, an understanding of the typical range of bone tissue composition, structure, and mechanical behavior is required.

In general, bone is a fiber-matrix composite with organic and inorganic material constituents along with water (~25%, 65% and 10% by weight, respectively) [29]. The organic phase is primarily composed of collagenous proteins, the most abundant being Type I collagen. The inorganic phase is almost entirely composed of hydroxyapatite mineral crystals. The structural organization of these components at various length scales (illustrated in Figure 3) provide impressive mechanical performance.

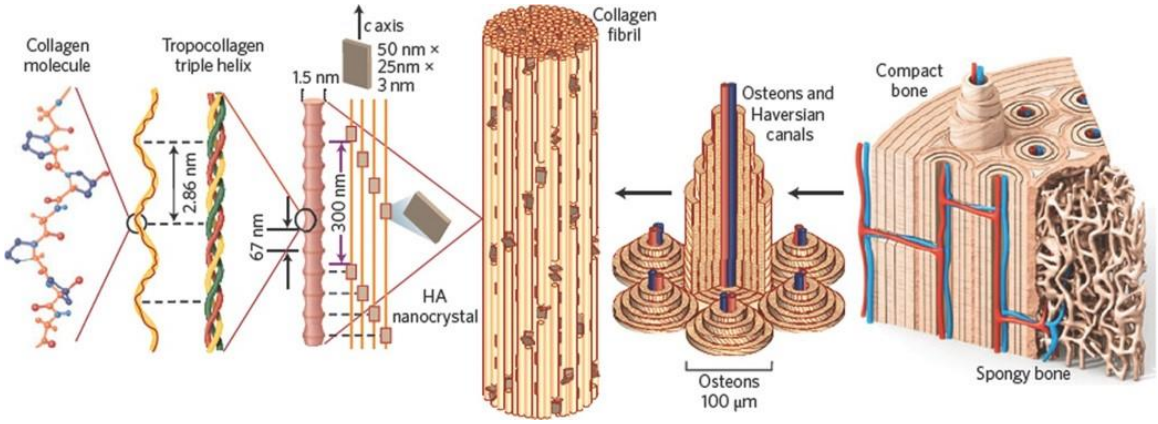

Figure 1-3. Hierarchical structure of bone tissue. (from left to right) Collagen molecules combine to form the tropocollagen triple helices which are arranged into microfibirils. Hydroxyapatite nanocrystals nucleate and grow in small gaps within microfibrils. Microfibrils aggregate to form mineralized collagen fibrils, which are bundled together to form mineralized collagen fibers with diameters ranging from hundreds of nanometers to one micrometer. Mineralized collagen fibers serve as the basic building block of lamellar bone observed in cortical (dense) and trabecular (porous) bone tissues that make up whole bones. Reproduced with permission from [99].

At the nanoscale, three Type I collagen molecules combine to form triple-helical tropocollagen molecules approximately 300 nm long and 1.5 nm in diameter [28–30]. Next, five tropocollagen molecules are assembled into microfibrils through hydrophobic and electrostatic forces. Tropocollagen molecules are staggered within microfibrils, leaving small gaps (~40 nm long and 1.5 nm wide) in which intrafibrillar hydroxyapatite crystals nucleate and grow [31]. There has been some debate regarding the morphology of these hydroxyapatite crystals; however, most agree that they are plate-like structures 2-10 nm thick, 20-50 nm long, and 15-30 nm wide [30,32]. Microfibrils aggregate laterally and longitudinally to form mineralized collagen fibrils with diameters around 100 nm (lengths of these fibrils are too large to measure at the scale they are observable) [29]. Finally, these microfibrils are bundled together to form mineralized collagen fibers with diameters ranging from hundreds of nanometers to one micrometer [28]. These mineralized collagen fibers act as the basic building block of bone tissue at larger length scales.

There are two common microstructures observed in bone tissue: ‘woven’ and ‘lamellar’ bone. In woven bone, mineralized collagen fibers are arranged randomly to form a disorganized network of bone tissue [33]. Woven bone is immature bone tissue commonly found in embryonic skeletons and bone calluses during fracture healing. Over time, woven bone is remodeled into an organized, layered microstructure known as lamellar bone. In lamellar bone tissue, individual layers of bone matrix approximately 3 – 7 μm thick are created from highly aligned mineralized collagen fibers [30]. Collagen fiber orientation alternates in adjacent lamella, similar to the alternating grain orientation of plywood layers [34,35]. At larger length scales, this layered microstructure forms the basis for both cortical and trabecular bone tissues present in whole bones.

Cortical and trabecular bone both exhibit lamellar microstructures of aligned, mineralized collagen fibers, but differ in terms of microscale organization and macroscopic architecture. Dense cortical bone (aka compact bone) has a tissue porosity typically reported between 5-15% [36–43] and contributes to around 80% of skeletal mass. Cortical bone tissue is most prominent in the diaphysis of long bones where it can be several millimeters thick and serves as a load bearing structure. Additionally, a thin cortical shell is present along the outer surface of long bone metaphyses and epiphyses, as well as the external surfaces of short bones, flat bones, and irregular bones. The basic structural units of cortical bone are microscopic cylindrical structures known as osteons or Haversian systems (for this reason, it is sometimes referred to as osteonal or Haversian bone). Osteons are composed of 3-8 concentric lamella surrounding a central pore (Haversian canal), and are on the order of 100-300 μm in diameter and a few millimeters in length [44,45]. Osteons are classified as either primary or secondary, the former related to initial bone modeling,

and the latter a result of continuous bone remodeling. Due to remodeling processes (discussed in more detail in the following section), secondary osteons are separated from the surrounding bone matrix by a peripheral cement line. Histological techniques have demonstrated that cement lines are collagen deficient and less mineralized than surrounding lamellar bone [41,46]. Haversian canals contain the blood vessels and nerves responsible for supplying nutrients and innervation to cortical bone tissue. The long axis of osteons are typically aligned parallel to the long axis of the bone in order to resist the primary stresses generated during physiological loading.

Contrary to cortical bone, trabecular bone is a porous, cellular structure that exists in the remaining volume of whole bones, except for the diaphysis of long bones. The cellular architecture is composed of many interconnected rod-like struts, and can be up to 95% porous [47]. Trabecular bone provides structural integrity to whole bones at a significantly reduced weight compared to cortical bone. This feature is important for living animals, as it reduces the metabolic cost of skeletal locomotion. Unlike cortical bone, osteons are rarely found in trabecular bone tissue since the trabecular rods are often thinner than typical osteon diameters. Instead, trabeculae feature adjacent, crescent-shaped lamella referred to as hemi-osteons or trabecular packets. Nutrients are supplied to trabeculae surfaces through the vasculature of bone marrow present in the pore space of the cellular architecture.

Trabecular bone architecture is often characterized in terms of indices including bone volume fraction (BV/TV; bone tissue volume per total volume), trabecular thickness (Tb.Th.; average thickness of struts), trabecular separation (Tb.Sp; average distance between struts), trabecular number (Tb.N; average number of struts per unit length), and

connectivity density (Conn.D; number of strut connections per unit volume) [48]. Additionally, various fabric tensors have been used to quantify the spatial organization of trabecular bone architectures [49]. The morphology of trabecular and cortical bone just described, along with the morphology of whole bones, is largely dictated by bone remodeling processes.

1.5.2. Bone Remodeling and Functional Adaptation

Bone remodeling allows bone to repair damage and adapt to its loading environment. Bone remodeling continually replaces old and damaged bone with younger, healthy bone tissue. During remodeling, osteoclasts and osteoblasts work in coordination as a basic multicellular unit (BMU). BMUs drive bone remodeling in five phases: activation, resorption, reversal, formation, and mineralization. Osteoclasts are recruited to the remodeling site during activation and subsequently dissolve and digest old bone tissue during the resorption phase. Reversal involves osteoclast apoptosis and the migration of osteoblasts to the remodeling site. During formation, osteoblasts lay down new bone matrix (osteoid) which is then mineralized over time. Within 5 – 10 days osteoid will be approximately 70% mineralized, but full mineralization can take up to six months [50]. Once mineralization is complete, bone tissue is considered to be at rest until the cycle repeats. Remodeling takes place on bone surfaces and significantly influences microscopic bone morphology.

Cortical bone remodeling occurs primarily on internal surfaces as BMUs dig tunnels through the cortex that result in the cylindrical structure of secondary osteons. Some remodeling also occurs on endosteal and periosteal surfaces of cortical bone tissue which leads to changes in cross-sectional properties of long bone diaphyses over time.

Conversely, remodeling of trabecular bone occurs primarily on the surface of trabeculae as BMUs dig and refill pits forming the crescent shaped hemi-osteons. In both cases, cement lines formed during the reversal phase offer evidence of previous remodeling events via histological analysis. In addition to influencing the microstructure of lamellar bone tissue, remodeling also alters the gross structure of whole bones through functional adaptation.

There is strong evidence that remodeling alters skeletal mass and geometry in order to maintain strain levels within a certain range during peak physiological activity. This concept was initially suggested from in vivo data that demonstrated similar strain magnitudes arising during routine activities across a wide range of species [51,52]. Since then, several studies in support of this theory have demonstrated reduced bone mass in cases of disuse (i.e. bed rest or spaceflight) [53,54], and elevated bone mass in cases of overuse or increased physical activity [55–60]. The effect is so substantial that inter-arm variability is present when comparing bone properties of the dominant and non-dominant arms of tennis players. Specifically, bone mineral content and cortical area are both increased in bones of the playing arm compared to those of the non-playing arm [60]. Along with the relatively short-term phenotypic plasticity that occurs continuously via bone remodeling, there is also evidence of functional adaptations occurring over evolutionary time.

Long-term (evolutionary) adaptations in bone tissue composition provide a range of bone mechanical properties to meet the demands of whole bones with different physiological functions dependent on species and skeletal location [61]. For example,

bovine femur has intermediate mineral content, strength, and toughness[1] compared to less mineralized but tougher red deer antler and highly mineralized and stiffer whale bulla (ear bone) [61]. Compositional differences in these three bones seem to result in mechanical properties well-suited for the vastly different mechanical functions of each bone [33,61]. In the case of deer antler, toughness is of utmost importance to prevent catastrophic failure resulting from dynamic forces experienced during fighting. The high toughness is achieved by larger deformations in the less mineralized and more compliant antler compared to bovine femoral bone. For the whale bulla, very high mineralization provides very high stiffness which is beneficial to provide efficient sound transmission in the ear. Strength and toughness are not important for bulla since they are protected from external forces. Finally, in the case of the bovine femur, a balance is reached between adequate stiffness required for weight bearing and sufficient strength and toughness required to prevent failure during physiological activity. Ultimately, the many examples of functional adaptation found in bone demonstrate the strong link between composition, structure, and mechanical properties of this musculoskeletal tissue.

1.5.3. Bone Mechanical Behavior

The mechanical behavior of bone is well documented due to financial implications of bone fractures and disease in healthcare. Since cortical and trabecular bone share similar lamellar architectures microscopically but differ vastly macroscopically, it is beneficial to discuss bone properties at both the tissue level and continuum level. At the tissue level, bone properties depend strongly on local tissue composition. It is well established that the

[1] Throughout this dissertation, the word toughness is used to generally refer to a materials ability to absorb energy and undergo plastic deformation prior to fracture. This is not to be confused with the terms fracture toughness or modulus of toughness, which are quantifiable material properties.

mineral phase of bone tissue dominates the elastic response and contributes to bone stiffness while collagen properties dictate the plastic response of bone post-yield [62]. Mechanical properties of cortical and trabecular bone at the tissue level are often regarded as similar due to comparable tissue compositions. With that said, studies comparing tissue level properties of cortical and trabecular bone generally find that trabecular bone is approximately 20-30% less stiff than cortical bone. This reduction in stiffness is presumably due to the reduced mineral content that arises from increased trabecular bone turnover [63–67]. These findings are supported by additional studies that have shown increased mineral content is positively correlated with greater elastic modulus and yield strength but decreased ductility of bone tissue [36,62,68–70]. The composite nature of bone tissue also results in viscoelastic behavior. Several studies have shown that increased strain rates lead to stiffer and more brittle behavior of bone tissue which likely plays a role in traumatic fractures from falls and impacts [71–74]. Moving from the tissue level to continuum level, different material models are needed to describe the behavior of cortical and trabecular bone.

In general, cortical bone is described well by a transversely isotropic material model due to the microstructural arrangement of osteons. Human cortical bone is stiffest (E = 17 GPa) when loaded longitudinally (parallel to the long axis of osteons) and demonstrates reduced stiffness in the isotropic transverse plane (11.5 GPa) [75]. In addition to transverse isotropy, ultimate properties of human cortical bone are also asymmetric (i.e. depend on the applied loading mode). Early work on cortical bone mechanics demonstrated that cortical bone is strongest when loaded under longitudinal compression (σ_{ult} = 193 MPa) and weakest under transverse tension (σ_{ult} = 51 MPa) [75]. Tissue level porosity also

influences the mechanical properties of cortical bone and several studies have demonstrated that increased tissue porosity results in decreased bone strength and stiffness [36,43,76]. This may not come as a surprise due to the stress concentrations present at microscopic pores. There is also strong evidence that cement lines surrounding osteons enhance cortical bone toughness by arresting and deflecting microcracks [77–82].

Although cracks are easily initiated at stress concentrations from microscopic porosity, propagating cracks below 300 μm are often arrested or deflected upon encountering an osteon. Energy dissipated through the formation of non-critical and tortuous microcracks is then unavailable to drive propagation of catastrophic macrocracks. This is known as "microcrack toughening." Although microcrack accumulation eventually weakens bone [83], targeted remodeling typically repairs damaged bone before catastrophic failure occurs. This cyclic process of damage accumulation and repair makes microcrack toughening particularly effective in healthy bone tissue. This may be one benefit of the repairable horncore bone being the primary energy absorber during ramming, as opposed to the avascular keratin horn which cannot be repaired once damaged. Histological methods have been developed for quantifying osteon population density (number of osteons per unit area) which serves as a measure of remodeling occurrence in a region of interest. Using these methods, studies have shown that osteon population density is positively correlated with regional strain modes and magnitudes [84] and bone fracture toughness [80]. These findings provide additional evidence in support of the theories of functional adaptation and microcrack toughening, particularly for cortical bone. Since trabecular bone typically lacks osteons and is much more porous than cortical bone, different models are needed to describe its mechanical behavior.

Trabecular bone properties at the continuum level depend on intrinsic tissue level properties as well as the overall trabecular architecture. Thus, it is common practice to use a similar approach to modeling cellular solids (i.e. bulk continuum materials formed by repetition of a single unit cell) to describe the apparent properties of trabecular bone at the continuum level. Factors influencing the intrinsic material properties of trabecular bone tissue have been discussed previously. In terms of architecture, studies have shown that Tb.Th, Tb.Sp, and Conn.D scale allometrically in birds and mammals. Larger animals – with increased mechanical demands of weight bearing and locomotion – demonstrate greater strut thickness and spacing, but reduced connectivity density [47]. These relationships holds true even for the largest animals whose bones require extraordinary weight bearing capacity. For example, when comparing the trabecular bone in the femoral head of Asian elephants (~3400kg) and long-eared hedgehogs (~0.22 kg), similar BV/TV values (47.9 % and 52.0 %, respectively) are achieved via drastically different architectures. In the more massive elephant, struts are thicker and more widely separated (Tb.Th = 0.511 mm, Tb.Sp = 0.851 mm) than similar measures for the hedgehog (Tb.Th = 0.138 mm, Tb.Sp = 0.194 mm). Interestingly, bone volume fraction is relatively constant over a wide range of animal sizes despite varying significantly depending on species and skeletal location (from ~0.05 – 0.7) [47]. It has been suggested that this is a geometric adaptation to limit local bone strains in individual trabeculae. This theory is supported by our current understanding of functional adaptation in bone, as well as efforts to model the continuum mechanics of trabecular bone tissue.

Computational modeling has offered valuable insight into how trabecular indices influence the apparent properties of trabecular bone at the continuum level. One study

investigated trabecular bone mechanics from species representing a wide range of body masses (~1 – 10,000 kg) and found that the apparent stiffness of trabecular bone is positively correlated with body mass [85]. Additionally, the correlation between apparent stiffness and body mass appeared to maintain local bone strains of individual trabeculae across the wide range species investigated. It seems intuitive that larger animals require increased bone stiffness to prevent excessive deformation during loading, and these findings agree with the theory of strain-controlled functional adaptation. Additionally, apparent stiffness was best predicted by Tb.Th, Tb.Sp, or Conn.D, corroborating the allometric scaling relationships demonstrated for these indices but not BV/TV. Interestingly, another study on human trabecular bone demonstrated that the bone volume fraction and fabric anisotropy are the primary determinants of the apparent stiffness and yield properties of trabecular bone. It was concluded that bone volume fraction alone is the best parameter to estimate trabecular bone mechanical properties, describing 89% and 75% of the variation in stiffness and yield strength, respectively [86,87]. These results appear to conflict with the other allometric scaling relationships reported, but comparisons are confounded by the narrow range of samples taken only from humans in this study.

Despite the extensive body of work measuring the mechanical properties of mammalian bone tissue mechanics, horncore cortical and velar bone properties have not been quantified. However, horncore bone material and velar architecture may be well-suited for impact performance due to functional adaptation to the extreme mechanical environment of ramming impacts. Regardless of these possibilities, another important aspect of bighorn sheep ramming is energy transfer between the impacted horn and energy

absorbing horncore. Thus, there is also motivation to investigate the structure-property relationships of the horn-horncore interface.

1.6. Horn-Bone Interfaces

1.6.1. Equine Hooves and the Laminar Junction

Work thus far has focused largely on the roles of horn and horncore in energy absorption and injury mitigation during ramming, but neglected the connective tissue interface between these structures. However, to facilitate energy storage in the horncore, the connective tissue interface must provide efficient load transfer between the impacted horn and internal horncore. One biological structure that plays a similar physiological role is the equine laminar-junction. Equine digits are composed of the distal phalanx (bone), the dermis, the laminar-junction, and the stratum medium (hoof wall) [88]. During locomotion, the laminar-junction transfers the ground-reaction force acting on the hoof-wall to the appendicular skeleton. Accelerations experienced by the equine hooves during trotting are on the order of 50 g [89], much lower than those experienced by bighorn sheep horn during ramming. Due to the larger impact accelerations involved in bighorn sheep ramming, the horn-horncore interface is expected to be stronger than the analogous laminar junction in equine hooves.

The morphology of the laminar junction has been studied extensively due to financial implications for the equine industry and a condition known as laminits. In a single hoof, 550 – 600 keratinized primary epidermal lamellae (PEL) extend from the inner hoof wall radially inward toward the distal phalanx. An additional 100 – 150 non-keratinized secondary epidermal lamellae branch from each PEL [88,90]. Similar primary and

secondary dermal lamellae extend from the dermis, and secondary lamellae from epidermal and dermal tissues are intertwined to provide attachment of the hoof wall to the distal phalanx. The interdigitation of the dermal and epidermal lamellae increases the contact area between the hoof wall and distal phalanx, which has been estimated to be up to 2.4 m^2 for a single hoof [90]. This lamellar structure ultimately dictates the mechanics of this interfacial tissue.

Though less work has been done to quantify the stress-strain behavior of the equine laminar junction, data available in the literature demonstrates non-linear, strain-hardening behavior similar to other soft tissues. This was shown to be true when the laminar junction is loaded in tension and shear [91]. Additionally, the spacing of primary epidermal lamellae varies throughout the laminar junction and is negatively correlated with regional stress magnitudes estimated computationally [92]. It has been suggested that this ensures even energy transfer between the hoof wall and appendicular skeleton during locomotion since more tightly packed lamella provide increased contact area and reduce the actual stress magnitudes generated during loading. It is possible that the morphology of the horn-horncore interface in bighorn sheep also increases the contact area microscopically in order to facilitate efficient energy transfer between the impacted horn and energy absorbing horncore. However, the laminar junction is unique as it acts as a suspensory apparatus to sling the distal phalanx within the hoof capsule. Conversely, ram horns are more rigidly attached to the bony horncore, similar to the rigid attachment of the keratin-rich rhamphotheca to the beak bones of avian species.

1.6.2. Avian Beaks

Beaks serve of variety of important biological functions in avian species including feeding, tool manipulation, sexual selection, and thermal regulation. While there is considerable variation in beak shape, size, and function among species, gross anatomical features of bird beaks are similar across species. Beaks are composed of the underlying premaxillary and mandibular bones (upper and lower jaw bones, respectively) covered by a dermis and epidermis [93]. Beak bones feature a dense, cortical bone shell filled with a trabecular bone architecture. The foam-like trabeculae provide structural support required for mechanical functions (i.e. seed crushing) while maintaining low weight required for flight. Studies have demonstrated correlations between trabecular bone organization and feeding habits, likely reflecting the adaptive nature of bone tissue discussed previously [94]. The microanatomy of the dermis and epidermis structures is less studied, but has been investigated in the black-capped chickadee and Darwin's finches.

The dermis of avian beaks, which is directly adjacent to the beak bones, contains connective tissue, blood vessels, nerves, and mechanosensory receptors including Herbst and Grandry corpuscles [95,96]. Additionally, in Java and Darwin's finches, the dermis is characterized by dense bundles of collagen fibers which regularly penetrate the adjacent cortical bone as Sharpey's fibers to anchor the dermis to the bone [96]. The epidermis is separated from the dermis by a thin basement membrane and is a layered structure composed of tightly packed keratinocytes.

Within the epidermis, keratinocytes migrate outward from the germinative layer to the fully cornified outer surface known as the rhamphotheca. The germiniative layer can be further divided into the stratum basale (inner most layer), stratum intermedium, and

stratum transitivum (outer most layer). The stratum basale is a single layer of columnar and/or cuboidal basal cells which forms a tight dermo-epidermal junction via interdigitations with the dermis visible between cells. The stratum intermedium is several cells thick and demonstrates nuclear degradation as cells migrate outward. Within the stratum transitivum, cells are polyhedral in shape and gradually flatten as they merge with the stratum corneum. Finally, the stratum corneum consists of lamina of squamous, denucleated, and fully cornified cells that form the rhamphotheca. While these descriptions are useful for understanding the attachment of the rhamphotheca to the beak bones, no work has been done to quantify the mechanical behavior of this interface. With that said, interdigitations of the dermo-epidermal junction may serve to increase the contact area of this interface to reduce stress magnitudes generated during loading, similar to the interdigitated structure of the equine laminar junction. Additionally, the presence of Sharpey's fibers may contribute to the rigidity of this interface since collagen is a tensile structure resistant to extension [96]. It's possible that similar mechanisms exist to reduce stress magnitudes and provide efficient load transfer between the horn and horncore in bighorn sheep during ramming.

1.7. Rationale for Dissertation Research

This research characterized the horncore bone tissue and connective tissue interface found in bighorn sheep horns, and investigated their roles in injury mitigation during ramming.

1.7.1. Specific Aims 1-2: Quantifying the composition, microstructure, and mechanical properties of bighorn sheep horncore cortical and velar bone.

Bighorn sheep do not show signs of injury after high-impact head-butting suggesting they may have evolved physiological mechanisms to mitigate brain trauma from head impacts. With growing concern surrounding brain injury in humans, there is motivation to investigate injury mitigation mechanisms involved in bighorn sheep ramming. Efforts to date have focused largely on the protective role of the keratin-rich horn and bony horncore since these structures typically bear the brunt of the collision. Horn material has demonstrated a remarkable ability to store energy under extreme deformation without permanent damage, especially during high-strain rate loading [23–26]. Additionally, computational models have shown that the bony horncore inside the horn plays a critical role in reducing post-impact brain cavity accelerations [13]. The latter findings have implications for brain injury mitigation in humans; however, the material properties of horncore bone tissue remain unknown.

The horncore is composed of a cortical bone shell filled with a unique porous bone architecture known as velar bone [20]. Although material properties of horncore cortical and velar bone remain unknown, other mammalian bone tissues have been studied extensively. It is well established that bone tissue adapts to its mechanical environment via alterations in tissue composition and microstructure [33,61]. Specifically, reduced mineral content leads to increased ductility while a higher prevalence of secondary osteons has been associate with increased energy absorption during loading [36,80]. Horncore cortical and velar bone are exposed to an extreme loading environment during ramming; thus, it's possible these tissues possess unique compositions and microstructures that provide

extraordinary energy absorption capacity well-suited for this environment. Here, we use common experimental methodology to explore these possibilities.

Here, the mechanical properties, composition, and microstructure of horncore cortical (Aim 1) and velar (Aim 2) bone tissues were quantified. Quasi-static three-point bend tests were used to measure the elastic modulus and estimate failure properties including ultimate strength and modulus of toughness. Velar bone was also subjected to dynamic mechanical analysis in order to quantify viscoelastic properties including storage modulus and loss factor. Additionally, microstructural features including tissue porosity and osteon population density were quantified via histological methods. Finally, bone mineral content of each tissue was calculated using a standard ashing procedure. Statistical methods were used to explore correlations between these variables to elucidate specific bone properties that may be important for dissipating energy and mitigating injury during ramming.

1.7.2. Specific Aim 3: Quantifying the composition, microstructure, and mechanical properties of bighorn sheep horn-horncore interfacial tissue.

Previous work has demonstrated that the bony horncore of bighorn sheep rams plays a critical role in storing impact energy during ramming [13]. In order for the horncore to store significant amounts of energy, efficient load transfer must occur between the impacted horn and internal horncore. However, little is known about the structure or mechanics of the connective tissue interface that anchors the horn to the horncore. With that said, similar horn-bone junctions are found elsewhere in nature, including equine hooves and avian beaks.

In equine hooves, the laminar junction slings the distal phalanx bone within the keratin-rich hoof and transfers the ground reaction force to the appendicular skeleton during locomotion. Load transfer is facilitated by the interdigitated structure of the dermo-epidermal junction. Interlocking lamellae increase the contact surface area between the hoof and bone, thereby reducing stress magnitudes generated during loading [88]. Regional differences in laminar spacing have been correlated to local variation in stress magnitudes throughout the laminar junction estimated computationally [90]. This variation is evidence of functional adaptation that provides evenly distributed energy transfer between the hoof wall and distal phalanx. A similar interdigitated microstructure may exist in bighorn sheep to provide efficient load transfer between the horn and horncore; however, gross observation revels the horn is rigidly attached to the horncore in bighorn sheep. This rigid attachment is more analogous to the dermo-epidermal junction of avian beaks than the suspensory apparatus found in equine hooves, thus the underlying microstructure may share similarities with avian beaks as well.

Avian beaks are grossly shaped by underlying upper and lower jaw bones which are each covered by a dermis and epidermis. The epidermis is several layers thick in which keratinocytes migrate from a single layer of cuboidal/columnar cells within the germinative layer to the flattened, fully keratinzed cell layers that form the rhamphotheca. At the innermost surface of the germanitive layer, interdigitations between cells of the stratum basale and dermis are observed, forming a tight dermo-epidermal junction. Then, within the dermis, bundles of collagen fibers frequently penetrate the adjacent cortical bone as Sharpey's fibers and anchor the dermis to the beak bones [95,96]. It seems likely that dermo-epidermal interdigitations increase contact surface area and reduce stress

magnitudes during mechanical loading similar to the equine laminar junction. Furthermore, the additional presence of Sharpey's fibers likely provide a more rigid interface than the suspensory apparatus of equine hooves due to collagen's resistence to extension [97]. However, no studies have been conducted on the mechanics of the rhamphotheca-bone interface to confirm this observation. With that said, it seems plausible that similar mechanisms exist in the horn-horncore interface of bighorn sheep to provide efficient load transfer between the impacted horn and energy absorbing horncore during ramming. Ultimately, understanding the microstructure, composition, and mechanics of this interface – as well as the structure-composition-property relationships between these quantified parameters – may inspire novel interface design for load transfer in impact applications.

This research used experimental methods to quantify the mechanical behavior, microstructure and composition of the horn-horncore interface and investigate correlations between the measured parameters. Lap-shear testing was used to measure the shear modulus and shear strength of the tissue. Standard histologic techniques were used to prepare thin sections of tissue to quantify microstructural features, and special stains were used to assess interfacial tissue composition. Mechanical test specimens and histological sections were prepared from samples taken from several regions of the horn-horncore interface in order to investigate regional variation in measured parameters via statistical methods. Additionally, predictive modeling was used to assess structure-composition-property relationships of the horn-horncore interface.

1.7.3. Specific Aim 4: Investigating the role of velar bone architecture in impact energy absorption.

The bony horncore of bighorn sheep rams has been shown to play a critical role in absorbing energy and reducing injury-related brain cavity accelerations during ramming. However, to this point, little work has been done to elucidate specific mechanisms of protection. The horncore is composed of a dense cortical bone shell filled with a porous bone architecture referred to as velar bone. Velar bone is similar to trabecular bone in that it resembles a cellular structure composed of many interconnected struts. The mechanics of cellular solids (porous bone architectures included) are governed by a combination of intrinsic material properties and geometric properties of the entire structure. While Aim 2 of this work will provide an improved understanding of velar bone properties at the tissue level, this aim will investigate the mechanical behavior of the gross velar bone architecture.

Porous bone architectures are commonly found in avian and mammalian species and provide adequate mechanical support at significantly reduced weight compared to a solid structure. This is important for living animals in order to reduce the metabolic cost of locomotion. Studies have shown that trabecular thickness (Tb.Th) and trabecular separation (Tb.Sp) scale allometrically in mammals, while bone volume fraction (BV/TV) remains relatively constant over a wide range of animal masses [47]. It has been suggested that this correlation is a geometric adaptation to limit local bone strains of individual trabeculae and prevent dangerous levels of micro damage accumulation [47]. Interestingly, while the BV/TV of velar bone (~20%) falls within the range of values reported for mammalian trabecular bone (~15-65%), velar thickness (2.87 ± 0.78 mm) and separation (11.91 ± 0.88 mm) are orders of magnitude larger than even the most massive animals

studied. Since the BV/TV of the velar bone architecture does not offer any substantial advantage in terms of reduced weight and metabolic cost of locomotion, it is curious why bighorn sheep have evolved this unique porous bone architecture. It's possible that this is another example of functional adaptation - in this case providing a structure well-suited to the demands of the dynamic high impact environment that the horncore is exposed to. Understanding how differences between velar and trabecular bone architectures influence the mechanical behavior of these structures in static and dynamic loading environments may provide insight into the design of lightweight structures for impact applications (helmets, vehicle crash boxes, etc.)

In this work, CT scan data was used to generate physiologically accurate finite element models of velar and trabecular bone architectures. Velar bone models were developed at a range of length scales and subjected to uniaxial compression in computational models to investigate velar bone mechanics are influenced by the size of the volume considered. Trabecular bone models were also subjected to idealized uniaxial compression to compare the energy storage capacity of velar and trabecular bone architectures. Furthermore, linear perturbation analysis was used to compare the buckling behavior of trabecular and velar bone architectures. Finally, structural indices (BV/TV, Tb.Th/V.Th, Tb.Sp/V.Sp) were quantified for the volume meshes used in finite element modeling and used to develop structure-property relationships for velar and trabecular bone architectures.

1.8. Hypotheses and Specific Aims

Hypothesis 1: Bighorn sheep horncore cortical bone has a lower mineral content and elastic modulus, but higher osteon population density and modulus of toughness than typical cortical bone tissue found in mammalian long bones and antlers.

Aim 1: Cortical bone was extracted from the horncore of six adult bighorn sheep rams with ages estimated from 3 – 8 years old to quantify cortical bone properties. Samples were prepared from bone tissue excised from regions of the horncore exposed to different stress modes (tension and compression) as demonstrated in computational modeling. Mechanical properties (elastic modulus, ultimate strength, and modulus of toughness) were measured through quasi-static three-point bend tests. Microstructural features (tissue porosity and osteon population density) were quantified through the preparation of semi-thick (~90 μm) sections of bone using standard histological techniques. Bone mineral content was determined using an ashing technique commonly applied to bone tissues. Student's t-test were used to compare measured properties between tensile and compressive regions of the horn. Linear regression was used to investigate correlations between quantified properties and horn curl length, using horn curl length as a surrogate measure of age and size. Additionally, stepwise linear regression was used to build predictive models of horncore cortical bone mechanical properties using curl length, tissue porosity, osteon population density, and bone mineral content as predictor variables. Finally, a one-way analysis of variance (ANOVA) was used to compare horncore cortical bone properties measured in this work to bone properties published for cortical bone taken from black bear femurs and red deer antler.

Hypothesis 2: Bighorn sheep horncore velar bone modulus of toughness is positively correlated with osteon population density, and the velar bone modulus of toughness and damping factor are negatively correlated with velar bone mineral content.

Aim 2: Velar bone struts were extracted from various anatomical regions of the horncore of four adult bighorn sheep rams estimated to be 5 – 8 years old. Struts were used to prepare prismatic beams of velar bone for mechanical testing. Mechanical test specimens were prepared such that the long axis of the beam reflects either longitudinal or transverse orientation within the horncore. Beams were subjected to dynamic mechanical analysis in a tensile loading configuration to determine the storage modulus and loss factor under a range of loading frequencies. Subsequently, beams were tested to failure under quasi-static three-point bending to determine the elastic properties including the elastic modulus, ultimate strength, and modulus of toughness. Following mechanical testing, one half of the fractured test specimens was subjected to ashing to determine bone mineral content, while the other half was used to prepare semi-thick (~90 μm) histological sections. Histological sections were stained with toluidine blue to quantify velar bone tissue porosity and osteon population density. Two-factor ANOVA was used to assess the differences in bone properties from samples with different positions and orientations within the horncore. Additionally, stepwise linear regression was used to create predictive models of velar bone mechanical properties using tissue porosity, osteon population density, and bone mineral content as independent variables.

Hypothesis 3: The horn-horncore interface is an interdigitated structure that increases surface contact area between horn and bone, and interface surface area is positively correlated with shear modulus and shear strength.

Aim 3: Horn-horncore interface sections were collected from four adult bighorn sheep rams (5 – 8 years old) to quantify interface properties. Proximal and distal sections were taken from each anatomical quadrant of the horn-horncore structure to investigate regional differences in interface properties. Sections were used to mill lap-shear specimens for mechanical testing to measure interface shear modulus and shear strength. Tissue longitudinally adjacent to lap-shear specimens was used to prepare thin (~7 μm) histological sections with transverse and longitudinal orientations. Histological sections were stained with Masson's trichrome to distinguish tissue components and estimate interface composition via area fractions. Additionally, average interface thickness and a surrogate measure of contact surface area were estimated through image analysis. A two-way ANOVA was used to investigate differences in measured properties due to longitudinal position and anatomical quadrant of interface samples. Furthermore, orientation-based differences in interface morphology were assed via paired t-tests. Additionally, stepwise linear regression was used to develop models to predict mechanical properties of the interface based on measured compositional and microstructural parameters.

Hypothesis 4: The unique velar bone architecture provides increased strain energy density and greater resistance to buckling compared to trabecular bone architectures with similar bone volume fractions.

Aim 4: A bighorn sheep ram skull was scanned using computed tomography and used to generate physiologically accurate volume meshes of velar bone architectures at various length scales. Computational modeling was used to simulate uniaxial compression of velar bone architectures and determine how the characteristic length of each model

influenced the mechanical behavior of velar bone. Physiologically accurate volume meshes of trabecular bone architectures were created using similar methodology from μCT scan data made available by previous researchers [47,98]. Trabecular bone architectures were subjected subject to uniaxial compression to compare the energy storage capacity of velar and trabecular bone architectures with similar BV/TV. In addition, velar and trabecular bone models were subjected to linear perturbation analyses to compared the buckling behavior of these two distinct porous bone architectures. Structural indices were calculated for all the volume meshes used in finite element models and used to explore structure-property relationships of velar and trabecular bone architectures.

1.9. References

[1] Centers for Disease Control and Prevention, Report to Congress on Traumatic Brain Injury in the United States: Epidemiology and Rehabilitation, National Center for Injury Prevention and Control; Division of Unitentional Injury Prevention. Atlanta, GA. (2015).

[2] Centers for Disease Control and Prevention, Report to Congress on Mild Traumatic Brain Injury in the United States: Steps to Prevent a Serious Public Health Problem, Atlanta, GA: Centers for Disease Control and Prevention. (2003).

[3] J.D. Cassidy, L.J. Carroll, P.M. Peloso, J. Borg, H. von Holst, L. Holm, J. Kraus, V.G. Coronado, Incidence, risk factors and prevention of mild traumatic brain injury: Results of the WHO Collaborating Centre Task Force on Mild Traumatic Brain Injury, J Rehabil Med Suppl. (2004) 28–60. https://doi.org/10.1080/16501960410023732.

[4] D.H. Daneshvar, L.E. Goldstein, P.T. Kiernan, T.D. Stein, A.C. McKee, Post-traumatic neurodegeneration and chronic traumatic encephalopathy, Molecular and Cellular Neuroscience. 66 (2015) 81–90. https://doi.org/10.1016/j.mcn.2015.03.007.

[5] N.W.B. Finkbeiner, J.E. Max, S. Longman, C. Debert, Knowing what we don't know: Long-term psychiatric outcomes following adult concussion in sports, Canadian Journal of Psychiatry. 61 (2016) 270–276. https://doi.org/10.1177/0706743716644953.

[6] Z.Y. Kerr, S.W. Marshall, H.P. Harding, K.M. Guskiewicz, Nine-year risk of depression diagnosis increases with increasing self-reported concussions in retired professional football players, American Journal of Sports Medicine. 40 (2012) 2206–2212. https://doi.org/10.1177/0363546512456193.

[7] K.M. Guskiewicz, S.W. Marshall, J. Bailes, M. Mccrea, H.P. Harding, A. Matthews, J.R. Mihalik, R.C. Cantu, Recurrent concussion and risk of depression in retired professional football players, Med Sci Sports Exerc. 39 (2007) 903–909. https://doi.org/10.1249/mss.0b013e3180383da5.

[8] C. Bergamo, Traumatic brain injury and risk of dementia in older veterans: Barnes DE, Kaup A, Kirby KA, et al. Neurology 2014;83:312-9., Journal of Emergency Medicine. 47 (2014) 617–618. https://doi.org/10.1016/j.jemermed.2014.09.023.

[9] J.H. Bower, D.M. Maraganore, B.J. Peterson, S.K. McDonnell, J.E. Ahlskog, W.A. Rocca, Head trauma preceding PD: A case-control study, Neurology. 60 (2003) 1610–1615. https://doi.org/10.1212/01.WNL.0000068008.78394.2C.

[10] D. Meaney, D. Smith, Biomechanics of concussion, Concussion. 30 (2012) 14–27. https://doi.org/10.1159/000358748.

[11] G. DiGiacomo, S. Tsai, M. Bottlang, Impact Performance Comparison of Advanced Snow Sport Helmets with Dedicated Rotation-Damping Systems, Ann Biomed Eng. 49 (2021) 2805–2813. https://doi.org/10.1007/s10439-021-02723-0.

[12] S.J. Bonin, A.L. DeMarco, G.P. Siegmund, The Effect of MIPS, Headform Condition, and Impact Orientation on Headform Kinematics Across a Range of Impact Speeds During Oblique Bicycle Helmet Impacts, Ann Biomed Eng. 50 (2022) 860–870. https://doi.org/10.1007/s10439-022-02961-w.

[13] A. Drake, T.L. Haut Donahue, M. Stansloski, K. Fox, B.B. Wheatley, S.W. Donahue, Horn and horn core trabecular bone of bighorn sheep rams absorbs impact energy and reduces brain cavity accelerations during high impact ramming of the skull, Acta Biomater. 44 (2016) 41–50. https://doi.org/10.1016/j.actbio.2016.08.019.

[14] Y.Z. Liu, X.M. Qiu, H.L. Ma, W.W. Fu, T.X. Yu, A study of woodpecker's pecking process and the impact response of its brain, Int J Impact Eng. 108 (2017) 263–271. https://doi.org/10.1016/j.ijimpeng.2017.05.016.

[15] P.R.A. May, J.M. Fuster, J. Haber, A. Hirschman, Woodpecker Drilling Behavior: An Endorsement of the Rotational Theory of Impact Brain Injury, Arch Neurol. 36 (1979) 370–373. https://doi.org/10.1001/archneur.1979.00500420080011.

[16] K.M. Guskiewicz, J.P. Mihalik, V. Shankar, S.W. Marshall, D.H. Crowell, S.M. Oliaro, M.F. Ciocca, D.N. Hooker, Measurement of head impacts in collegiate football players: Relationship between head impact biomechanics and acute clinical outcome after concussion, Injury Prevention. 61 (2007) 1244–1253. https://doi.org/10.1227/01.NEU.0000280146.37163.79.

[17] G. Farah, D. Siwek, P. Cummings, Tau accumulations in the brains of woodpeckers, PLoS One. 13 (2018) 1–12. https://doi.org/10.1371/journal.pone.0191526.

[18] N.L. Ackermans, M. Varghese, T.M. Williams, N. Grimaldi, E. Selmanovic, A. Alipour, P. Balchandani, J.S. Reidenberg, P.R. Hof, Evidence of traumatic brain injury in headbutting bovids, Acta Neuropathol. (2022). https://doi.org/10.1007/s00401-022-02427-2.

[19] S.H. Yoon, S. Park, A mechanical analysis of woodpecker drumming and its application to shock-absorbing systems, Bioinspir Biomim. 6 (2011). https://doi.org/10.1088/1748-3182/6/1/016003.

[20] T.W. Seek, Exploration of Unique Porous Bone Materials for Candidacy in Bioinspired Material Design, Masters Thesis, Colorado State University, 2018.

[21] J. McKittrick, P.Y. Chen, S.G. Bodde, W. Yang, E.E. Novitskaya, M.A. Meyers, The structure, functions, and mechanical properties of keratin, Jom. 64 (2012) 449–468. https://doi.org/10.1007/s11837-012-0302-8.

[22] H.H. Bragulla, D.G. Homberger, Structure and functions of keratin proteins in simple, stratified, keratinized and cornified epithelia, J Anat. 214 (2009) 516–559. https://doi.org/10.1111/j.1469-7580.2009.01066.x.

[23] W. Huang, A. Zaheri, J.-Y. Jung, H.D. Espinosa, J. Mckittrick, Hierarchical structure and compressive deformation mechanisms of bighorn sheep (Ovis canadensis) horn, Acta Biomater. 64 (2017) 1–14. https://doi.org/10.1016/j.actbio.2017.09.043.

[24] L. Tombolato, E.E. Novitskaya, P.Y. Chen, F.A. Sheppard, J. McKittrick, Microstructure, elastic properties and deformation mechanisms of horn keratin, Acta Biomater. 6 (2010) 319–330. https://doi.org/10.1016/j.actbio.2009.06.033.

[25] M.W. Trim, M.F. Horstemeyer, H. Rhee, H. el Kadiri, L.N. Williams, J. Liao, K.B. Walters, J. McKittrick, S.-J. Park, The effects of water and microstructure on the mechanical properties of bighorn sheep (Ovis canadensis) horn keratin., Acta Biomater. 7 (2011) 1228–40. https://doi.org/10.1016/j.actbio.2010.11.024.

[26] K.L. Johnson, M.W. Trim, D.K. Francis, W.R. Whittington, J.A. Miller, C.E. Bennett, M.F. Horstemeyer, Moisture, anisotropy, stress state, and strain rate effects on bighorn sheep horn keratin mechanical properties, Acta Biomater. 48 (2017) 300–308. https://doi.org/10.1016/j.actbio.2016.10.033.

[27] P. Maity, S.A. Tekalur, Finite element analysis of ramming in Ovis canadensis, J Biomech Eng. 133 (2011) 1–9. https://doi.org/10.1115/1.4003321.

[28] J.Y. Rho, L. Kuhn-Spearing, P. Zioupos, Mechanical properties and the hierarchical structure of bone, Med Eng Phys. 20 (1998) 92–102. https://doi.org/10.1016/S1350-4533(98)00007-1.

[29] Y. Liu, D. Luo, T. Wang, Hierarchical Structures of Bone and Bioinspired Bone Tissue Engineering, Small. 12 (2016) 4611–4632. https://doi.org/10.1002/smll.201600626.

[30] S. Weiner, W. Traub, Bone structure: from ångstroms to microns, The FASEB Journal. 6 (1992) 879–885. https://doi.org/10.1096/fasebj.6.3.1740237.

[31] W.J. Landis, R. Jacquet, Association of calcium and phosphate ions with collagen in the mineralization of vertebrate tissues, Calcif Tissue Int. 93 (2013) 329–337. https://doi.org/10.1007/s00223-013-9725-7.

[32] V. Ziv, S. Weiner, Bone Crystal Sizes: A Comparison of Transmission Electron Microscope and X-Ray Diffraction Line Width Broadening Techniques, Connect Tissue Res. 30 (1994) 165–175.

[33] J.D. Currey, The many adaptations of bone, J Biomech. 36 (2003) 1487–1495. https://doi.org/10.1016/S0021-9290(03)00124-6.

[34] M.M. Giraud-Guille, Twisted plywood architecture of collagen fibrils in human compact bone osteons, Calcif Tissue Int. 42 (1988) 167–180.

[35] S.A. Reid, A study of lamellar oranisation in juvenile and adult human bone, Anat Embryol (Berl). 174 (1986) 329–338.

[36] J.D. Currey, The Effect of Porosity and Mineral Content on the Young's Modulus of Elasticity of Compact Bone, J Biomech. 21 (1988) 131–139.

[37] J.D. Frank, M. Ryan, V.L. Kalscheur, C.P. Ruaux-Mason, R.R. Hozak, P. Muir, Aging and accumulation of microdamage in canine bone, Bone. 30 (2002) 201–206. https://doi.org/10.1016/S8756-3282(01)00623-8.

[38] K.B. Harvey, S.W. Donahue, Bending properties, porosity, and ash fraction of black bear (Ursus americanus) cortical bone are not compromised with aging despite

annual periods of disuse, J Biomech. 37 (2004) 1513–1520. https://doi.org/10.1016/j.jbiomech.2004.01.010.

[39] M.E. McGee-Lawrence, S.J. Wojda, L.N. Barlow, T.D. Drummer, K. Bunnell, J. Auger, H.L. Black, S.W. Donahue, Six months of disuse during hibernation does not increase intracortical porosity or decrease cortical bone geometry, strength, or mineralization in black bear (Ursus americanus) femurs, J Biomech. 42 (2009) 1378–1383. https://doi.org/10.1016/j.jbiomech.2008.11.039.

[40] T. Landete-Castillejos, J.D. Currey, F. Ceacero, A.J. García, L. Gallego, S. Gomez, Does nutrition affect bone porosity and mineral tissue distribution in deer antlers? The relationship between histology, mechanical properties and mineral composition, Bone. 50 (2012) 245–254. https://doi.org/10.1016/j.bone.2011.10.026.

[41] D.B. Burr, M.B. Schaffler, R.G. Frederickson, Composition of the cement line and its possible mechanical role as a local interface in human compact bone., J Biomech. 21 (1988) 939–945. https://doi.org/10.1016/0021-9290(88)90132-7.

[42] S.J. Wojda, D.R. Weyland, S.K. Gray, M.E. Mcgee-Lawrence, T.D. Drummer, S.W. Donahue, Black bears with longer disuse (hibernation) periods have lower femoral osteon population density and greater mineralization and intracortical porosity, Anatomical Record. 296 (2013) 1148–1153. https://doi.org/10.1002/ar.22720.

[43] E.F. Morgan, G.U. Unnikrisnan, A.I. Hussein, Bone Mechanical Properties in Healthy and Diseased States, Annu Rev Biomed Eng. 20 (2018) 119–143. https://doi.org/10.1146/annurev-bioeng-062117-121139.

[44] S.W. Donahue, S.A. Galley, Microdamage in Bone: Implications for Fracture, Repair, Remodeling, and Adaptation, Crit Rev Biomed Eng. 34 (2012) 215–271. https://doi.org/10.1615/critrevbiomedeng.v34.i3.20.

[45] R.B. Martin, D.B. Burr, Structure, Function, and Adaptation of Compact Bone, Raven Press, New York, 1989.

[46] M.B. Schaffler, D.B. Burr, R.G. Frederickson, Morphology of the osteonal cement line in human bone., Anat Rec. 217 (1987) 223–228. https://doi.org/10.1002/ar.1092170302.

[47] M. Doube, M.M. Kłosowski, A.M. Wiktorowicz-Conroy, J.R. Hutchinson, S.J. Shefelbine, Trabecular bone scales allometrically in mammals and birds, Proceedings of the Royal Society B: Biological Sciences. 278 (2011) 3067–3073. https://doi.org/10.1098/rspb.2011.0069.

[48] A.M. Parfitt, M.K. Drezner, F.H. Glorieux, J.A. Kanis, H. Malluche, P.J. Meunier, S.M. Ott, R.R. Recker, Bone histomorphometry: Standardization of nomenclature, symbols, and units: Report of the asbmr histomorphometry nomenclature committee, Journal of Bone and Mineral Research. 2 (1987) 595–610.

[49] A. Odgaard, Three-dimensional methods for quantification of cancellous bone architecture, Bone. 20 (1997) 315–328. https://doi.org/10.1016/S8756-3282(97)00007-0.

[50] W.S.S. Jee, Skeletal Development, in: S.C. Cowin (Ed.), Bone Mechanics Handbook, Second, CRC Press LLC, 2001: pp. 24–33.

[51] C.T. Rubin, L.E. Lanyon, Regulation of bone mass by mechanical strain magnitude, Calcif Tissue Int. 37 (1985) 411–417.

[52] C.T. Rubin, L.E. Lanyon, Dynamic strain similarity in vertebrates; an alternative to allometric limb bone scaling, J Theor Biol. 107 (1984) 321–327.

[53] H.K. Uhthoff, Z.F.G. Jaworski, Bone loss in response to long-term immobilisation, J Bone Joint Surg. 60-B (1978) 420–429.

[54] Ph. Collet, D. Uebelhart, L. Vico, L. Moro, D. Hartmann, M. Roth, C. Alexandre, Effects of 1- and 6-Month Spaceflight on Bone Mass and Biochemistry in Two Humans, Bone. 20 (1997) 547–551.

[55] S.L. Bass, L. Saxon, R.M. Daly, C.H. Turner, A.G. Robling, E. Seeman, S. Stuckey, The effect of mechanical loading on the size and shape of bone in pre-, peri-, and postpubertal girls: A study in tennis players, Journal of Bone and Mineral Research. 17 (2002) 2274–2280. https://doi.org/10.1359/jbmr.2002.17.12.2274.

[56] E.J. Bassey, S.J. Ramsdale, Increase in femoral bone density in young women following high-impact exercise, Osteoporosis International. 4 (1994) 72–75.

[57] A.E. Goodship, L.E. Lanyon, H. McFie, Functional adaptation of bone to increased stress: An experimental study, Journal of Bone and Joint Surgery. 61 (1979) 539–546.

[58] A.E. Churches, D.C.R. Howlett, Functional Adaptation of Bone in Response to Sinusoidally Varying Controlled Compressive Loading of the Ovine Metacarpus, Clin Orthop Relat Res. 168 (1982) 265–280.

[59] T.J. Chambers, M. Evans, T.N. Gardner, A. Turner-Smith, J.W.M. Chow, Induction of bone formation in rat tail vertebrae by mechanical loading, Bone Miner. 20 (1993) 167–178.

[60] J. Sanchis-Moysi, C. Dorado, G. Vicente-Rodríguez, L. Milutinovic, G.L. Garces, J.A.L. Calbet, Inter-arm asymmetry in bone mineral content and bone area in postmenopausal recreational tennis players, Maturitas. 48 (2004) 289–298. https://doi.org/10.1016/j.maturitas.2004.03.008.

[61] J.D. Currey, Mechanical properties of bone tissues with greatly differing functions, J Biomech. 12 (1979) 313–319. https://doi.org/10.1016/0021-9290(79)90073-3.

[62] A.H. Burstein, J.M. Zika, K.G. Heiple, L. Klein, Contribution of collagen and mineral to the elastic-plastic properties of bone, J Bone Joint Surg. 57-A (1975) 956–961.

[63] X.E. Guo, Mechanical Properties of Cortical Bone and Cancellous Bone Tissue, in: S.C. Cowin (Ed.), Bone Mechanics Handbook, Second, CRC Press LLC, 2001: pp. 10.1-10.23.

[64] J.Y. Rho, R.B. Ashman, C.H. Turner, Young's Modulus of Trabecular and Cortical Bone Material: Ultrasonic and Microtensile Measurements, J Biomech. 26 (1993) 111–119.

[65] K. Choi, S.A. Goldstein, A comparison of the fatigue behavior of human trabecular and cortical bone tissue, J Biomech. 25 (1992) 1371–1381. https://doi.org/10.1016/0021-9290(92)90051-2.

[66] K. Choi, J.L. Kuhn, M.J. Ciarelli, S.A. Goldstein, The Elastic Moduli of Human Subchondral, Trabecular, and Cortical Bone Tissue and the Size Dependency of Cortical Bone Modulus, J. Biomechanics. 23 (1990) 1103–1113. https://doi.org/10.1016/0021-9290(90)90003-L.

[67] J.L. Kuhn, S.A. Goldstein, R. Choi, M. London, L.A. Feldkamp, L.S. Matthews, Comparison of the trabecular and cortical tissue moduli from human iliac crests, Journal of Orthopaedic Research. 7 (1989) 876–884. https://doi.org/10.1002/jor.1100070614.

[68] J.D. Currey, Tensile yield in compact bone is determined by strain, post-yield behaviour by mineral content, J Biomech. 37 (2004) 549–556. https://doi.org/10.1016/j.jbiomech.2003.08.008.

[69] J.D. Currey, G. Butler, The mechanical properties of bone tissue in children, Journal of Bone and Joint Surgery - American Volume. 57 (1975) 810–814.

[70] J.D. Currey, K. Brear, Hardness, Young's modulus and yield stress in mammalian mineralized tissues, J Mater Sci Mater Med. 1 (1990) 14–20. https://doi.org/10.1007/BF00705348.

[71] J. Lei, L. Li, Z. Wang, F. Zhu, Characterizing Strain Rate-Dependent Mechanical Properties for Bovine Cortical Bones, J Biomech Eng. 142 (2020) 1–8. https://doi.org/10.1115/1.4046690.

[72] U. Hansen, P. Zioupos, R. Simpson, J.D. Currey, D. Hynd, The effect of strain rate on the mechanical properties of human cortical bone, J Biomech Eng. 130 (2008) 1–8. https://doi.org/10.1115/1.2838032.

[73] J. Yamashita, B.R. Furman, H.R. Rawls, X. Wang, C.M. Agrawal, The use of dynamic mechanical analysis to assess the viscoelastic properties of human cortical bone, J Biomed Mater Res. 58 (2001) 47–53. https://doi.org/10.1002/1097-4636(2001)58:1<47::AID-JBM70>3.0.CO;2-U.

[74] A.A. Abdel-Wahab, K. Alam, V. v. Silberschmidt, Analysis of anisotropic viscoelastoplastic properties of cortical bone tissues, J Mech Behav Biomed Mater. 4 (2011) 807–820. https://doi.org/10.1016/j.jmbbm.2010.10.001.

[75] D.T. Reilly, A.H. Burstein, The elastic and ultimate properties of compact bone tissue., J Biomech. 8 (1975) 393–405. https://doi.org/10.1016/0021-9290(75)90075-5.

[76] M.B. Schaffler, D.B. Burr, Stiffness of compact bone: effects of porosity and density, J Biomech. 21 (1988) 13–16.

[77] D. Vashishth, J.C. Behiri, W. Bonfield, Crack growth resistance in cortical bone: Concept of microcrack toughening, J Biomech. 30 (1997) 763–769. https://doi.org/10.1016/S0021-9290(97)00029-8.

[78] O. Akkus, K.J. Jepsen, C.M. Rimnac, Microstructural aspects of the fracture process in human cortical bone, J Mater Sci. 35 (2000) 6065–6074. https://doi.org/10.1023/A:1026719531300.

[79] M.E. Launey, M.J. Buehler, R.O. Ritchie, On the mechanistic origins of toughness in bone, 2010. https://doi.org/10.1146/annurev-matsci-070909-104427.

[80] Y.N. Yeni, C.U. Brown, Z. Wang, T.L. Norman, The influence of bone morphology on fracture toughness of the human femur and tibia, Bone. 21 (1997) 453–459. https://doi.org/10.1016/S8756-3282(97)00173-7.

[81] F.J.O. Brien, D. Taylor, T.C. Lee, The effect of bone microstructure on the initiation and growth of microcracks, Journal of Orthopaedic Research. 23 (2005).

[82] S. Mohsin, F.J. O'Brien, T.C. Lee, Osteonal crack barriers in ovine compact bone, J Anat. 208 (2006) 81–89. https://doi.org/10.1111/j.1469-7580.2006.00509.x.

[83] Z. Seref-Ferlengez, O.D. Kennedy, M.B. Schaffler, Bone microdamage, remodeling and bone fragility: how much damage is too much damage?, Bonekey Rep. 4 (2015) 1–7. https://doi.org/10.1038/bonekey.2015.11.

[84] T.P. Gocha, A.M. Agnew, Spatial variation in osteon population density at the human femoral midshaft: Histomorphometric adaptations to habitual load environment, J Anat. (2016). https://doi.org/10.1111/joa.12433.

[85] T.G. Aguirre, A. Ingrole, L. Fuller, T.W. Seek, A.R. Fiorillo, J.J.W. Sertich, S.W. Donahue, Differing trabecular bone architecture in dinosaurs and mammals contribute to stiffness and limits on bone strain, PLoS One. 15 (2020) 1–20. https://doi.org/10.1371/journal.pone.0237042.

[86] S.N. Musy, G. Maquer, J. Panyasantisuk, J. Wandel, P.K. Zysset, Not only stiffness, but also yield strength of the trabecular structure determined by non-linear μFE is best predicted by bone volume fraction and fabric tensor, J Mech Behav Biomed Mater. 65 (2017) 808–813. https://doi.org/10.1016/j.jmbbm.2016.10.004.

[87] G. Maquer, S.N. Musy, J. Wandel, T. Gross, P.K. Zysset, Bone volume fraction and fabric anisotropy are better determinants of trabecular bone stiffness than other morphological variables, Journal of Bone and Mineral Research. 30 (2015) 1000–1008. https://doi.org/10.1002/jbmr.2437.

[88] C.C. Pollitt, Clinical anatomy and physiology of the normal equine foot, Equine Vet Educ. 4 (1992) 219–224.

[89] J.L. Lanovaz, H.M. Clayton, L.G. Watson, In vitro attenuation of impact shock in equine digits, Equine Vet J. 26 (1998) 96–102.

[90] B. Faramarzi, Morphological and biomechanical properties of equine laminar junction, J Equine Vet Sci. 34 (2014) 589–592. https://doi.org/10.1016/j.jevs.2013.12.007.

[91] J.E. Douglas, T.L. Biddick, J.J. Thomason, J.C. Jofriet, Stress/strain behaviour of the equine laminar junction, Journal of Experimental Biology. 201 (1998) 2287–2297.

[92] J.J. Thomason, H.L. McClinchey, B. Faramarzi, J.C. Jofriet, Mechanical behavior and quantitative morphology of the equine laminar junction, Anatomical Record - Part A Discoveries in Molecular, Cellular, and Evolutionary Biology. 283 (2005) 366–379. https://doi.org/10.1002/ar.a.20173.

[93] P.R. Stettenheim, The integumentary morphology of modern birds-an overview, Am Zool. 40 (2000) 461–477. https://doi.org/10.1093/icb/40.4.461.

[94] J. Soons, A. Genbrugge, J. Podos, D. Adriaens, P. Aerts, J. Dirckx, A. Herrel, Is beak morphology in Darwin's finches tuned to loading demands?, PLoS One. 10 (2015). https://doi.org/10.1371/journal.pone.0129479.

[95] C. van Hemert, C.M. Handel, J.E. Blake, R.M. Swor, T.M. O'Hara, Microanatomy of passerine hard-cornified tissues: Beak and claw structure of the black-capped chickadee (Poecile atricapillus), J Morphol. 273 (2012) 226–240. https://doi.org/10.1002/jmor.11023.

[96] A. Genbrugge, D. Adriaens, B. De Kegel, L. Brabant, L. Van Hoorebeke, J. Podos, J. Dirckx, P. Aerts, A. Herrel, Structural tissue organization in the beak of Java and Darwin's finches, J Anat. 221 (2012) 383–393. https://doi.org/10.1111/j.1469-7580.2012.01561.x.

[97] S.A. Wainwright, W.D. Biggs, J.D. Currey, J.M. Gosline, Collagen, in: Mechanical Design in Organisms, Halsted Press, 1976: pp. 81–94.

[98] M. Doube, M.M. Kłosowski, J. Hutchinson, S.J. Shefelbine, X-ray microtomography images of trabecular bone from the femoral head and condyle of 18 avian, 72 mammalian and one crocodilian species., (2018). https://doi.org/10.6084/m9.figshare.7257179.v1.

[99] U.G.K. Wegst, H. Bai, E. Saiz, A.P. Tomsia, R.O. Ritchie, Bioinspired structural materials, Nat Mater. 14 (2015) 23–36. https://doi.org/10.1038/nmat4089.

CHAPTER 2

2. HORNCORE CORTICAL BONE CHARACTERIZATION

Material properties of bighorn sheep (*Ovis canadensis*) horncore bone with implications for energy absorption during impacts

Luca H. Fuller, Seth W. Donahue

Published in the Journal of the Mechanical Behavior of Biomedical Materials, 2021

J Mech Behav Biomed Mater 114, 2021

2.1. Abstract

Bighorn sheep rams participate in high impact head-butting without overt signs of brain injury, thus providing a naturally occurring animal model for studying brain injury mitigation. Previously published finite element modeling showed that both the horn and bone materials play important roles in reducing brain cavity accelerations during ramming. However, in that study the elastic modulus of bone was assumed to be similar to that of human bone since the modulus of ram bone was unknown. Therefore, the goal of this study was to quantify the mechanical properties, mineral content, porosity, and microstructural organization of horncore cortical bone from juvenile and adult rams. Mineral content and elastic modulus increased with horn size, and porosity decreased. However, modulus of toughness did not change with horn size. This latter finding raises the possibility that the horncore cortical bone has not adapted exceptional toughness despite an extreme loading environment and may function primarily as an interface material between the horn and the porous bone within the horncore. Thus, geometric properties of the horn and horncore,

including the porous bone architecture, may be more important for energy absorption during ramming than the horncore cortical bone. Results from this study can be used to improve accuracy of finite element models of bighorn sheep ramming to investigate these possibilities moving forward.

2.2. Introduction

Athletes and military personnel are commonly diagnosed with concussions after experiencing head trauma from collisions or falls [1,2]. Repeated concussions, also known as mild traumatic brain injuries (mTBIs), can lead to several conditions of long-term neurodegeneration including chronic traumatic encephalopathy [3,4]. Currently available helmets are effective in preventing severe TBI and skull fracture, however, efficacy in preventing concussion is less evident [5]. Concussion etiology is not fully understood, but many investigations have demonstrated a correlation between translational and rotational head accelerations and clinical diagnosis of mTBI [6]. Studies involving head impact in football have demonstrated a range of head accelerations linked to concussive injury, with average translational accelerations leading to brain injury frequently reported near 100 g [6–8]. Ultimately, these findings have motivated the research and development of novel head protection systems aimed at reducing brain cavity accelerations in order to prevent concussive injury [9].

One avenue for developing state-of-the-art head protection is studying the injury mitigation mechanisms employed by animals that experience frequent head impacts such as bighorn sheep (*Ovis canadensis*) and woodpeckers [10–16]. In nature, male bighorn sheep experience repetitive head impacts as they butt heads to establish dominance and

earn mating privileges. Brain cavity translational accelerations during these collisions have been estimated near 400 g in computational studies, much larger than head-to-head collisions in football players [16]. Similarly, woodpeckers' high impact pecking behavior can lead to translational accelerations as high as 1000 g [14,15]. While recent evidence has debunked previous theories that woodpeckers entirely prevent brain injury [17], the absence of overt concussive symptoms supports the idea that woodpeckers have mechanisms to mitigate TBI despite high impact head collisions. Naturally occurring animal models can be insightful for understanding how to prevent and treat injuries in humans [18]. The goal of this study was to quantify the material behavior of the cortical bone in bighorn sheep horncores, which will help us understand how these animals evolved mechanisms to mitigate brain injury during head impacts. These findings may also guide bioinspired designs that mitigate concussive injuries in humans.

Bighorn sheep horns are permanent cranial appendages composed of a bony horncore projecting from the skull covered by a keratin horn. The bony horncore consists of a dense cortical bone shell filled with porous bone that resembles enlarged trabecular bone (Figure 2-1). The porous bone architecture has a bone volume fraction similar to trabecular bone (~20%), but its strut thickness (~3 mm) and separation (~12 mm) are considerably larger than in trabecular bone [19]. To date, most research has focused on characterizing the horn material [10–13].

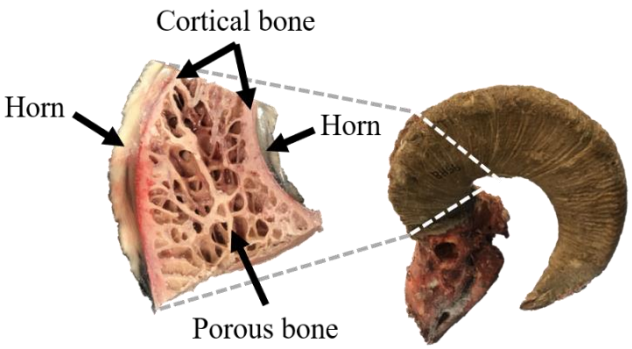

Figure 2-1. A longitudinal section of the proximal region of the horn showing the organization of bone

However, a computational study of bighorn sheep ramming demonstrated that the bony horncore plays a larger role than the horn in energy storage and the reduction of brain cavity accelerations [16].

One advantage of the bony horncore absorbing more energy than the horn is bone's ability to self-repair mechanically induced damage via targeted bone remodeling [20–22]. Bone remodeling replaces primary bone with secondary bone and results in histological features known as secondary osteons. The peripheral cement lines of secondary osteons make them distinguishable from primary osteons, which lack cement lines [23,24]. Cement lines toughen cortical bone by arresting and deflecting cracks [25,26]. The resulting accumulation of microdamage and formation of torturous crack patterns dissipates energy and limits crack length [27,28]. Thus, it is not surprising that osteon population density has been positively correlated with bone toughness [29]. While extensive levels of microdamage accumulation can impair bone properties and lead to stress fractures [30,31], healthy bone tissue uses targeted remodeling to repair mechanical damage before failure occurs [20–22]. Additionally, selective pressures have led to many bone tissues with specialized compositions that provide mechanical properties tuned to meet various functional requirements [32,33]. For example, red deer antler has a relatively low mineral content compared to bovine femur which provides the increased toughness antlers need to perform well in interspecies combat [34]. Therefore, considering the large magnitude impact loading that arises during bighorn head-butting, we hypothesized that horncore cortical bone from bighorn sheep has a lower mineral content and elastic modulus, but higher osteon population density and modulus of toughness than typical cortical bone tissue found in mammalian long bones and antlers. The aims of this study were to quantify the

composition, microstructure, and mechanical properties of horncore cortical bone tissue from bighorn sheep rams.

2.3. Materials and Methods

2.3.1. Samples

Six (n=6) male bighorn sheep skulls were provided for research purposes by the Colorado Department of Natural Resources under Colorado Parks and Wildlife scientific collection license number 14SALV2052A2. The skulls were obtained from sheep that were killed by motor vehicle accidents and frozen shortly after death. One animal had inadequate tag information to determine collection date, but other deaths occurred in May (n=1), June (n=3), or November (n=1). Animal ages were not certain due to circumstantial deaths but were estimated between 3 – 8 years old by counting annual growth rings on the horns [35]. Since bighorn sheep rams typically reach sexual maturity around 2.5 years old, younger rams in this study likely have little or no ramming history while older rams could have participated in five or more seasonal ruts prior to death [36]. Additionally, horn curl lengths were measured from the proximal point of skull attachment to the distal horn tip along the outermost surface of the horn. Since horns are grown throughout the life of a sheep, horn length measurements can provide surrogates of animal age and size. The two youngest rams had notably smaller curl lengths (51 and 54 cm) corresponding to approximately half of a full curl rotation. The other rams had curl lengths ranging from 71 – 85 cm, corresponding to approximately 5/8 – 1 full curl rotation. Following horn length measurements, the left horn was separated from the skull using a hacksaw, then a transverse

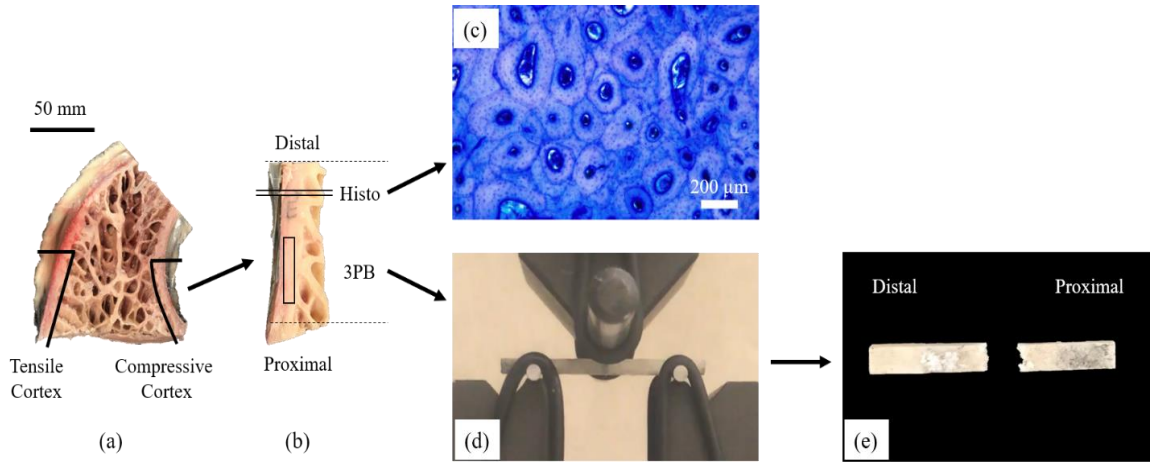

Figure 2-2. (a) Longitudinal sections of bighorn sheep horns were cut to expose tensile and compressive stress cortices of the horncore. (b) Sections of cortical bone 60 mm long (between the dashed lines) were removed from tensile and compressive cortices using a bandsaw and separated from the horn using a scalpel. (c) Histology slides were prepared from the distal portion of cortical bone sections. (d) Cortical bone mechanical test coupons (30 mm long) were prepared from the proximal portion of cortical bone sections and loaded to failure in three-point bending. (e) The distal half of the fractured coupon was used for mineral content quantification.

section was cut from the proximal end of the horn. Next, each proximal section of horn was divided longitudinally into medial and lateral halves to separate the regions that experience high tensile and compressive stresses during ramming (Figure 2-2a). Stress distributions from finite element models of bighorn sheep ramming were used to determine regions of maximum compressive and tensile stresses (anteriomedial and posteriolateral cortices of the horn, respectively) [16].

2.3.2. Mechanical Testing

Test samples for three-point bending were milled into prismatic beams with dimensions of 2 mm x 3.5 mm x 30 mm (thickness x width x length) using a CNC mill as previously done for cortical bone samples from long bones [37,38]. Machining was performed such that the long axis of each beam corresponded to the growth direction of the horncore. The width and depth of each beam were aligned approximately

circumferentially and radially in the horncore, respectively. Machining was performed on samples submerged in water to provide lubrication, cooling, and hydration. Samples were polished using 800 grit silicon carbide paper to remove surface defects. Average cross-sectional dimensions of polished beams were determined to the nearest 0.01 mm using digital caliper measurements taken at five equally spaced points along the 20 mm test span. Test specimens were wrapped in saline soaked gauze and kept frozen at -20 °C prior to testing; previous studies indicate that this is an effective means of preserving the mechanical properties of bone tissue postmortem [39–41].

Beam specimens were loaded to failure in three-point bending based on American Society for Testing and Materials Standard D5934-96 using a span of 20 mm. The periosteal surface was tested in tension for samples collected from tensile stress cortices and in compression for samples harvested from compressive stress cortices. This reflects the stress state that the periosteal surfaces in these cortices would experience during ramming. Samples were thawed in a solution of 0.9% saline at room temperature for at least 30 minutes, then kept wrapped in saline soaked gauze until immediately prior to testing. Three-point bend tests were performed in air using a constant crosshead speed of 1 mm s^{-1} while the applied force and beam displacement were measured using a 450 N load cell (Futek, Irvine, CA) and an MTS Bionix universal testing system (MTS Systems Corporation; Eden Prairie, MN), respectively. Mechanical properties were determined using engineering beam theory as follows. Force-displacement (*F*-*d*) data was used to generate stress-strain (σ-ε) curves using Equations 2.1 and 2.2, where *L* is the span of the test fixture, *w* is the beam width, and *t* is the beam thickness (in the direction of the applied load) [37,42].

$$\sigma = \frac{3}{2} * \frac{F * L}{w * t^2} \tag{2.1}$$

$$\varepsilon = d * \frac{6 * t}{L^2} \tag{2.2}$$

Bending modulus (E) was calculated as the approximate linear slope of the elastic region of the stress-strain curve. The modulus of toughness (u_t) was calculated as the area under the stress-strain curve up to failure, and is related to the work-to-fracture (U) by Equation 2.3 [42].

$$u_t = U * \frac{9}{L * w * t} \tag{2.3}$$

2.3.4. Composition

After mechanical testing, the distal halves of fractured specimens were subjected to an ashing process to determine the mineral content of the bone similar to previous studies [37]. The specimens were dried in a furnace at 100 °C for 24 hours and weighed to determine a dry weight (DW) then returned to the furnace at 600 °C for 48 hours to remove the organic material and reweighed to obtain an ash weight (AW). The bone mineral content (BMC) was calculated as the dry weight percentage of mineral according to Equation 2.4.

$$BMC\ [\%] = \frac{AW}{DW} \times 100\% \tag{2.4}$$

2.3.5. Histology

Bone tissue adjacent to mechanically tested tissue was used for histology (Figure 2-2b). Histology samples were fixed in 70% ethanol then embedded in polymethyl

methacrylate (Ortho-Jet BCA, Lang Dental Mfg. Co., Inc; Wheeling, IL). Next, 150 µm sections were cut using a Buehler Isomet precision saw with a diamond-coated blade. Sections were polished to a final thickness of 70-90 µm using silicon carbide (SiC) polishing pads and a Buehler EcoMet, then rinsed of residual debris. Polished sections were stained with toluidine blue following a procedure used for the staining of cement lines [43]. In short, samples were subjected to an acid etching process by immersion in 0.2M formic acid for 3 minutes and 15 seconds, then rinsed in 70% ethanol for 15 minutes and stained in a toluidine blue solution for 5 minutes. The toluidine blue solution consisted of 1 g of toluidine blue O powder and 1 g of sodium tetraborate decahydrate per 100 ml of deionized water. After staining, samples were rinsed in a graded series of ethanol and left to dry under a weight to prevent warping. Once dry, samples were mounted and cover slipped on glass microscope slides. Slides were imaged at 100x magnification on a Leica Laborlux S microscope (Leica Camera AG; Wetzlar, Germany) equipped with an Olympus DP40 camera (Olympus Corperation; Tokyo, Japan) connected to the Olympus CellSens software package. Histology samples were used to quantify bone tissue porosity, osteon population density, and the areas of individual secondary osteons.

For each sample, a region of interest approximately 5 mm x 5 mm was selected in the central region of the cortical bone cortex. In each region of interest, the number of intact secondary osteons (N.On) and secondary osteon fragments (N.On.Fg) were identified and counted manually. Secondary osteons were identifiable via cement lines (Figure 2-3a). Secondary osteons were considered intact if a complete cement line was clearly visible around the entire periphery of an osteon with a central Haversian canal (Figure 2-3a). Conversely, remnants of secondary osteons that had been encroached upon by younger

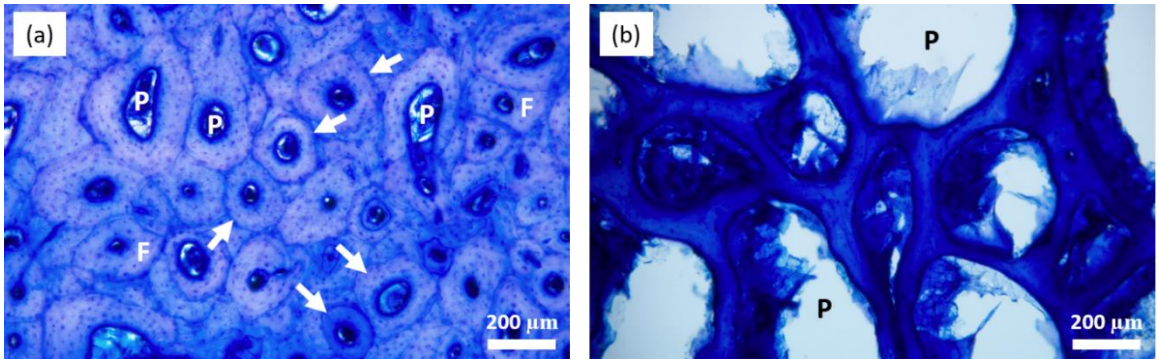

Figure 2-3. Histological images of bighorn sheep horncore cortical bone stained with toluidine blue. (a) Intact secondary osteons were distinguishable by peripheral cement lines (arrows). Examples of pore spaces (P) and secondary osteon fragments (F) are also visible. (b) Secondary osteons were not present in samples from the two younger rams which displayed extreme cortical porosity due to large pore spaces (P).

secondary osteons or resorption cavities were counted as secondary osteon fragments (Figure 2-3a). These definitions are similar to those used in previous studies of bone histomorphometry [44,45]. BioQuant Osteo (BIOQUANT Image Analysis Corporation; Nashville, TN) was used to measure the total tissue area, pore area, and areas of individual secondary osteons in the region of interest. For each sample, porosity (φ; Equation 2.5), osteon population density (OPD; Equation 2.6), and the mean secondary osteon area (MSOA) were reported. However, due to extreme cortical porosity in younger rams and absence of secondary osteons, OPD and MSOA could not be quantified for two of the samples (Figure 2-3b).

$$\varphi\,[\%] = \frac{Pore\ Area}{Total\ Area} \times 100\% \tag{2.5}$$

$$OPD\ \left[\frac{\#}{mm^2}\right] = \frac{N.On + N.On.Fg}{Total\ Area} \tag{2.6}$$

2.3.6. Statistics

Paired t-tests were used to compare results from the tensile and compressive cortices of each animal. Additionally, linear regression analysis was used to investigate

correlations between all measured parameters and horn curl length for each cortex (compressive or tensile). Stepwise regression was used to investigate the contributions of bone mineral content and cortical porosity to mechanical properties from each cortex. One-way analysis of variance (ANOVA) with Tukey post-hoc was used to compare results to published data for cortical bone from black bear tibias [37] and red deer antler [46] quantified with similar methodology. Equation 2.3 was used to convert the normalized work-to-fracture values reported in these studies to modulus of toughness values for comparison. These species provide valuable comparisons since black bear tibia exhibits mechanical properties in the mid-range of cortical bone values for a wide range of species [47], while red deer antler represents a tough bone tissue specialized for intraspecific combat [34]. JMP Pro (SAS Institute; Cary, NC) was used to conduct all statistical analysis, and a p-value less than 0.05 was considered significant for all statistical analyses. Data are presented as means +/- standard error.

2.4. Results

2.4.1. Mechanical Properties

Mechanical properties for each ram and mean values for each cortex are shown in Table 1. Paired t-tests demonstrated the bending modulus was higher in the compressive stress cortex ($p = .0036$) but modulus of toughness was similar between cortices ($p = .1054$). Additionally, bending modulus was found to have a strong positive correlation with curl length in both cortices ($p = .0029$ and $r^2 = 0.913$ in the compressive cortex; $p = .0046$ and $r^2 = 0.891$ in the tensile cortex; Figure 2-4a). Modulus of toughness was not correlated with curl length in either cortex ($p = .7292$ in compressive cortex, $p = .1677$ in tensile

cortex; Figure 2-4b). The bending modulus of horncore cortical bone was similar to red deer antler and lower than black bear bone (Figure 2-5a); however, modulus of toughness was similar between all species (Figure 2-5b). Stepwise regression indicated a strong correlation between BMC and cortical porosity ($p < .0001$, $r^2 = 0.8836$) that caused multicollinearity in the models. Therefore, since porosity was a better predictor variable for the mechanical properties of horncore bone tissue, BMC was removed from the models. Bending modulus was correlated with porosity in the compressive ($p = .0041$, $r^2 = 0.897$; Figure 2-6) and tensile ($p = .0046$, $r^2 = 0.892$; Figure 2-6) cortices. Modulus of toughness was correlated with porosity in the tensile cortex ($p = .0402$, $r^2 = 0.691$; Figure 2-6), but not the compressive cortex ($p = .5063$).

2.4.2. Composition

The bone mineral content (BMC) for each sample and mean values for each stress cortex are shown in Table 1. Similar to the bending modulus, BMC was higher in the compressive stress cortex compared to the tensile stress cortex ($p = .0289$) and had a strong positive correlation with curl length in both cortices ($p = .0265$ and $r^2 = 0.747$ in the compressive cortex; $p = .0187$ and $r^2 = 0.785$ in the tensile cortex; Figure 2-4c). Horncore cortical bone had a mineral content similar to red deer antler but lower than black bear bone (Figure 2-5c).

2.4.3. Histomorphometry

Porosity, osteon population density (OPD) and mean secondary osteon area (MSOA) for each sample and means for each stress cortex are shown in Table 2-1. In four of the samples (1C, 1T, 2C, and 2T) no secondary osteons were observed due to high tissue

porosity; as a result, OPD and MSOA are not reported for these samples. There were no differences between cortices for any of the histomorphometric properties. Porosity had a strong negative correlation with curl length in each cortex ($p = .0087$ and $r^2 = 0.852$ in the compressive cortex; $p = .0080$ and $r^2 = 0.858$ in the tensile cortex; Figure 2-4d). OPD and MSOA showed no correlation with curl length in either cortex. Horncore cortical porosity was higher than red deer antler and black bear bone (Figure 2-5d).

*Table 2-1. Tabulated experimental results for individual compressive (C) and tensile (T) samples along with summary data from each cortex expressed as Mean ± SE. Results from paired t-tests are expressed as p-values below the summary data with **bold** values indicating significant differences between cortices ($p < .05$). Measured parameters include horn curl length (CL), the bending modulus (E), modulus of toughness (u_t), bone mineral content (BMC), porosity, osteon population density (OPD), and mean secondary osteon area (MSOA).*

Sample	CL [cm]	E [GPa]	u_t [MPa]	BMC [%]	Porosity [%]	OPD [#/mm^2]	MSOA [mm^2]
1C	51.0	2.1	2.6	58.9	49.15	-	-
1T	51.0	1.2	1.7	56.1	60.44	-	-
2C	55.5	4.1	2.5	53.7	53.60	-	-
2T	55.5	2.6	2.2	53.6	65.34	-	-
3C	70.0	10.4	3.6	63.3	22.42	2.12	0.0194
3T	70.0	8.1	9.0	63.4	11.32	3.36	0.0210
4C	75.0	16.5	4.8	65.1	9.62	5.86	0.0262
4T	75.0	13.6	9.6	63.5	7.45	5.43	0.0276
5C	82.0	14.2	8.6	66.2	7.77	7.44	0.0161
5T	82.0	11.8	10.0	62.6	8.03	5.94	0.0175
6C	85.0	16.4	2.3	65.0	16.55	3.56	0.0250
6T	85.0	12.3	4.4	64.0	7.53	4.76	0.0202
Compressive	69.8 ± 5.7	10.6 ± 2.6	4.1 ± 1.0	62.0 ± 2.0	26.52 ± 8.16	4.74 ± 1.18	0.0217 ± 0.0024
Tensile	69.8 ± 5.7	8.3 ± 2.1	6.1 ± 1.6	60.5 ± 1.8	26.68 ± 11.48	4.88 ± 0.56	0.0216 ± 0.0022
Paired t-test		**.0036**	.1054	**.0289**	.1325	.8607	.4219

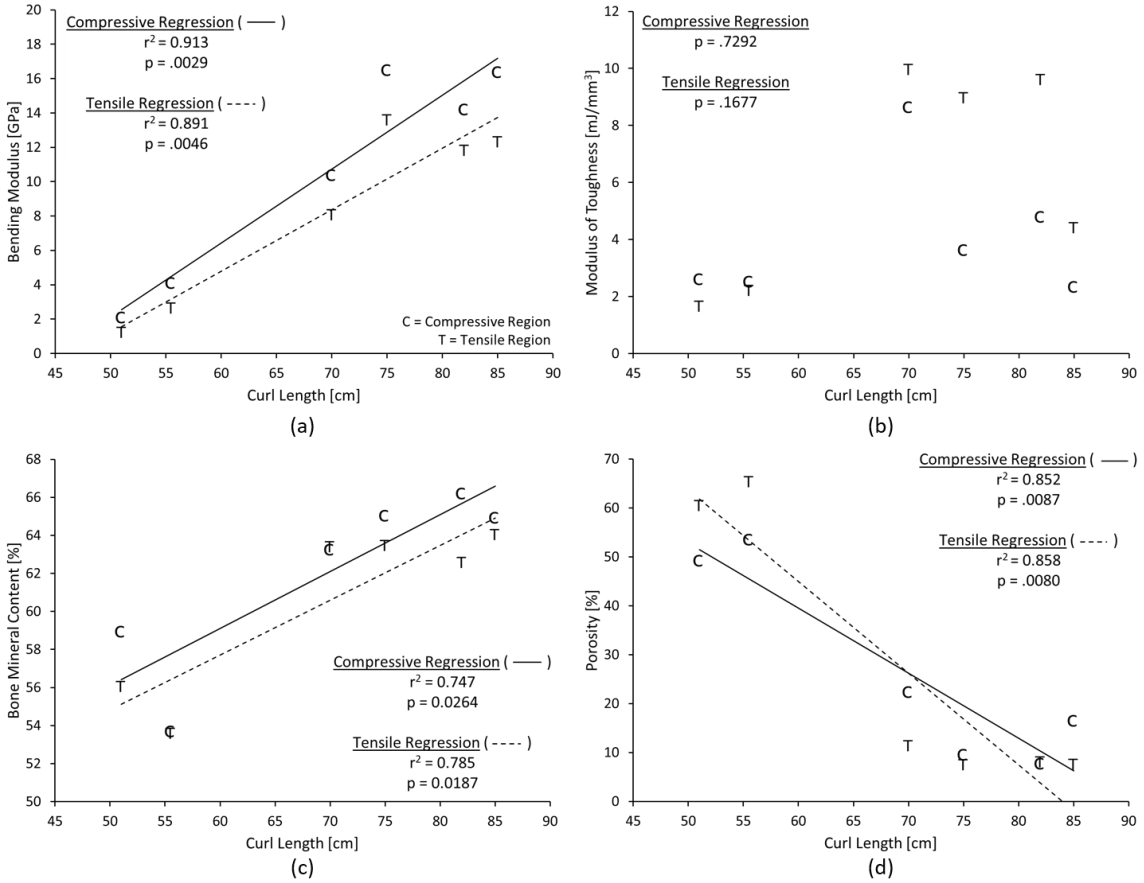

Figure 2-4. Curl length regressions for: (a) the bending modulus, (b) modulus of toughness, (c) bone mineral content, and (d) porosity of bighorn sheep horncore cortical bone tissue. Data points represented with a 'C' and 'T' are from compressive and tensile cortices, respectively. Regression lines shown for significant correlations ($p < .05$).

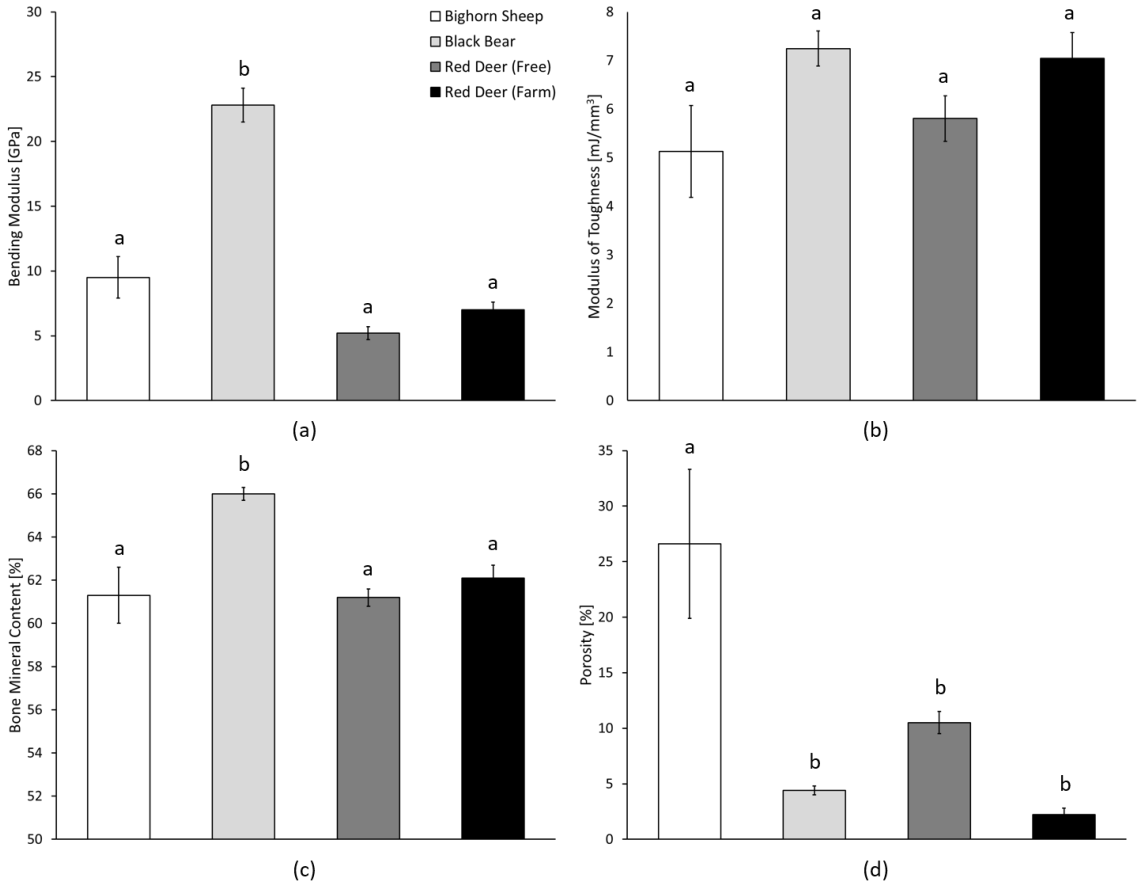

Figure 2-5. Comparisons between cortical bone properties of bighorn sheep horncores, black bear tibias [37]*, and red deer antlers from two populations: free-ranging (free) and farm raised (farm)* [46]*. Comparisons include (a) bending modulus, (b) modulus of toughness, (c) bone mineral content, and (d) porosity. Error bars represent standard error.*

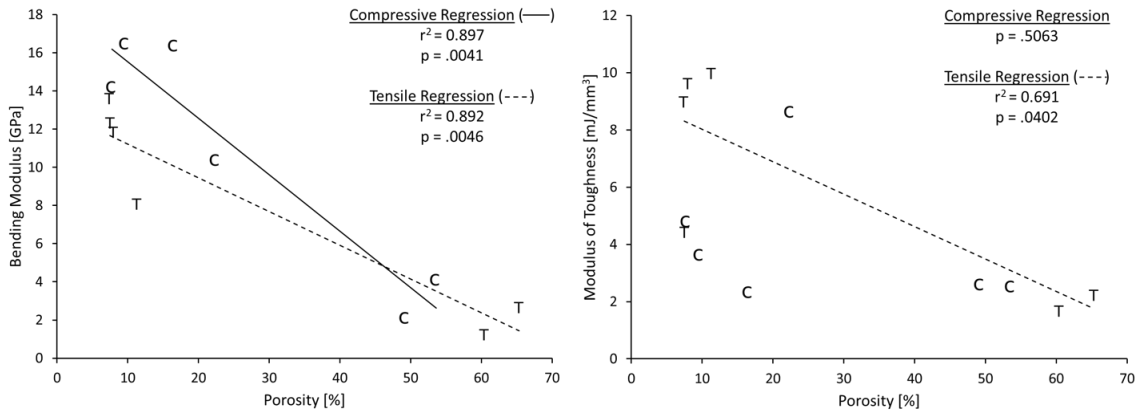

Figure 2-6. Porosity was the best predictor variable for bending modulus (E) and modulus of toughness (u_t). Data points represented with a 'C' and 'T' are from compressive and tensile cortices, respectively. Regression lines shown for significant correlations ($p < .05$).

2.5 Discussion

Since bone adapts to its mechanical environment and bighorn sheep horncore bone tissue is exposed to extreme impact loading, we hypothesized the horncore bone composition and microstructure would provide superior toughness compared to other mammalian cortical bone tissues. Since rams typically show no observable symptoms of brain injury after high magnitude head impacts, studying the structure-function relationships of horncore bone tissue has implications for brain injury prevention in humans. Results from this study indicate that horncore cortical bone tissue does have a lower mineral content and reduced stiffness compared to other mammalian cortical bone and is similar to antler in that regard. However, the modulus of toughness of the horncore cortical bone did not exceed that of tibial cortical bone or antler, which is possibly due to higher porosity in horncore bone.

Limitations of this study include a low sample size and various times of sample collection relative to the mating season when the repetitive high impact loading occurs. Samples were only available when animals were found deceased with collection dates ranging from May to November. Since horncore bone is loaded primarily during rut (October – January for Rocky Mountain bighorn sheep [48]), bone collected before and after rut may demonstrate different mechanical behavior due to differences in microdamage and intracortical porosity due to targeted remodeling. Thus, mechanical behavior quantified here may not be representative of bone tissue present in the horncore during ramming. Another limitation is that the samples were tested at a strain rate of approximately 0.01 ε/s which is much lower than estimated physiological strain rate of approximately 6 ε/s that occurs during ramming [16]. However, this strain rate was chosen

to enable comparisons to bone tissue from other mammalian species that were quantified with similar methodology [37,46]. Performing mechanical testing in air can also lead to local dehydration on sample surfaces which may alter the measured mechanical properties. However, it is unlikely substantial dehydration occurred in the very short time frame from when the saline soaked gauze was removed and the test was performed. Furthermore, similar methodology has been applied to cortical bone tissue previously [37,38,46], and is beneficial for obtaining a first estimate of the mechanical properties of this unique bone tissue. Despite these limitations, this research provides valuable new insight on the microstructure, composition, and mechanical behavior of bighorn sheep horncore bone tissue.

Our results suggest that horncore cortical bone does not have a greater modulus of toughness than other mammalian cortical bone tissues despite its exposure to high impact loading. The horncore cortical bone mineral content was found to be similar to deer antler and lower than black bear tibia (Figure 2-5c). Low BMC was expected to promote high toughness in horncore cortical bone as previously demonstrated for antler [34]. Surprisingly, the modulus of toughness of horncore cortical bone was not different from red deer antler and black bear tibia (Figure 2-5b). Furthermore, while larger rams would benefit from less mineralized bone tissue as they experience higher magnitude impacts, we found that horncore cortical bone becomes more mineralized as horn curl length increases (Figure 2-4c). These results are consistent with age related changes previously reported for cortical bone from black bear tibias and human femurs [37,38], but they are not conducive to increased toughness during high magnitude impacts. Paired t-tests showed that horncore cortical bone tissue is more highly mineralized in the compressive stress cortex than the

tensile stress cortex (Table 2-1). This likely explains why the compressive stress cortex also has a higher bending modulus (Table 2-1). This result is consistent with previous studies on mule deer calcaneus [49] and human femoral cortical bone [50] but not equine radial bone [51]. Results from this study support the assumptions made for the material properties of horncore bone used in previous computational models of bighorn sheep ramming [16]. In that finite element modeling study, horncore bone was assigned an elastic modulus of 15 GPa which is higher than the average bending modulus reported here (9.5 GPa) but falls in the range of the comparably large sheep in this study (E = 8.1 – 16.5 GPa; Table 2-1). Future computational modeling of bighorn sheep ramming can use the range of tissue properties quantified in this study to investigate the role of tissue level material properties on energy absorption and injury mitigation. However, mechanical properties reported for horncore cortical bone in this study were quantified at quasi-static strain rates, and are not likely representative of material behavior at the higher strain rates estimated to occur in the horncore during ramming (~ 6 ε/s; Drake et al., 2016). Previous studies on the viscoelastic behavior of cortical bone have demonstrated that bone strength and stiffness increase, but failure strain decreases as bone transitions from ductile to brittle behavior [52–54]. It is reasonable to expect that similar relationships exist for horncore cortical bone tissue and should be accounted for in future modeling studies. Furthermore, the low mineral content of antler maintains stable crack growth at high strain rates and results in a remarkable 4-fold increase in toughness from quasi-static to impact testing conditions [55]. Thus, it is possible that the horncore cortical bone demonstrates a similar increase in toughness at higher strain rates since it has a mineral content comparable to antler. Future modeling of bighorn sheep head impacts should consider accounting for the strain rate

sensitivity of bone when approximating material properties. Further insight on the mechanical properties of horncore cortical bone tissue can be gained by looking at results from histomorphometry.

Similar to the mechanical properties, microstructural differences were observed between cortical bone tissue from bighorn sheep horncores and other mammalian species. Younger, smaller rams (sheep 1 and 2) demonstrated an abnormally high cortical porosity (57.13 ± 3.59%) which may promote increased vascularization that is beneficial for rapid growth and development similar to plexiform bone in large mass mammals [56–58]. Mature bighorn sheep demonstrated a horncore cortical porosity (11.34 ± 1.92%) in the upper range of typical values for mammalian Haversian bone (typically less than 15%) [23,37,45–47,59,60]. Results from the stepwise regressions indicate that cortical porosity predicts horncore bone mechanical properties better than other parameters measured in this study (Figure 2-6). Since porosity was negatively correlated with the modulus of toughness, this result may explain why the horncore cortical bone was not tougher than less porous cortical bone from black bear tibia or red deer antler. Bone porosity can transiently increase due to osteoclastic activity initiated by targeted bone remodeling to repair microdamage [20,21,61–63]. Therefore, it is possible that high cortical porosity may arise due to increased bone resorption that occurs outside of the rut season, if repetitive high magnitude head impacts during the rut activates targeted remodeling in response to high microdamage accumulation. [20,21]. However, horncore cortical bone demonstrated low OPD values (4.81 ± 0.61 osteons/mm^2) compared to cortical bone from adult sheep radii (20 ± 1.49 osteons/mm^2; exact ages unknown [64]), mature macaque femurs (9.00 ± 0.53 osteons/mm^2; ages 6 – 27 years [65]), and adult human femurs (26.01 ± 0.76; ages 34

– 94 years [66]). Conversely, the OPD of horncore cortical bone was only slightly lower than values for femoral cortical bone from black bears (6.19 ± 0.31; ages 1 – 19 years [45]) which have been shown to suppress remodeling activity during annual periods of disuse (hibernation) [37,45,59]. Thus, it is possible that bone remodeling activity in horncore cortical bone may become substantially suppressed following a burst of targeted remodeling to repair damage accumulated during rut.

Overall, the results from this study do not support the hypothesis that bighorn sheep horncore cortical bone is a tougher material than cortical bone from other species. Therefore, it is possible that horncore cortical bone serves another purpose such as providing an interface between the impacted horn and porous bone within the horncore, which are likely the primary energy absorbers. Horn has previously been demonstrated to be a tough, impact resistant material [10–13], and the porous, trabecular-like region of the horncore was shown to absorb more energy during impact than the horn [16]. Thus, future studies that quantify the horn-cortical bone interface strength and the material properties of porous horncore bone will be valuable for advancing our understanding of the energy absorption mechanisms utilized by bighorn sheep.

2.6. Acknowledgements

The authors thank the State of Colorado Department of Natural Resources for providing the Scientific collection license to obtain the bighorn sheep skulls used in this study. The authors would also like to acknowledge and thank Steve Johnson at Colorado State University and Greg Lucarelli at the University of Massachusetts for their assistance in preparing mechanical test samples and histology slides, respectively.

This research did not receive any specific grant from funding agencies in the public, commercial, or not-for-profit sectors.

2.7. References

[1] A.C. McKee, M.E. Robinson, Military-related traumatic brain injury and neurodegeneration, Alzheimer's and Dementia. 10 (2014) S242–S253. https://doi.org/10.1016/j.jalz.2014.04.003.

[2] N. Didehbani, C.M. Cullum, S. Mansinghani, H. Conover, J. Hart, Depressive symptoms and concussions in aging retired NFL players, Archives of Clinical Neuropsychology. 28 (2013) 418–424. https://doi.org/10.1093/arclin/act028.

[3] D.H. Daneshvar, L.E. Goldstein, P.T. Kiernan, T.D. Stein, A.C. McKee, Post-traumatic neurodegeneration and chronic traumatic encephalopathy, Molecular and Cellular Neuroscience. 66 (2015) 81–90. https://doi.org/10.1016/j.mcn.2015.03.007.

[4] N.W.B. Finkbeiner, J.E. Max, S. Longman, C. Debert, Knowing what we don't know: Long-term psychiatric outcomes following adult concussion in sports, Canadian Journal of Psychiatry. 61 (2016) 270–276. https://doi.org/10.1177/0706743716644953.

[5] J.Y. Sone, D. Kondziolka, J.H. Huang, U. Samadani, Helmet efficacy against concussion and traumatic brain injury: a review, J Neurosurg. 126 (2017) 768–781. https://doi.org/10.3171/2016.2.JNS151972.

[6] S.P. Broglio, B. Schnebel, J.J. Sosnoff, S. Shin, X. Feng, X. He, J. Zimmerman, The Biomechanical Properties of Concussions in High School Football, Medicine and Science in Sports and Excercise. 42 (2010) 2064–2071. https://doi.org/10.1249/MSS.0b013e3181dd9156.

[7] K.M. Guskiewicz, J.P. Mihalik, V. Shankar, S.W. Marshall, D.H. Crowell, S.M. Oliaro, M.F. Ciocca, D.N. Hooker, Measurement of head impacts in collegiate football players: Relationship between head impact biomechanics and acute clinical outcome after concussion, Injury Prevention. 61 (2007) 1244–1253. https://doi.org/10.1227/01.NEU.0000280146.37163.79.

[8] E.J. Pellman, D.C. Viano, A.M. Tucker, I.R. Casson, J.F. Waeckerle, Concussion in Professional Football: Reconstruction of Game Impacts and Injuries, Neurosurgery. 53 (2003) 796. https://doi.org/10.1227/01.NEU.0000083559.68424.3F.

[9] D.F. Meaney, D.H. Smith, Biomechanics of Concussion, Clin Sports Med. 30 (2011) 19–vii. https://doi.org/10.1016/j.csm.2010.08.009.

[10] M.W. Trim, M.F. Horstemeyer, H. Rhee, H. el Kadiri, L.N. Williams, J. Liao, K.B. Walters, J. McKittrick, S.-J. Park, The effects of water and microstructure on the mechanical properties of bighorn sheep (Ovis canadensis) horn keratin., Acta Biomater. 7 (2011) 1228–40. https://doi.org/10.1016/j.actbio.2010.11.024.

[11] L. Tombolato, E.E. Novitskaya, P.Y. Chen, F.A. Sheppard, J. McKittrick, Microstructure, elastic properties and deformation mechanisms of horn keratin, Acta Biomater. 6 (2010) 319–330. https://doi.org/10.1016/j.actbio.2009.06.033.

[12] W. Huang, A. Zaheri, J.-Y. Jung, H.D. Espinosa, J. Mckittrick, Hierarchical structure and compressive deformation mechanisms of bighorn sheep (Ovis canadensis) horn, Acta Biomater. 64 (2017) 1–14. https://doi.org/10.1016/j.actbio.2017.09.043.

[13] K.L. Johnson, M.W. Trim, D.K. Francis, W.R. Whittington, J.A. Miller, C.E. Bennett, M.F. Horstemeyer, Moisture, anisotropy, stress state, and strain rate effects on bighorn sheep horn keratin mechanical properties, Acta Biomater. 48 (2017) 300–308. https://doi.org/10.1016/j.actbio.2016.10.033.

[14] Y.Z. Liu, X.M. Qiu, H.L. Ma, W.W. Fu, T.X. Yu, A study of woodpecker's pecking process and the impact response of its brain, Int J Impact Eng. 108 (2017) 263–271. https://doi.org/10.1016/j.ijimpeng.2017.05.016.

[15] P.R.A. May, J.M. Fuster, J. Haber, A. Hirschman, Woodpecker Drilling Behavior: An Endorsement of the Rotational Theory of Impact Brain Injury, Arch Neurol. 36 (1979) 370–373. https://doi.org/10.1001/archneur.1979.00500420080011.

[16] A. Drake, T.L. Haut Donahue, M. Stansloski, K. Fox, B.B. Wheatley, S.W. Donahue, Horn and horn core trabecular bone of bighorn sheep rams absorbs impact energy and reduces brain cavity accelerations during high impact ramming of the skull, Acta Biomater. 44 (2016) 41–50. https://doi.org/10.1016/j.actbio.2016.08.019.

[17] G. Farah, D. Siwek, P. Cummings, Tau accumulations in the brains of woodpeckers, PLoS One. 13 (2018) 1–12. https://doi.org/10.1371/journal.pone.0191526.

[18] S.W. Donahue, Krogh's principle for musculoskeletal physiology and pathology, Journal of Musculoskeletal Neuronal Interactions. 18 (2018) 284–291.

[19] T.W. Seek, Exploration of Unique Porous Bone Materials for Candidacy in Bioinspired Material Design, Masters Thesis, Colorado State University, 2018.

[20] D.B. Burr, R.B. Martin, M.B. Schaffler, E.L. Radin, Bone Remodeling in Response to in vivo Fatigue Microdamage, J Biomech. 18 (1985) 189–200.

[21] T.C. Lee, A. Staines, D. Taylor, Bone adaptation to load: Microdamage as a stimulus for bone remodelling, J Anat. 201 (2002) 437–446. https://doi.org/10.1046/j.1469-7580.2002.00123.x.

[22] Z. Seref-Ferlengez, O.D. Kennedy, M.B. Schaffler, Bone microdamage, remodeling and bone fragility: how much damage is too much damage?, Bonekey Rep. 4 (2015) 1–7. https://doi.org/10.1038/bonekey.2015.11.

[23] M.B. Schaffler, D.B. Burr, Stiffness of compact bone: effects of porosity and density, J Biomech. 21 (1988) 13–16.

[24] M.B. Schaffler, D.B. Burr, R.G. Frederickson, Morphology of the osteonal cement line in human bone., Anat Rec. 217 (1987) 223–228. https://doi.org/10.1002/ar.1092170302.

[25] S.W. Donahue, S.A. Galley, Microdamage in Bone: Implications for Fracture, Repair, Remodeling, and Adaptation, Crit Rev Biomed Eng. 34 (2012) 215–271. https://doi.org/10.1615/critrevbiomedeng.v34.i3.20.

[26] D.B. Burr, M.B. Schaffler, R.G. Frederickson, Composition of the cement line and its possible mechanical role as a local interface in human compact bone., J Biomech. 21 (1988) 939–945. https://doi.org/10.1016/0021-9290(88)90132-7.

[27] D. Vashishth, K.E. Tanner, W. Bonfield, Experimental validation of a microcracking-based toughening mechanism for cortical bone, J Biomech. 36 (2003) 121–124. https://doi.org/10.1016/S0021-9290(02)00319-6.

[28] D. Vashishth, J.C. Behiri, W. Bonfield, Crack growth resistance in cortical bone: Concept of microcrack toughening, J Biomech. 30 (1997) 763–769. https://doi.org/10.1016/S0021-9290(97)00029-8.

[29] Y.N. Yeni, C.U. Brown, Z. Wang, T.L. Norman, The influence of bone morphology on fracture toughness of the human femur and tibia, Bone. 21 (1997) 453–459. https://doi.org/10.1016/S8756-3282(97)00173-7.

[30] M.B. Schaffler, K. Choi, C. Milgrom, Aging and matrix microdamage accumulation in human compact bone, Bone. 17 (1995) 521–525. https://doi.org/10.1016/8756-3282(95)00370-3.

[31] D.B. Burr, C.H. Turner, P. Naick, M.R. Forwood, W. Ambrosius, M. Sayeed Hasan, R. Pidaparti, Does microdamage accumulation affect the mechanical properties of bone?, J Biomech. 31 (1998) 337–345. https://doi.org/10.1016/S0021-9290(98)00016-5.

[32] J.D. Currey, The Evolution of the Mechanical Properties of Amniote Bone, J Biomech. 20 (1987) 1035–1044.

[33] A.H. Doherty, C.K. Ghalambor, S.W. Donahue, Evolutionary physiology of bone: Bone metabolism in changing environments, Physiology. 30 (2015) 17–29. https://doi.org/10.1152/physiol.00022.2014.

[34] J.D. Currey, Mechanical properties of bone tissues with greatly differing functions, J Biomech. 12 (1979) 313–319. https://doi.org/10.1016/0021-9290(79)90073-3.

[35] V. Geist, Validity of Horn Segment Counts in Aging Bighorn Sheep, J Wildl Manage. 30 (1966) 634–635. http://www.jstor.com/stable/3798763.

[36] P.R. Krausman, R.T. Bowyer, Mountain Sheep (Ovis canadensis and O. dalli), in: G.A. Feldhamer, B.C. Thompson, J.A. Chapman (Eds.), Wild Mammals of North America: Biology, Management, and Conservation, Second, Johns Hopkins University Press, Baltimore, MD, 2003: pp. 1095–1118.

[37] K.B. Harvey, S.W. Donahue, Bending properties, porosity, and ash fraction of black bear (Ursus americanus) cortical bone are not compromised with aging despite annual periods of disuse, J Biomech. 37 (2004) 1513–1520. https://doi.org/10.1016/j.jbiomech.2004.01.010.

[38] J.D. Currey, G. Butler, The mechanical properties of bone tissue in children, Journal of Bone and Joint Surgery - American Volume. 57 (1975) 810–814.

[39] R.B. Martin, N.A. Sharkey, The Mechanical Effects of Preserving Bone, in: S.C. Cowin (Ed.), Bone Mechanics Handbook, Second Edi, 2001: pp. 20-6-20–12.

[40] E.D. Sedlin, A Rheologic Model for Cortical Bone: A Study of the Physical Properties of Human Femoral Samples, Acta Orthop Scand. 36 (1965) 1–77. https://doi.org/10.3109/ort.1965.36.suppl-83.01.

[41] J.C.H. Goh, E.J. Ang, K. Bose, Effect of preservation medium on the mechanical properties of cat bones, Acta Orthop Scand. 60 (1989) 465–467. https://doi.org/10.3109/17453678909149321.

[42] D.B. Burr, C.H. Turner, Mechanical Testing Methods, in: S.C. Cowin (Ed.), Bone Mechanics Handbook, Second, 2001: pp. 7–6 to 7–24.

[43] D.L. Osborne, J. Curtis, A protocol for the staining of cement lines in adult human bone using toluidine blue, J Histotechnol. 28 (2005) 73–79. https://doi.org/10.1179/his.2005.28.2.73.

[44] A.C. Beresheim, S.K. Pfeiffer, A. Alblas, The Influence of Body Size and Bone Mass on Cortical Bone Histomorphometry in Human Ribs, Anatomical Record. 301 (2018) 1788–1796. https://doi.org/10.1002/ar.23933.

[45] S.J. Wojda, D.R. Weyland, S.K. Gray, M.E. Mcgee-Lawrence, T.D. Drummer, S.W. Donahue, Black bears with longer disuse (hibernation) periods have lower femoral osteon population density and greater mineralization and intracortical porosity, Anatomical Record. 296 (2013) 1148–1153. https://doi.org/10.1002/ar.22720.

[46] T. Landete-Castillejos, J.D. Currey, F. Ceacero, A.J. García, L. Gallego, S. Gomez, Does nutrition affect bone porosity and mineral tissue distribution in deer antlers? The relationship between histology, mechanical properties and mineral composition, Bone. 50 (2012) 245–254. https://doi.org/10.1016/j.bone.2011.10.026.

[47] J.D. Currey, The Effect of Porosity and Mineral Content on the Young's Modulus of Elasticity of Compact Bone, J Biomech. 21 (1988) 131–139.

[48] H.K. Buechner, The Bighorn Sheep in the United States, Its Past, Present, and Future, Wildlife Monographs. 4 (1960) 3–174. https://doi.org/10.1017/CBO9781107415324.004.

[49] J.G. Skedros, K.J. Hunt, R.D. Bloebaum, Relationships of Loading History and Structural and Material Characteristics of Bone: Development of the Mule Deer Calcaneus, J Morphol. 259 (2004) 281–307. https://doi.org/10.1002/jmor.10167.

[50] M. Portigliatti Barbos, P. Bianco, A. Ascenzi, Distribution of osteonic and interstitial components in the human femoral shaft with reference to structure, calcification and mechanical properties., Acta Anat (Basel). 115 (1983) 178–186. https://doi.org/10.1159/000145688.

[51] M.W. Mason, J.G. Skedros, R.D. Bloebaum, Evidence of strain-mode-related cortical adaptation in the diaphysis of the horse radius, Bone. 17 (1995) 229–237. https://doi.org/10.1016/8756-3282(95)00213-W.

[52] J.H. McElhaney, Dynamic response of bone and muscle tissue., J Appl Physiol. 21 (1966) 1231–1236. https://doi.org/10.1152/jappl.1966.21.4.1231.

[53] J. Lei, L. Li, Z. Wang, F. Zhu, Characterizing Strain Rate-Dependent Mechanical Properties for Bovine Cortical Bones, J Biomech Eng. 142 (2020) 1–8. https://doi.org/10.1115/1.4046690.

[54] U. Hansen, P. Zioupos, R. Simpson, J.D. Currey, D. Hynd, The effect of strain rate on the mechanical properties of human cortical bone, J Biomech Eng. 130 (2008) 1–8. https://doi.org/10.1115/1.2838032.

[55] J.D. Currey, K. Brear, P. Zioupos, Strain rate dependence of work of fracture tests on bone and similar tissues: Reflections on testing methods and mineral content effects, Bone. 128 (2019) 115038. https://doi.org/10.1016/j.bone.2019.115038.

[56] R. Mori, T. Kodaka, S. Soeta, J. Sato, J. Kakino, S. Hamato, H. Takaki, Y. Naito, Preliminary study of histological comparison on the growth patterns of long-bone cortex in young calf, pig, and sheep, Journal of Veterinary Medical Science. 67 (2005) 1223–1229. https://doi.org/10.1292/jvms.67.1223.

[57] J.W. Barrera, A. Le Cabec, M.M. Barak, The orthotropic elastic properties of fibrolamellar bone tissue in juvenile white-tailed deer femora, J Anat. 229 (2016) 568–576. https://doi.org/10.1111/joa.12500.

[58] J.D. Currey, The many adaptations of bone, J Biomech. 36 (2003) 1487–1495. https://doi.org/10.1016/S0021-9290(03)00124-6.

[59] M.E. McGee-Lawrence, S.J. Wojda, L.N. Barlow, T.D. Drummer, K. Bunnell, J. Auger, H.L. Black, S.W. Donahue, Six months of disuse during hibernation does not increase intracortical porosity or decrease cortical bone geometry, strength, or mineralization in black bear (Ursus americanus) femurs, J Biomech. 42 (2009) 1378–1383. https://doi.org/10.1016/j.jbiomech.2008.11.039.

[60] J.D. Frank, M. Ryan, V.L. Kalscheur, C.P. Ruaux-Mason, R.R. Hozak, P. Muir, Aging and accumulation of microdamage in canine bone, Bone. 30 (2002) 201–206. https://doi.org/10.1016/S8756-3282(01)00623-8.

[61] R.B. Martin, Is all cortical bone remodeling initiated by microdamage?, Bone. 30 (2002) 8–13. https://doi.org/10.1016/S8756-3282(01)00620-2.

[62] B. Martin, A theory of fatigue damage accumulation and repair in cortical bone., J Orthop Res. 10 (1992) 818–825. https://doi.org/10.1002/jor.1100100611.

[63] R.B. Martin, Targeted bone remodeling involves BMU steering as well as activation, Bone. 40 (2007) 1574–1580. https://doi.org/10.1016/j.bone.2007.02.023.

[64] S. Mohsin, F.J. O'Brien, T.C. Lee, Osteonal crack barriers in ovine compact bone, J Anat. 208 (2006) 81–89. https://doi.org/10.1111/j.1469-7580.2006.00509.x.

[65] L.M. Havill, Osteon Remodeling Dynamics in Macaca mulatta: Normal Variation with Regard to Age, Sex, and Skeletal Maturity, Calcif Tissue Int. 74 (2004) 95–102. https://doi.org/10.1007/s00223-003-9038-3.

[66] S.H. Han, S.H. Kim, Y.W. Ahn, G.Y. Huh, D.S. Kwak, D.K. Park, U.Y. Lee, Y.S. Kim, Microscopic age estimation from the anterior cortex of the femur in Korean adults, J Forensic Sci. 54 (2009) 519–522. https://doi.org/10.1111/j.1556-4029.2009.01003.x.

CHAPTER 3

3. CHARACTERIZATION OF HORNCORE VELAR BONE

3.1. Introduction

The bony horncore of bighorn sheep absorbs substantial energy during head-to-head impacts which reduces brain cavity accelerations and helps protect the brain from injury [1]. Despite this finding, investigations on the properties of bovid horncore bone are few [2,3]. One study on the horncore bone of the common eland demonstrated that mechanical properties are highest at the proximal base of the horn, where contact and bending stresses from combat are at a maximum [2]. In another study, cortical bone material from the horncore of bighorn sheep was found to be similar in toughness to other cortical bone tissues, suggesting it does not offer an advantage for energy absorption during ramming [3]. However, most of the bighorn sheep horncore consists of a unique porous bone material referred to as velar bone [4]. Velar bone has a similar bone volume fraction to mammalian trabecular bone (~20%), but larger sail thickness (2.87 ± 0.78 mm) and separation (11.91 ± 0.88 mm) compared to analogous measures of trabecular strut thickness (0.12 ± 0.02 mm) and separation (0.57 ± 0.08 mm) in the proximal tibia of grizzly bears [4]. The solid portions of velar bone are also more sail-like in morphology compared to the strut-like features of trabeculae bone (Figure 3-1) [4]. Trabecular bone is found extensively in various mammalian bones, but velar bone is unknown to exist outside of ovine horncore bone, suggesting it may be adapted specifically for the unique mechanical function of protecting the brain during intraspecific combat. The material behavior of velar bone tissue has not been characterized despite its apparent role in injury mitigation during

high-impact head butting. Quantification of velar bone tissue microstructure, composition, and mechanical properties will provide insight into the high energy absorption mechanisms of horncore bone and improve computational modeling of bighorn sheep ramming.

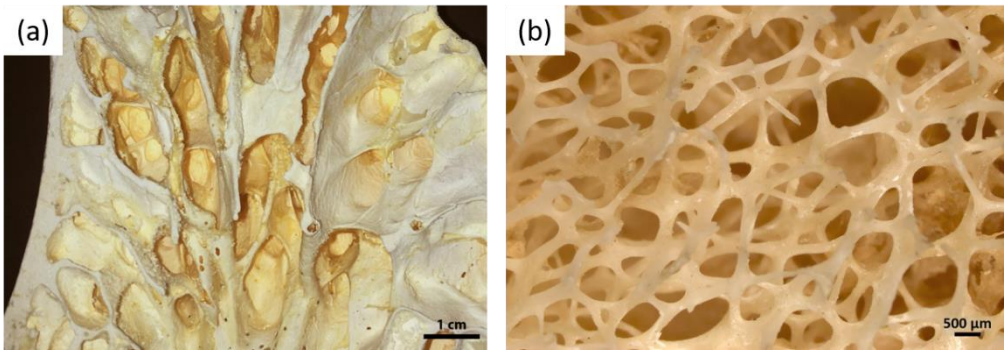

Figure 3-1. (a) Velar bone in the horncore of a bighorn sheep ram illustrating the sail-like morphology of this unique porous bone architecture. (b) Trabecular bone typically displays a more rod-like strut morphology with a much smaller size scale compared to velar bone.

Previous studies of bone tissue have extensively demonstrated phenotypic plasticity (short-term) and evolutionary (long-term) functional adaptations to mechanical loading [5–17]. Short term remodeling processes respond to external loading to alter whole bone geometry and tissue level microstructure to maintain physiological strain magnitudes [5–15]. Intracortical remodeling produces secondary osteons with cement line boundaries that arrest and deflect propagating cracks to toughen bone [18–22]. These toughening mechanisms are particularly effective in bone tissue since remodeling also allows bone to repair microdamage to mitigate damage accumulation and the risk of catastrophic failure. This may be one advantage of rams absorbing large amounts of energy via the bony horncore instead of the impacted horn, since the avascular horn cannot repair itself once damaged. Bone is a composite material with a mineral phase that contributes to strength and stiffness and a protein phase that contributes to ductility and toughness. There is

evidence that long-term evolutionary adaptation has resulted in specialized bones with tissue compositions that are well suited to meet specific functional demands. For example, compared to femoral bone, antler bone has reduced mineral content that provides increased work-to-fracture which is beneficial for supporting the high stresses generated during combat [16,17]. Furthermore, the composite nature of bone results in viscoelastic material properties such as strain rate sensitivity. Bone becomes stiffer and more brittle as loading rates increase, which plays a role in traumatic fractures from impacts (e.g., falls or car crashes) [23–25]. Based on the evolutionary adaptation of bone tissue demonstrated previously, it is possible that velar bone has a unique composition that provides superior energy absorption under impact loading.

Since osteons effectively toughen bone tissue and bone composition can adapt to its mechanical environment, it is possible that horncore velar bone has a unique microstructure and composition that provide efficient energy absorption to mitigate brain injury during ramming. We hypothesized the modulus of toughness is positively correlated with osteon population density in velar bone. Additionally, we hypothesized the modulus of toughness and damping factor are negatively correlated with bone mineral content in velar bone. The aims of this study were to quantify the microstructure, composition, and mechanical properties of velar bone tissue, and compare them to similar measures published for other mammalian bone tissues. This work increases our understanding of unique mechanical adaptations in bone tissue [26,27], improves our ability to computationally model bighorn sheep ramming [1,28], and provides insight for bioinspired design of energy absorbing materials for impact applications [29,30].

3.2. Materials and Methods

3.2.1. Samples

Four mature bighorn sheep (BHS) ram skulls were provided by the state of Colorado Department of Natural Resources under Colorado Parks and Wildlife scientific collection license number 14SALV2052A2. Horncore cortical bone properties from these rams were quantified in Aim 1 of this work [3]. BHS 1-6 in aim 1 are numbered in order of increasing horn curl length (ie, 1 has the shortest curl, 6 the longest). BHS 1 and 2 were not included in the velar bone study because the horns were too small to obtain a sufficient number of velae for mechanical testing. Exact ages were unknown, but the rams were estimated to be 5 – 8 years old by counting growth annuli on the horns [31]. Thus, these animals were old enough to have likely participated in routine head butting during the rut. Additionally, individual horn lengths were measured along the outer circumference from the proximal point of skull attachment to the distal tip. Curl length measurements serve as a surrogate measure of animal age and size since horns grow continuously throughout the life of a ram. Horn lengths ranged from 70.0 – 85.0 cm, corresponding to horn curls ranging from three-quarters to full curl (Figure 3-2a). Following horn length measurements, the left horn was cut from the skull using a hacksaw, then a transverse section was cut from the proximal end of the horn. The proximal-transverse horn sections were cut into medial and lateral halves to expose the velar bone tissue (Figure 3-2a). Rotary and oscillating Dremmel tools were used to extract 12 sections of velar bone (each approximately 20 mm long) from the lateral half of each horncore. To facilitate mechanical testing sample preparation, care was taken to identify and extract velar bone sections that were relatively straight,

adequately thick, and large enough to hold in a vice. This resulted in a total of 48 samples (n = 48) taken from 4 different rams (subjects).

Prior to extraction, the velar bone sections were grouped based on approximate anatomical position in the horncore. Two separate position groups were defined: proximo-distal position and anterior-posterior position (Figure 3-2a). Velae extracted from the proximal half of the horncore were assigned to the proximal group, and those from the distal half were assigned to the distal group. Similarly, sections extracted from the anterior region of the horncore were categorized as anterior, and those from the most posterior region were considered posterior. Since the horn and horncore grow proximo-distally, we were interested in how differences in bone tissue age along the length of the horncore may result in varying bone properties [20]. Furthermore, computational models have demonstrated a stress gradient from tensile stress in the anterior portion of the horncore to compressive stress in the posterior portion of the horn due to bending produced during ramming. Therefore, we were curious if bone tissue from these regions displayed different properties to accommodate the different loading modes [21,22]. Velar bone samples were also grouped based on their orientation within the horncore to investigate the influence of orientation on measured properties (Figure 3-2b). Mechanical test specimens prepared from velar bone sections (described in detail in the next section) were defined as either longitudinal or transverse. Sections were considered longitudinal if the long axis of the beam was most closely aligned with the growth direction of the horn (proximo-distal direction) and transverse if they were oriented most closely to a transverse plane. Samples were selectively extracted to achieve an even distribution of samples among the anatomical

positions and orientations, but final sample distributions were ultimately limited by material availability within in the horncore.

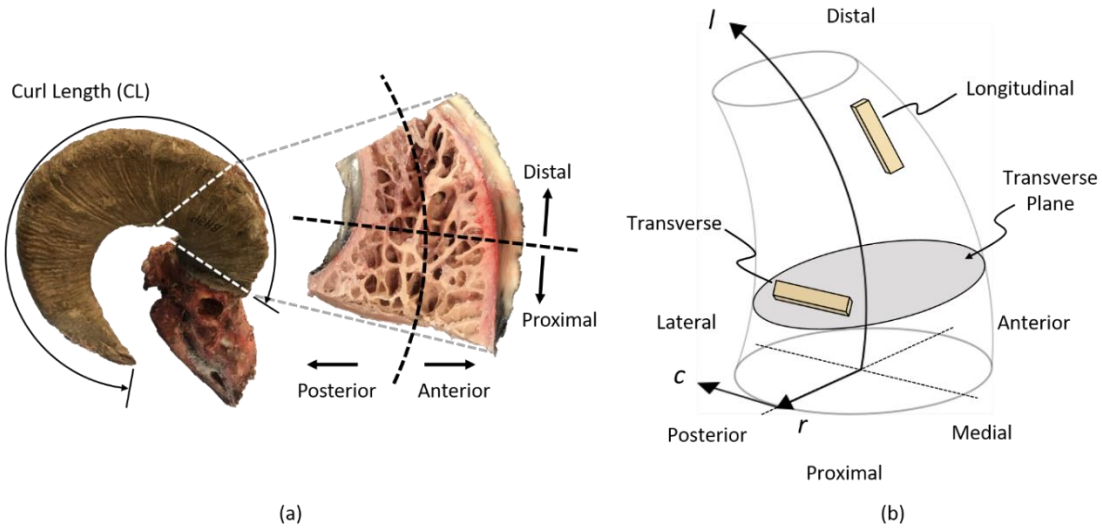

Figure 3-2. (a) Anterior/posterior and proximal/distal locations of velar extraction. (b) Schematic illustration of approximate orientation of longitudinal and transverse mechanical test specimens.

3.2.2. Mechanical Testing

3.2.2.1. Specimen Prep

Prismatic beams (0.6 mm thick x 1.05 mm wide x 14.5 mm long) were prepared from velar bone sections for dynamic mechanical analysis and three-point bend testing. Mechanical test specimens were prepared using methods similar to those used to prepare specimens from the thin cortical wall of the femoral neck [32]. Extracted velar bone sections (Figure 3-3a and b) were gripped in a vice and sectioned into thin strips approximately the width of final test specimens (Figure 3-3c and d) using a precision saw equipped with a diamond coated blade (Buehler IsoMet 1000; Lake Bluff, IL). These strips were subsequently cut to a final length of 14.5 mm using a precision saw, then ground to a

final thickness of 0.6 mm using a grinder-polisher (Buehler EcoMet 30; Lake Bluff, IL) with 800 grit silicon carbide polishing pads. During grinding, a series of slotted polishing blocks with constant slot width (~1.05 mm) and decreasing slot depth (from ~2 – 0.6 mm) were used to hold test specimens and maintain perpendicularity between adjacent surfaces until the final desired thickness was obtained (Figure 3-3e). Final mechanical test specimens (Figure 3-3f) were polished with 1200 grit silicon carbide polishing pads to remove surface defects. Final dimensions of each specimen were measured to the nearest 0.01 mm using digital calipers. Width and thickness measurements were made at three locations along the length of each specimen including the midpoint and points 5 mm from each end. Cross-sectional properties were calculated by averaging these values. Mechanical test specimens were wrapped in saline soaked gauze and stored frozen at -20 °C until mechanical testing. Previous research has shown that this is an effective method of preserving the mechanical properties of bone tissue postmortem [33–35].

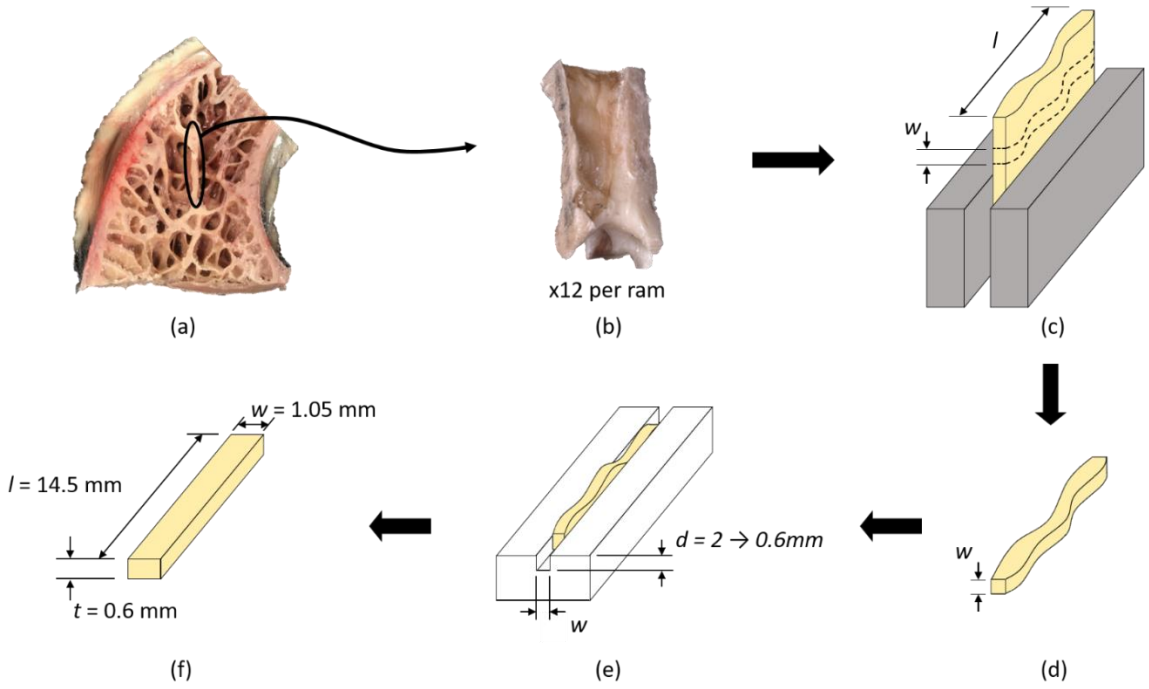

Figure 3-3. Sample preparation procedure. (a-b) 12 velar bone sails were cut from each horncore using an oscillating dremmel. (c-d) Sails were gripped in a vice to cut a strip with uniform width (w = ~1.05 mm) using a precision saw. (e) Cut strips were held in slotted plastic blocks and ground to final specimen thickness on rotating SiC polishing pads. A series of slotted plastic blocks with constant slot wdith (equal to specimen width ~1.05 mm) and decreasing slot depth (d = 2 to 0.6 mm) were used to maintain perpindicularity between adjacent walls as thickness was reduced during grinding process. (f) Final mechanical test specimens were ~14.5 mm long, 1.05 mm wide, and 0.6 mm thick.

3.2.2.2. Dynamic Mechanical Analysis

Dynamic mechanical analysis (DMA) was performed on mechanical test specimens to assess viscoelastic material properties of velar bone tissue using the Discovery DMA 850 (TA Instruments; New Castle, DE). Specimens were thawed and rehydrated in physiological saline at room temperature for at least 30 minutes prior to testing. Approximately 4 mm of each end of test specimens were loaded into tensile test grips leaving approximately 6.5 mm gauge length for testing. The actual gauge length of each

specimen was measured by the machine prior to testing. A bolt torque of 2 in-lb (22.6 N-cm) was applied to each grip to maintain consistent clamping forces at the ends of all specimens. Dynamic mechanical analysis was performed using a stress-controlled frequency sweep in a tensile loading configuration with a static pre-stress of 2.5 MPa superimposed with a sinusoidal oscillating stress of 2.1 MPa. Frequencies ranged from 0.1-100 Hz and data was collected at a rate of 10 points/decade. During testing, the exposed gauge lengths of specimens were wrapped in saline soaked gauze to minimize sample dehydration throughout the 30 minute test. DMA outputs included the storage modulus (E'), loss modulus (E"), and damping factor (tanδ). The storage modulus is a measure of a materials elastic response and represents the energy stored in the sample during loading. Conversely, the loss modulus is a measure of a materials viscous response and represents the energy dissipated due to friction and internal motion. The damping factor is the ratio between energy lost and energy stored and is a measure of how efficiently a material dissipates energy [36]. The applied stress used here was determined through a pilot study to ensure an adequate signal-to-noise ratio was achieved based on results from previous studies that used DMA to investigate the viscoelastic properties of bone tissue [25]. The maximum applied stress of 4.6 MPa is well below published values of tensile yield strength of compact bone [37] and resulted in linear viscoelastic behavior without plastic deformation. Additionally, using stress values well below the tensile yield strength of bone were used to minimize damage to the tissue prior to subsequent three-point bend testing.

3.2.2.3. Three-point Bending

Following DMA, mechanical test specimens were loaded to failure under three-point bending similar to previous studies on the mechanical properties of bone tissue

[3,38,39]. Three-point bending tests were performed on an MTS Bionix Test System (MTS Systems Corporation; Eden Prairie, MN) based on ASTM Standard D5934-96 [40]. Briefly, specimens were supported on a fixed span of 9.6 mm and a central load was applied via a loading nose in the direction of beam thickness at a constant rate of 0.768 mm/s. This loading rate results in an estimated strain rate of 0.03 s^{-1}, approximately equal to the strain rate achieved in previous three-point bend tests of larger specimens from bighorn sheep horncore cortical bone tested in Aim 1 [3]. The radii of the loading nose and support points were all 1 mm. Specimens were kept wrapped in saline soaked gauze at room temperature until immediately prior to testing to minimize specimen dehydration, then tests were completed in ambient conditions in under 60 seconds. During testing, force data was collected at 1024 Hz using a 2 lb load cell (FUTEK; Irvine, CA) while MTS actuator displacement provided a measure of mid-span deflection of the specimen (MTS Systems Corporation; Eden Prairie, MN). Engineering beam theory was used to calculate normal stress (σ; Equation 3.1) and normal strain (ε; Equation 3.2) from the measured force (F) and loader displacement (d) based on the support span (L), beam width (w), and beam thickness (t).

$$\sigma = F\left(\frac{3L}{2wt^2}\right) \tag{3.1}$$

$$\varepsilon = d\left(\frac{6t}{L^2}\right) \tag{3.2}$$

The bending modulus (E) was calculated as the slope of the linear region of the stress-strain curve. The yield point was determined using the 0.2% offset method, and yield stress (σ_y) and yield strain (ε_y) were defined as the stress and strain at the yield point, respectively. The modulus of resilience (u_r) was defined as the area under the stress-strain curve up to the yield point. The failure point was defined as the point at which the maximum load was achieved. Stress and strain calculated at the failure point were defined as the ultimate stress (σ_{ult}) and ultimate strain (ε_{ult}), respectively. It should be noted that these are not true measures of the ultimate stress and ultimate strain of the material since equations 1 and 2 are based off the assumption of linear elasticity which was generally violated at the maximum load due to bone plasticity. However, this approach is commonly used to provide an estimate of bone strength under three-point bending for comparative purposes. The modulus of toughness (u_t) was calculated as the area under the stress-strain curves to the failure point. Additionally, the fracture energy (W) was calculated as the area under the force-displacement curve normalized by the specimen cross-sectional area in order to compare velar bone energy absorption to other bone tissues characterized under three-point bending. These calculations do not account for any shear deformations that are inevitably present due to bending. As such, we are likely reporting an elastic modulus value that slightly underestimates the true elastic modulus of the velar bone material. However, error associated with this simplification is minimal for the support span to specimen thickness ratio of 16 used here [41]. Following mechanical testing, one-half of each fractured test specimen was used to prepare histological sections of specimen cross-sections while the other half was used for composition analysis.

3.2.3. Histomorphometry

Histology samples (one-half of fractured mechanical test specimens) were dehydrated in 70% ethanol for 24 hrs, then embedded in polymethyl methacrylate (PMMA; Lang Dental Ortho-Jet BCA; Florence, MA) in a pressure chamber charged to ~25 psi to prevent air bubble formation. After embedding, ~150 μm sections were cut transversely with respect to the long axis of mechanical test specimens using a precision saw equipped with a diamond coated blade. Subsequently, a grinder-polisher with an 800-grit silicon carbide polishing pad was used to grind sections to a final thickness of 70 – 90 μm. Ground sections were rinsed under running tap water and stained with toluidine blue following a modified protocol previously developed to distinguish cement lines in human cortical bone [42]. Briefly, samples were placed in 0.2 M formic acid for 1 minute and 45 seconds, rinsed in distilled water, transferred to 70% ethanol for 15 minutes, and then immediately immersed in the toluidine blue staining solution for 5 min. All steps were performed on an orbital shaker plate oscillating at 120 rpm to provide agitation to the samples in solution. The toluidine blue stain contained 1 g toluidine blue powder (Acros Organics; ThermoFisher Scientific; Waltham, MA) and 1 g sodium tetraborate decahydrate (Fisher Chemical; ThermoFisher Scientific; Waltham, MA) per 100 mL of distilled water. After staining, samples were dipped in distilled water, then dehydrated through a graded series of ethanol concentrations (70%, 95%, and two changes of 100%, ~30 seconds each). Stained sections were mounted on microscope slides and cover slipped with Cytoseal XYL (Thermo Scientific; Waltham, MA).

Sections were observed under a light microscope (Laborlux S; Leica Camera AG; Wetzlar, Germany) from 100 – 250x magnification to facilitate manual counting of intact

and fragmented secondary osteons following previously established definitions of these remodeling events [43]. However, previous studies on the histomorphometry of cortical bone have largely used transverse sections from the diaphysis of long bones where osteons are primarily aligned with the bone's long axis. As such, osteons appear mostly circular in these sections. Conversely, velar bone coupons had varying orientations within the horncore, and velar osteons had a range of orientations within sections. In most cases, cement lines were circular in appearance and therefore associated with velar osteons that were aligned with the long axis of the mechanical test coupons (Figure 3-4a). In other cases, elongated Haversian canals in the plane of the section provided evidence of velar osteons aligned either perpendicularly or obliquely to the long axis of mechanical test coupons (Figure 3-4b). Only osteons aligned with the long axis of velar coupons (i.e., circular cement lines and associated fragments) were counted toward the osteon population density (OPD) since it was difficult to reliably identify the cement lines of osteons aligned perpendicularly or obliquely to the long axis of velar coupons. Therefore, low OPD values in this study either indicate an absence of osteons or the presence of osteons aligned perpendicularly or obliquely to the long axis of velar bone coupons. After osteon counting, sections were imaged at 100x magnification using a stereoscope (Discovery.V20; Carl Zeiss AG; Oberkochen, Germany) equipped with a color camera (Axiocam 512 color; Carl Zeiss AG; Oberkochen, Germany). Images were imported into BioQuant (BIOQUANT Image Analysis Corporation; Nashville, TN) to quantify pore area and total area of each cross-section. Haversian canals and cavities related to resorption or refilling were included in the pore area measurements. Microstructural parameters of tissue porosity (φ) and osteon population density (OPD) were calculated by equations 3.3 and 3.4, respectively.

$$\varphi\,[\%] = \frac{Pore\ Area}{Total\ Area} \times 100\% \tag{3.3}$$

$$OPD\ \left[\frac{\#}{mm^2}\right] = \frac{\#\ of\ secondary\ osteons}{Total\ Area} \tag{3.4}$$

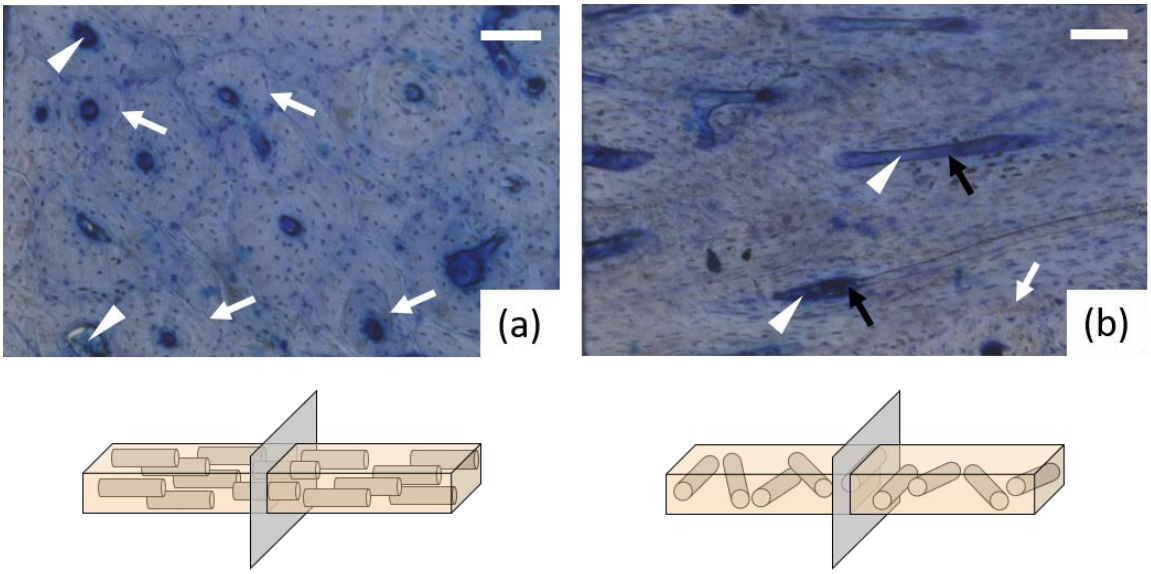

Figure 3-4. Histological cross-sections of velar bone mechanical test coupons. (a) Cross-section with secondary osteons (white arrows) that are mostly circular in shape and aligned with the long axis of the mechanical test coupon as indicated in the schematic below (schematic not to scale). These osteons were included in the calculation of OPD. A representative selection of pores (white triangles) that contributed to the calculated pore area are also shown. Scale bar = 100 μm. (b) Cross-section with elongated Haversian canals (black arrows) indicative of osteons aligned perpendicularly or obliquely to the long axis of the mechanical test coupon as illustrated in the schematic below (schematic not to scale). These osteons were not included in the calculation of OPD since it was difficult to reliably identify cement lines in this orientation. Secondary osteons aligned with the long axis of the mechanical test specimen (white arrow) and representative pores (white triangles) are also shown. Scale bar = 100 μm.

3.2.4. Composition Analysis

The remaining halves of fractured mechanical test specimens were used to estimate the composition of each specimen using methods similar to those described previously [3,38]. First, hydrated specimens were weighed on an analytical balance precise to 0.1 mg (ME204E; Mettler Toledo; Columbus, OH) to determine the wet mass (m_{wet}) of the sample. Next, specimens were dried in a muffle furnace (Barnstead Thermolyne Corporation;

Ramsey, MN) at 100 °C for 24 hours and reweighed to determine the dry mass (m_{dry}) of each sample. The difference between the wet and dry masses represents the mass of water lost during drying. Thus, the water content (WC) of each specimen can be estimated by taking the ratio of this difference and the total wet mass of each specimen (Equation 3.5). Finally, samples were returned to the furnace at 600 °C for 48 hours and weighed again to determine the ashed mass (m_{ash}) of each sample. At 600 °C, all organic matter present in the bone tissue is burned off, leaving only mineral behind. Therefore, the bone mineral content (BMC) can be calculated as the ratio of ashed mass to dry mass (Equation 3.6).

$$H_2O\ [\%] = \frac{m_{wet} - m_{dry}}{m_{wet}} \times 100\% \tag{3.5}$$

$$BMC\ [\%] = \frac{m_{ash}}{m_{dry}} \times 100\% \tag{3.6}$$

3.2.5. Statistics

A linear mixed model was used to investigate how anatomical position and orientation within the horncore influenced all the measured bone properties. In this model, fixed effects included the categorical variables of proximo-distal position (proximal or distal), anterior-posterior position (anterior or posterior), and orientation (longitudinal or transverse). Pairwise interaction terms between fixed effects were also included in the model. Additionally, the ram each sample came from (i.e. subject) was included as a random effect in the model. The random effect of ram provided greater model sensitivity to differences in measured properties within each horncore despite variation between individual rams due to uncontrollable differences (i.e. genetics, age, etc.). The viscoelastic properties (E', E", and tanδ) measured by DMA were assessed at frequencies of 0.1, 1, 10,

and 50 Hz. Simple linear regression was used to assess relationships between curl length (as a surrogate measure of ram age and size) and velar bone microstructure properties (φ and OPD) and composition properties (H_2O % and BMC). Additionally, linear stepwise regression was used to establish models to predict measured mechanical properties using measured values for curl length, φ, OPD, H_2O %, and BMC as predictor variables. Potential models were identified using forward stepwise regression using the minimum BIC selection criteria. Identified models were subsequently evaluated based on overall fit and interpretation of model parameters prior to final model selection. Finally, differences between velar bone properties and horncore cortical bone properties (from Aim 1) were assessed using a linear mixed model including bone type (velar or cortical) as a fixed effect and ram ID (i.e. subject) as a random effect. JMP Pro (SAS Institute; Cary, NC) was used for all statistical analyses and a p-value less than 0.05 was considered significant in all cases.

3.3. Results

3.3.1. Mechanical Testing

3.3.1.1. Specimen Prep

Final specimen distributions in terms of anatomical positions (proximo-distal and anterior-posterior) and orientation are shown for each ram in Figures 3-5 to 3-7. Overall, final specimen distributions are fairly well-balanced despite being limited to material available in each horncore. One section from BHS 6 broke during sample preparation resulting in 11 specimens for that ram. All 12 sections were successfully prepared for the other three sheep, resulting in a total of 47 specimens included in subsequent analyses.

Final mechanical test specimen dimensions for each ram are shown in Table 3-1. In general, the methodology used to prepare mechanical test specimens resulted in consistent prismatic beam specimens despite the curvature and irregularity of velar bone sections.

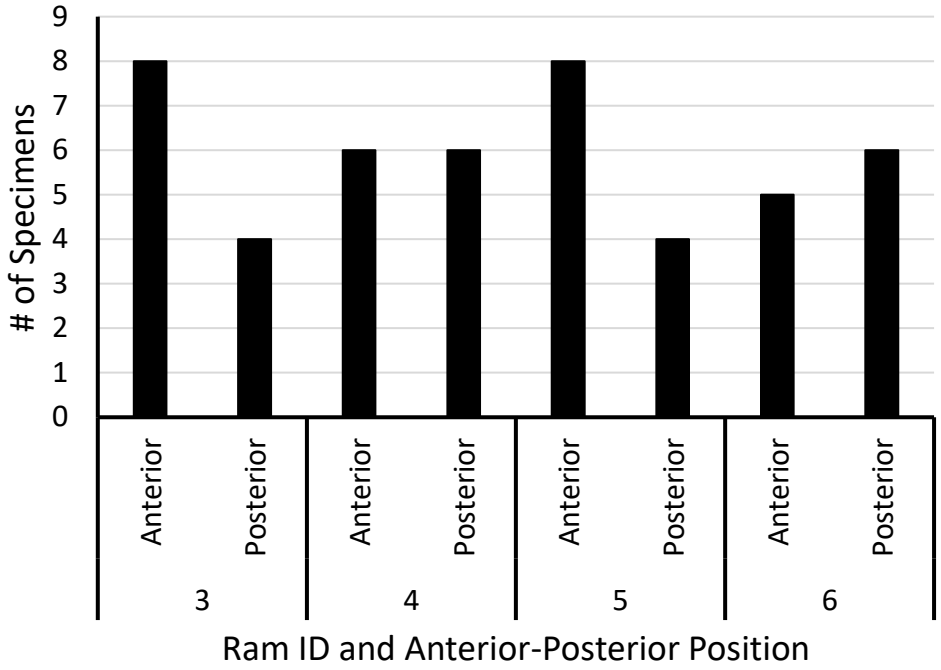

Figure 3-5. Specimen distribution for each ram in terms of anterior-posterior position.

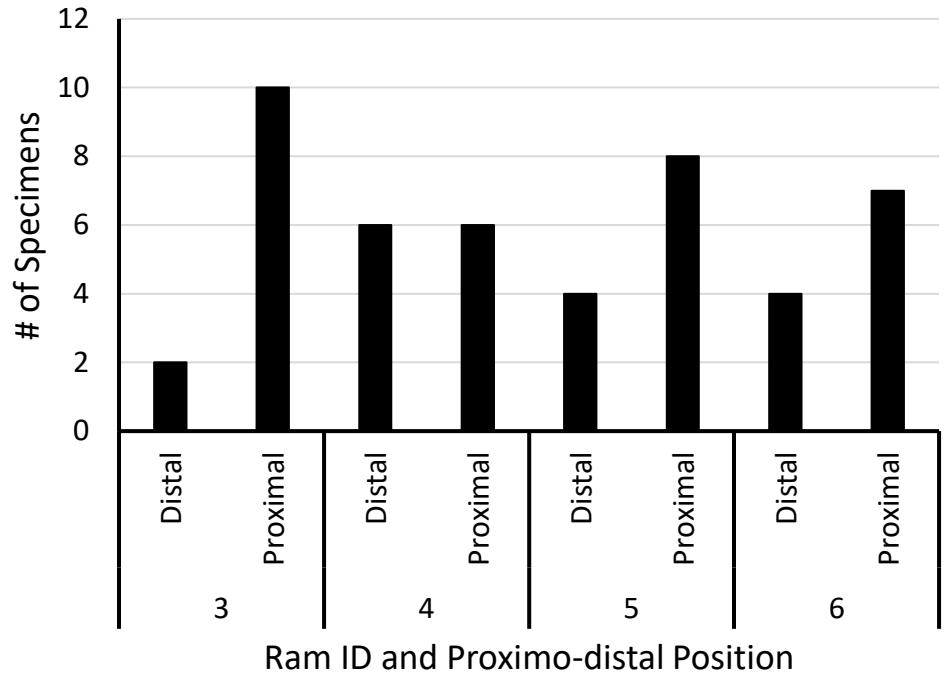

Figure 3-6. Specimen distribution for each ram in terms of proximo-distal position.

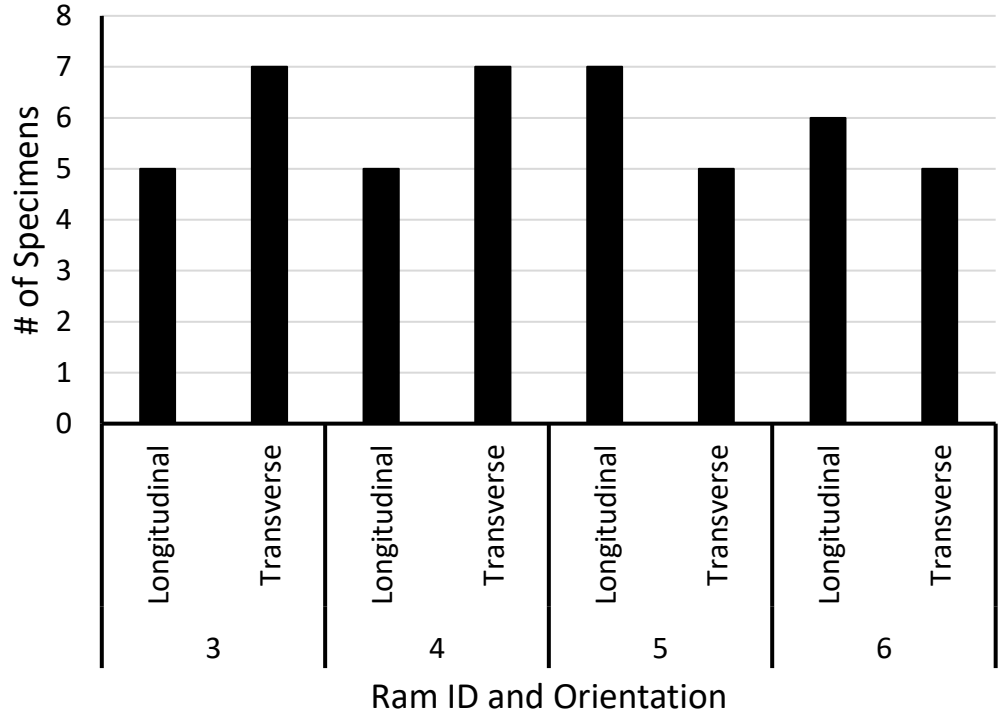

Figure 3-7. Specimen distribution for each ram in terms of orientation.

Table 3-2. Final dimensions of velar bone mechanical test specimens For each ram, values are presented as the average ± standard deviation of all specimens. Note: width and thickness of each specimen were determined by averaging three measurements taken along specimen length.

	Length [mm]	Width [mm]	Thickness [mm]
BHS 3	14.63 ± 0.69	1.05 ± 0.07	0.58 ± 0.05
BHS 4	14.17 ± 1.06	1.02 ± 0.05	0.58 ± 0.04
BHS 5	14.28 ± 0.49	1.04 ± 0.03	0.59 ± 0.06
BHS 6	14.77 ± 0.29	1.05 ± 0.04	0.62 ± 0.09

3.3.1.2. Dynamic Mechanical Analysis

The storage modulus (E'), loss modulus (E"), and damping factor (tanδ) measured for frequencies ranging from 0.1 to 50 Hz are plotted in Figures 3-8, 3-9, and 3-10, respectively. Data measured beyond 50 Hz was excluded from analysis due to erroneous data attributed to inertial effects at high frequencies. Storage modulus values tended to increase while loss modulus and damping factor decreased with increasing frequencies. Average values of E', E", and tanδ at 0.1, 1, 10, and 50 Hz are shown in Table 3-2. Results from mixed model analyses at each frequency of interest (0.1, 1, 10, and 50 Hz) are presented in Table 3-3. Results from the mixed model demonstrated a significant ($p < .05$) interaction effect between anterior-posterior position and orientation for the measured storage modulus for all frequencies investigated (Table 3-3). At each frequency, longitudinal samples had a higher storage modulus in the anterior region of the horncore while transverse specimens had a higher storage modulus in the posterior region (Figure 3-11). Despite the significant interaction effect, post-hoc pairwise comparisons using Tukey HSD with Tukey-Kramer adjustment found no significant differences between individual pairs at each frequency. No other model effects were significant.

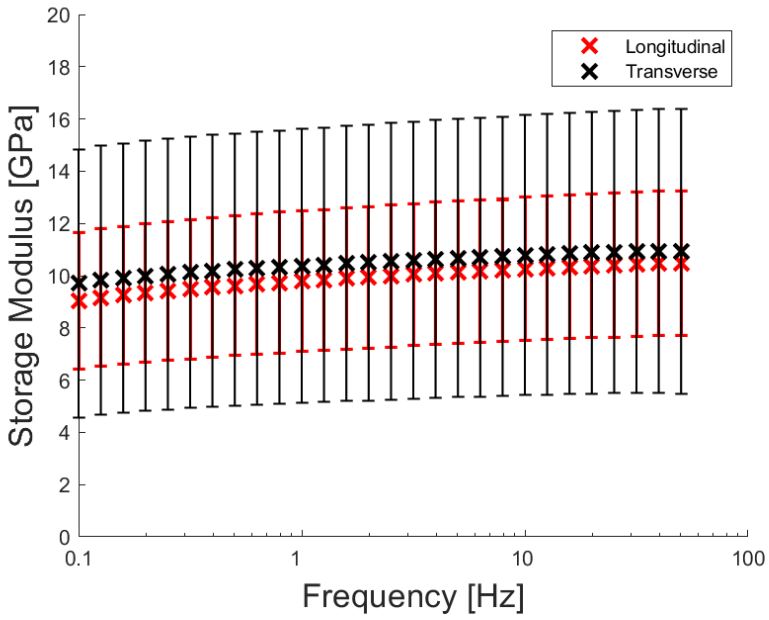

Figure 3-8. Storage modulus of velar bone specimens from 0.1-50 Hz separated by orientation. Storage modulus increased with increasing frequency in both orientations. Data shown as means ± standard deviation.

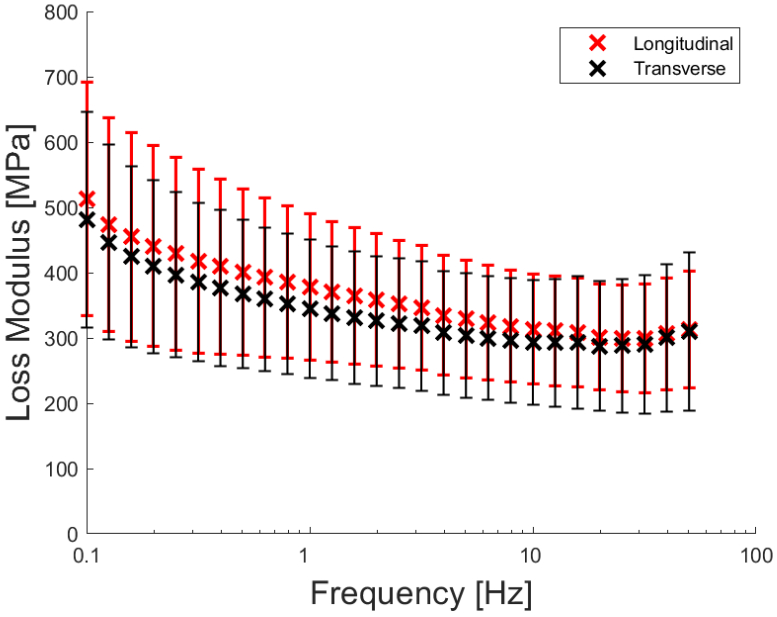

Figure 3-9. Loss modulus of velar bone specimens from 0.1-50 Hz separated by orientation. Loss modulus decreased with increasing frequency in both orientations.

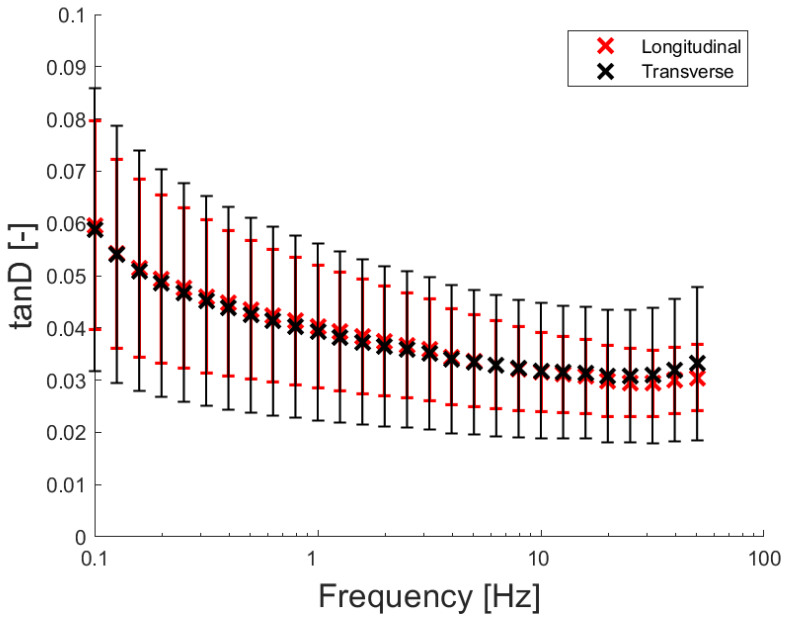

Figure 3-10. Damping factor of velar bone specimens from 0.1-50 Hz separated by orientation. Damping factor decreased with increasing frequency in both orientations.

Table 3-3. Storage modulus (E'), loss modulus (E"), and damping factor (tanδ) measured via dynamic mechanical analysis (DMA) at 0.1, 1.0, 10, and 50 Hz. Values presented as Mean ± Standard Deviation for all specimens.

	Frequency [Hz]			
	0.1	**1.0**	**10.0**	**50.0**
E' [GPa]	9.37 ± 4.06	10.09 ± 4.16	10.52 ± 4.25	10.71 ± 4.32
E" [MPa]	496.46 ± 170.96	360.94 ± 109.12	303.33 ± 89.66	311.25 ± 105.55
tanδ [-]	0.06 ± 0.02	0.04 ± 0.01	0.03 ± 0.01	0.03 ± 0.01

*Table 3-4. P-values from mixed model analyses of storage modulus, loss modulus, and damping factor measured via dynamic mechanical analysis at 0.1, 1.0, 10, and 50 Hz. Significant values ($p < 0.05$) shown in **bold**.*

	Frequency				
	0.1 Hz	**1.0 Hz**	**10.0 Hz**	**50.0 Hz**	**Source of Variation**
Storage Modulus	.9821	.9523	.9531	.9217	**Proximal/Distal**
	.3063	.3313	.3314	.3621	**Anterior/Posterior**
	.3551	.3902	.4032	.4395	**Orientation**
	.7966	.8278	.8390	.8151	**Proximal/Distal*Anterior/Posterior**
	.9293	.9717	.9968	.9850	**Proximal/Distal*Orientation**
	.0306	**.0276**	**.0266**	**.0288**	**Anterior/Posterior*Orientation**
Loss Modulus	.8002	.5488	.7630	.9285	**Proximal/Distal**
	.9335	.3438	.3560	.4012	**Anterior/Posterior**
	.8382	.8594	.8977	.6677	**Orientation**
	.8841	.4523	.8905	.9320	**Proximal/Distal*Anterior/Posterior**
	.5630	.3146	.5772	.7243	**Proximal/Distal*Orientation**
	.3855	.1345	.2376	.2802	**Anterior/Posterior*Orientation**
Damping Factor	.4029	.5259	.7573	.9588	**Proximal/Distal**
	.1605	.5525	.4033	.3530	**Anterior/Posterior**
	.3557	.8803	.8038	.9329	**Orientation**
	.5752	.6679	.9318	.8924	**Proximal/Distal*Anterior/Posterior**
	.9426	.4792	.7816	.8713	**Proximal/Distal*Orientation**
	.1600	.1856	.0655	.0648	**Anterior/Posterior*Orientation**

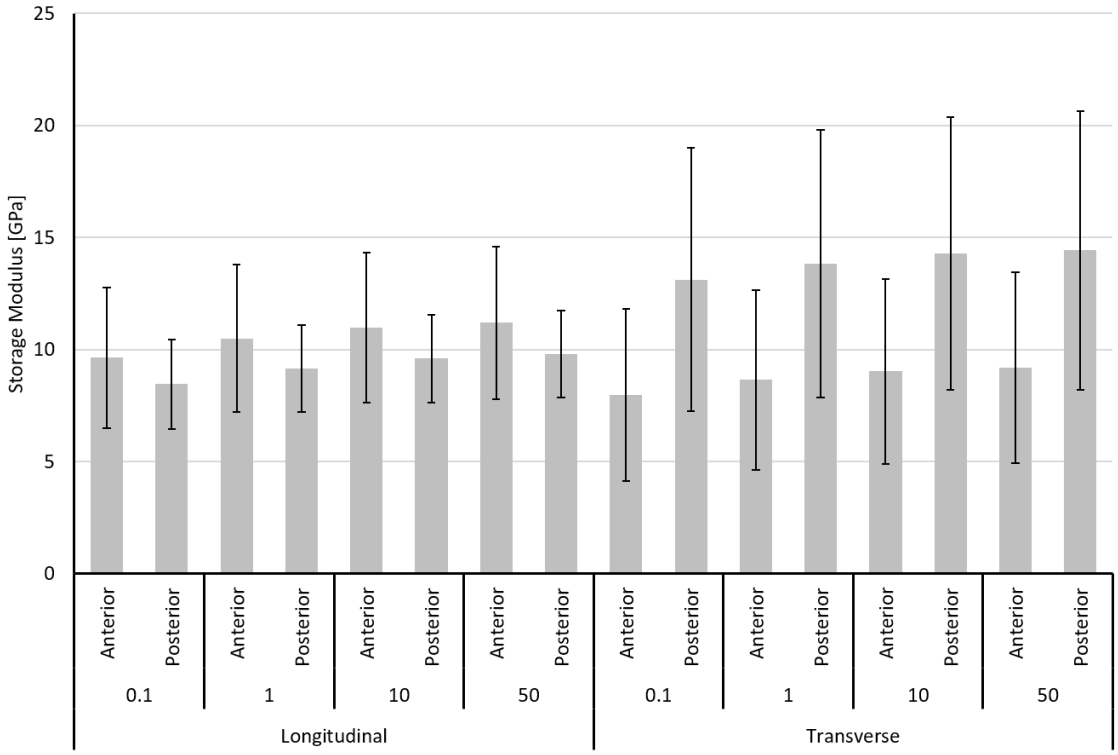

Figure 3-11. Interaction between anterior-posterior position and orientation on measured storage modulus at each investigated frequency. Values presented as mean ± standard deviation. Longitudinal samples tend to have higher storage modulus in the anterior region while transverse specimens have a higher storage modulus in the posterior region. Pairwise comparison at each frequency using Tukey HSD with Tukey-Kramer adjustment found no significant differences between individual pairs.

3.3.1.3. Three-point Bending

Mixed model analyses of mechanical properties measured in three-point bending showed that velar bone yield strain, modulus of resilience, modulus of toughness, and fracture energy were all significantly higher in transversely oriented samples ($p = .0070$, $p = .0291$, $p = .0371$, and $p = .0371$, respectively, Table 3-4). Additionally, the interaction term between anterior-posterior position and orientation explained a significant amount of variation in the bending modulus ($p = .0218$), yield strength ($p = .0042$), modulus of resilience ($p = .0023$), ultimate strength ($p = .0061$), modulus of toughness ($p=.0046$), and fracture energy ($p = .0046$) (Table 3-5). This significant interaction is indicative of the fact

that the comparisons between longitudinal and transverse samples for these mechanical properties were codependent on which region of the horncore samples were being compared. For example, the bending modulus of longitudinal samples was higher than transverse samples in the anterior region of the horn, but lower than transverse samples in the posterior region of the horn (Figure 3-12a). Alternatively, longitudinal and transverse samples had comparable modulus of toughness values in the anterior region of the horncore, but transvers samples had greater modulus of toughness in the posterior region of the horncore (Figure 3-13b). All similar cases of codependent comparisons resulted in a significant interaction effect (Table 3-4). Conversely, the average yield strain of transverse samples was higher than longitudinal samples in the anterior and posterior regions of the horncore (Figure 3-12c). Accordingly, the corresponding interaction term was non-significant for yield strain (Table 3-4). However, significant interaction effects were not always accompanied by significant pairwise comparisons. Post-hoc analysis using Tukey HSD with Tukey-Kramer adjustment indicated the only notable pairwise comparisons were between longitudinal and transverse samples in the posterior region, where transverse samples had significantly higher yield strength ($p = .0475$, Figure 3-12b), modulus of resilience ($p = .0127$, Figure 3-13a), modulus of toughness ($p = .0222$, Figure 3-13b), fracture energy ($p = .0222$), and marginally higher ultimate strength ($p = .0763$, Figure 3-12d).

*Table 3-5. P-values from linear mixed model analyses of mechanical properties measured via three-point bending including bending modulus (E), yield strength (σ_y), yield strain (ε_y), modulus of resilience (u_r), ultimate strength (σ_{ult}), ultimate strain (ε_{ult}), modulus of toughness (u_t), and fracture energy (W). Significant values ($p < 0.05$) indicated in **bold**.*

Source of Variation	E	σ_y	ε_y	u_r	σ_{ult}	ε_{ult}	u_t	W
Proximal/Distal	.9366	.8778	.8351	.7599	.8757	.7644	.5795	.5795
Anterior/Posterior	.6290	.3654	.5657	.2242	.4301	.8180	.3001	.3001
Orientation	.5946	.1181	**.0070**	**.0291**	.1740	.0604	**.0371**	**.0371**
Proximal/Distal*Anterior/Posterior	.9640	.9247	.4864	.8822	.8882	.9003	.8562	.8562
Proximal/Distal*Orientation	.7425	.8277	.7405	.8896	.6985	.8367	.7712	.7712
Anterior/Posterior*Orientation	**.0218**	**.0042**	.1885	**.0023**	**.0061**	.2325	**.0046**	**.0046**

Table 3-6. Results from three-point bending showing bending modulus (E), yield strength (σ_y), yield strain (ε_y), modulus of resilience (u_r), ultimate strength (σ_{ult}), ultimate strain (ε_{ult}), modulus of toughness (u_t), and fracture energy (W). Values presented as Mean ± Standard Deviation for each ram (BHS 3-6), and means for all rams (Mean)

	E [GPa]	σ_y [MPa]	ε_y [-]	u_r [MJ/m^3]	σ_{ult} [MPa]	ε_{ult} [-]	u_t [MJ/m^3]	W [kJ/m^2]
BHS 3	7.7 ± 2.8	99.4 ± 42.5	0.0140 ± 0.0018	0.83 ± 0.41	135.1 ± 52.4	0.0444 ± 0.0110	4.90 ± 2.85	5.2 ± 3.0
BHS 4	9.6 ± 3.7	122.1 ± 60.4	0.0139 ± 0.0027	1.02 ± 0.63	154.8 ± 75.4	0.0366 ± 0.0165	4.78 ± 4.20	5.1 ± 4.5
BHS 5	9.7 ± 3.6	109.3 ± 47.2	0.0127 ± 0.0019	0.83 ± 0.47	142.8 ± 55.7	0.0308 ± 0.0106	3.22 ± 1.86	3.4 ± 2.0
BHS 6	7.2 ± 3.7	87.8 ± 49.0	0.0138 ± 0.0028	0.70 ± 0.44	114.3 ± 61.2	0.0324 ± 0.0121	2.57 ± 1.97	2.7 ± 2.1
Mean	8.6 ± 3.5	105.0 ± 50.2	0.0136 ± 0.0023	0.85 ± 0.49	137.2 ± 61.5	0.0362 ± 0.0134	3.90 ± 2.97	4.2 ± 3.2

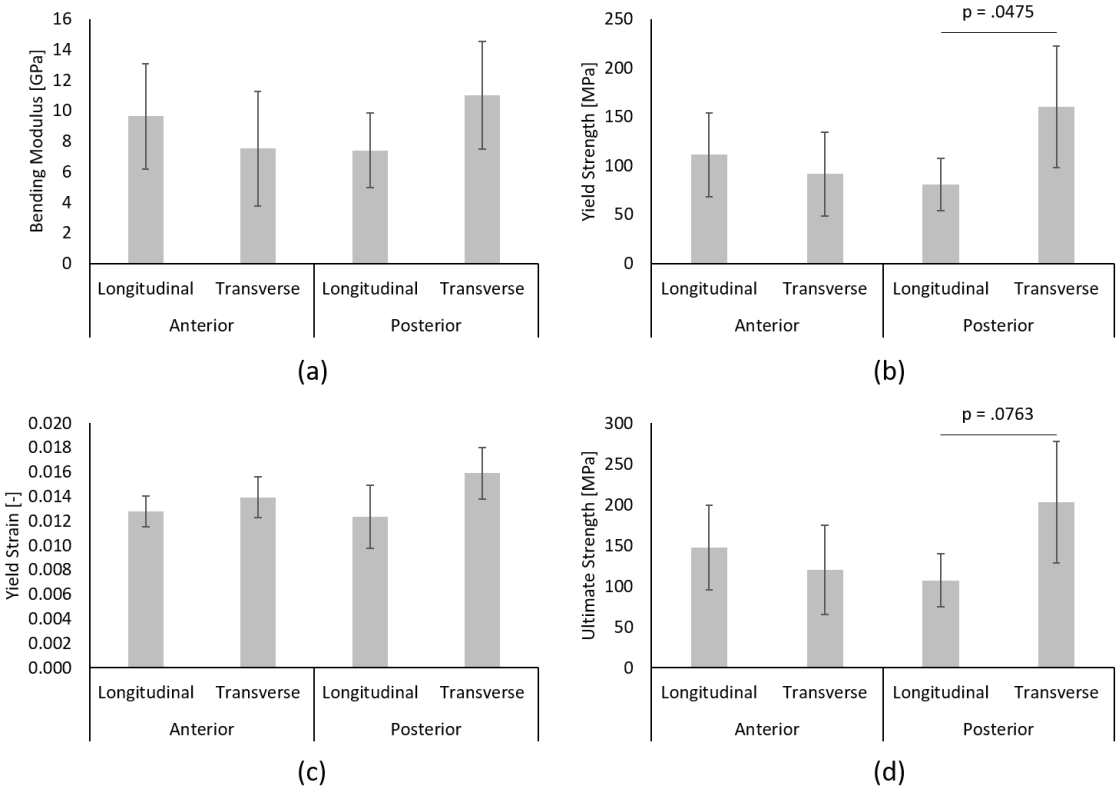

Figure 3-12. Pairwise comparisons of (a) bending modulus, (b) yield strength, (c) yield strain, and (d) bending strength based on anterior-posterior position and orientation of each sample. Data presented as mean ± standard deviation in all plots. Results from mixed model analyses indicated that the interaction term between anterior-posterior position and orientation significantly influenced the bending modulus, yield strength, and ultimate strength (Table 5). Longitudinal samples tended to have higher bending modulus and strength in the anterior region, while transverse samples had increased elastic modulus and strength in the posterior region (a, b, d). In the posterior region of the horncore, transverse samples had significantly higher yield strength ($p = .0475$) and marginally higher bending strength ($p = .0763$) than longitudinal samples. Other pairwise comparisons for bending modulus, yield strength and ultimate strength were insignificant. Meanwhile, yield strain was significantly higher in transverse samples compared to longitudinal samples regardless of other factors ($p = .0070$).

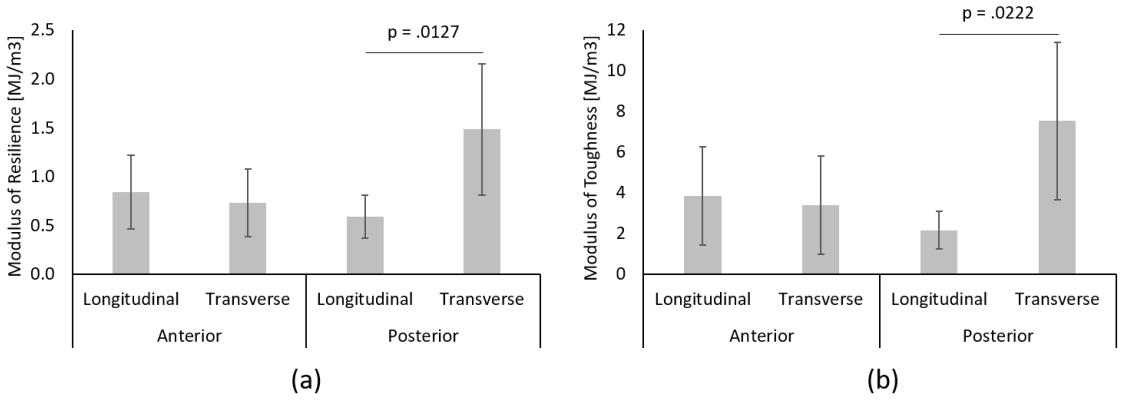

Figure 3-13. Pairwise comparisons of modulus of resilience (a) and modulus of toughness (b) based on anterior-posterior position and orientation of each sample. Data presented as mean ± standard deviation in both plots. Results from mixed model analyses indicated that transverse samples had significantly higher modulus of resilience (p = .0291) and modulus of toughness (p = .0371) than longitudinal samples. Additionally, the interaction term between anterior-posterior position and orientation significantly influenced the each of these properties (Table 5). For longitudinal samples, energy storage and absorption were greater in the anterior region but transverse samples demonstrated greater energy storage and absorption in the posterior region. However, pairwise comparisons indicated that the only significant differences in these values were found in the posterior region of the horncore, where transverse samples had significantly higher modulus of resilience (p = .0127) and modulus of toughness (p = .0222) than longitudinal samples. The fracture energy demonstrated identical trends to the modulus of toughness and is therefore not presented for brevity.

3.3.2. Histomorphometry

Microstructural parameters of velar bone porosity (φ) and osteon population density (OPD) measured via histomorphometry are shown in Table 3-6. Results from mixed model analyses for microstructural parameters are shown in Table 3-7. No significant sources of variation were identified for histomorphometric results. However, closer inspection of the marginally significant interaction term between anterior-posterior position and orientation for osteon population density and porosity highlighted some interesting trends. Osteon population density and porosity values were relatively constant for transverse samples regardless of anterior-posterior position. However, longitudinal

samples in the posterior region had significantly higher porosity (p = .0293) but marginally lower OPD (p = .0609) than longitudinal samples in the anterior region (Figure 3-14). In addition, longitudinal samples from the posterior region had significantly higher tissue porosity than transverse samples from the anterior region (p = .0355, Figure 3-14).

Table 3-7. Results from histomorphometry and composition analysis showing velar bone porosity (φ), osteon population density (OPD), bone mineral content (BMC), and bone water content (H_2O). Data presented as mean ± standard deviation for individual rams (BHS 3-6) and the means from all rams (Mean).

	φ [%]	OPD [#/mm^2]	BMC [%]	H_2O [%]
BHS 3	5.51 ± 4.28	3.11 ± 4.28	63.7 ± 5.1	17.2 ± 6.5
BHS 4	5.53 ± 2.91	9.70 ± 6.84	64.7 ± 5.8	19.0 ± 5.7
BHS 5	3.89 ± 2.08	7.29 ± 7.90	66.1 ± 4.6	18.3 ± 7.4
BHS 6	12.27 ± 9.38	2.86 ± 3.58	70.0 ± 7.5	19.4 ± 6.7
Mean	6.68 ± 6.06	5.80 ± 6.46	66.0 ± 6.0	18.4 ± 6.4

Table 3-8. P-values from linear mixed model analyses of results from histomorphometry and composition analyses. No significant (p < 0.05) sources of variation were identified.

Source of Variation	φ [%]	OPD [#/mm^2]	BMC [%]	H_2O [%]
Proximal/Distal	0.4328	0.0989	0.0756	0.0761
Anterior/Posterior	0.1709	0.1842	0.2489	0.9609
Orientation	0.1673	0.6654	0.4504	0.7744
Proximal/Distal*Anterior/Posterior	0.8487	0.1538	0.3819	0.7602
Proximal/Distal*Orientation	0.5368	0.3227	0.5014	0.6697
Anterior/Posterior*Orientation	0.0574	0.1107	0.5411	0.5040

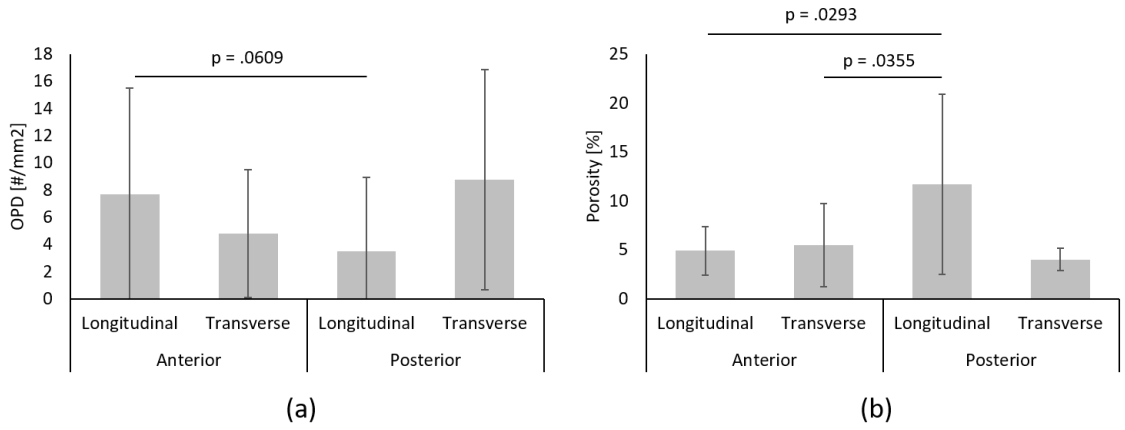

Figure 3-14. Pairwise comparisons of osteon population density (OPD) (a), and porosity (b) based on anterior-posterior position and orientation. Data presented as least-square (LS) means ± standard error. Transverse samples had similar values of OPD and porosity in both regions (anterior and posterior) of the horncore. However, longitudinal samples from the anterior region tended to have higher OPD (marginally significant, p = .0609) and significantly lower porosity (p = .0293) compared to longitudinal samples from the posterior region. Additionally, velar bone porosity was significantly higher in longitudinal samples from the posterior region than transverse samples from the anterior region (p = .0355).

3.3.3. Composition

Measured bone mineral content (BMC) and water content (H_2O) of velar bone samples is shown in Table 3-6. Results from mixed model analyses of compositional parameters (BMC and H_2O) are shown in Table 3-7. Distal samples tended to have marginally higher bone mineral content (p = .0756) and water content (p = .0761) than proximal samples. No other significant differences were identified by the mixed model.

3.3.4. Regression Analyses

Linear regression demonstrated that bone mineral content had a significant but weak positive correlation with curl length (p = .0203, r^2 = 0.119, Figure 3-15). Porosity also tended (p = .0634) to increase with increasing curl length, but curl length explained

less than 10% of the total variation in velar bone porosity ($r^2 = 0.0745$). Velar bone water content and osteon population density were not correlated with curl length.

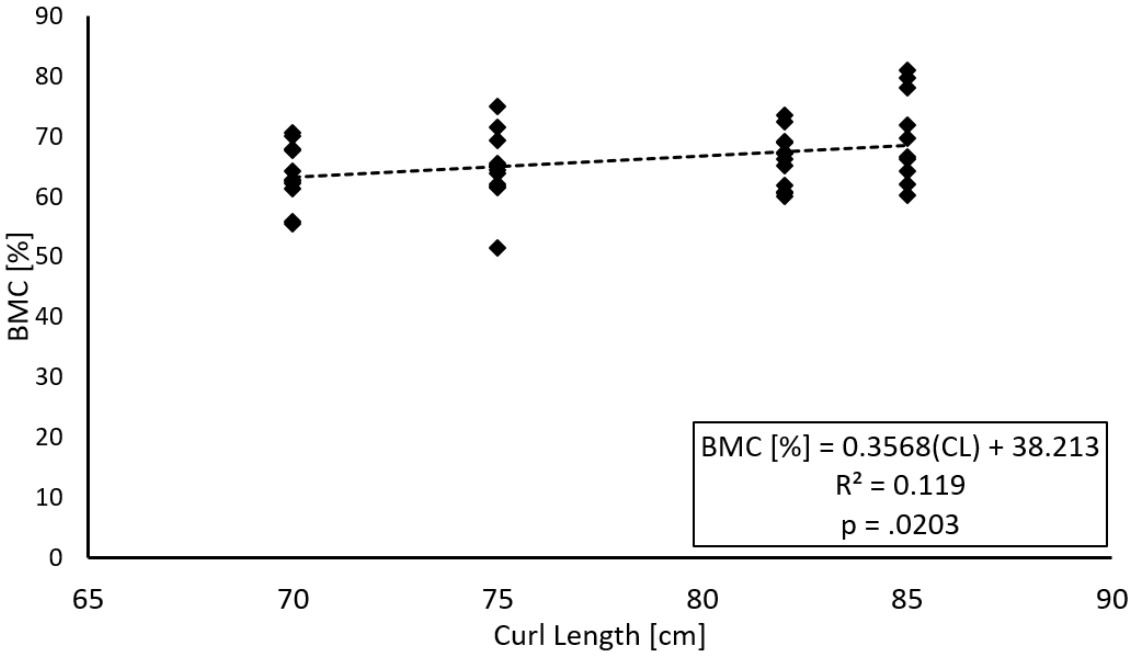

Figure 3-15. Bone mineral content had a significant but weak positive correlation with curl length ($p = .0203$, $r^2 = 0.119$).

Stepwise regression demonstrated that osteon population density was the best predictor variable of viscoelastic properties measured via DMA. OPD had a significant positive correlation and explained close to 40% of the total variation in storage modulus at 0.1 Hz ($p < .0001$, $r^2 = 0.3838$, Figure 3-16a), 1.0 Hz ($p < .0001$, $r^2 = 0.3788$, Figure 3-16b), 10 Hz ($p < .0001$, $r^2 = 0.3735$, Figure 3-16c), and 50 Hz ($p < .0001$, $r^2 = 0.3700$, Figure 3-16d). Conversely, OPD was negatively correlated with the velar bone loss factor at 0.1 Hz ($p = .0050$, $r^2 = 0.1623$, Figure 3-16e), 1.0 Hz ($p = .0008$, $r^2 = 0.2218$, Figure 3-16f), 10 Hz ($p = .0014$, $r^2 = 0.2044$, Figure 3-16g), and 50 Hz ($p = .0069$, $r^2 = 0.1513$, Figure 3-16h). No significant correlations between loss modulus and predictor variables were identified at low frequencies (0.1 Hz and 1.0 Hz). However, OPD and water content

together provided significant, but weak correlations with loss modulus at 10 Hz ($p = .0069$, $r^2 = 0.2111$) and 50 Hz ($p < .0016$, $r^2 = 0.2634$). Estimated coefficients for each significant DMA regression are listed in Table 3-8.

Table 3-9. Estimated regression coefficients for predictive models of viscoelastic properties measured using DMA including storage modulus (E'), loss modulus (E"), and loss factor (tanδ).

		Intercept		OPD [#/mm^2]		H_2O [%]		Overall Regression	
Frequency [Hz]	**Variable**	**Estimate**	**Std. Error**	**Estimate**	**Std. Error**	**Estimate**	**Std. Error**	**r^2**	**p**
0.1	E' [GPa]	7.108	0.635	0.389	0.0736	-	-	0.3838	< .0001
		p < .0001		p < .0001					
	tanδ [-]	0.0678	0.0043	-0.0014	0.0005	-	-	0.1623	.0050
		p < .0001		p = .0050					
1.0	E' [GPa]	7.788	0.653	0.396	0.0757	-	-	0.3788	< .0001
		p < .0001		p < .0001					
	tanδ [-]	0.0458	0.0025	-0.0011	0.0003	-	-	0.2218	.0008
		p < .0001		p = .0008					
10	E' [GPa]	8.198	0.669	0.401	0.0775	-	-	0.3734	< .0001
		p < .0001		p < .0001					
	E" [MPa]	194.0	40.9	5.475	1.902	412.1	192.9	0.2112	.0069
		p < .0001		p = .0063		p = .0386			
	tanδ [-]	0.0359	0.0019	-0.00074	0.00022	-	-	0.2044	.0014
		p < .0001		p = .0014					
50	E' [GPa]	8.349	0.683	0.407	0.0791	-	-	0.3700	< .0001
		p < .0001		p < .0001					
	E" [MPa]	172.9	46.4	7.419	2.162	503.9	219.2	0.2634	.0016
		p = .0006		p=.0014		p = .0266			
	tanδ [-]	0.0358	0.0021	-0.00068	0.00024	-	-	0.1513	.0069
		p < .0001		p = .0069					

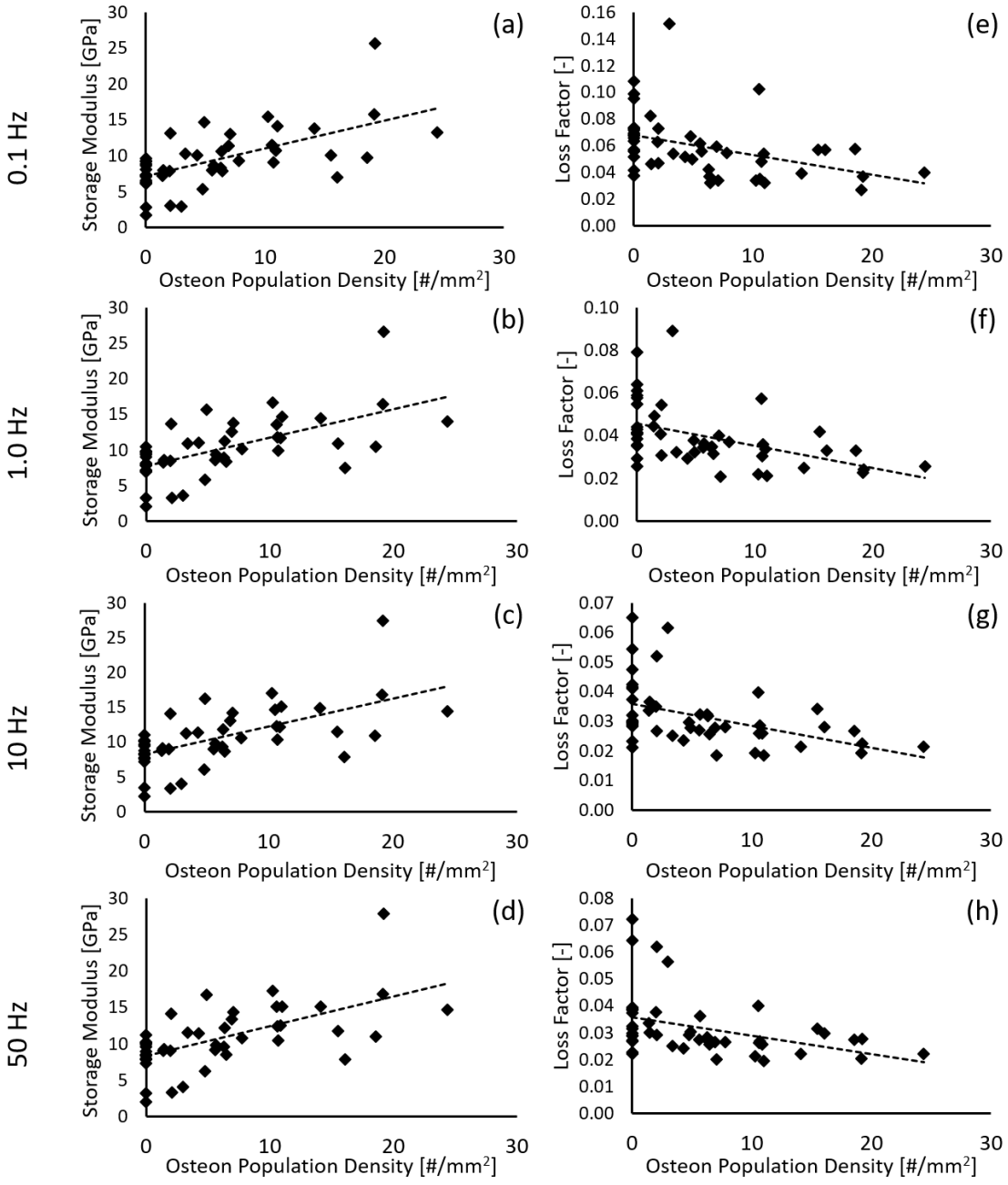

Figure 3-16. Storage modulus was positively correlated with osteon population density at 0.1 Hz (a), 1.0 Hz (b), 10 Hz (c) and 50 Hz (d). Loss factor was negatively correlated with osteon population density at 0.1 Hz (e), 1.0 Hz (f), 10 Hz (g) and 50 Hz (h). Regression model parameter estimates are presented in Table 8.

OPD was also positively correlated with many of the mechanical properties measured in three-point bending including the bending modulus ($p < .0001$, $r^2 = 0.3389$, Figure 3-17a), yield strength ($p < .0001$, $r^2 = 0.4150$, Figure 3-17b), yield strain ($p = .0191$, $r^2 = 0.1161$, Figure 3-17c), and ultimate strength ($p < .0001$, $r^2 = 0.3918$, Figure 3-17d). The only significant correlation that did not include OPD, was the positive correlation between velar bone ultimate strain and curl length ($p = .0106$, $r^2 = 0.1366$, Figure 3-17f). No significant regression models were identified for the remaining elastic properties measured in three-point bending (modulus of resilience, fracture energy, or modulus of toughness). Estimated regression parameters are shown in Table 3-9.

Table 3-10. Estimated regression coefficients for predictive models for elastic properties measured via three-point bending including bending modulus (E), yield strength (σ_y), yield strain (ε_y), ultimate strength (σ_{ult}), and ultimate strain (ε_{ult}).

	Intercept		OPD [#/mm^2]		Curl Length [cm]		Overall Regression	
Variable	**Estimate**	**Std. Error**	**Estimate**	**Std. Error**	**Estimate**	**Std. Error**	**r^2**	**p**
E [GPa]	6.73	0.57	0.319	0.066	-	-	0.3389	< .0001
	p < .0001		p < .0001					
σ_y [MPa]	76.02	7.64	5.00	0.89	-	-	0.4150	< .0001
	p < .0001		p < .0001					
ε_y [-]	0.0129	0.0004	0.000123	0.000050	-	-	0.1161	.0191
	p < .0001		p = .0191					
u_r [MJ/mm^3]	0.5688	0.0753	0.05	0.01	-	-	0.4067	< .0001
	p < .0001		p < .0001					
σ_{ult} [-]	102.67	9.55	5.96	1.11	-	-	0.3918	< .0001
	p < .0001		p < .0001					
ε_{ult} [-]	0.1016	0.0246	-	-	-0.000841	0.000315	0.1366	.0106
	p = .0002				p = .0106			
u_t [MJ/mm^3]	14.8086	4.7144	0.24	0.05	-0.157792	0.060163	0.3702	< .0001
	p = .0030		p < .0001		p = .0119			
W [J/m^2]	15.7959	5.0287	0.25	0.06	-0.168311	0.064174	0.3702	< .0001
	p = .0030		p < .0001		p = .0119			

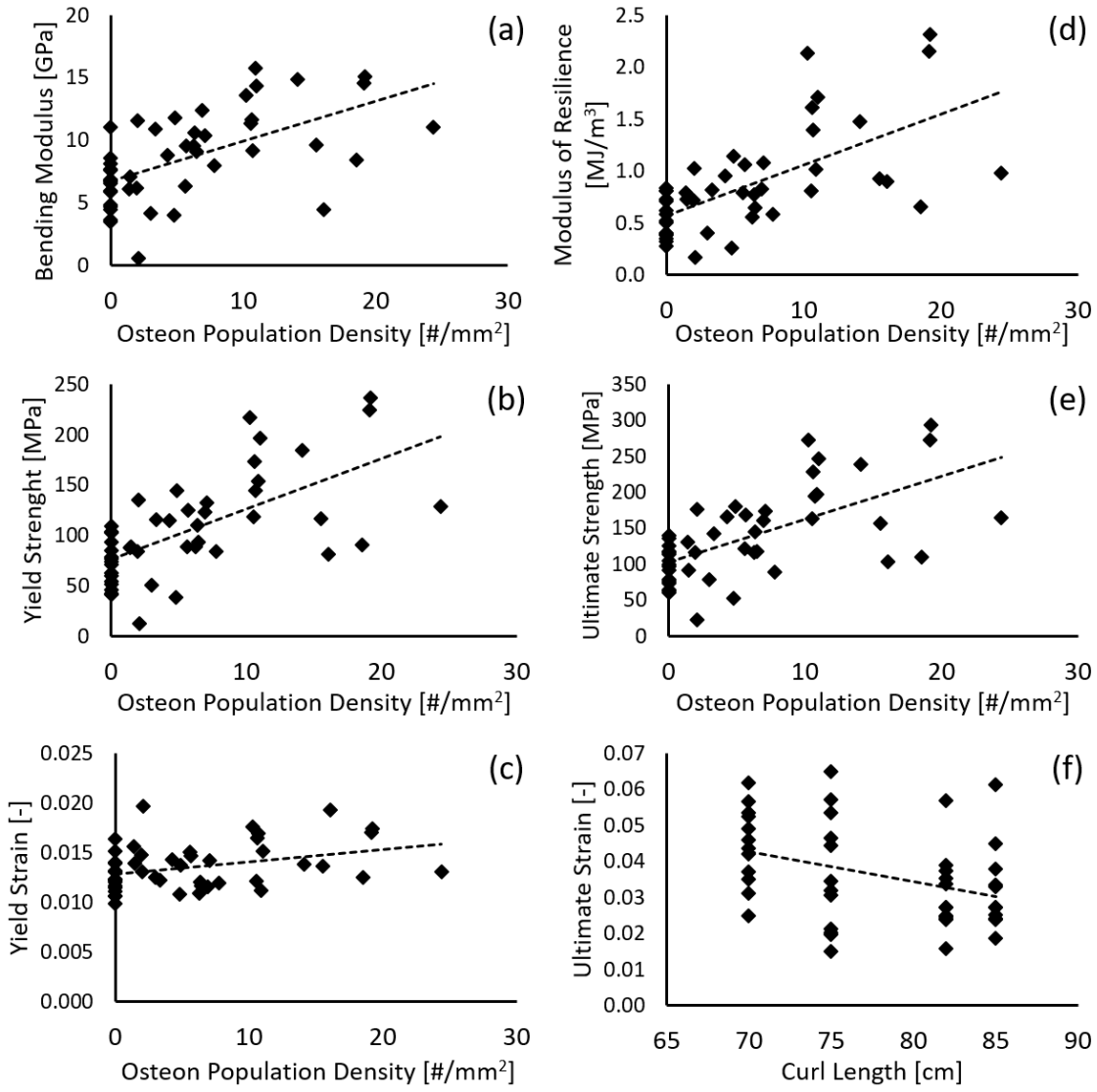

Figure 3-17. Bending modulus (a), yield strength (b), yield strain (c), modulus of resilience (d), and ultimate strength (e) were positively correlated with osteon population density. Ultimate strain was negatively correlated with curl length (f). Estimated regression coefficients for each regression model are shown in Table 9.

3.3.5. Horncore Velar vs. Cortical Bone

Velar bone had significantly lower porosity ($p = .0310$; Figure 3-18a), bending modulus ($p = .0014$; Figure 3-18b), yield strength ($p = .0011$; Figure 3-18c), ultimate strength ($p = .0261$; Figure 3-18d), modulus of resilience ($p = .0015$; Figure 3-18e), and

fracture energy ($p < .0001$; Figure 3-18f) than horncore cortical bone. In addition, velar bone yield strain was marginally lower ($p = .0764$) than horncore cortical bone. Average values of OPD and BMC were higher than those reported for horncore cortical bone, however these differences were not determined to be significant based on the linear mixed model.

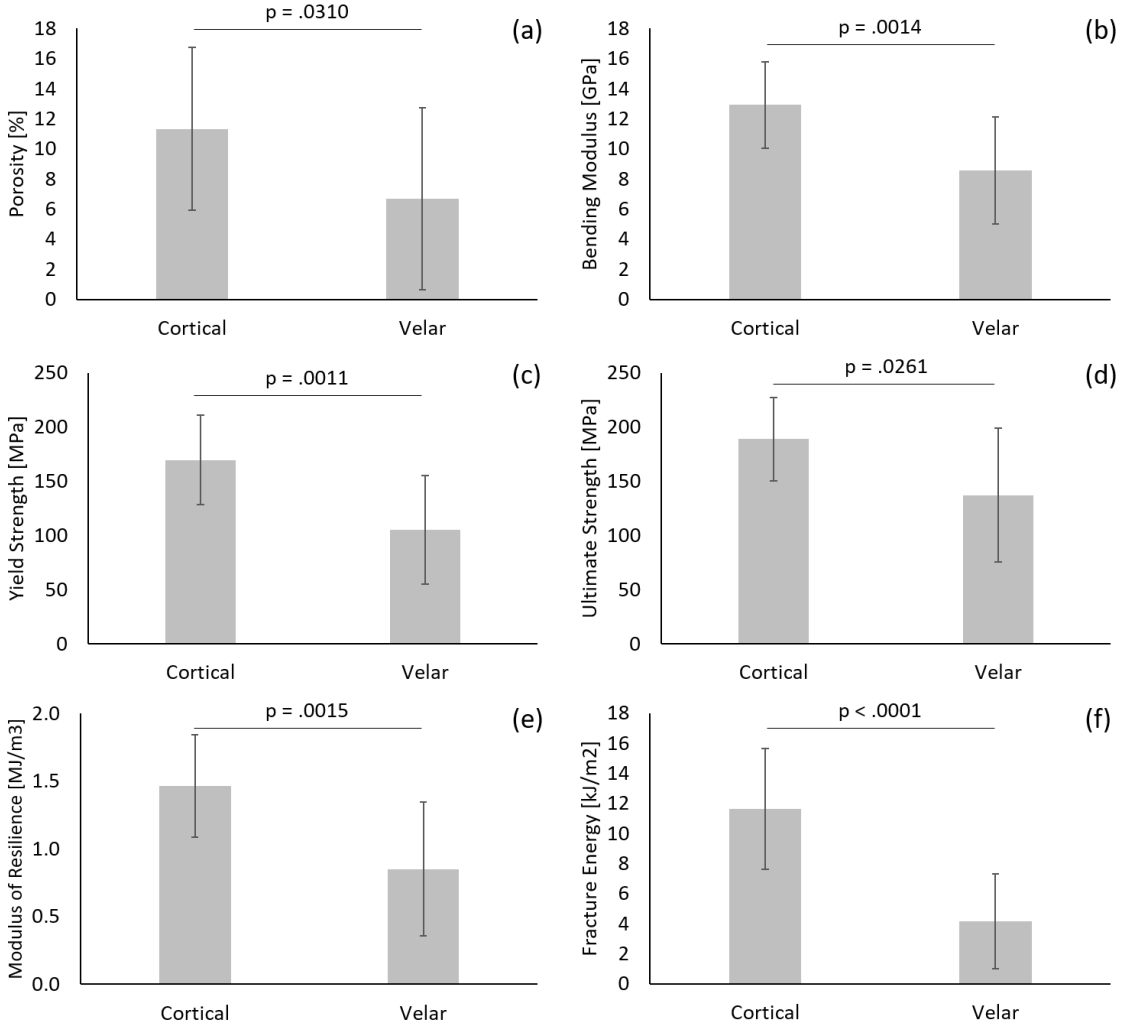

Figure 3-18. Comparison of horncore bone properties between cortical and velar bone tissues. Velar bone had significantly lower porosity (a), bending modulus (b), yield strength (c), ultimate strength (d), modulus of resilience (e), and fracture energy (f) than cortical bone based on a linear mixed model including tissue type (velar or cortical) as a fixed effect and ram ID as a random effect.

3.4. Discussion

The goal of this work was to quantify the composition, microstructure, and mechanical properties of velar bone tissue, explore how these properties vary based on position and orientation within the horncore, and investigate relationships between measured parameters. Ultimately, we were interested in how this material may contribute to energy absorption and injury mitigation during bighorn sheep ramming. We hypothesized that the modulus of toughness of velar bone tissue would be positively correlated with osteon population density (OPD). Additionally, we hypothesized that the modulus of toughness and damping factor of velar bone would be negatively correlated with bone mineral content (BMC). Stepwise regression demonstrated that velar bone modulus of toughness was indeed positively correlated with OPD, though this correlation was rather weak, and was improved by the inclusion of horn curl length. Surprisingly, BMC was not found to be correlated with modulus of toughness or damping factor, and was not included in any of the final predictive models developed via stepwise regression. These results also demonstrate an interesting interaction between sample orientation and position in the horn that influence the mechanical properties. Specifically, we found that transverse velar bone samples exhibit higher mechanical properties in the posterior region of the horncore than in the anterior region. It is possible that these differences are related to the different stress modes that arise in the anterior and posterior regions due to bending from impact, and may provide efficient energy storage and buckling resistance during ramming. Finally, it is noteworthy that velar bone sails contain osteons since Haversian systems are rare in mammalian trabecular bone. Osteons toughen cortical bone via crack arrest and deflection and may play a similar role in velar bone toughness. Thus, it is possible that the

unique combination of a large scale trabecular-like architecture with osteon-filled sails is beneficial for horncore energy absorption during ramming.

Limitations of this study include a small sample size of four individual rams. It is difficult to obtain ram horn material due to the limited availability. Most died as a result of motor vehicle collisions (BHS 3-5) and one was found dead entangled in a fence (BHS 6). As a result, tissues were not frozen immediately following animal death which may have led to some deterioration of bone properties prior to measurement. However, those involved in motor vehicle collisions were frozen within 24 hours of death. Additionally, it is impossible to know the exact age or ramming history of each ram. However, previous studies on bighorn sheep behavior suggested that participation in dominance fights begin as early as 2 years old, with the most intense combat occurring between rams 6 – 8 years old with horns of at least three-quarter curl [44]. Based on our estimated age range of 5 – 8 years old and the fact that all horns are at least three-quarter curl, it is reasonable to assume all rams included in this study were actively participating in combat during the rut.

Our mechanical testing methods had limitations as well. First, mechanical test specimens had reduced dimensions compared to many previous studies on the mechanical properties of cortical bone [38,45–47]. However, previous studies have demonstrated that the bending modulus remains relatively constant when specimen thickness is above 550 μm. Based on these findings, we chose a specimen thickness of 600 μm (0.6 mm) in order to maximize the number of samples we could obtain from the thin and irregular velar bone sails without compromising the accuracy of mechanical testing results. Additionally, we chose to use a constant displacement rate of 0.768 mm/s during three-point bend tests. This loading rate is associated with an estimated strain rate of 0.03 s^{-1} which is comparable to

the estimated strain rate applied to horncore cortical bone specimens in Chapter 2. This quasi-static loading rate was chosen to justify comparison of properties measured in this study to those reported for horncore cortical bone and other cortical bone tissues previously quantified with similar methods. However, the estimated strain rate is orders of magnitude lower than the peak strain-rate estimated to occur in horncore bone during ramming (~ 6 s^{-1} [1]). Given the known strain-rate sensitivity of bone [48], our results likely underestimate some of the mechanical properties (i.e., elastic modulus and strength) and overestimate others (i.e., yield strain) that the material would exhibit at the strain rates estimated to occur during ramming. To offer some insight into this discrepancy, an empirical model based on experimental data on the strain rate sensitivity of bovine cortical bone [48] was used to estimate that velar bone would have an elastic modulus of ~16.6 GPa at the strain-rate estimated to occur during ramming (~6 ε/s). Despite these limitations, these results are still valuable since the composition, microstructure, and mechanical behavior of this unique bone tissue, and how they compare to the properties of other mammalian bone, were previously unknown.

Results from this study suggest that velar bone tissue does not have exceptional material properties despite being exposed to an extreme mechanical environment. Velar bone tissue porosity (6.76 ± 1.69%) and bone mineral content (66.0 ± 1.2%) were both comparable to previously published values for cortical bone from a variety of species and skeletal locations [38,49–54]. Velar bone osteon population density (5.76 ± 1.55 osteons/mm^2) was lower than reported values for mature cortical bone from sheep radii (~20 osteons/mm^2 [55]) and human femora (~26 osteons/mm^2 [56]) but comparable to cortical bone from black bear femora (~6 osteons/mm^2 [49]). DMA results had more

variability but generally agreed with viscoelastic properties of bovine cortical bone measured with similar methodology. Velar bone and bovine cortical bone storage moduli increased slightly and loss factors decreased up to 50% as the loading frequency increased from 0.1 – 10 Hz. These trends are consistent with the increase in stiffness and elastic behavior of bone tissue observed with increasing strain-rates [23,24]. However, the velar bone storage modulus was in the high end of the range reported for bovine cortical bone storage modulus (7 – 12 GPa, Figure 3-19) while the velar bone loss factor was in the low end of the range of bovine cortical bone values (0.03 – 0.1, Figure 3-20) [57]. The elastic behavior of velar bone would not be beneficial for material level energy dissipation during ramming. However, it is possible that velar bone elasticity promotes side-to-side horn tip oscillations post impact, which have been shown to be an important mechanism of energy dissipation through vibrational damping. Results from three-point bending similarly demonstrate that velar bone may not be a better energy absorber than other cortical bone tissues.

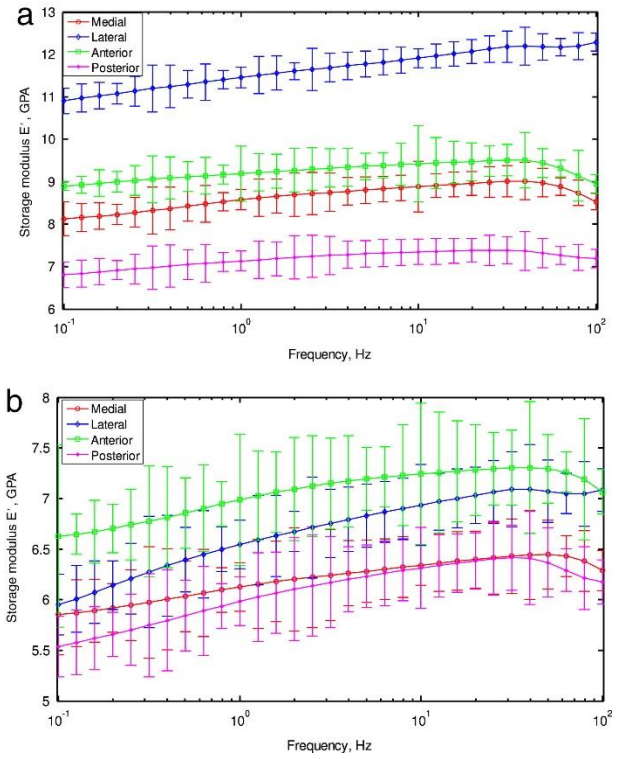

Figure 3-19. Storage modulus measured from 0.1 – 100 Hz for samples of bovine cortical bone taken from the medial, lateral, anterior, and posterior quadrants of the femoral diaphysis. Reproduced with permissions from [57].

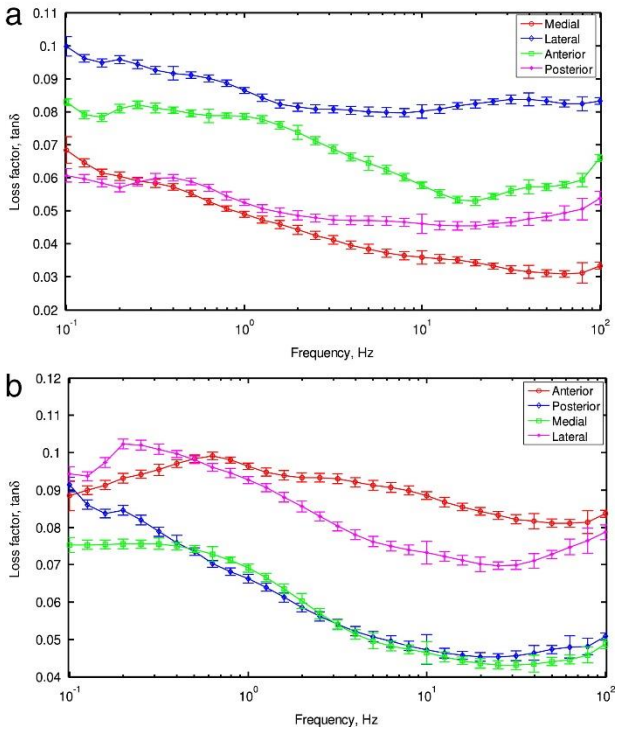

Figure 3-20. Loss factor (i.e., damping factor) measured from 0.1 – 100 Hz for samples of bovine cortical bone taken from the medial, lateral, anterior, and posterior quadrants of the femoral diaphysis. Reproduced with permissions from [57].

Velar bone properties measured under three-point bending were generally inferior to bighorn sheep horncore cortical bone properties despite these tissues having similar mineral content and OPD values. Velar bone bending modulus was shown to be 30% less ($p = .0014$) than the bending modulus of horncore cortical bone from the same rams. This result is similar to previous findings that trabecular bone tissue is approximately 20-30% less stiff than cortical bone tissue [58–61]. Reduced stiffness of trabecular bone tissue is typically attributed to a reduction in bone mineral content due to increased trabecular bone turnover (i.e., surface remodeling as opposed to intracortical remodeling). Compact bone stiffness has also been negatively correlated with tissue porosity in previous work [51]. Interestingly, velar bone demonstrated reduced stiffness compared to horncore cortical bone despite having lower tissue porosity and similar measures of bone mineral content

and osteon population density. This finding may be due to the variable osteon orientation in velar bone samples compared to the more consistent alignment of horncore cortical bone osteons with the long axis of mechanical test specimens. Another possible explanation for these differences is variation in collagen fiber orientation of mechanical test specimens which was not accounted for in this study. In addition to reduced stiffness, we found that velar bone had lower yield strength, ultimate strength, modulus of resilience and fracture energy compared to horncore cortical bone tissue. While velar bone tissue does not appear to outperform the mechanical properties of cortical bone tissue, it remains possible that velar bone offers increased energy absorption compared to the tissue level properties of typical trabecular bone.

Osteons were frequently observed in the cross-sections of velar bone specimens which may provide improved energy absorption compared to trabecular bone tissue which rarely has osteons. This may be one reason velar bone bending modulus (~8.6 GPa) appears to be greater than previously published values for trabecular bone tissue tested in bending (~4 – 6 GPa [59,60]). However, in order to obtain prismatic beams from individual trabeculae, mechanical test specimens were ~120 μm thick (compared to a specimen thickness ~600 μm for velar bone). Due to the dramatic differences in mechanical test specimen sizes, direct comparisons between the elastic modulus of velar and trabecular bone are confounded. Furthermore, the modulus of toughness of trabecular bone tissue measured in bending has not been reported for comparison to velar bone. With that said, previous research has shown that cortical bone has significantly higher fatigue strength than trabecular bone tissue when tested under the same conditions. It was suggested that increased fatigue strength of cortical bone was a consequence of crack arrest and deflection

provided by osteon cement lines [59]. In other studies, the fracture toughness of cortical bone has been positively correlated with osteon population density [18]. It is possible that osteon filled velae are more resistant to crack propagation and provide increased energy absorption via microdamage accumulation than if the horncore were filled with osteon-free trabeculae. This may be one benefit of the horncore having thicker velar sails that support internal remodeling processes that form osteons as opposed to thinner trabeculae which primarily undergo surface remodeling. Regardless of this possibility, we can gain further insight into how velar bone material contributes to the mechanics of the entire horncore by looking at statistical results from regression analysis and linear mixed models.

Regression analysis demonstrated that osteon population density is correlated with velar bone modulus of toughness as hypothesized. However, OPD alone only explained around 25% of total variation in the modulus of toughness. Adding curl length to the predictive model increased the strength of the correlation, but OPD and curl length together still accounted for less than 40% of total variation in modulus of toughness. Surprisingly, bone mineral content was not included as a significant factor in any of the models used to predict measured mechanical properties. Overall, regression models identified in this study provided weak correlations with mechanical properties, with the best model only explaining 41% of the total variation in velar bone yield strength. This finding suggests other factors not quantified here play a critical role in determination of velar bone mechanical properties. One possible factor is collagen fiber orientation, which has been shown to be highly correlated with cortical bone properties [62]. Furthermore, collagen fiber orientation varies regionally depending on predominant strain modes such that collagen fibers are primarily oriented longitudinally in cortices exposed to tension and

transversely in cortices that support compression [63–66]. Although we did not quantify collagen fiber organization, our results indicate similar regional and orientation dependent variation in velar bone properties throughout the horncore.

Results from linear mixed model analysis demonstrated an interesting interaction between sample orientation and anterior-posterior position that influenced many of the mechanical properties. Figures 3-12 and 3-13 illustrate that mechanical properties measured in the anterior region of the horncore were generally higher in longitudinal samples than transverse samples. This may provide efficient resistance to the tensile stresses that arise in the anterior region of the horncore due to bending during ramming. Conversely, transversely oriented samples had increased properties compared to longitudinal samples in the posterior region of the horncore. Here, transverse velar bone sails may act as important stiffening members to resist structural buckling due to the compressive bending stresses that develop in the posterior region during impact. Once again, these differences cannot be explained well by regional or orientation-based differences in composition or microstructure indicating the need for additional explanatory variables in future studies (i.e., collagen fiber orientation). Regardless, an improved understanding of velar bone properties at the tissue level provide insight into how this material may contribute to impact energy absorption and will improve future efforts to investigate the role of velar bone architecture in injury mitigation during ramming.

In summary, our findings suggest that velar bone is a unique combination of trabecular-like foam with osteon filled struts. Although velar bone material does not offer increased toughness compared to mammalian cortical bone, osteon-filled velae may resist crack propagation to increase energy dissipation via microdamage accumulation compared

to osteon-free trabeculae. This may be one advantage of the unique velar bone architecture having thicker sails than trabecular bone struts since trabeculae are too thin to support the internal remodeling that forms secondary osteons. Furthermore, preferential arrangement of velar bone tissue appears to play a role in resisting regional variation in bending stresses that develop in the horncore during ramming. However, further work is necessary to elucidate the specific mechanisms that influence velar bone mechanical properties as the compositional and microstructural parameters measured in this study had weak predictive power. Moving forward, these results can be used to improve computational modeling of bighorn sheep ramming, and guide further characterization of this interesting bone tissue. Additionally, this work may inspire novel synthetic materials that utilize fiber-matrix composites in the design of lattice structures for energy absorption applications.

3.5. References

[1] A. Drake, T.L. Haut Donahue, M. Stansloski, K. Fox, B.B. Wheatley, S.W. Donahue, Horn and horn core trabecular bone of bighorn sheep rams absorbs impact energy and reduces brain cavity accelerations during high impact ramming of the skull, Acta Biomater. 44 (2016) 41–50. https://doi.org/10.1016/j.actbio.2016.08.019.

[2] J. Cappelli, A.J. García, R. Kotrba, P. Gambín Pozo, T. Landete-Castillejos, L. Gallego, F. Ceacero, The bony horncore of the common eland (Taurotragus oryx): composition and mechanical properties of a spiral fighting structure, J Anat. 232 (2018) 72–79. https://doi.org/10.1111/joa.12708.

[3] L.H. Fuller, S.W. Donahue, Material properties of bighorn sheep (Ovis canadensis) horncore bone with implications for energy absorption during impacts, J Mech Behav Biomed Mater. 114 (2020) 104224. https://doi.org/10.1016/j.jmbbm.2020.104224.

[4] T.W. Seek, Exploration of Unique Porous Bone Materials for Candidacy in Bioinspired Material Design, Masters Thesis, Colorado State University, 2018.

[5] C.T. Rubin, L.E. Lanyon, Regulation of bone mass by mechanical strain magnitude, Calcif Tissue Int. 37 (1985) 411–417.

[6] C.T. Rubin, L.E. Lanyon, Dynamic strain similarity in vertebrates; an alternative to allometric limb bone scaling, J Theor Biol. 107 (1984) 321–327.

[7] C.T. Rubin, L.E. Lanyon, Regulation of bone formation by applied dynamic loads, J Bone Joint Surg. 66-A (1984) 397–402. https://archive.org/details/sim_journal-of-bone-and-joint-surgery_1984-03_66-a_3.

[8] H.K. Uhthoff, Z.F.G. Jaworski, Bone loss in response to long-term immobilisation, J Bone Joint Surg. 60-B (1978) 420–429.

[9] Ph. Collet, D. Uebelhart, L. Vico, L. Moro, D. Hartmann, M. Roth, C. Alexandre, Effects of 1- and 6-Month Spaceflight on Bone Mass and Biochemistry in Two Humans, Bone. 20 (1997) 547–551.

[10] E.J. Bassey, S.J. Ramsdale, Increase in femoral bone density in young women following high-impact exercise, Osteoporosis International. 4 (1994) 72–75.

[11] S.L. Bass, L. Saxon, R.M. Daly, C.H. Turner, A.G. Robling, E. Seeman, S. Stuckey, The effect of mechanical loading on the size and shape of bone in pre-, peri-, and postpubertal girls: A study in tennis players, Journal of Bone and Mineral Research. 17 (2002) 2274–2280. https://doi.org/10.1359/jbmr.2002.17.12.2274.

[12] A.E. Goodship, L.E. Lanyon, H. McFie, Functional adaptation of bone to increased stress: An experimental study, Journal of Bone and Joint Surgery. 61 (1979) 539–546.

[13] A.E. Churches, D.C.R. Howlett, Functional Adaptation of Bone in Response to Sinusoidally Varying Controlled Compressive Loading of the Ovine Metacarpus, Clin Orthop Relat Res. 168 (1982) 265–280.

[14] T.J. Chambers, M. Evans, T.N. Gardner, A. Turner-Smith, J.W.M. Chow, Induction of bone formation in rat tail vertebrae by mechanical loading, Bone Miner. 20 (1993) 167–178.

[15] J. Sanchis-Moysi, C. Dorado, G. Vicente-Rodríguez, L. Milutinovic, G.L. Garces, J.A.L. Calbet, Inter-arm asymmetry in bone mineral content and bone area in postmenopausal recreational tennis players, Maturitas. 48 (2004) 289–298. https://doi.org/10.1016/j.maturitas.2004.03.008.

[16] J.D. Currey, Mechanical properties of bone tissues with greatly differing functions, J Biomech. 12 (1979) 313–319. https://doi.org/10.1016/0021-9290(79)90073-3.

[17] J.D. Currey, The many adaptations of bone, J Biomech. 36 (2003) 1487–1495. https://doi.org/10.1016/S0021-9290(03)00124-6.

[18] Y.N. Yeni, C.U. Brown, Z. Wang, T.L. Norman, The influence of bone morphology on fracture toughness of the human femur and tibia, Bone. 21 (1997) 453–459. https://doi.org/10.1016/S8756-3282(97)00173-7.

[19] M.E. Launey, M.J. Buehler, R.O. Ritchie, On the mechanistic origins of toughness in bone, 2010. https://doi.org/10.1146/annurev-matsci-070909-104427.

[20] J.B. Phelps, G.B. Hubbard, X. Wang, C.M. Agrawal, Microstructural heterogeneity and the fracture toughness of bone, J Biomed Mater Res. 51 (2000) 735–741. https://doi.org/10.1002/1097-4636(20000915)51:4<735::AID-JBM23>3.0.CO;2-G.

[21] D. Vashishth, K.E. Tanner, W. Bonfield, Experimental validation of a microcracking-based toughening mechanism for cortical bone, J Biomech. 36 (2003) 121–124. https://doi.org/10.1016/S0021-9290(02)00319-6.

[22] D. Vashishth, J.C. Behiri, W. Bonfield, Crack growth resistance in cortical bone: Concept of microcrack toughening, J Biomech. 30 (1997) 763–769. https://doi.org/10.1016/S0021-9290(97)00029-8.

[23] U. Hansen, P. Zioupos, R. Simpson, J.D. Currey, D. Hynd, The effect of strain rate on the mechanical properties of human cortical bone, J Biomech Eng. 130 (2008) 1–8. https://doi.org/10.1115/1.2838032.

[24] J. Lei, L. Li, Z. Wang, F. Zhu, Characterizing Strain Rate-Dependent Mechanical Properties for Bovine Cortical Bones, J Biomech Eng. 142 (2020) 1–8. https://doi.org/10.1115/1.4046690.

[25] J. Yamashita, B.R. Furman, H.R. Rawls, X. Wang, C.M. Agrawal, The use of dynamic mechanical analysis to assess the viscoelastic properties of human cortical bone, J Biomed Mater Res. 58 (2001) 47–53. https://doi.org/10.1002/1097-4636(2001)58:1<47::AID-JBM70>3.0.CO;2-U.

[26] C.H. Turner, Three rules for bone adaptation to mechanical stimuli, Bone. 23 (1998) 399–407. https://doi.org/10.1016/S8756-3282(98)00118-5.

[27] A.H. Doherty, C.K. Ghalambor, S.W. Donahue, Evolutionary physiology of bone: Bone metabolism in changing environments, Physiology. 30 (2015) 17–29. https://doi.org/10.1152/physiol.00022.2014.

[28] P. Maity, S.A. Tekalur, Finite element analysis of ramming in Ovis canadensis, J Biomech Eng. 133 (2011) 1–9. https://doi.org/10.1115/1.4003321.

[29] A. Ingrole, T.G. Aguirre, L. Fuller, S.W. Donahue, Bioinspired energy absorbing material designs using additive manufacturing, J Mech Behav Biomed Mater. 119 (2021) 104518. https://doi.org/10.1016/j.jmbbm.2021.104518.

[30] T.G. Aguirre, L. Fuller, A. Ingrole, T.W. Seek, B.B. Wheatley, B.D. Steineman, T.L.H. Donahue, S.W. Donahue, Bioinspired material architectures from bighorn sheep horncore velar bone for impact loading applications, Sci Rep. 10 (2020) 1–14. https://doi.org/10.1038/s41598-020-76021-5.

[31] V. Geist, Validity of Horn Segment Counts in Aging Bighorn Sheep, J Wildl Manage. 30 (1966) 634–635.

[32] D. Gastaldi, M. Baleani, R. Fognani, F. Airaghi, L. Bonanni, P. Vena, An experimental procedure to perform mechanical characterization of small-sized bone specimens from thin femoral cortical wall, J Mech Behav Biomed Mater. 112 (2020) 104046. https://doi.org/10.1016/j.jmbbm.2020.104046.

[33] J.C.H. Goh, E.J. Ang, K. Bose, Effect of preservation medium on the mechanical properties of cat bones, Acta Orthop Scand. 60 (1989) 465–467. https://doi.org/10.3109/17453678909149321.

[34] R.B. Martin, N.A. Sharkey, The Mechanical Effects of Preserving Bone, in: S.C. Cowin (Ed.), Bone Mechanics Handbook, Second Edi, 2001: pp. 20-6-20–12.

[35] E.D. Sedlin, A Rheologic Model for Cortical Bone: A Study of the Physical Properties of Human Femoral Samples, Acta Orthop Scand. 36 (1965) 1–77. https://doi.org/10.3109/ort.1965.36.suppl-83.01.

[36] K.P. Menard, Dynamic Testing, in: Dynamic Mechanical Analysis: A Practical Introduction, CRC Press LLC, 1999: pp. 61–89.

[37] J.D. Currey, Tensile yield in compact bone is determined by strain, post-yield behaviour by mineral content, J Biomech. 37 (2004) 549–556. https://doi.org/10.1016/j.jbiomech.2003.08.008.

[38] K.B. Harvey, S.W. Donahue, Bending properties, porosity, and ash fraction of black bear (Ursus americanus) cortical bone are not compromised with aging despite annual periods of disuse, J Biomech. 37 (2004) 1513–1520. https://doi.org/10.1016/j.jbiomech.2004.01.010.

[39] C.G. Ambrose, M. Soto Martinez, X. Bi, J. Deaver, C. Kuzawa, L. Schwartz, B. Dawson, A. Bachim, U. Polak, B. Lee, C. Crowder, Mechanical properties of infant bone, Bone. 113 (2018) 151–160. https://doi.org/10.1016/j.bone.2018.05.015.

[40] ASTM International, Standard Test Method for Determination of Modulus of Elasticity for Rigid and Semi- Rigid Plastic Specimens by Controlled Rate of Loading, ASTM International. (2002).

[41] D.B. Burr, C.H. Turner, Mechanical Testing Methods, in: S.C. Cowin (Ed.), Bone Mechanics Handbook, Second, 2001: pp. 7–6 to 7–24.

[42] D.L. Osborne, J. Curtis, A protocol for the staining of cement lines in adult human bone using toluidine blue, J Histotechnol. 28 (2005) 73–79. https://doi.org/10.1179/his.2005.28.2.73.

[43] C. Crowder, J. Heinrich, S.D. Stout, Rib histomorphometry for adult age estimation, Methods in Molecular Biology. 915 (2012) 109–127. https://doi.org/10.1007/978-1-61779-977-8_7.

[44] V. Geist, Mountain Sheep: A Study in Behavior and Evolution, University of Chicago Press, 1971.

[45] J.D. Currey, What determines the bending strength of compact bone?, 1999.

[46] J.D. Currey, G. Butler, The mechanical properties of bone tissue in children, Journal of Bone and Joint Surgery - American Volume. 57 (1975) 810–814.

[47] J.D. Currey, T. Landete-Castillejos, J. Estevez, F. Ceacero, A. Olguin, A. Garcia, L. Gallego, The mechanical properties of red deer antler bone when used in fighting, Journal of Experimental Biology. 212 (2009) 3985–3993. https://doi.org/10.1242/jeb.032292.

[48] J.H. McElhaney, Dynamic response of bone and muscle tissue., J Appl Physiol. 21 (1966) 1231–1236. https://doi.org/10.1152/jappl.1966.21.4.1231.

[49] S.J. Wojda, D.R. Weyland, S.K. Gray, M.E. Mcgee-Lawrence, T.D. Drummer, S.W. Donahue, Black bears with longer disuse (hibernation) periods have lower femoral osteon population density and greater mineralization and intracortical porosity, Anatomical Record. 296 (2013) 1148–1153. https://doi.org/10.1002/ar.22720.

[50] M.E. McGee-Lawrence, S.J. Wojda, L.N. Barlow, T.D. Drummer, K. Bunnell, J. Auger, H.L. Black, S.W. Donahue, Six months of disuse during hibernation does not increase intracortical porosity or decrease cortical bone geometry, strength, or mineralization in black bear (Ursus americanus) femurs, J Biomech. 42 (2009) 1378–1383. https://doi.org/10.1016/j.jbiomech.2008.11.039.

[51] J.D. Currey, The Effect of Porosity and Mineral Content on the Young's Modulus of Elasticity of Compact Bone, J Biomech. 21 (1988) 131–139.

[52] J.D. Frank, M. Ryan, V.L. Kalscheur, C.P. Ruaux-Mason, R.R. Hozak, P. Muir, Aging and accumulation of microdamage in canine bone, Bone. 30 (2002) 201–206. https://doi.org/10.1016/S8756-3282(01)00623-8.

[53] T. Landete-Castillejos, J.D. Currey, F. Ceacero, A.J. García, L. Gallego, S. Gomez, Does nutrition affect bone porosity and mineral tissue distribution in deer antlers? The relationship between histology, mechanical properties and mineral composition, Bone. 50 (2012) 245–254. https://doi.org/10.1016/j.bone.2011.10.026.

[54] M.B. Schaffler, D.B. Burr, Stiffness of compact bone: effects of porosity and density, J Biomech. 21 (1988) 13–16.

[55] S. Mohsin, F.J. O'Brien, T.C. Lee, Osteonal crack barriers in ovine compact bone, J Anat. 208 (2006) 81–89. https://doi.org/10.1111/j.1469-7580.2006.00509.x.

[56] S.H. Han, S.H. Kim, Y.W. Ahn, G.Y. Huh, D.S. Kwak, D.K. Park, U.Y. Lee, Y.S. Kim, Microscopic age estimation from the anterior cortex of the femur in Korean adults, J Forensic Sci. 54 (2009) 519–522. https://doi.org/10.1111/j.1556-4029.2009.01003.x.

[57] A.A. Abdel-Wahab, K. Alam, V. v. Silberschmidt, Analysis of anisotropic viscoelastoplastic properties of cortical bone tissues, J Mech Behav Biomed Mater. 4 (2011) 807–820. https://doi.org/10.1016/j.jmbbm.2010.10.001.

[58] X.E. Guo, Mechanical Properties of Cortical Bone and Cancellous Bone Tissue, in: S.C. Cowin (Ed.), Bone Mechanics Handbook, Second, CRC Press LLC, 2001: pp. 10.1-10.23.

[59] K. Choi, S.A. Goldstein, A comparison of the fatigue behavior of human trabecular and cortical bone tissue, J Biomech. 25 (1992) 1371–1381. https://doi.org/10.1016/0021-9290(92)90051-2.

[60] K. Choi, J.L. Kuhn, M.J. Ciarelli, S.A. Goldstein, The Elastic Moduli of Human Subchondral, Trabecular, and Cortical Bone Tissue and the Size Dependency of Cortical Bone Modulus, J. Biomechanics. 23 (1990) 1103–1113. https://doi.org/10.1016/0021-9290(90)90003-L.

[61] J.L. Kuhn, S.A. Goldstein, R. Choi, M. London, L.A. Feldkamp, L.S. Matthews, Comparison of the trabecular and cortical tissue moduli from human iliac crests, Journal of Orthopaedic Research. 7 (1989) 876–884. https://doi.org/10.1002/jor.1100070614.

[62] R.B. Martin, D.L. Boardman, The effects of collagen fiber orientation, porosity, density, and mineralization on bovine cortical bone bending properties, J Biomech. 26 (1993) 1047–1054.

[63] J.K. Kalmey, C.O. Lovejoy, Collagen Fiber Orientation in the Femoral Necks of Apes and Humans: Do Their Histological Structures Reflect Differences in Locomotor Loading?, Bone. 31 (2002) 327–332.

[64] M.W. Mason, J.G. Skedros, R.D. Bloebaum, Evidence of strain-mode-related cortical adaptation in the diaphysis of the horse radius, Bone. 17 (1995) 229–237. https://doi.org/10.1016/8756-3282(95)00213-W.

[65] J.G. Skedros, S.D. Mendenhall, C.J. Kiser, H. Winet, Interpreting cortical bone adaptation and load history by quantifying osteon morphotypes in circularly polarized light images, Bone. (2009). https://doi.org/10.1016/j.bone.2008.10.053.

[66] J.G. Skedros, M.W. Mason, M.C. Nelson, R.D. Bloebaum, Evidence of structural and material adaptation to specific strain features in cortical bone, Anatomical Record. 246 (1996) 47–63. https://doi.org/10.1002/(SICI)1097-0185(199609)246:1<47::AID-AR6>3.0.CO;2-C.

CHAPTER 4

4. CHARACTERIZATION OF THE HORN-HORNCORE INTERFACE

4.1. Introduction

The cranial appendages of bighorn sheep rams must withstand high magnitude impacts without failure during intraspecific combat involving head-to-head collisions. This has generated interest and motivation to study the materials and structures of these exceptional mechanical structures and their role in injury mitigation during ramming. The namesake appendages of bighorn sheep are composed of a keratin-rich horn anchored to a bony horncore projecting from the skull by a connective tissue interface. The bony horncore is further characterized by a dense, cortical bone shell filled with a unique porous bone architecture [1]. Previous studies have characterized the structure-function relationships of the horn and found that this material is capable of absorbing large amounts of energy without damage, especially under hydrated conditions [2–6]. Furthermore, computational modeling of bighorn sheep ramming demonstrated that the porous bone architecture of the horncore absorbs more energy than the horn and significantly reduces brain cavity accelerations during head butting [7,8]. For the horncore to absorb energy during ramming, there must be efficient load transfer between the impacted horn and energy absorbing horncore. However, properties of the connective tissue interface between the horn and horncore are currently unknown. Quantifying the composition, microstructure, and mechanical properties of the horn-horncore interface may provide

insight into the role of these complex cranial appendages in injury mitigation during ramming.

The equine laminar junction is a well-studied interface that is similar to the bighorn sheep horn-horncore interface as it joins the keratin-rich hoof wall to the distal phalanx bone. Previous studies have demonstrated that the laminar junction features a microstructure that increases the contact surface area to reduce shear stress during loading [9–13]. During gait, equine hooves experience ground reaction forces (per unit body mass) of ~11.5 – 16.1 N/kg [14]. The laminar junction attaches the inner surface of the hoof wall to the parietal surface of the distal phalanx bone to transfer the ground reaction force to the appendicular skeleton. On the innermost layer of each hoof wall, 550 – 600 keratinized primary epidermal lamellae (PEL) run along the proximo-distal length of the hoof and extend radially inward toward the distal phalanx [12,15]. An additional 150 – 200 non-keratinized secondary epidermal lamellae branch from each PEL and interlock with the collagenous dermal lamellae [12,15]. Studies on the mechanical behavior of the equine laminar junction have demonstrated non-linear strain stiffening with nearly a 13-fold increase in shear moduli from low-strain (396 ± 312 kPa) to high-strain (5.38 ± 1.49 MPa) [16]. The interdigitating structure increases the contact area between the hoof wall and distal phalanx to reduce stress concentrations and promote uniform energy transfer during loading [12]. Similar adaptations of the horn-horncore interface in bighorn sheep rams may also increase the contact area to reduce local stress magnitudes and promote efficient energy transfer during ramming.

Bird beaks are another example of a dermo-epidermal junction that provides attachment between a keratin rich structure (i.e., the rhamphotheca) and bone. Ultimately,

bird beaks are formed from mandibular bones covered by a dermis and epidermis [17]. The dermis is directly adjacent to the underlying bone structure and contains connective tissue, blood vessels, nerves, and mechanosensory receptors such as Herbst and Grandry corpuscles [18,19]. Sharpey's fibers penetrate the adjacent bone tissue and anchor the dermis to the bone [18]. Moving outward, a thin basement membrane separates the epidermis from the dermis. The epidermis is a layered structure featuring tightly packed keratinocytes that migrate outward from the germinative layer to the fully cornified outer surface known as the rhamphotheca. The innermost region of the germinative layer is the stratum basale which is a single layer of basal cells that forms a tight dermo-epidermal junction via interdigitations with the dermins that are visible between cells. Although no work has been done to quantify the mechanical properties of the dermo-epidermal junction of bird beaks, the interdigitions of the stratum basale may provide increased contact area beneficial for load transfer like the morphology of the equine laminar junction. Furthermore, the Sharpey's fibers anchoring the dermis to the bone may contribute to increased rigidity of the rhamphotheca-bone interface due to collagen's resistance to tensile extension [18,20].

Considering the importance of load transfer between impacted horn and the energy absorbing horncore in ram horns, it is possible that the horn-horncore interface morphology increases the contact area between horn and bone similar to the dermo-epidermal junctions of equine hooves and bird beaks. It was hypothesized that the microstructural contact area of the horn-horncore interface is larger than the nominal contact area due to microstructural features present in the interface, similar to the equine hoof. Additionally, it was hypothesized that the microstructural contact area is positively correlated with the shear

strength of this interface. The aims of this study were to quantify the microstructure, composition, and mechanical behavior of the horn-horncore interface, and investigate structure-property relationships between the measured properties. Variation of horn-horncore interfacial properties with respect to anatomical position and orientation within the horncore was also examined. Understanding the structure-function relationships of this interface will improve computational models of bighorn sheep ramming and provide insight for the design of load transferring interfaces for impact applications such as helmets or vehicle components.

4.2. Methods

4.2.1. Samples

Four skulls (i.e., those used for the velar bone study) with fully intact horns were obtained from deceased mature bighorn sheep rams provided by the Colorado Department of Natural Resources under Colorado Parks and Wildlife scientific collection license number 14SALV2052A2. Rams were estimated to be between 5 and 8 years old by counting growth annuli visible on horn surfaces [21]. Before destructive sample preparation, horn curl lengths were measured in the longitudinal direction along the outermost horn surface from proximal skull attachment to the distal tip (Figure 1a). Curl lengths ranged from 70 – 85 cm, corresponding to approximately three-quarters to one full curl. Rams in this age range and with similar sized horns are known to participate in intraspecific combat during rut.

A hacksaw was used to separate the left horn from the skull and cut a transverse section from the proximal end of the horn (Figure 4-1a). Proximal-transverse sections were

cut into medial and lateral halves to expose the internal horn structure and obtain interface samples (Figure 4-1b). A quasi-cylindrical coordinate system was defined for the horn-horncore structure. The longitudinal axis was defined along the curvilinear centerline of the horn in the proximo-distal direction of horn growth (Figure 4-1c). In any transverse plane normal to the longitudinal axis, radial and circumferential axes are defined as normal and tangent to the outer surface of the horn, respectively (Figure 4-1d). A band saw was used to cut interface samples at least 32 mm long (longitudinally) and 10 mm wide (circumferentially) from proximal and distal regions of the medial, lateral, anterior and posterior cortices of the horn (Figure 4-1c). This resulted in eight interface samples being extracted from each of the four rams (32 samples total). Extracted interface samples included horncore cortical bone, interfacial tissue, and horn, and will henceforth be referred to simply as "samples." Total sample thickness in the radial direction varied due to variation in the cortical bone and horn thicknesses. A vertical end mill was used to mill samples to a final uniform width of 6 mm (in the circumferential direction). Next, a precision saw was used to cut a 2 mm segment and 6 mm segment from the proximal end of each interface sample to prepare histological sections in transverse and longitudinal orientations, respectively (Figure 4-1d). Processing interface samples in this order resulted in transverse and longitudinal histological sections with similar widths (~6 mm). The width of transverse histology sections was approximately aligned with the circumferential direction while longitudinal histology section width was aligned longitudinally (Figure 4-1d). The remaining distal portion of each sample was cut to a final length of 24 mm and used to prepare lap-shear specimens for mechanical testing (Figure 4-1d). In total, one

longitudinal section, one transverse section, and one lap-shear specimen was prepared from each of the 32 interface samples.

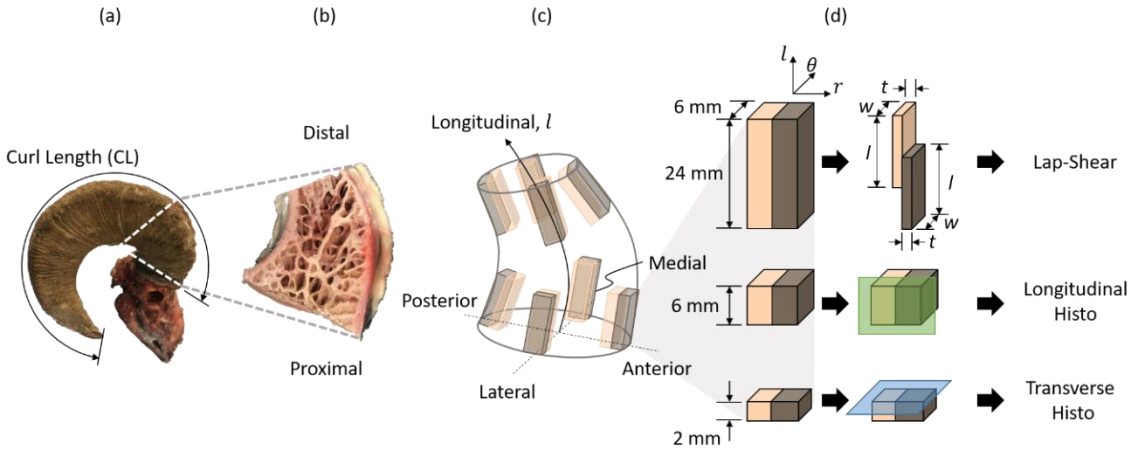

Figure 4-1. Sample extraction and processing. (a) Full skull and horn indicating the measured curl length and location of the proximal transverse section (gray dashed lines) cut from the horn. (b) Longitudinal section of proximal transverse section of horn. (c) The anatomical locations of extracted samples and the longitudinal axis defined in the quasi-cylindrical coordinate system. (d) Interface sections were segmented to prepare lap-shear specimens for mechanical testing and histological sections with transverse (blue plane) and longitudinal (green plane) orientations. The coordinate system shown indicates the longitudinal (l), circumferential (θ), and radial (r) axes of each interface sample.

4.2.2. Mechanical Testing

4.2.2.1. Lap-shear specimen preparation

Lap-shear testing was used to quantify the mechanical properties of the interface under shear loading. Lap-shear testing is commonly performed to assess the mechanics of adhesive bonds for use in mechanical design [22–25], including those of horn/bone interfaces [16]. Traditional lap-shear specimens consist of overlapping adherends of the same material bound by the adhesive to be tested. Here, one adherend was horncore cortical bone, the other was horn, and the interfacial tissue represented the adhesive bond to be tested in shear. Lap-shear specimens had a total length of 24 mm in the longitudinal

direction and total width of 6 mm in the circumferential direction. Prior to this point, lap-shear specimen length and width were achieved as described in the previous section. Individual adherends were designed to be 15 mm long, 6 mm wide, and approximately 2 mm thick (*l, w, and t*, respectively; Figure 4-1d). This resulted in an approximately 6 mm x 6 mm nominal area of intact interface (A_{int} = 36 mm^2) between overlapping bone and horn adherends. Mechanical test specimens were prepared using a vertical end mill and a custom work-holding fixture. The fixture was designed with stepped jaws such that the entire interface section (including horn and bone) was gripped securely on one end (fixed end) while the top material (either bone or horn) was left exposed above the jaws on the opposite end (free end). This set up ensured the soft tissue interface was kept intact while the lap-shear specimen was milled. Additionally, variability in total interface sample thickness could be accommodated by utilizing parallels of various heights in combination with the stepped jaws. Briefly, the milling procedure was as follows. First, the outer surfaces of bone and keratin were milled to obtain uniform surfaces and final adherend thicknesses (~2 mm) (Figure 4-2a and b). During these milling operations, the samples were clamped in a normal vice such that the soft-tissue interface was secured in the jaws while the material to be milled was exposed above the jaws. Initially, the specimen was clamped with the interface parallel to the top surface of the jaws based solely on visual inspection. After the first material was milled, parallels were used to support that sample in subsequent milling operations to ensure parallelism and alignment between the outer horn and bone surfaces and the interface (Figure 4-2b). Once the outer surfaces of bone and horn had been made uniform, the sample was secured in the custom work-holding fixture to finalize the adherend dimensions. In these steps, excess material on the free end

was milled all the way to the bottom material while obtaining the 15 mm long adherend of the top material (Figure 4-2c and d). Physiological saline was used to provide lubrication and maintain sample hydration throughout mechanical test specimen preparation. The final width (w_{int}) of each lap-shear specimen was measured to the nearest 0.01 mm at the center of the intact interface using digital calipers. Additionally, lap-shear specimens were imaged at 16x magnification using reflected light on a stereoscope (Discovery.V20; Carl Zeiss AG; Oberkochen, Germany) equipped with a color camera (Axiocam 512 color; Carl Zeiss AG; Oberkochen, Germany). These images were used to obtain accurate measures of intact lap-shear interface length ($l_{int,\,LS}$) and lap-shear interface thickness ($t_{int,\,LS}$) via image analysis. First, images were imported into BioQuant image analysis software and the horn and bone surfaces on each side of the interface were manually traced. Next, BioQuant's built in double labeled surface measurement option was used to automatically measure the distance between the traced surfaces in 5 µm increments. The average value of all these measurements taken over the entire length of the interface was defined as $t_{int,\,LS}$ (Figure 4-3). Additionally, the average length of the two traced surfaces were calculated and defined as $l_{int,\,LS}$ (Figure 4-3). After imaging, lap-shear specimens were wrapped in saline soaked gauze and kept frozen at -20 °C until testing.

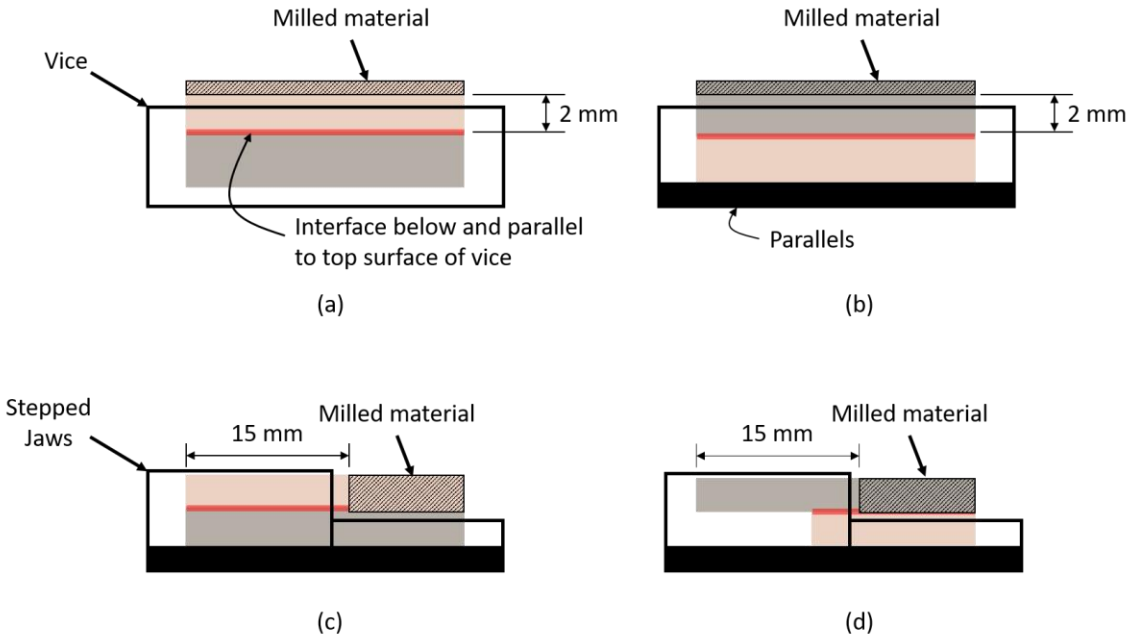

Figure 4-2. Lap-shear specimen milling procedue. (a) Sample secured in vice and top material milled to final adherend thickness of 2 mm. (b) Sample flipped over, and milled surface from (a) positioned on parallels to mill second material to final adherend thickness of 2 mm. (c) Sample secured in custom fixture with stepped jaws and exposed material on free end milled completely to bottom material to finalize first adherend length of ~15 mm. (d) Sample flipped over to repeat (c) on opposite side to obtain second adherend length (~15 mm) and finalize lap-shear specimen.

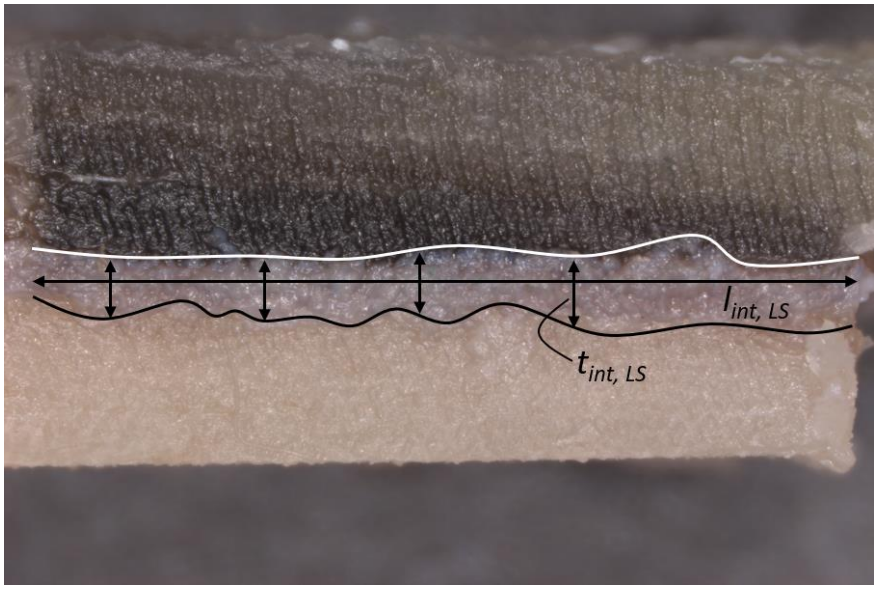

Figure 4-3. Reflected light stereoscope image used to measure lap-shear interface length ($l_{int, LS}$) and lap-shear interface thickness ($t_{int, LS}$) of final lap-shear specimens. Images were loaded into BioQuant, and the horn surface (white curved line) and bone surface (black curved line) adjacent to the soft-tissue interface were manually traced. The double labeled surface measurement was used to calculate the average length of these two surfaces ($l_{int, LS}$) as well as the average distance between these two surfaces from individual measurements made in 5 µm increments ($t_{int, LS}$).

4.2.2.2. Lap-shear testing

Lap-shear specimens were tested to failure using an MTS Bionix Test System (MTS Systems Corporation; Eden Prairie, MN) based on ASTM Standard D1002-05 [23], and similar to previous studies on horn/bone interface of equine hoof [16]. Tensile test grips (Mark-10 Corporation; Copiague, NY) with self-aligning and self-tightening jaws were used to grip each adherend and apply a tensile load to induce shear loading of the interface. An initial tensile preload of 1 N was applied at a constant rate of 0.5 mm/s to alleviate any possible low levels of compression that may have been applied to the sample by the self-tightening grips. The preload was held for 1 second prior to loading to failure with a constant crosshead displacement rate of 8.3 mm/s. This loading rate is similar to previous studies on the stress-strain behavior of the equine laminar junction [16]. The

applied force (*F*) was measured using a 445 N load cell (Interface Force Measurements Ltd.; Crowthorne, UK) while MTS actuator displacement was used to measure the deformation (*d*) between adherends during testing (MTS Systems Corporation; Eden Prairie, MN). All data was collected at a rate of 1024 Hz. Engineering mechanics were used to estimate the apparent shear stress (τ_{app}) and apparent shear strain (γ_{app}) acting on the interface using equations 4.1 and 4.2.

$$\tau_{app} = \frac{F}{w_{int,LS} * l_{int,LS}} \tag{4.1}$$

$$\gamma_{app} = \tan^{-1}\left(\frac{d}{t_{int,LS}}\right) \tag{4.2}$$

Similar to other soft-tissues, the connective tissue interface displayed non-linear stress-strain behavior with three distinct regions: (1) toe – initial low-stiffness linear region followed by non-linear stiffening, (2) elastic region – linear region with higher stiffness than toe, (3) failure – decreased stiffness due to material yield and ultimate failure. Similar to previous studies on the stress-strain behavior of the equine laminar junction, two different shear moduli were calculated: a low-strain shear modulus in the toe region ($G_{low\text{-}strain}$) and a high-strain shear modulus in the elastic region ($G_{high\text{-}strain}$). Each shear modulus was defined as the slope of the linear portion of the stress-strain curve in each region (Figure 4-4). Additionally, the ultimate apparent shear strength (τ_{ult}) and ultimate apparent shear strain (γ_{ult}) were defined as the apparent shear stress and apparent shear strain, respectively, calculated at the maximum load (Figure 4-4). The total strain energy density (SED) was also calculated for each sample as the area under the stress-strain curve up to failure.

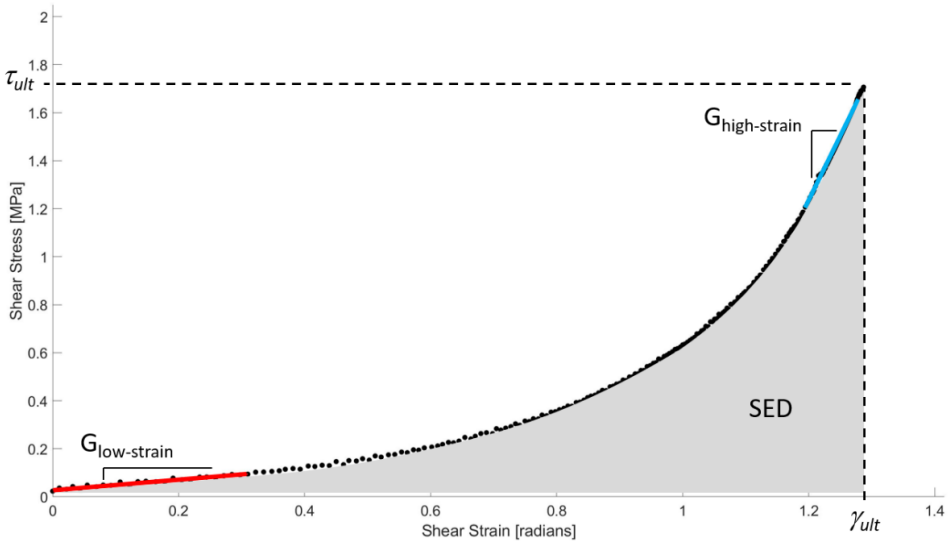

Figure 4-4. Representative stress-strain curve from lap-shear testing illustrating the low-strain shear moduli ($G_{low\text{-}strain}$, red line), high-strain shear moduli ($G_{high\text{-}strain}$, blue line), ultimate apparent shear strength (τ_{ult}), ultimate apparent shear strain (γ_{ult}), and strain energy density (SED, grey area under the stress-strain curve).

4.2.3. Histology

Segments cut from each sample for preparation of histological sections were fixed in 10% neutral buffered formalin for 48 hours, then decalcified in a solution of 8% formic acid for 7 days to allow for thin sectioning of the cortical bone present in the interface sections. After decalcification, samples were processed using standard histological tissue processing including dehydration in ethanol, clearing in xylene, and submersion in liquid paraffin using an automated tissue processor (Leica TP1020, Leica Biosystems, Wetzlar, Germany).[2] Following tissue processing, samples were embedded in paraffin wax to facilitate sectioning. A manual rotary microtome (Leica HistoCore BIOCUT, Leica Biosystems, Wetzlar, Germany) was used to cut thin sections (7 µm) from each paraffin

[2] The full tissue processing program included 1 hour in 70% ethanol, 1 hour in 85% ethanol, 45 minutes in 90% ethanol, 1 hour in 90% ethanol, three changes of 1 hour each in 100% ethanol, 1 hour and 30 minutes in Xylene, 2 hours in Xylene, 2 hours and 15 minutes in Xylene, 2 hours and 15 minutes in liquid paraffin at 58 °C and under vacuum, and 3 hours and 30 minutes in liquid paraffin at 58 °C and under vacuum. Subsequent steps listing the same reagent indicate a change to fresh reagent. The agitation setting on the tissue processor was kept on throughout the duration of the program.

block. Sections were mounted on glass microscope slides and stained using Masson's Trichrome to allow for distinction between collagen fibers (stained blue) and keratin fibers (stained red) present in the horn-horncore interface [19]. Mineralized bone tissue also stains red but is distinguishable from keratin fibers due to morphological differences. Prior to staining, slides were baked at 45 °C overnight, deparaffinized in two changes of xylene, and rehydrated in a series of decreasing ethanol concentrations (from 100% to 80%). Slides were stained following the manufacturer's recommended procedure.[3] Following staining, slides were dehydrated in two changes of 95% ethanol followed by two changes of 100% ethanol, then cleared in two changes of xylene. Stained slides were coverslipped and imaged at 100x magnification via transmitted light microscopy on a stereoscope (Discovery.V20; Carl Zeiss AG; Oberkochen, Germany) equipped with a color camera (Axiocam 512 color; Carl Zeiss AG; Oberkochen, Germany).

[3] Slides were submerged in Bouin's fixative at 56 °C for 1 hour, washed in running tap water until the water ran clear, rinsed in distilled water, submerged in Weigert's Hematoxylin Working Solution for 10 minutes, washed under running tap water for 10 minutes, rinsed in distilled water, submerged in Biebrich Scarlet Acid Fuchsin for 2 minutes, rinsed in distilled water, submerged in phosphotungstic-phosphomolybdic acid for 10 minutes, transferred directly into Analine Blue for 5 minutes, rinsed in distilled water, and submerged in Acetic Acid for 3 min.

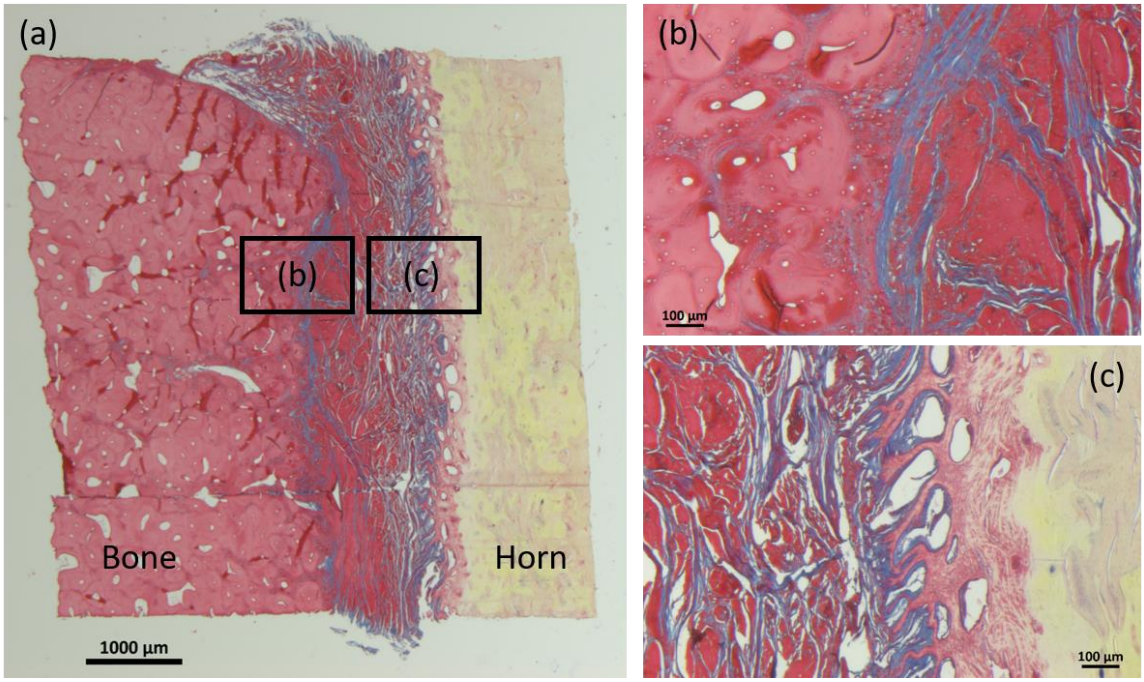

Figure 4-5. Representative image of interface histology section. (a) Entire section with mature bone (red) on the left, dense horn (yellow) on the right, and interfacial tissue with a mix of collagen (blue) and keratin (red) fibers. (b) Bone side of the interface showing unmineralized collagen fibers stained blue on the right side of the image. (c) Horn side of the interface showing the unorganized network of keratin fibers (red) and collagen fibers (blue) on the left and horn on the right. Within the horn, a region of keratinized tissue adjacent to the interfacial tissue is stained red, but the horn tissue eventually transitions to yellow staining as the keratinocytes become squamous and more densely packed.

4.2.4. Image Analysis

Images were imported into BioQuant (BIOQUANT Image Analysis Corporation; Nashville, TN) to quantify microstructural parameters of the interfacial tissue. In the stained sections, mature bone tissue was stained red, dense horn keratin was stained yellow, and collagen fibers and keratin fibers in the interface were stained blue and red, respectively (Figure 4-5). A region of interest (ROI) was defined for each section that included the entire area of imaged interfacial tissue, from the periosteal surface of red-stained bone on one side to just beyond the surface pores observed on the innermost surface of the horn on the opposite side (Figure 4-6). BioQuant RGB thresholding was used to

measure the total area (A_{ROI}) of each ROI, as well as the areas of blue-stained collagen (A_{col}) and red-stained keratin (A_{ker}). The area fractions of collagen ($A_{f,col}$) and keratin ($A_{f,ker}$) were then calculated by equations 4.3 and 4.4, respectively.

$$A_{f,col}\,[\%] = \frac{A_{col}}{A_{ROI}} \tag{4.3}$$

$$A_{f,ker}\,[\%] = \frac{A_{ker}}{A_{ROI}} \tag{4.4}$$

Additionally, the interface thickness in the radial direction was measured in BioQuant by manually tracing the horn and bone surfaces used to define the ROI then using the double labeled surface technique to measure the distance between the traced surfaces in 5 μm increments. The average of all incremental measurements was calculated and defined as the interface thickness (t_{int}, Figure 4-6). Additionally, the contact length (l_{cont}) was estimated as the sum of the total length of the undulated horn surface and the perimeters of microscopic pores (Equation 4.5) in the red-stained region of the inner horn surface that precluded the denser, yellow-stained horn (Figure 4-6). RGB thresholding was useful for selecting the undulated horn surface for many samples, but occasionally manual editing and tracing was needed to obtain an accurate selection. The nominal length (l_{nom}) was defined as the straight-line length approximately parallel to the inner horn surface of the ROI. Finally, the length ratio (LR) (Equation 4.6) was defined as the ratio of the contact length to the nominal length. Assuming the observed microstructure is similar in serial sections, the measured contact length provides a surrogate estimate of the actual contact area of each sample. Thus, the length ratio calculated represents the increase in contact area resulting from the undulated and porous horn surface observed microscopically compared to the nominal contact area of a perfectly flat surface. Furthermore, defining the

length ratio by normalizing the contact length by the nominal length provides a means of making comparisons that are not influenced by variation in histological section widths. Subscripts were used to distinguish between morphological parameters quantified in longitudinal (L) and transverse (T) histology sections (i.e., $t_{int,T}$ represents the interface thickness measured in the transverse histology section of a given sample).

$$l_{cont}\ [mm] = l_{undulated\ surface} + \sum l_{horn\ pore\ perimeters} \tag{4.5}$$

$$LR\ [-] = \frac{l_{cont}}{l_{nom}} \tag{4.6}$$

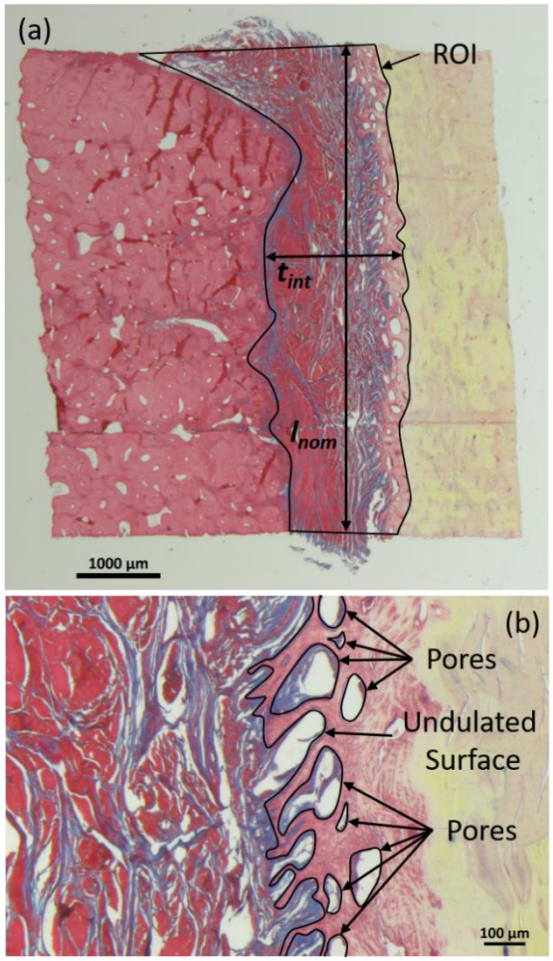

Figure 4-6. Example measurements of interface histology images. (a) Representative region of interest (ROI) used to calculate area fractions of collagen (blue) and keratin (red) observed in the interface. Average interface thickness (t_{int}) was measured in the radial direction by averaging incremental measurements between manually traced bone and horn surfaces using the double labeled surface measurement in BioQuant. Nominal contact length (l_{nom}) was measured as the straight-line edge-to-edge distance parallel to the horn surface. (b) Magnified view of histology section illustrating the undulated horn surface and horn pore perimeters used to calculate the contact length (l_{cont}) using Equation 4.5. Pores along the inner horn surface were included if they were contained within the red-stained region that precluded the yellow-stained horn.

4.2.5. Statistics

A paired t-test was used to compare the collagen area fraction to the keratin area fraction measured in each individual histology sections. In these tests, the collagen area fraction and keratin area fraction measured in the same histology *section* were paired.

Paired t-tests were also used to compare morphological parameters measured in transverse and longitudinal sections for each sample. In these tests, equivalent morphological parameters measured from the same sample were paired (i.e., $t_{int,L}$ and $t_{int,T}$ from the same *sample* were paired). Linear mixed model analysis was used to investigate the influence of anatomical position on interface morphology and mechanical properties. The linear mixed model included fixed effects of longitudinal position (proximal or distal) and quadrant (anterior, posterior, medial or lateral) as well as the random effect of ram ID. Transverse section morphology and longitudinal section morphology were considered separately in linear mixed models. In cases of statistically significant model effects, post-hoc analysis using Tukey HSD with Tukey-Kramer adjustment was used to evaluate significant differences of pairwise comparisons. Additionally, stepwise regression was used to investigate relationships between measured horn-horncore interface properties. Measured curl length (CL) and transverse section morphology ($A_{f,col,T}$, $A_{f,ker,T,}$ $t_{int,T}$ and LR_T) were included as predictor variables for each mechanical property (τ_{ult}, γ_{ult}, $G_{low\text{-}strain}$, $G_{high\text{-}strain}$, and SED). Only transverse section morphology was included in the regression models since transverse sections were cut perpendicular to the long axis of interface samples and are most representative of the lap-shear specimen cross-sections. Curl length was also included as a potential predictor variable in regression models to investigate the influence of animal age/size on interface mechanical properties. In each regression model, forward stepwise regression using the minimum BIC selection criteria was used to identify potential predictive models. Identified models were subsequently assessed for overall quality prior to final model selection. All statistical analyses were carried out using JMP Pro (SAS Institute; Cary, NC) with p-values less than 0.05 considered significant in all cases.

4.3. Results

4.3.1. Lap-shear Testing

The milling procedure used to obtain lap-shear specimens generally resulted in consistent dimensions near target values (Table 4-1). Five lap-shear specimens broke during milling and were discarded. Failed lap-shear specimens were inspected at increased magnification with a stereoscope using reflected light to determine the failure mode of each specimen. Almost all (20 out of 27) specimens failed due to the interface tissue separating from the horn but remaining attached to the bone (Figure 4-7a). Four lap-shear specimens demonstrated cohesive failure, meaning that the interface tissue failed within the interface thickness, and remnants of the interface were present on both bone and horn adherends after testing (Figure 4-7b). Two other lap-shear specimens demonstrated substrate failure where the bone adherend fractured prior to interface failure (Figure 4-7c). Since bone adherend failure precluded interface failure in these specimens, results inevitably underestimate the interface failure properties. As such, these two samples were excluded from the statistical analysis of the failure properties (τ_{ult}, γ_{ult}, and SED). However, the shear moduli measured for these specimens were not obvious outliers and were therefore included in the final statistical analysis. Finally, two lap-shear specimens failed at abnormally low test loads resulting in exceptionally noisy load cell data due to a reduced signal-to-noise ratio. These specimens were excluded from further analysis since poor quality data prevented accurate calculation of mechanical properties. It is possible that the integrity of these lap-shear specimens was compromised during lap-shear specimen preparation or while loading into test grips. Final statistical analyses included 23 lap-shear specimens for all mechanical properties, and 25 lap-shear specimens for the analyses

involving shear moduli. The final distribution of mechanical test specimens with respect to anatomical position for each ram is shown in Table 4-2.

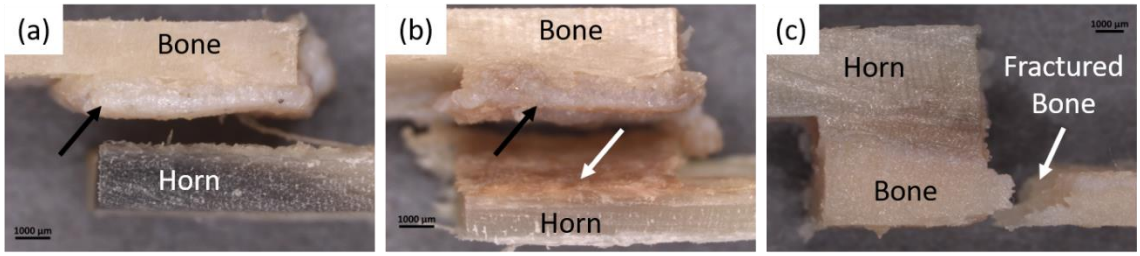

Figure 4-7. Failure modes of lap-shear specimens. (a) Interface failure along horn surface with interfacial tissue still attached to bone (black arrow). (b) Cohesive interface failure with remnants of interfacial tissue still attached to bone (black arrow) and horn (white arrow). (c) Failure due to fractured bone adherend (white arrow).

Table 4-1. Final lap-shear specimen dimensions including keratin adherend length ($l_{keratin}$) and thickness ($t_{keratin}$), bone adherend length (l_{bone}) and thickness (t_{bone}) as well as the width, length, and thickness ($w_{int,LS}$, $l_{int,LS}$, and $t_{int,LS}$, respectively) of the intact interface used in calculations of stress and strain to determine mechanical properties. Values shown as mean ± standard deviation for each ram (BHS 3-6), and all specimens combined (mean).

Ram ID	$l_{keratin}$	$t_{keratin}$	l_{bone}	t_{bone}	$w_{int,LS}$	$l_{int,LS}$	$t_{int,LS}$
3	15.20 ± 0.25	2.15 ± 0.34	15.25 ± 0.35	2.01 ± 0.30	5.79 ± 0.12	5.62 ± 0.61	0.552 ± 0.248
4	15.18 ± 0.20	2.00 ± 0.25	15.16 ± 0.24	1.85 ± 0.15	5.76 ± 0.08	5.90 ± 0.94	0.867 ± 0.337
5	15.08 ± 0.25	2.08 ± 0.17	15.16 ± 0.33	1.91 ± 0.15	5.77 ± 0.14	6.23 ± 1.04	0.493 ± 0.241
6	15.12 ± 0.16	1.99 ± 0.34	15.26 ± 0.31	1.83 ± 0.19	5.76 ± 0.08	6.09 ± 0.87	0.655 ± 0.165
Mean	15.15 ± 0.21	2.05 ± 0.28	15.21 ± 0.29	1.90 ± 0.21	5.77 ± 0.10	5.94 ± 0.85	0.661 ± 0.286

Table 4-2. Distribution of the anatomical position of lap-shear specimens included in statistical analyses (grey boxes) for each ram. The triple asterisks (***) indicates the two samples that failed due to bone adherend fracture which were excluded from statistical analysis of failure properties (τ_{ult}, γ_{ult}, and SED).

		Ram ID			
		3	**4**	**5**	**6**
Distal	**Anterior**				
	Posterior				
	Medial				***
	Lateral				***
Proximal	**Anterior**				
	Posterior				
	Medial				
	Lateral				

Linear mixed model analysis indicated that quadrant had a significant effect on the ultimate apparent shear strength ($p = .0423$) but none of the other mechanical properties ($p \geq .0703$). Post-hoc analysis of the effect of quadrant on ultimate apparent shear strength demonstrated that the posterior quadrant had a marginally lower ultimate shear strength compared to the medial ($p = .0533$) quadrant (Figure 4-8). Longitudinal position (proximal or distal) did not have a significant effect on any of the calculated mechanical properties ($p \geq .0998$). Interface lap-shear properties are summarized in Table 4-3 and results from the linear mixed model analysis are summarized in Table 4-4.

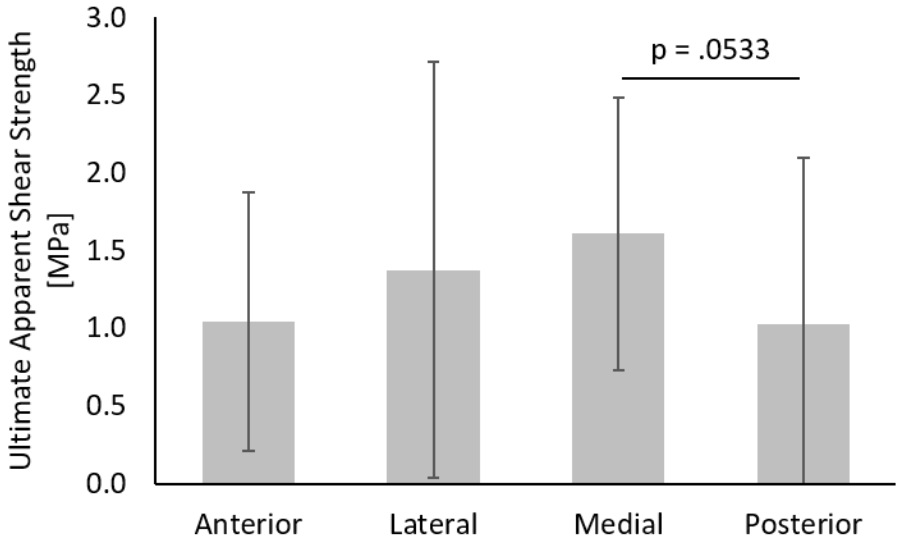

Figure 4-8. Comparison of ultimate apparent shear strength calculated from samples in each quadrant. Results from the linear mixed model showed that quadrant was a significant fixed effect ($p = .0319$). Post-hoc pairwise comparisons showed that the posterior quadrant had marginally lower ultimate apparent shear strength than the medial ($p = .0533$) quadrant.

Table 4-3. Summary of mechanical testing results including ultimate apparent shear strength (τ_{ult}), ultimate apparent shear strain (γ_{ult}), low-strain modulus ($G_{low\text{-}strain}$), high-strain modulus ($G_{high\text{-}strain}$), and total strain energy density (SED) for each ram and all mechanical tests combined (total). All values shown as Mean ± Standard Deviation.

Ram ID	τ_{ult} [MPa]	γ_{ult} [radians]	$G_{low\text{-}strain}$ [kPa]	$G_{high\text{-}strain}$ [MPa]	SED [MJ/m^3]
3	0.66 ± 0.16	1.22 ± 0.14	83.60 ± 68.16	2.56 ± 1.00	0.19 ± 0.07
4	0.75 ± 0.54	1.07 ± 0.21	150.02 ± 85.21	2.19 ± 1.81	0.24 ± 0.15
5	1.17 ± 0.87	1.17 ± 0.11	109.05 ± 42.82	3.67 ± 3.74	0.35 ± 0.22
6	2.84 ± 0.50	1.28 ± 0.06	250.47 ± 69.39	9.32 ± 2.67	0.89 ± 0.20
Mean	1.23 ± 1.00	1.17 ± 0.17	154.63 ± 95.15	4.47 ± 3.73	0.38 ± 0.31

*Table 4-4. P-values from mixed model analysis results showing significance of fixed effects on calculated mechanical properties including ultimate apparent shear strength (τ_{ult}), ultimate apparent shear strain (γ_{ult}), low-strain modulus ($G_{low\text{-}strain}$), high-strain modulus ($G_{high\text{-}strain}$), and total strain energy density (SED). Significant p-values ($p < .05$) are shown in **bold**.*

Source of Variation	τ_{ult} [MPa]	γ_{ult} [radians]	$G_{low\text{-}strain}$ [kPa]	$G_{high\text{-}strain}$ [MPa]	SED [MJ/m^3]
Longitudinal Position	.6664	.8979	.1624	.0998	.9787
Quadrant	**.0423**	.9237	.7254	.0703	.1019

4.3.2. Histology

Several histology samples were discarded due to issues encountered during thin section preparation. In some cases, the horn and bone were completely separated during sectioning before thin sections were obtained. In other cases, thin sections were successfully obtained but had large tears, folds, or other quality issues that made them inadequate for analysis. Ultimately, 20 longitudinal sections and 18 transverse sections of adequate quality were obtained. The final distribution of histological sections for each ram is shown in Table 4-5.

Table 4-5. Distribution of the anatomical positions of longitudinal (L) and transverse (T) histological sections included in statistical analyses (grey boxes) for each ram.

		Ram ID & Section Orientation							
		3		4		5		6	
		L	T	L	T	L	T	L	T
Distal	Anterior								
	Posterior								
	Medial								
	Lateral								
Proximal	Anterior								
	Posterior								
	Medial								
	Lateral								

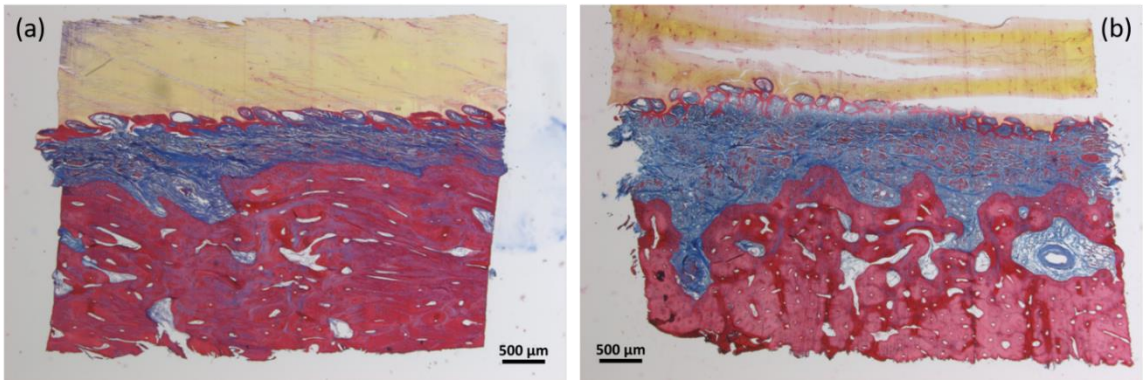

Figure 4-9. (a) Longitudinal and (b) transverse horn-horncore interface sections from the same sample. Sections were stained with Masson's trichrome. The interfacial tissue between horn (yellow) and bone (red) was an unorganized network of collagen fibers (blue) and keratin fibers (red). Longitudinal and transverse section morphologies were not different ($p \geq .1242$). Scale bars = 500 µm.

No differences were found between longitudinal and transverse section morphologies (Figure 4-9, $p \geq .1242$). In stained sections, interfacial tissue between bone (red) and horn (yellow) was an unorganized network of collagen fibers (blue) and keratin fibers (red), with collagen being the more abundant protein ($p < .0001$). Collagen fibers resembling Sharpey's fibers were frequently observed anchored to the bone surface at near

perpendicular angles (Figure 4-10). Larger collagen fiber bundles that penetrated deeper into the horncore bone were also observed along the bone surface, though these were rare (Figure 4-10d). Tightly packed, concentric collagen fibers surrounding a central pore were also seen in the horncore bone tissue near the interface, but these were rare (Figure 4-11d). On the horn side of the interface, there was typically a narrow region of keratinized tissue (red) that precluded the denser, fully cornified horn (yellow). Microscopic pores with keratinized walls were commonly observed in this region, and collagen fibers were typically seen along the inner periphery of these pores (Figure 4-10b), but filling the pores entirely in some cases (Figure 4-11b). On occasion, branched interdigitating structures were observed extending from the horn surface into the interfacial tissue (Figure 4-11c).

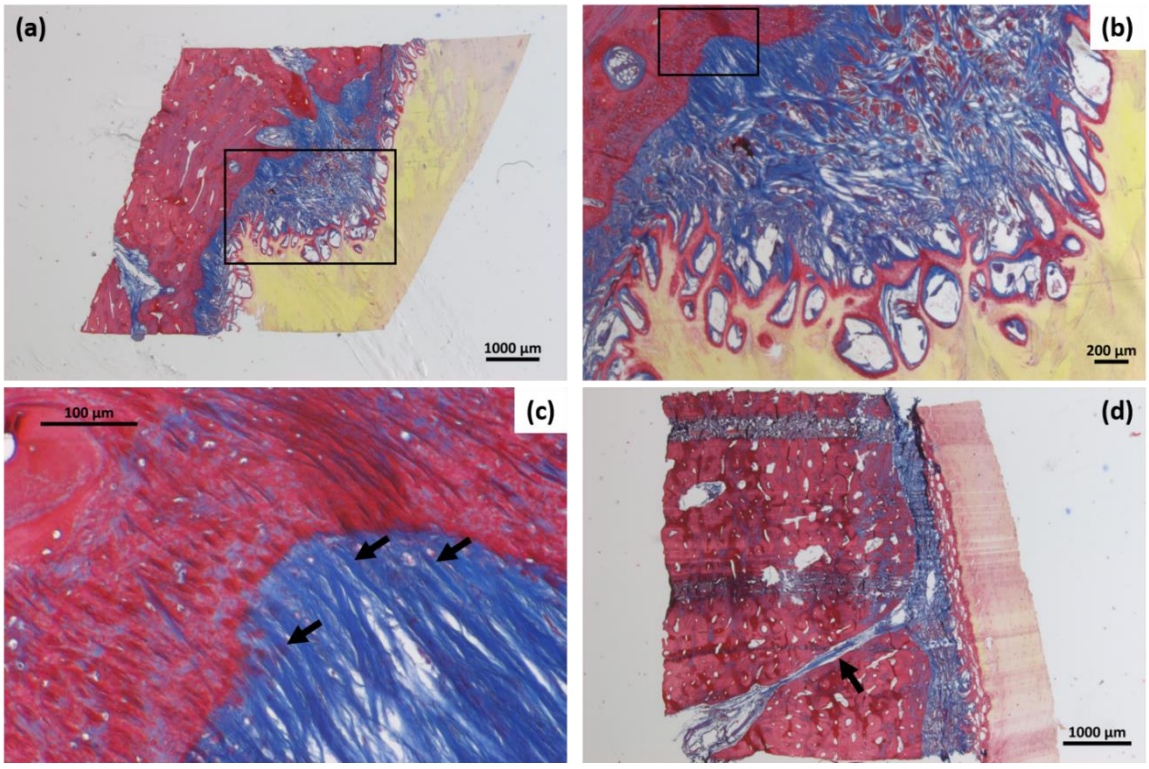

Figure 4-10. Histology sections stained with Masson's Trichrome. Dense horn is stained yellow, bone is stained red, and the interfacial tissue is an unorganized matrix of collagen fibers (blue) and keratin fibers (red). (a) Full histology cross section showing horn surface undulation and porosity where collagen attaches to horn. (b) Increased magnification of black box region in (a), showing unorganized matrix of collagen (blue) and keratin (red) fibers. (c) Black box in (b) showing Sharpey's fibers (black arrows) penetrating bone. (d) Collagen fiber bundle (black arrow) penetrating several millimeters into horncore cortical bone.

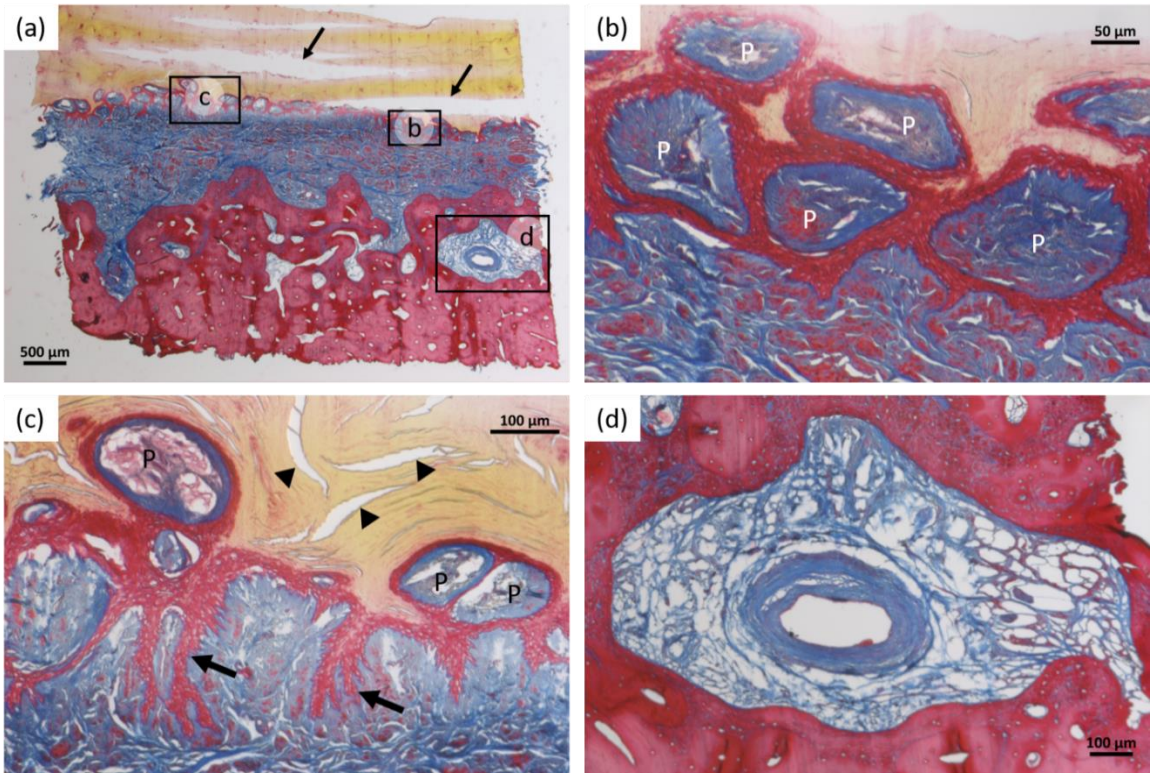

Figure 4-11. Histology sections stained with Masson's trichrome. Dense horn is stained yellow, mature bone is stained red, and the interfacial tissue is an unorganized matrix of collagen fibers (blue) and keratin fibers (red). (a) Sectioning tearing artifacts (black arrows) visible in the horn. (b) Black box labeled 'b' in (a) showing keratinized tissue forming the walls of pores (P) filled with collagen (blue) and trace amounts of keratin (red) (c) Black box 'c' in (a) showing keratinized tissue extensions forming branched structures (black arrows) within the surrounding interface tissue. Additional pores (P) can also be seen. (d) Dense network of collagen fibers arranged circumferentially to form a tubular structure in the bone.

Mix model analysis indicated that interface thickness was significantly higher ($p = .0316$) in proximal samples compared to distal samples in transverse histology sections only (Figure 4-12). Longitudinal position did not have a significant influence on any other morphometric measurements in transverse sections ($p \geq .1491$) or longitudinal sections ($p \geq .1905$). Quadrant was not found to be a significant model effect for any of the measured properties in transverse sections ($p \geq .2079$) or longitudinal sections ($p \geq .1805$).

Histomorphometry data is summarized in Table 4-6 and the results from linear mixed model analysis is summarized in Table 4-7.

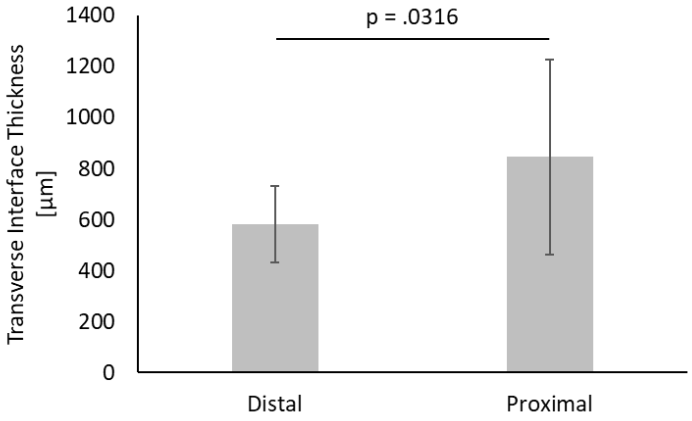

Figure 4-12. Linear mixed model analysis demonstrated that transverse interface thickness was higher in proximal samples than distal samples (p = .0316). Data shown as mean ± standard deviation.

Table 4-6. Summarized histology data for longitudinal and transverse sections including interface thickness (t_{int}), the length ratio (LR), and the area fractions of collagen ($A_{f,col}$) and keratin ($A_{f,ker}$). Data shown as mean ± standard deviation for each ram (BHS 3-6) and all rams combined (mean). P-values from paired t-tests between morphologic parameters quantified in longitudinal and transverse sections from the same samples shown in the bottom row.

Ram ID	Orientation	t_{int} [µm]	LR [-]	$A_{f,col}$ [%]	$A_{f,ker}$ [%]
3	Transverse	476.60 ± 230.88	8.0 ± 4.0	38.47 ± 13.42	33.90 ± 7.09
	Longitudinal	551.11 ± 231.10	2.8 ± 2.4	47.77 ± 17.27	23.50 ± 14.62
4	Transverse	930.35 ± 361.47	3.1 ± 1.4	37.20 ± 10.81	32.82 ± 12.88
	Longitudinal	953.46 ± 342.88	2.6 ± 0.5	43.41 ± 5.72	29.87 ± 4.72
5	Transverse	743.98 ± 375.54	2.6 ± 1.7	45.10 ± 15.09	12.24 ± 4.20
	Longitudinal	818.30 ± 561.90	2.2 ± 1.1	56.48 ± 11.64	17.32 ± 4.07
6	Transverse	724.57 ± 296.41	3.2 ± 1.5	48.88 ± 6.84	25.69 ± 11.31
	Longitudinal	1115.19 ± 686.48	3.5 ± 3.1	51.69 ± 13.28	26.37 ± 5.99
Mean	Transverse	757.22 ± 343.75	3.8 ± 2.7	42.20 ± 11.90	25.70 ± 12.83
	Longitudinal	859.52 ± 496.67	2.8 ± 1.9	49.83 ± 12.64	24.26 ± 9.11
	Paired t-test	0.5768	0.3959	0.1242	0.8487

*Table 4-7. P-values from mixed model analysis of histomorphometric results for each orientation (transverse and longitudinal sections) including interface thickness (t_{int}), the length ratio (LR), and the area fractions of collagen ($A_{f,col}$) and keratin ($A_{f,ker}$). Significant values ($p < .05$) shown in **bold**.*

Orientation	Source of Variation	t_{int} [µm]	LR [-]	$A_{f,col}$ [%]	$A_{f,ker}$ [%]
Transverse	Longitudinal Position	**0.0316**	0.7423	0.1491	0.1988
	Quadrant	0.2665	0.2079	0.4183	0.5704
Longitudinal	Longitudinal Position	0.1905	0.9397	0.7741	0.3885
	Quadrant	0.1805	0.7162	0.7328	0.7141

4.3.3. Regression Analysis

Regression analysis included all interface samples for which lap-shear properties and transverse section histomorphometry data was available. Ultimate shear strain was negatively correlated with the transverse interface thickness ($p = .0124$, $r^2 = 0.3702$; Figure 4-13). Curl length and the transverse length ratio were positively correlated with ultimate shear strength ($p = .0008$, $r^2 = 0.6687$), high-strain shear modulus ($p = .0101$, $r^2 = 0.5072$), and total strain energy density ($p = .0016$, $r^2 = 0.6289$). Finally, curl length, the transverse length ratio, and the transverse interface thickness were all positively correlated with the low-strain shear modulus ($p = .0210$, $r^2 = 0.5421$). Estimated model parameters, model equations, and the overall regression statistics for all final regression models are summarized in Table 4-8.

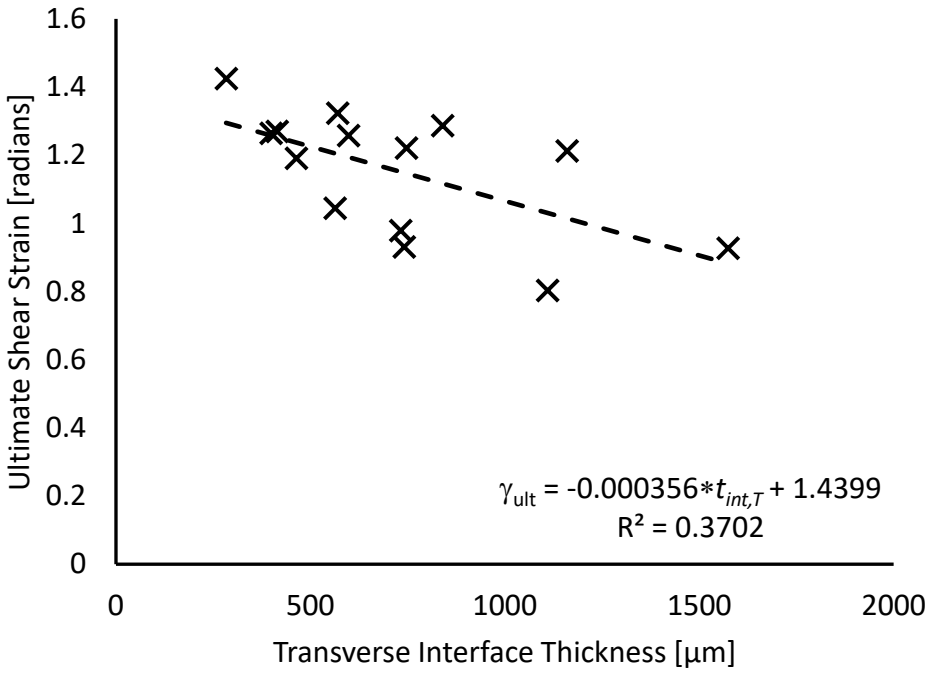

Figure 4-13. Regression model demonstrating negative correlation between ultimate shear strain and transverse interface thickness.

Table 4-8. Parameter estimates for regression models used to predict mechanical properties. Independent variables included in the final models included the curl length (CL) along with the interface thickness and length ratio measured in transverse histology sections ($t_{int,T}$ and LR_T, respectively). Equations presented in the bottom row of each mechanical property.

	Intercept		CL [cm]		$t_{int,T}$ [µm]		LR_T [-]		Overall Regression	
Variable	**Estimate**	**Std. Error**	**Estimate**	**Std. Error**	**Estimate**	**Std. Error**	**Estimate**	**Std. Error**	**r^2**	**p-value**
τ_{ult} [MPa]	-12.52	2.76	0.171	0.034			0.1557	0.0687		
	p = .0006		p = .0002				p = .0412			
Final Model:	**$\tau_{ult} = -12.52 + 0.171(CL) + 0.1557(LR_T)$**								**0.6687**	**.0008**
γ_{ult} [rad]	1.44	0.10			-0.0003560	0.0001240				
	p < .0001				p = .0124					
Final Model:	**$\gamma_{ult} = 1.44 - 0.0003560(t_{int,T})$**								**0.3702**	**.0124**
$G_{low\text{-}strain}$ [MPa]	-0.72	0.29	0.009	0.003	0.0001360	0.0000506	0.0149	0.0071		
	p = .0286		p = .0180		p = .0198		p = .0561			
Final Model:	**$G_{low\text{-}strain} = -0.72 + 0.009(CL) + 0.0001360(t_{int,T}) + 0.0149(LR_T)$**								**0.5421**	**.0210**
$G_{high\text{-}strain}$ [MPa]	-42.73	13.10	0.581	0.159			0.5583	0.3256		
	p = .0062		p = .0029				p = .1102			
Final Model:	**$G_{high\text{-}strain} = -42.73 + 0.581(CL) + 0.5583(LR_T)$**								**0.5072**	**.0101**
SED [MJ/m^3]	-3.49	0.84	0.048	0.010			0.0451	0.0210		
	p = .0012		p = .0004				p = .0512			
Final Model:	**$SED = -3.49 + 0.048(CL) + 0.0451(LR_T)$**								**0.6289**	**.0016**

4.4. Discussion

The goal of this study was to quantify the composition, microstructure, and mechanical properties of the horn-horncore interface in bighorn sheep rams and determine if these properties vary with respect to position and orientation within the overall horn-horncore structure. Additionally, statistical modeling was used to explore correlations between measured properties and identify important structure-function relationships of this unique interface. The purpose of this work was to better understand the role this interface plays in load transfer and injury mitigation during bighorn sheep ramming. It was hypothesized that the horn-horncore interface would have morphological features that increase the contact area between the horn and horncore bone, and that the increase in contact area would be positively correlated with the shear strength of the interface. The inner horn surface displayed an undulated surface with microscopic pores that increase the contact area between the horn and soft tissue interface. Conversely, the soft tissue interface is anchored to the bone surface via Sharpey's fibers. Lap-shear specimens primarily failed along the inner horn surface, suggesting that the horn-interface connection is weaker than the bone-interface attachment facilitated by Sharpey's fibers. The length ratio (LR) – representing the microscopic contact area between the horn and soft tissue interface – was positively correlated with many mechanical properties including the ultimate apparent shear stress, high-strain shear modulus, and strain energy density. These properties were also positively correlated with horn curl length which may suggest the interface becomes stiffer and stronger as rams grow older and more actively engaged in combat. The ultimate strain was not correlated with horn curl length or the length ratio, but was negatively correlated with the interface thickness; thus, interface failure may be a stain-controlled

phenomenon dictated by the interface thickness. Despite a markedly different morphology, the shear moduli of the horn-horncore interface were comparable to the equine laminar junction. These findings are supportive of the hypotheses and provide insight into the mechanisms responsible for load transfer between the impacted horn and energy absorbing horncore during ramming.

This work was limited by a low sample size of four bighorn sheep rams due to limited availability. Most rams included in this study died from motor vehicle collisions (BHS 3-5) while one ram was found dead entangled in a fence (BHS 6). It is possible that some tissue degradation occurred prior to measurement of interface properties, but effort was made to preserve tissues by freezing as quickly as possible after death. All rams involved in motor vehicle accidents were frozen within 24 hrs. The exact age and ramming history of each ram was also unknown. Rams included in this study were estimated to be 5-8 years old using the well documented technique of counting growth annuli visible on horn surfaces [21]. Furthermore, all rams included in this study had horns with at least three-quarters of a full curl. Bighorn sheep ramming behavior has been extensively documented and is most intense among rams 6-8 years old with horns of at least three-quarters of a full curl [26]. Thus, it is reasonable to assume that all rams included in this study were actively engaged in combat during the rut. It should also be noted that the shear properties reported here are not true material properties of the interface tissue. Lap-shear tests generate a complex stress distribution and generally result in failure from peel forces that arise due to adherend bending caused by misalignment of the tensile loads applied to each adherend [27]. As such, the reported shear strength is likely underestimating the true shear strength of this interface. However, lap-shear testing is valuable due to its simplicity

and for comparison to previous studies on similar biological interfaces. Another limitation arose in the preparation of thin histology sections of hard bone and horn tissues. Decalcification allowed for bone sectioning, however sectioning artifacts and lost samples remained inevitable. This resulted in a further reduction of the already limited sample size for histomorphometric characterization. However, the data presented here is still valuable since this is the first study to quantify the morphology of this interesting biological tissue interface.

Results from lap-shear testing indicate that mechanical properties are mostly consistent throughout the horncore and demonstrate non-linear strain stiffening during loading. The ultimate apparent shear strength in the posterior quadrant was 36% lower than the medial quadrant, but this difference was marginal ($p = .0533$, Figure 4-8). All other mechanical properties were similar regardless of longitudinal position or quadrant ($p > .0703$, Table 4-4). A similar study on the equine laminar junction reported similar findings with minimal regional variation in mechanical properties and non-linear strain stiffening upon increased deformation. Furthermore, the low-strain and high-strain shear moduli reported for the laminar junction tested in proximodistal shear were 398 ± 312 kPa and 5.38 ± 1.49 MPa, respectively [16]. These mean values are comparable to the low-strain modulus (154.63 ± 95.15 kPa) and high-strain modulus (4.47 ± 3.73 MPa) of the bighorn sheep horn-horncore interface (Table 4-3). Comparison of the ultimate properties calculated in this work is not possible since the previous study on the equine laminar junction did not test samples to failure. It should also be noted that comparisons of the shear moduli are confounded by different equations used to calculate shear strain in each study. The previous study used the small angle approximation to calculate shear strains

since laminar junction samples were not tested to failure and experienced less total deformation. However, the small angle approximation was not justifiable for calculation of apparent shear strain in this work since horn-horncore interface samples displayed large total deformations when tested to failure. Regardless, similarities in the calculated shear moduli and overall shape of the stress-strain curves reported in each study provide confidence in the results presented here. Despite comparable lap-shear properties, similarities between the horn-horncore interface and the equine laminar junction were not as evident when looking at results from histomorphometry.

Histomorphometric analysis revealed that the horn-horncore interface morphology shares some similarities to other dermo-epidermal junctions studied previously but also demonstrates some unique microstructural features. Collagen fibers were seen penetrating the horncore cortical bone surface as Sharpey's fibers (Figure 4-10c) which have been identified at the interface between the keratin-rich beak and the underlying bone in avian species as well [18]. The attachment mechanism between the horn and interfacial tissue is currently unclear since there was no evidence of fibrous penetration along the horn surface like the Sharpey's fibers observed along the bone surface. The inner horn surface displayed an undulated morphology with microscopic pores. Along the undulated surface, there was typically a narrow region of keratinized tissue, which was distinguishable from the denser cornified horn by bright red staining. This keratinized tissue often formed the walls of microscopic pores with polyhedral shapes that ranged from approximately 50 – 300 μm in diameter, though this was not rigorously quantified (Figure 4-11b). In addition to these pores, keratinized tissue frequently extended radially inward from the horn surface, forming branched structures within the collagenous interface (Figure 4-11c). These

interdigitating structures share some resemblance to the equine laminar junction, with the main body representing the primary epidermal lamellae and the smaller branches being analogous to the secondary epidermal lamellae. However, these structures are much less numerous and consistent than lamellae of the laminar junction. Collagen was often visible adjacent to keratinized interdigitations and within horn surface pores, either peripherally (Figure 4-10b) or entirely filling the pore (Figure 4-11b, c). The proximity of collagenous and keratinized tissue throughout this morphology may provide an increased contact area that facilitates attachment like the lamellar structure of the equine laminar junction. Furthermore, it is possible that the entanglement of collagen with the undulated and porous horn surface facilitates a hook and loop style attachment mechanism, with collagen acting as the loops wrapping around the hook-like walls of horn pores. Empty pores and pores with collagen only around the perimeter are not supportive of this theory, but these may be artifacts of tissue processing and histological section preparation. Although the horn-interface attachment mechanism cannot be determined from this work, it appears to be weaker than the bone-interface attachment via Sharpey's fibers since lap-shear specimens generally failed along the horn surface. Regardless, findings from stepwise regression support the theory that the increased microscopic contact area provided by the horn surface morphology reduces local attachment stress magnitudes and promotes efficient load transfer between the impacted horn and energy absorbing horncore.

Results from the regression analyses showed that the microscopic contact area is positively correlated with many of the lap-shear properties including lap-shear strength, as hypothesized. More specifically, the length ratio measured along the inner horn surface was positively correlated with all calculated mechanical properties that were dependent on

the calculated shear stress (τ_{ult}, $G_{low\text{-}strain}$, $G_{high\text{-}strain}$, SED, Table 4-8). This is indicative of lap-shear specimens with larger length ratios achieving higher ultimate loads during testing since apparent shear stress was calculated using the nominal contact area, which was similar across specimens. This finding supports the suggestion that the increased contact area provided by the morphology of the horn surface is beneficial for reducing local stress magnitudes during loading. Furthermore, the ultimate apparent shear strain was not dependent on the length ratio which may suggests strain-controlled failure of the interface. With that said, it is interesting that the ultimate apparent shear strain was negatively correlated with interface thickness (Figure 4-13), since thicker interfaces would be expected to deform more prior to failure. It is possible that this result is a consequence of the lap-shear testing method as thicker interfaces would lead to larger misalignment of applied forces, thereby increasing adherend bending and associated peel forces acting on the interface. Another interesting finding is the positive correlation between mechanical properties and horn curl length. This may suggest that the interface becomes stiffer and strong as rams grow older and larger and become more actively engaged in ramming during the rut. However, a larger sample size would be needed to draw any conclusions from this result. Regardless, these findings provide an improved understanding of the composition, microstructure, and mechanical properties of the horn-horncore interface and offer insight into the role this structure plays in load transfer during ramming.

Results from this work have demonstrated that the horn-horncore interface has a unique morphology that contributes to non-linear strain stiffening under shear loading. Despite morphological differences compared to the equine laminar junction, the microscopic porosity and branching interdigitations of the keratinized horn surface also

increase the microscopic contact area of the interface. Positive correlations between the microscopic contact area and lap-shear properties of this interface support the theory that the increased contact area is beneficial for reducing local stress magnitudes and promoting efficient load transfer between the impacted horn and energy absorbing horncore. Considering the role horncore bone plays in energy absorption and reduction of brain cavity accelerations during ramming, these findings have implications for brain injury mitigation in bighorn sheep. Moving forward, these results can be used to improve computational models of bighorn sheep ramming which have previously modeled this interface as a rigid attachment. Additionally, findings presented here can be used to guide additional experimental work at smaller and larger length scales to further improve our understanding of this intriguing interface.

4.5. References

[1] T.W. Seek, Exploration of Unique Porous Bone Materials for Candidacy in Bioinspired Material Design, Colorado State University, 2018.

[2] K.L. Johnson, M.W. Trim, D.K. Francis, W.R. Whittington, J.A. Miller, C.E. Bennett, M.F. Horstemeyer, Moisture, anisotropy, stress state, and strain rate effects on bighorn sheep horn keratin mechanical properties, Acta Biomater. 48 (2017) 300–308. https://doi.org/10.1016/j.actbio.2016.10.033.

[3] M.W. Trim, M.F. Horstemeyer, H. Rhee, H. el Kadiri, L.N. Williams, J. Liao, K.B. Walters, J. McKittrick, S.-J. Park, The effects of water and microstructure on the mechanical properties of bighorn sheep (Ovis canadensis) horn keratin., Acta Biomater. 7 (2011) 1228–40. https://doi.org/10.1016/j.actbio.2010.11.024.

[4] L. Tombolato, E.E. Novitskaya, P.Y. Chen, F.A. Sheppard, J. McKittrick, Microstructure, elastic properties and deformation mechanisms of horn keratin, Acta Biomater. 6 (2010) 319–330. https://doi.org/10.1016/j.actbio.2009.06.033.

[5] W. Huang, A. Zaheri, J.-Y. Jung, H.D. Espinosa, J. Mckittrick, Hierarchical structure and compressive deformation mechanisms of bighorn sheep (Ovis canadensis) horn, Acta Biomater. 64 (2017) 1–14. https://doi.org/10.1016/j.actbio.2017.09.043.

[6] Y. Zhang, W. Huang, C. Hayashi, J. Gatesy, J. McKittrick, Microstructure and mechanical properties of different keratinous horns, J R Soc Interface. 15 (2018). https://doi.org/10.1098/rsif.2018.0093.

[7] A. Drake, T.L. Haut Donahue, M. Stansloski, K. Fox, B.B. Wheatley, S.W. Donahue, Horn and horn core trabecular bone of bighorn sheep rams absorbs impact energy and reduces brain cavity accelerations during high impact ramming of the skull, Acta Biomater. 44 (2016) 41–50. https://doi.org/10.1016/j.actbio.2016.08.019.

[8] P. Maity, S.A. Tekalur, Finite element analysis of ramming in Ovis canadensis, J Biomech Eng. 133 (2011) 1–9. https://doi.org/10.1115/1.4003321.

[9] C.C. Pollitt, S.N. Collins, The suspensory apparatus of the distal phalanx in normal horses, Equine Vet J. 48 (2016) 496–501. https://doi.org/10.1111/evj.12459.

[10] C.C. Pollitt, Clinical anatomy and physiology of the normal equine foot, Equine Vet Educ. 4 (1992) 219–224.

[11] J.J. Thomason, H.L. McClinchey, B. Faramarzi, J.C. Jofriet, Mechanical behavior and quantitative morphology of the equine laminar junction, Anatomical Record - Part A Discoveries in Molecular, Cellular, and Evolutionary Biology. 283 (2005) 366–379. https://doi.org/10.1002/ar.a.20173.

[12] B. Faramarzi, Morphological and biomechanical properties of equine laminar junction, J Equine Vet Sci. 34 (2014) 589–592. https://doi.org/10.1016/j.jevs.2013.12.007.

[13] P. Kochová, K. Witter, R. Cimrman, J. Mezerová, Z. Tonar, A preliminary study into the correlation of stiffness of the laminar junction of the equine hoof with the length density of its secondary lamellae, Equine Vet J. 45 (2013) 170–175. https://doi.org/10.1111/j.2042-3306.2012.00632.x.

[14] J.L. Lanovaz, H.M. Clayton, L.G. Watson, In vitro attenuation of impact shock in equine digits, Equine Vet J. 26 (1998) 96–102.

[15] C.C. Pollitt, The anatomy and physiology of the hoof wall., Equine Vet Educ. 10 (1998) 318–325.

[16] J.E. Douglas, T.L. Biddick, J.J. Thomason, J.C. Jofriet, Stress/strain behaviour of the equine laminar junction, Journal of Experimental Biology. 201 (1998) 2287–2297.

[17] P.R. Stettenheim, The integumentary morphology of modern birds-an overview, Am Zool. 40 (2000) 461–477. https://doi.org/10.1093/icb/40.4.461.

[18] A. Genbrugge, D. Adriaens, B. De Kegel, L. Brabant, L. Van Hoorebeke, J. Podos, J. Dirckx, P. Aerts, A. Herrel, Structural tissue organization in the beak of Java and Darwin's finches, J Anat. 221 (2012) 383–393. https://doi.org/10.1111/j.1469-7580.2012.01561.x.

[19] C. van Hemert, C.M. Handel, J.E. Blake, R.M. Swor, T.M. O'Hara, Microanatomy of passerine hard-cornified tissues: Beak and claw structure of the black-capped chickadee (Poecile atricapillus), J Morphol. 273 (2012) 226–240. https://doi.org/10.1002/jmor.11023.

[20] S.A. Wainwright, W.D. Biggs, J.D. Currey, J.M. Gosline, Collagen, in: Mechanical Design in Organisms, Halsted Press, 1976: pp. 81–94.

[21] V. Geist, Validity of Horn Segment Counts in Aging Bighorn Sheep, J Wildl Manage. 30 (1966) 634–635.

[22] ASTM-D5656-04, Standard Test Method for Thick-Adherend Metal Lap-Shear Joints for Determination of the Stress-Strain Behavior of Adhesives in Shear by Tension Loading, Annual Book of ASTM Standards. 10 (2004) 1–8. https://doi.org/10.1520/D5656-10R17.2.

[23] ASTM D 1002-05, Standard Test Method for Apparent Shear Strength of Single-Lap-Joint Adhesively Bonded Metal Specimens by Tension Loading (Metal-to-Metal), Standards. 10 (2005) 1–5. https://doi.org/10.1520/D1002-10.on.

[24] A. Bonds, A. Bonds, Standard Guide for Use of Adhesive-Bonded Single Lap-Joint Specimen Test, i (2012) 1–6. https://doi.org/10.1520/D4896-01R08E01.2.

[25] American Society for Testing Materials, ASTM D3983-98: Standard Test Method for Measuring Strength and Shear Modulus of Nonrigid Adhesives by the Thick-Adherend Tensile-Lap Specimen, 1 (2019) 1–11. https://doi.org/10.1520/D3983-98R19.2.

[26] V. Geist, Mountain Sheep: A Study in Behavior and Evolution, University of Chicago Press, 1971.

[27] A. v. Pocius, Shear Loading of Adhesive Bonds, in: Adhesion and Adhesives Technology: An Introduction, 2002.

CHAPTER 5

5. COMPUTATIONAL MODELING OF VELAR BONE ARCHITECTURES

5.1. Introduction

Trabecular bone is an important structural tissue that provides mechanical competence at significantly reduced weight compared to less porous cortical bone. Standard indices[4] have been developed to quantify trabecular bone architecture [1] while various fabric tensors have been used to describe the structural anisotropy and spatial organization of trabecular bone [2]. Studies covering a wide range of animal masses (0.003 – 3400 kg) have demonstrated trabecular thickness and trabecular spacing scale allometrically in mammals and birds but bone volume fraction has no clear correlation with animal size [3,4]. It was suggested that these relationships represent geometric adaptations to limit local bone strains of individual trabeculae without compromising the weight savings provided by the low bone volume fraction compared to cortical bone. This theory is supported by computational modeling that demonstrated Tb.Th, Tb.Sp, and Conn.D were the best predictor variables for the apparent stiffness of trabecular bone across a wide range of animal sizes (1 – 10,000 kg) [5]. Accordingly, trabecular bone apparent stiffness was positively correlated with body mass, and this correlation maintained local strains in individual trabeculae near typical physiological values. Quantifying similar relationships

[4] Structural indices of trabecular bone include the bone volume fraction (BV/TV; bone tissue volume per total volume), trabecular thickness (Tb.Th; average thickness of struts), trabecular separation (Tb.Sp; average distance between struts), trabecular number (Tb.N; average number of struts per unit length), and connectivity density (Conn.D; number of strut connections per unit volume).

for velar bone architectures is an important first step in understanding whether or not the velar bone architecture is mechanically advantageous in terms of energy absorption.

Horncore velar bone plays a vital role in energy absorption and reduction of brain cavity accelerations during ramming [6]. Efforts to characterize the mechanics of velar bone architecture are limited despite its potential role in brain injury mitigation during ramming [7]. Velar bone has a porous bone architecture that has a bone volume fraction (BV/TV) of 21 ± 5% [8], which is in the range of mammalian trabecular bone (15 – 65%). Interestingly, velar thickness (2.87 ± 0.78 mm, [8]) and separation (11.9 ± 0.9 mm, [8]) are an order of magnitude larger than the trabecular thickness (0.511 mm) and trabecular separation (0.851 mm) of the most massive animal previously studied, the Asian elephant [3]. Since velar bone does not offer any weight advantage compared to trabecular bone with similar BV/TV values, it is not clear why this architecture has developed in the horncore of bighorn sheep rams as opposed to the horncore being filled with trabecular bone. One possible explanation is that velar bone architecture has a mechanical advantage for energy absorption during ramming compared to trabecular architecture. Porous architectures, both engineered and natural, are commonly modeled as cellular solids which are materials formed by repetition of a common unit cell. The mechanics of cellular solids are dependent on architectural organization along with the intrinsic material properties of the solid phase. Aim 2 of this work explored velar bone properties at the tissue level, providing insight into the intrinsic material properties of this distinctive bone structure. However, it is still unclear how the velar bone architectural organization throughout the entire horncore affects its mechanical behavior compared to a horncore filled with trabecular bone. Exploring velar bone mechanics at a size scale containing a lattice network

of numerous velae may provide insight into why this unique architecture has developed in the horncore of bighorn sheep rams.

Velar bone architecture may offer a mechanical advantage for energy absorption compared to trabecular bone considering the importance of horncore energy absorption during bighorn sheep ramming. This work used computational modeling approaches to investigate how the mechanical response of velar bone was influenced by the volume of velar bone considered. Additionally, simulated compression loading was used to compare the performance of velar and trabecular bone architectures in terms of strain energy density and buckling resistance. It was hypothesized that velar bone would have a greater capacity to store strain energy and increased resistance to buckling compared to trabecular bone. An improved understanding of the structure-property relationships of velar bone lattices at length scales relevant to the entire horncore level will offer insight into the role this unique bone architecture plays in energy absorption and injury mitigation during ramming. Furthermore, this work will provide a framework for continued investigation of velar bone mechanics moving forward.

5.2. Materials and Methods

5.2.1. Samples

The skull of one deceased mature bighorn sheep ram was provided by the Colorado Department of Natural Resources under Colorado Parks and Wildlife scientific collection license number 14SALV2052A2. This ram was estimated to be 8 years old by counting growth rings visible on the horn surfaces [9]. The curl length of this ram was 85 cm and corresponded to a full, 360° curl of the horn. Detailed images of the skull morphology were

obtained via computed tomography (CT) scanning. The skull was scanned using a Gemini Time-of-Flight Big Bore PET/16 slice CT scanner (Philips Healthcare, Andover, MA, USA) using a 140 kV voltage, 321 mA current, and 350 mAs time of exposure. These scan settings produced cubic voxels with an edge length of 0.73 mm/pixel.

5.2.2. Representative Volume Elements

5.2.2.1. Velar Bone

Cubic volumes were cropped from the left horncore to create representative volume elements (RVEs) of the velar bone architecture. DICOM data from CT scans was imported into Seg3D (version 2.5.1, University of Utah, Salt Lake City, UT) as a data volume. The cropping tool was used to isolate a 45 mm cube of velar bone from the left horncore (Figure 5-1). This was the largest cube that could be obtained without including any cortical bone. Next, the threshold tool was used to create a layer segmentation of velar bone by manually adjusting threshold values until the segmentation and bone tissue visible in the CT scan data were in close agreement (Figure 5-2a, b). Automatic thresholding provided a good first approximation of velar bone segmentation from DICOM data, but tissue heterogeneity made it difficult to accurately represent all bone tissue visible in CT scans. Velar bone segmentations were manually repaired using the paint

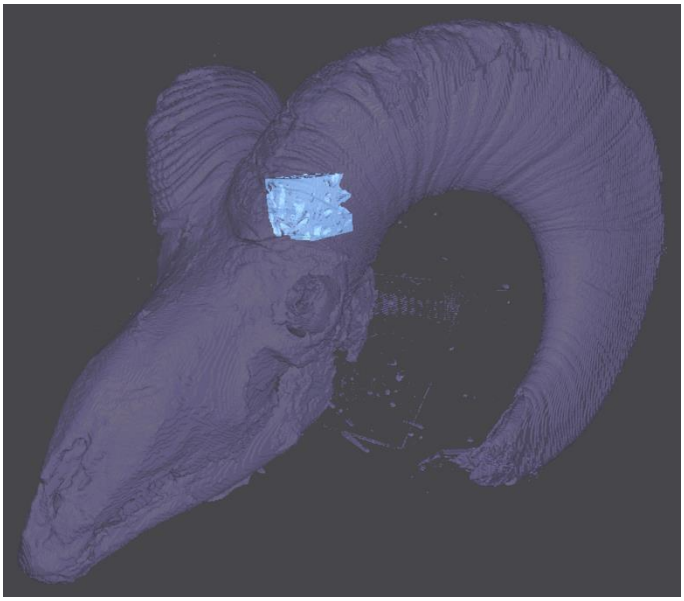

Figure 5-1. Isolated 45 mm representative volume element (RVE) cropped from the left horncore.

brush tool to fill in any gaps and remove any excess material from velar bone segmentations (Figure 5-2c, d). The isosurface of the repaired segmentation was computed and visually inspected for any processing artifacts prior to obtaining additional RVEs.

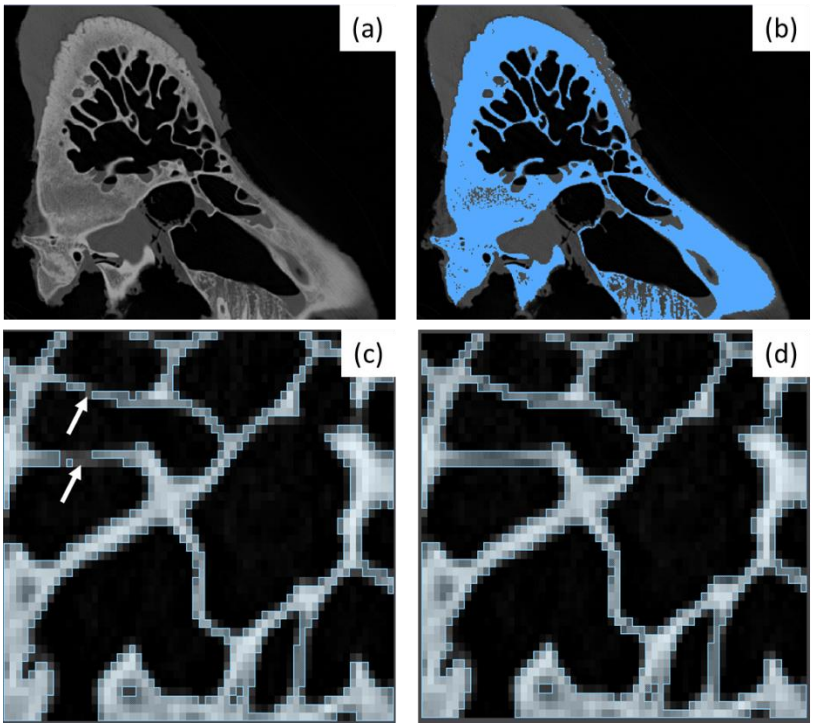

Figure 5-2. Thresholding and segmentation layer repair process. (a) Raw CT scan image. (b) Automatic thresholding adjusted so the included bone tissue (blue) closely matches the bone tissue visible in the raw images. (c) Regions of bone tissue missed by automatic thresholding (white arrows) (d) Repaired segmentation layer with pixel values added to regions missed by automatic thresholding.

Once it was determined that the initial layer segmentation accurately represented the velar bone architecture, four additional RVEs were cropped from the repaired segmentation. The cropping tool was used to crop the repaired segmentation layer in 5 mm increments such that all RVEs had a common center point. This negated the need for manual repair of each additional segmentation and resulted in five cubic RVEs with cube side lengths of 25, 30, 35, 40, and 45 mm (Figure 5-3). All cubes also shared the same local coordinate system which was oriented such that the x, y, and z axes were approximately aligned with the anteroposterior, proximodistal, and mediolateral anatomical axes,

respectively. Isosurfaces were computed for each RVE and exported as ASCII STL files. RVEs were then imported into Meshmixer (Autodesk, Inc., San Rafael, CA) for final preparation prior to volume meshing. The inspector function was used to identify and repair any errors in the STL mesh which primarily included non-manifold (zero-thickness) features. The automatic repair feature with default settings was generally sufficient to repair all features, but manual repair was performed when necessary. The transform function was also used to translate the center point of RVEs to the origin to simplify later processing. The 45 mm RVE was then used to create mirrored RVEs (MRVEs) to increase the size range included in the study.

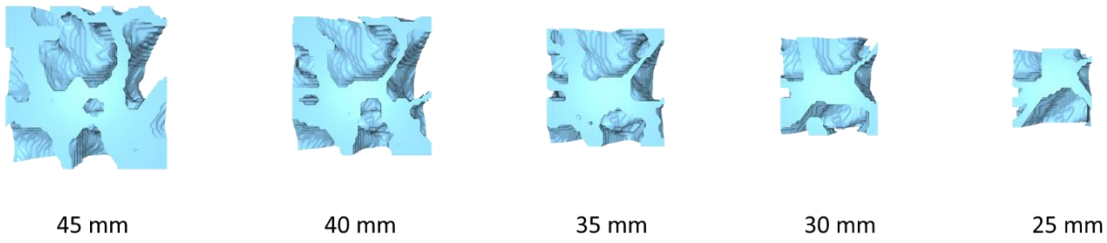

Figure 5-3. The original 45 mm cubic RVE and 40, 35, 30, and 25 mm RVEs cropped from the 45 mm geometry.

In Meshmixer, the 45 mm RVE was mirrored about each axis to produce a 90 mm cubic MRVE consisting of eight 45 mm RVEs (Figure 5-4). Mirroring was completed such that the corner coincident with the lateral, posterior, and proximal faces of the original 45 mm RVE became the center of the 90mm MRVE. In addition to the 90 mm MRVE, 60 and 75 mm MRVEs were cropped from the 90 mm MRVE using the plane cut tool. MRVEs were not created in 5 mm increments due to significantly increased computational cost of MRVEs. Similar to original RVEs, the inspector and transform tools were used to repair

STL meshes and translate cube centers to the origin. All RVEs and MRVEs were then exported from Meshmixer as ASCII STL files for finite element modeling.

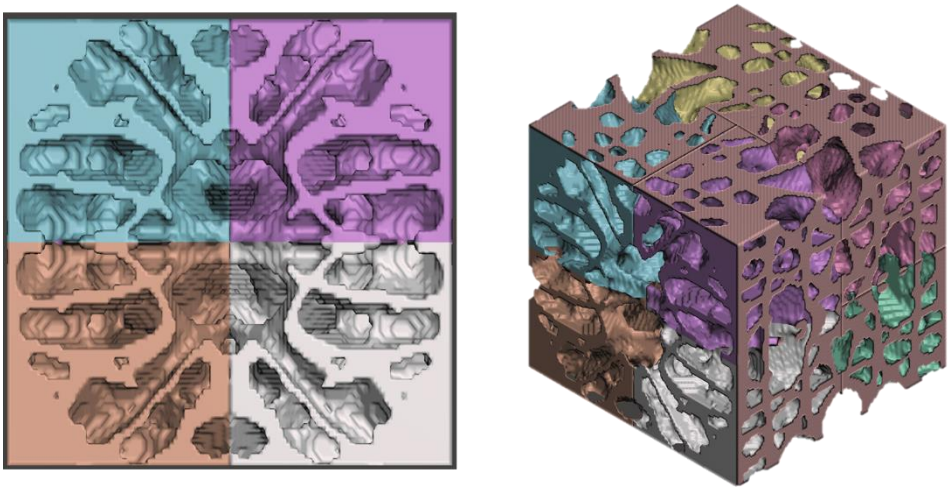

Figure 5-4. Mirrored representative volume element (MRVE) with eight 45 mm RVEs making up the 90 mm MRVE.

5.2.2.2. Trabecular Bone

CT scan data of trabecular bone architecture was obtained from the database available from previously published studies on the allometric scaling relationships of trabecular bone [3,10]. Trabecular bone from the femoral condyle of a domestic sheep was chosen for this study since the BV/TV of this trabecular architecture (0.342) was comparable to the BV/TV of the 45 mm RVE from velar bone (0.386). The file size of trabecular bone DICOM data was much larger than bighorn sheep CT scans and caused Seg3D to crash when importing raw data. Thus, two additional processing steps were necessary to obtain 3D models of trabecular bone architectures. First, ImageJ was used to isometrically scale DICOM data by 25% prior to segmentation in Seg3D. Then, the model was rescaled to its original size prior to meshing in Ansys. All other steps used in generation of trabecular bone RVEs were identical to those developed for velar bone models. The trabecular bone architecture developed from the original DICOM data will

henceforth be referred to as the physiological trabecular bone architecture (as opposed to dilated models, which will be discussed later).

5.2.3. Finite Element Modeling

Finite element modeling (FEM) was used to investigate how geometry and size of RVE/MRVEs influence velar bone mechanics in uniaxial compression. Additionally, FEM was used to compare the mechanical performance of velar bone and trabecular bone architectures.

5.2.3.1. Volume Meshing, Constraints, and Boundary Conditions

The following meshing procedure, rigid body constraints, and boundary conditions were applied to all subsequent finite element models to facilitate loading in the proximodistal direction. Volume meshes of RVE/MRVEs with linear tetrahedra elements were generated using the 'Robust (Octree)' meshing algorithm available in Ansys ICEM CFD 2020 R2 (Ansys, Inc., Canonsburg, PA). Volume elements in all models were assigned material properties with constant elastic modulus (E = 8.6 GPa) based on experimental results from Aim 2. Bone density (ρ = 1.725 g/cm^3) and poisson's ratio (ν = 0.28) were assigned values consistent with pervious computational modeling of velar bone tissue [6]. Trabecular bone models were assigned identical material properties in order to directly compare the architectures being considered. Input files were written by Ansys and imported as models into ABAQUS (Dassault Systemes SE, Velizy-Villacoublay, France). Once in ABAQUS, reference points were defined at the center of the proximal and distal surfaces of each RVE/MRVE (Figure 5-5). Rigid body constraints were defined between surface reference points and all nodes on the corresponding surface. For example, the

reference point at the center of the proximal surface was tied to all nodes on the proximal surface via a rigid body constraint (Figure 5-5). Rigid body constraints were used to simulate rigid load platens and facilitate the application of loads and boundary conditions. The proximal surface was fixed by applying an encastre boundary condition to the reference point on this surface. Additional loads and boundary conditions were applied to the distal surface reference point and were dependent on the specific analysis.

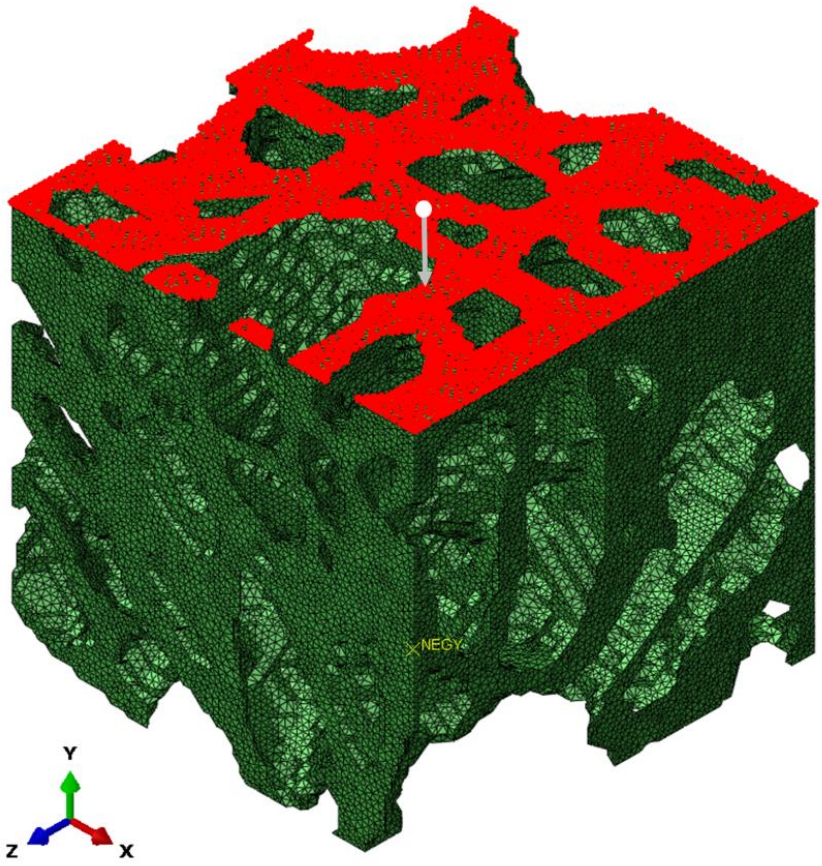

Figure 5-5. Nodes of distal surface (red points) were tied to the distal surface reference point (white point) with a rigid body boundary condition. Loads/displacement boundary conditions were applied to the distal surface reference point (white point) to impose compression in the proximodistal direction (grey arrow).

5.2.3.2. Uniaxial Compression Models

Explicit modeling in ABAQUS was used to simulate quasi-static, uniaxial compression of velar bone and trabecular architectures. Explicit analysis was used since implicit analysis of large MRVEs failed. Compression was applied by displacing the distal reference point (and therefore the entire rigid body surface) proximally by a distance (δ) corresponding to an apparent compressive strain of 4,150 microstrain based on Equation 5.1.

$$\delta = 0.00415 * (RVE\ Cube\ Side\ Length) \tag{5.1}$$

All other degrees of freedom were constrained during displacement (i.e., no off-axis translation and no rotation). The applied apparent strain corresponds to one half of the trabecular bone compressive yield strain [11] and is equal to values used in previous computational models of trabecular bone mechanics [5]. The displacement boundary condition was applied over 0.01 seconds using a dynamic, explicit analysis step with non-linear geometry and automatic incrementation. Model kinetic energy was compared to model strain energy to check assumptions of quasi-static loading since the displacement was applied using explicit analysis with a 0.01 second step time. In quasi-static analysis, the total kinetic energy should be negligible compared to total strain energy. Model outputs included the reaction force (RF) at the proximal reference point and total model strain energy (ALLSE). These outputs were used to calculate the apparent stress ($\sigma_{apparent}$, Equation 5.2) and total strain energy density (u, Equation 5.3) for each architecture. The apparent stress and total strain energy density were compared for all velar bone RVEs/MRVEs to investigate how velar bone mechanics are influenced by the length scale of the velar bone volume considered. Additionally, the total strain energy density of the 45

mm velar bone RVE was compared to the physiological trabecular bone architecture to compare the energy storage capacity of velar and trabecular bone architectures with similar BV/TVs.

$$\sigma_{apparent}\,[MPa] = \frac{RF}{(RVE\ Cube\ Side\ Length)^2} \tag{5.2}$$

$$u\left[\frac{mJ}{mm^3}\right] = \frac{ALLSE}{Bone\ Volume} \tag{5.3}$$

5.2.3.3. Buckling Models

Linear perturbation analysis was used to investigate the buckling behavior of velar and trabecular bone architectures. A concentrated compressive force was applied to the distal surface reference point as a perturbation load. The perturbation load was assigned unit magnitude (1 N) such that reported eigenvalues are equivalent to the critical buckling load (P_{cr}) associated with the corresponding buckling mode (eigenmode). The subspace eigensolver was used to determine the first 10 eigen modes for each model. The resulting buckling mode shapes were examined in the visualization module to determine if any of the first 10 eigenmodes displayed non-local buckling behavior. Models that demonstrated non-local buckling in at least one of the first 10 mode shapes were selected for further analysis involving manipulation of the BV/TV to investigate how buckling behavior was influenced by apparent density.

Seg3D was used to artificially inflate the BV/TV of models that displayed non-local buckling modes to explore relationships between porous bone architectures and buckling behavior. For any RVE/MRVE that demonstrated non-local buckling, the dilate tool was used to uniformly increase strut thickness of layer segmentations established

previously. Dilation was performed in three incremental steps to obtain three new dilated RVEs (DRVE), each having a unique architecture with increased strut thickness (Figure 5-6). Segmentation dilation provided a range of BV/TVs from 0.293 - 0.829 for velar bone and 0.348 - 0.793 for trabecular bone. Segmentations of the newly acquired DRVEs were then subject to the same processing steps from ASCII STL export to linear perturbation analysis in ABAQUS. The apparent critical buckling stress (Equation 5.4) of the first non-local buckling mode was calculated for all buckling models for comparison.

$$\sigma_{app,cr}[MPa] = \frac{P_{cr}}{(RVE\ Cube\ Side\ Length)^2} \tag{5.4}$$

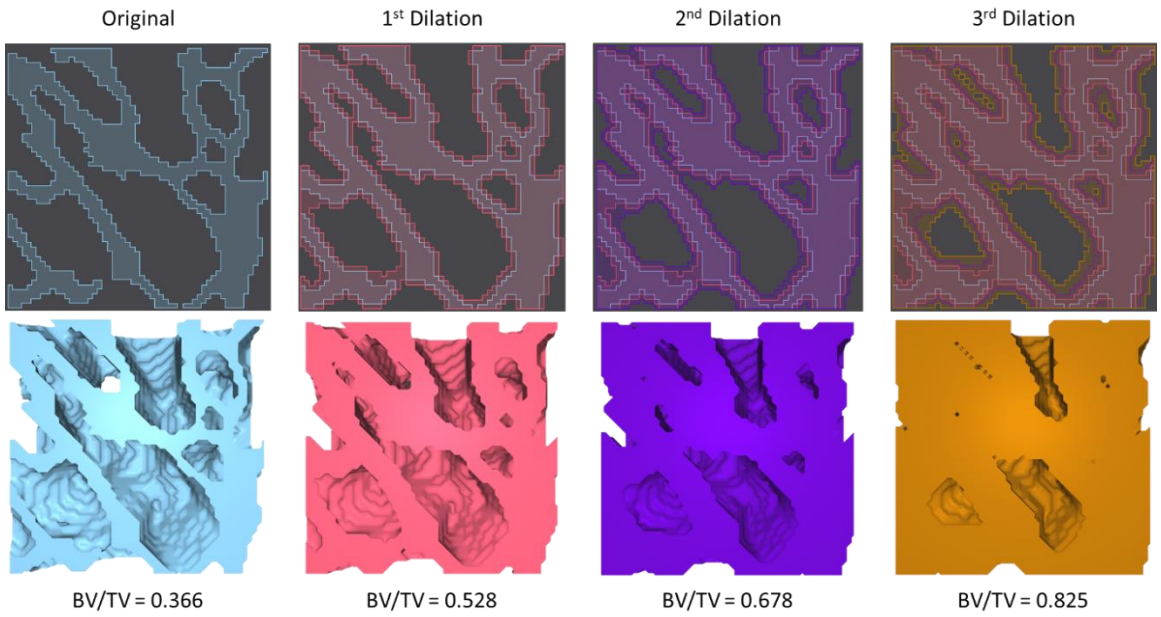

Figure 5-6. Dilation procedure to increase BV/TV of velar and trabecular bone models that demonstrate non-local buckling. 40 mm velar bone RVE shown. Top row shows layer segmentation with progressive dilation from left to right. Bottom row shows isosurfaces computed and exported from Seg3D.

Mesh Convergence

The original 45 mm velar bone RVE and the physiological trabecular bone model were used to perform mesh convergence studies prior to final simulations. The 45 mm RVE

was chosen for the velar bone mesh convergence study since this model was the origin of all other models. Seven unique velar bone volume meshes were created using the same meshing parameters previously described and varying the global mesh seed size from 0.5 - 1.0 in 0.1 increments. This produced models with mesh densities from ~14 to 112 elements/mm^3. Five unique trabecular bone volume meshes were created with global mesh seed sizes ranging from .07 - 0.2 which resulted in mesh densities from ~2900 – 41000 elements/mm^3. Uniaxial quasi-static compression was applied to each mesh in the proximodistal direction by displacing the distal surface reference point a distance (δ) corresponding to an apparent strain of 4,150 με. The reaction force was compared between models by calculating the error between the reaction force of each unique mesh (RF_i) and the densest mesh ($RF_{max,}$ Equation 5.5). Convergence was considered the point at which reaction force error was less than 3%.

$$Error\ [\%] = \frac{RF_i - RF_{max}}{RF_{max}} \times 100 \tag{5.5}$$

5.2.4. Model Architectural Indices

The architectural indices of the model geometries were quantified to investigate structure-property relationships of velar and trabecular bone. Segmentation layers were exported as DICOM data from Seg3D and imported into ImageJ. Segmentations of the MRVEs did not exist since these models were created with mirroring operations in MeshMixer. Therefore, 3D models of MRVEs were imported into 3D Slicer (https://www.slicer.org/), converted into segmentations, then exported as DICOM data and imported into ImageJ. The 'Make Binary' function was used to convert image sequences to binary format using the default settings. Then, the BoneJ plug-in was used to measure

the bone volume fraction (BV/TV), strut thickness (V.Th or Tb.Th), and strut separation (V.Sp or Tb.Sp) of velar and trabecular bone architectures. In addition to the standard architectural indices, a slenderness ratio (SR) was calculated for each architecture using the strut thickness and strut separation (Equation 5.6). While this is not a true slenderness ratio as defined for engineered plate and truss lattices, it is representative of the relative difference between the thickness and free span of individual struts.

$$SR = \frac{V.Sp}{V.Th} \; or \; \frac{Tb.Sp}{Tb.Th} \tag{5.6}$$

5.3. Results

5.3.1. Mesh Convergence

Velar bone models converged at a mesh density of ~41 elements/mm^3 with a global seed size of 0.7. At this mesh density the reaction force error was 2% compared to the model with a mesh density of ~112 elements/mm^3 (Figure 5-7a). The trabecular bone model converged at a mesh density of ~22900 elements/mm^3 with a global seed size of 0.085. At this mesh density the reaction force error was 2.7% compared to the model with a mesh density of ~41000 elements/mm^3 (Figure 5-7b).

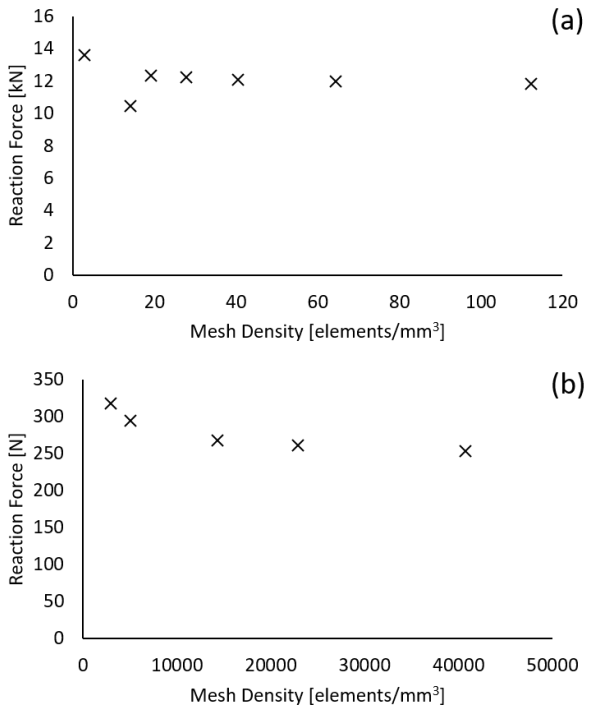

Figure 5-7. Results from the mesh convergence study for (a) velar bone and (b) trabecular bone.

5.3.2. Size Effects

The apparent stress (Figure 5-8a) and strain energy density (Figure 5-8b) both increased with increasing RVE size. However, it appears that both variables are beginning to converge in the larger, mirrored velar bone models developed in this work.

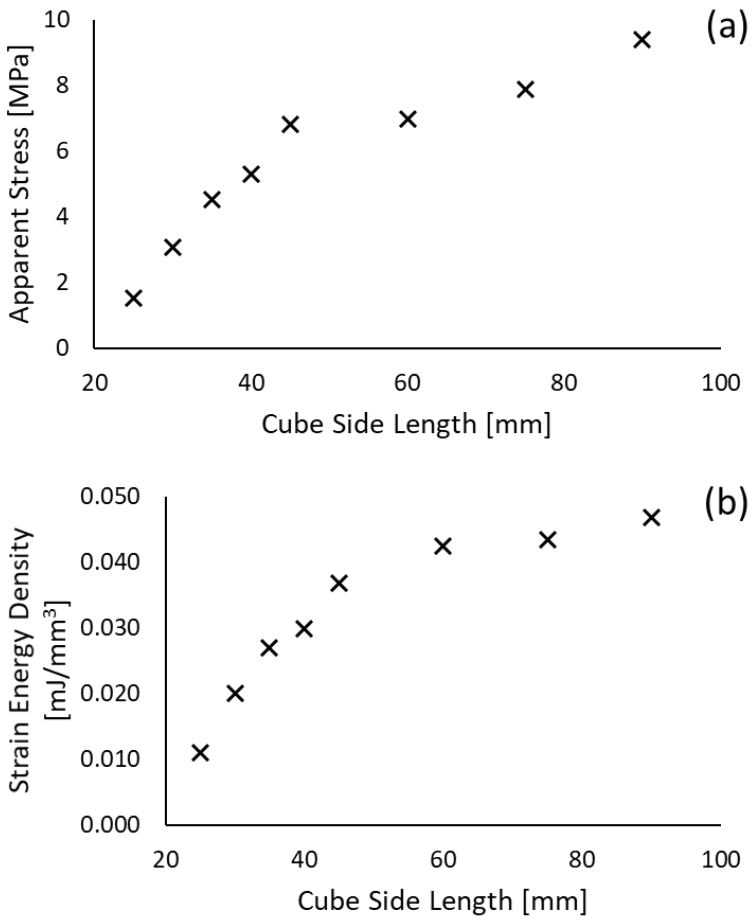

Figure 5-8. Influence of the RVE size on (a) apparent stress and (b) strain energy density. Both variables increase with increasing cube side length. Some evidence of convergence is demonstrated by larger MRVEs.

5.3.3. Strain Energy Density

The stress-strain behavior and total strain energy density of velar and trabecular bone architectures under compressive loading were very similar (Figure 5-9). However, the 45 mm velar bone RVE demonstrated slightly greater compressive stiffness than the physiological trabecular bone architecture (Figure 5-9a). Conversely, the physiological trabecular bone architecture displayed slightly greater strain energy density than the 45 mm

velar bone RVE under compressive loading, particularly at strains beyond ~3,500 με (Figure 5-9b).

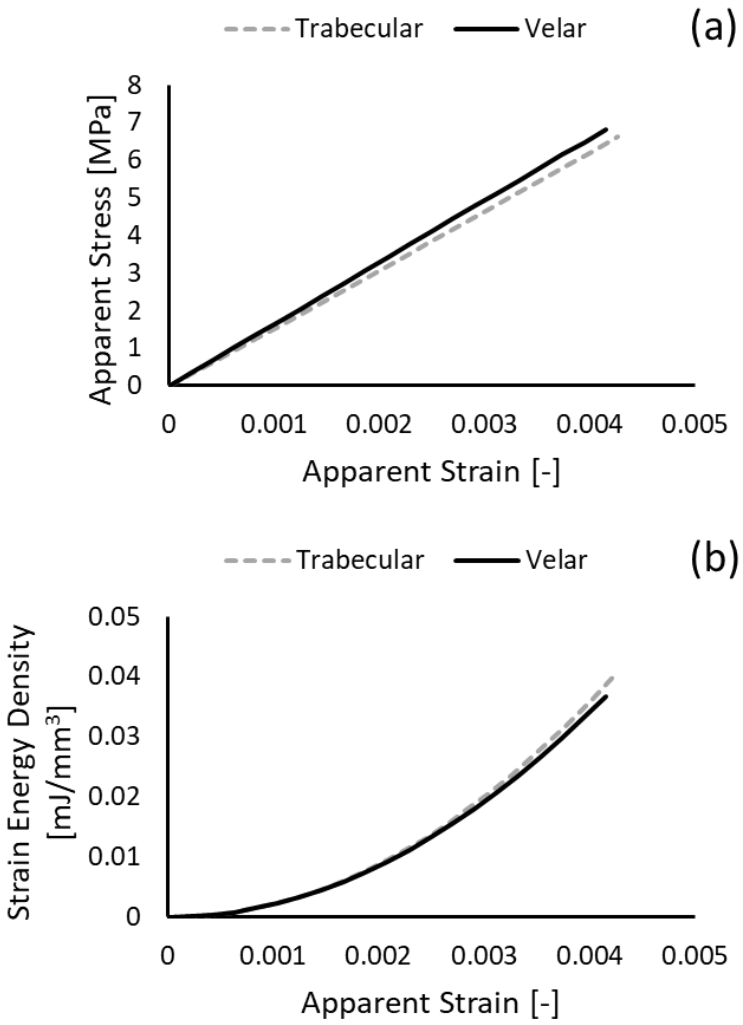

Figure 5-9. (a) Stress-strain behavior of the porous bone architectures demonstrated that the 45 mm velar bone RVE was slightly stiffer than the original trabecular bone architecture under compressive loading. (b) The original trabecular bone architecture stored greater total strain energy density than the 45 mm velar bone RVE under the applied apparent compressive strain.

5.3.4. Buckling

Early buckling modes typically demonstrated localized buckling of individual velar struts (Figure 5-10). However, RVEs of 40 mm and less demonstrated non-local buckling at higher buckling modes characterized by deformations distributed over a larger portion

of the model (Figure 5-10). Similar non-local buckling was observed in the physiological trabecular bone model as well. Velar bone models that displayed non-local buckling (25, 30, 35, and 40 mm RVEs) and the physiological trabecular bone model were dilated to investigate the influence of apparent density on buckling mechanics. The apparent critical buckling stress increased with increasing apparent density (higher BV/TV) and decreased with increasing slenderness ratio as expected (Figure 5-11). Interestingly, the trabecular bone models had higher apparent critical buckling stresses than velar bone models indicating a greater resistance to buckling.

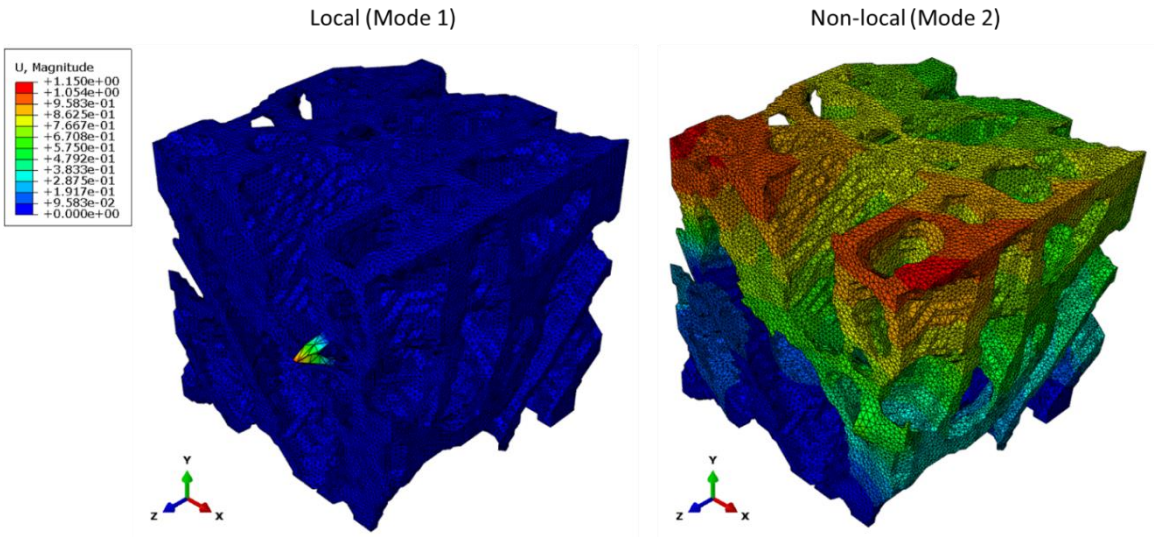

Figure 5-10. Local (left) and non-local (right) buckling modes demonstrated by 40 mm velar bone RVE. Colored gradient illustrating deformation magnitudes which have been visually scaled up by a factor of 4x.

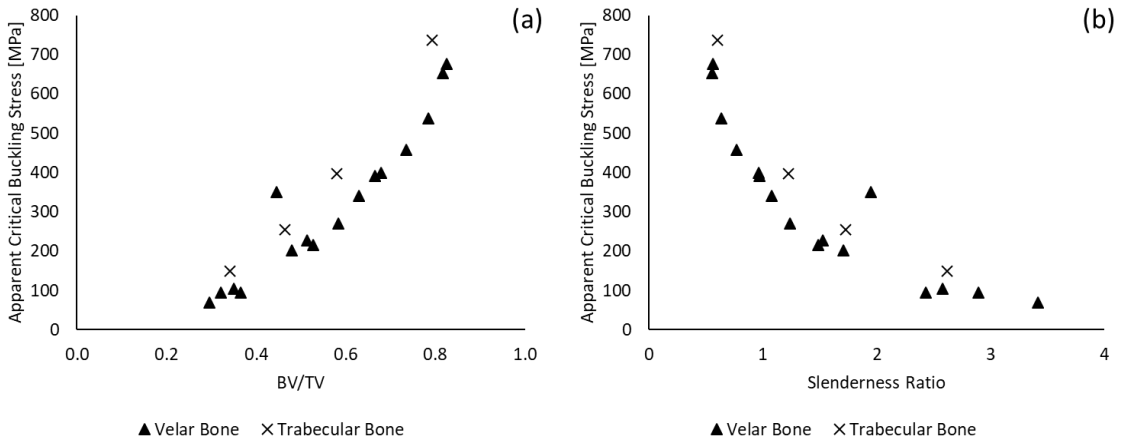

Figure 5-11. (a) Apparent critical buckling stress increased with increasing bone volume fraction (BV/TV) for velar and trabecular bone architectures. (b) Apparent critical buckling stress decreased with increasing slenderness ratio for velar and trabecular bone architectures.

5.4. Discussion

This work utilized computational modeling to explore the mechanics of velar bone at various length scales and compared the energy storage capacity (i.e., strain energy density) and buckling resistance of velar bone and trabecular bone architectures. The goal of this exploratory study was to provide an improved understanding of how the unique architecture of velar bone contributes to energy absorption during ramming. Furthermore, it was of interest to determine if velar bone offers any mechanical advantage compared to an equally lightweight trabecular architecture. It was hypothesized that velar bone would have increased strain energy density and greater resistance to buckling than trabecular bone due to its role in energy absorption during ramming. Velar bone displayed substantial size effects at the length scales considered and should not be treated as a material continuum since the minimum continuum dimension of velar bone exceeds the dimensions of the entire horncore. Surprisingly, velar bone displayed less strain energy density and was less resistant to buckling than trabecular bone which does not support the hypothesis that the

velar bone architecture is beneficial for energy absorption. Ultimately, this finding may reflect differences in physiological bending of the cantilever-like horncore versus the compressed femoral condyle and can be used to guide future studies on velar bone mechanics.

There are several limitations involved in this study, the first being the limited sample size. Here, only one bighorn sheep ram was included in the study making it difficult to make general predictions or conclusions regarding velar bone mechanics. However, this ram was chosen since it was the biggest skull with CT scan data available and provided the largest possible un-mirrored RVE to be obtained. This was important for this study in order to investigate size effects related to this architecture in an attempt to establish a continuum length scale similar to what's previously been done for trabecular bone. Other limitations of this work are the artifacts that arise from selectively cropping specific regions of porous bone architectures including artificially thin and unconstrained struts at the boundary of the cropped region. These artifacts combined with the boundary conditions used in this work are not representative of the physiological boundary conditions that velar bone and trabecular bone are subjected to in vivo. This likely contributed to the localized buckling observed in the early buckling modes of most models. Periodic boundary conditions applied to the unloaded surfaces (anterior, posterior, medial, and lateral surfaces) would have provided a closer approximation of in vivo loading, but at a significantly increased computational cost. While periodic boundary conditions may be a worthwhile addition to these models in the future, results from this work still provide valuable insight into several aspects of velar bone mechanics, and an initial comparison between velar and trabecular bone architectures.

Results from this study indicate that velar bone architectures do not fit the minimum continuum length scale criteria established for typical trabecular bone. For a continuum material, the minimum dimension of the sample must be much greater than the dimensions of its structural sub-units. In the case of porous bone architectures, the individual struts would be the structural sub-units forming the volume under consideration as a potential continuum. Previous studies have demonstrated that the minimum continuum length scale of trabecular bone is approximately five trabecular spacings or 5 – 10 mm depending on the specific sample [12,13]. If the same were true for velar bone, the minimum continuum length would be approximately 60 mm (based on a velar separation of ~12 mm). Representative volume elements this large could not be directly cropped from the horncore due to size constraints. However, mirrored RVEs were generated in order to approximate larger velar bone architectures. Although these structures are not necessarily physiologically accurate, previous studies have used similar methods to determine the effective properties of cancellous bone structures [14]. If velar bone continuum dimensions were achieved then equivalent apparent stresses would be expected to arise from the constant apparent strain applied to models in this work since continuum properties are invariable above the minimum length scale. Here, the apparent stress continued to increase as the size of cubic volumes increased indicating that continuum dimensions had not been achieved despite evidence that the apparent stress is beginning to converge in the largest mirrored models (Figure 5-8). This finding suggests that the structural organization of the velar bone architecture within the horncore likely has a large influence on the velar bone mechanical performance during ramming. With that said, the velar bone architecture does

not appear to increase horncore energy absorption compared to trabecular bone architectures based on the initial comparisons made here.

Compressive loading of velar bone and trabecular bone architectures indicate that trabecular bone offers increased strain energy density and greater resistance to buckling compared to velar bone architectures of similar BV/TV. Although the compressive stress-strain behavior of velar and trabecular bone architectures was similar, trabecular bone demonstrated greater strain energy density for the same applied apparent strain (Figure 5-9). This finding suggests that the trabecular bone architecture more efficiently stores elastic energy under compressive loading. Results from the linear perturbation analysis showed that trabecular bone architectures are also more resistant to buckling compared to velar bone architectures with similar bone volume fractions (Figure 5-11). Furthermore, the critical apparent buckling stress increased with increasing BV/TV (Figure 5-11a) and decreased with increasing slenderness ratio (Figure 5-11b) in both velar and trabecular bone architectures. This is not surprising since increased BV/TV and lower slenderness ratios are the result of thicker individual struts which are less likely to buckle under a compressive load. These relationships follow quadratic behavior which has also been demonstrated in previous buckling simulations of engineered plate-lattices [15]. It should be noted that the apparent stresses reported in the models with artificially inflated apparent density (dilated models) are not physiological relevant. The purpose of these models was to investigate how the buckling performance of porous bone architectures were influence by structural indices. Furthermore, it was impossible to artificially decrease apparent densities with the methodology presented as this led to fully eroded struts and loss of geometry connectivity. It was surprising that trabecular bone architectures had increased

strain energy density and greater resistance to buckling than velar bone architectures considering the importance of horncore energy absorption during ramming. This may reflect adaptation to the different physiological loading modes of the cantilever-like horncore and load bearing femoral condyle from which these architectures were obtained. During ramming, the horn and horncore are subjected to cantilever bending as a result of the impact. Thus, based on our current understanding of functional adaptation it would make sense that the velar bone architecture is better suited to resist bending than to support compressive loading. Conversely, it makes sense that trabecular bone from the femoral condyle provides efficient energy storage under uniaxial compression and is resistant to buckling since it is subjected to compressive loading during weight bearing. Previous studies have been interested in the compressive properties of velar bone and demonstrated velar bone inspired architectures provide increased performance under compressive loading. However, findings from this study suggest that studying the performance of this unique architecture as an energy absorbing cantilever spring may be more insightful moving forward.

This work has demonstrated that velar bone has a larger minimum continuum length scale than trabecular bone (relative to strut spacing) and that this length scale may not be achieved within the horncore. Accordingly, the structural organization of the velar bone architecture likely plays a key role in determining the behavior of the entire horncore during ramming as suggested previously [6]. Furthermore, velar bone architectures do not appear to offer any mechanical advantage over trabecular bone under compressive loading as trabecular bone demonstrates increased strain energy density and greater buckling resistance compared to velar bone architectures with similar bone volume fractions. This

may be a consequence of functional adaptations to the different loading modes since horncore velar bone is loaded in cantilever bending while trabecular bone in the femoral condyle is primarily subjected to compressive forces. This finding may guide the development of novel velar bone inspired energy absorbers that are designed to be loaded in bending in contrast to the compressive structures developed previously.

5.5. References

[1] A.M. Parfitt, M.K. Drezner, F.H. Glorieux, J.A. Kanis, H. Malluche, P.J. Meunier, S.M. Ott, R.R. Recker, Bone histomorphometry: Standardization of nomenclature, symbols, and units: Report of the asbmr histomorphometry nomenclature committee, Journal of Bone and Mineral Research. 2 (1987) 595–610.

[2] A. Odgaard, Three-dimensional methods for quantification of cancellous bone architecture, Bone. 20 (1997) 315–328. https://doi.org/10.1016/S8756-3282(97)00007-0.

[3] M. Doube, M.M. Kłosowski, A.M. Wiktorowicz-Conroy, J.R. Hutchinson, S.J. Shefelbine, Trabecular bone scales allometrically in mammals and birds, Proceedings of the Royal Society B: Biological Sciences. 278 (2011) 3067–3073. https://doi.org/10.1098/rspb.2011.0069.

[4] M.M. Barak, D.E. Lieberman, J.J. Hublin, Of mice, rats and men: Trabecular bone architecture in mammals scales to body mass with negative allometry, J Struct Biol. 183 (2013) 123–131. https://doi.org/10.1016/j.jsb.2013.04.009.

[5] T.G. Aguirre, A. Ingrole, L. Fuller, T.W. Seek, A.R. Fiorillo, J.J.W. Sertich, S.W. Donahue, Differing trabecular bone architecture in dinosaurs and mammals contribute to stiffness and limits on bone strain, PLoS One. 15 (2020) 1–20. https://doi.org/10.1371/journal.pone.0237042.

[6] A. Drake, T.L. Haut Donahue, M. Stansloski, K. Fox, B.B. Wheatley, S.W. Donahue, Horn and horn core trabecular bone of bighorn sheep rams absorbs impact energy and reduces brain cavity accelerations during high impact ramming of the skull, Acta Biomater. 44 (2016) 41–50. https://doi.org/10.1016/j.actbio.2016.08.019.

[7] T.G. Aguirre, L. Fuller, A. Ingrole, T.W. Seek, B.B. Wheatley, B.D. Steineman, T.L.H. Donahue, S.W. Donahue, Bioinspired material architectures from bighorn sheep horncore velar bone for impact loading applications, Sci Rep. 10 (2020) 1–14. https://doi.org/10.1038/s41598-020-76021-5.

[8] T.W. Seek, Exploration of Unique Porous Bone Materials for Candidacy in Bioinspired Material Design, Masters Thesis, Colorado State University, 2018.

[9] V. Geist, Validity of Horn Segment Counts in Aging Bighorn Sheep, J Wildl Manage. 30 (1966) 634–635.

[10] M. Doube, M.M. Kłosowski, J. Hutchinson, S.J. Shefelbine, X-ray microtomography images of trabecular bone from the femoral head and condyle of 18 avian, 72 mammalian and one crocodilian species., (2018). https://doi.org/10.6084/m9.figshare.7257179.v1.

[11] H.H. Bayraktar, E.F. Morgan, G.L. Niebur, G.E. Morris, E.K. Wong, T.M. Keaveny, Comparison of the elastic and yield properties of human femoral trabecular and cortical bone tissue, J Biomech. 37 (2004) 27–35. https://doi.org/10.1016/S0021-9290(03)00257-4.

[12] T.D. Brown, A.B. Ferguson, Mechanical property distributions in the cancellous bone of the human proximal femur, Acta Orthop. 51 (1980) 429–437. https://doi.org/10.3109/17453678008990819.

[13] R.B. Martin, D.B. Burr, N.A. Sharkey, D.P. Fyhrie, Material Properties of Cancellous Bone, in: Skeletal Tissue Mechanics, Second Edition, Springer New York, New York, NY, 2015. https://doi.org/10.1007/978-1-4939-3002-9.

[14] D.H. Pahr, P.K. Zysset, Influence of boundary conditions on computed apparent elastic properties of cancellous bone, Biomech Model Mechanobiol. 7 (2008) 463–476. https://doi.org/10.1007/s10237-007-0109-7.

[15] F. Derveni, A.J. Gross, K.D. Peterman, S. Gerasimidis, Postbuckling behavior and imperfection sensitivity of elastic–plastic periodic plate-lattice materials, Extreme Mech Lett. 50 (2022) 101510. https://doi.org/10.1016/j.eml.2021.101510.

CHAPTER 6

6. CONCLUSIONS AND FUTURE DIRECTIONS

6.1. Summary

Bighorn sheep rams experience violent head impacts during intraspecific combat without overt signs of brain injury. Computational modeling has demonstrated that horncore bone – especially the porous velar bone – plays a critical role in energy absorption and reduction of brain cavity accelerations during ramming, which likely aids in injury mitigation. Since bone has previously demonstrated short term phenotypic plasticity [1–6], and long-term evolutionary adaptation in response to mechanical loading [7–9], horncore bone was expected to be tougher than other mammalian bone tissues. However, horncore cortical bone (Chapter 2) and velar bone (Chapter 3) mechanical properties fall within the range of other mammalian cortical and trabecular bone tissues and are not likely to benefit energy absorption at the tissue level. This suggests the energy absorption capabilities of the porous horncore are due to the structural arrangement of velae at the whole horn level as opposed to the material level. With that said, unlike trabeculae, velae have osteons (Chapter 3) which likely provide toughening mechanisms (e.g. crack arrest and deflection) that absorb energy and prevent strut failure during ramming. Another advantage of osteonal remodeling is the repair of microdamage. Since horn tissue is incapable of repair, it is advantageous for large amounts of energy to be absorbed by the horncore, since even if the energy is large enough to damage the velar bone tissue, it can be self-repaired. Ultimately, the unique combination of a trabecular-like foam composed of osteon filled sails may increase the energy absorption capacity of the entire velar bone structure compared to a

similar volume of trabecular bone by allowing microdamage to accumulate and be repaired after the mating season. In addition to the tissue level properties of velar bone, the unique velar bone architecture was expected to benefit elastic energy absorption compared to more typical trabecular bone. However, computational models of small cubes of trabecular bone demonstrated increased strain energy density and greater resistance to buckling than velar bone cubes when loaded in compression (Chapter 5). With that said, velar bone mechanics displayed substantial size effects at length scales relevant to the horncore and should not be considered a continuum material. Therefore, functional adaptation may have organized velar bone architecture within the entire horncore to meet the functional demands of physiological loading (i.e., cantilever bending) more efficiently than typical trabecular bone.

The horn-horncore interface must provide efficient load transfer between the impacted horn and internal horncore to facilitate horncore energy absorption. In equine hooves, load transfer between the hoof wall and appendicular skeleton occurs through the laminar junction [10–13]. The highly interdigitated microstructure of the laminar junction is believed to increase contact area to reduce stress magnitudes and promote uniform energy transfer between the hoof and distal phalanx bone [14–16]. In bird beaks, another dermo-epidermal junction transfers load from the beak to the mandibular bones via attachment of Sharpey's fibers originating in the dermis and penetrating the adjacent cortical bone tissue [17,18]. The bighorn sheep horn-horncore interfacial tissue is a thin (~0.5 – 1.0 mm thick) unorganized network of collagen and keratin fibers that utilizes a mix of the attachment mechanisms found in equine hooves and bird beaks to anchor the horn to the horncore (Chapter 4). On the bone side of the interface, collagenous Sharpey's

fibers extend from the interfacial tissue and penetrate the cortical bone. On the horn side of the interface, interfacial collagen fibers are intertwined with keratinized interdigitations and microscopic pores that provide nearly a 4-fold increase in contact area between the horn and interface. These attachment mechanisms resulted in the horn-horncore interface having shear moduli comparable to the equine laminar junction [14]. Furthermore, lap-shear samples primarily failed on the horn side of the interface suggesting the Sharpey's fibers are the stronger attachment mechanism. This likely explains why lap-shear properties were strongly correlated to the contact area of interdigitations and surface porosity measured on the horn side of the interface.

6.2. Key Findings

- Bighorn sheep horncore cortical and velar bone tissue do not have exceptional material toughness compared to other mammalian bone tissues.
- Horncore velar bone has a unique bony architecture consisting of a trabecular-like foam with sails that are an order of magnitude thicker than trabecular struts and contain osteons
- Horncore velar bone mechanics demonstrate substantial size effects and should not be treated as a continuum material at length scales relevant to the entire horncore
- Velar bone cubes containing a lattice of several sails have lower strain energy density and less resistance to buckling than trabecular bone cubes in idealized uniaxial compression simulations
- The horn-horncore interface has shear moduli comparable to the equine laminar junction

- The horn-horncore interfacial tissue is more strongly attached to the bone side of the interface due to Sharpey's fibers penetrating cortical bone (evidenced by lap-shear failure occurring primarily on the horn side of the interface)
- The horn side of the interface has keratinized interdigitations and pores that increases the contact area with interfacial collagen fibers and this contact area is positively correlated with lap-shear properties

6.3. Future Research Directions

6.3.1. Strain rate sensitivity of horncore bone tissue

Bone tissue is known to display viscoelastic properties including strain rate sensitivity [19]. In this dissertation, horncore cortical and velar bone mechanical properties were quantified at quasi-static strain rates for comparison to a range of mammalian bone tissues previously tested with similar methodology. Dynamic mechanical analysis in this work provided some indication that velar bone tissue has similar strain rate sensitivity to other mammalian cortical bone. However, it would be interesting to investigate the strain rate sensitivity of both horncore cortical and velar bone across a wider range of strain rates. It would be especially beneficial to quantify mechanical properties of horncore bone at the strain rate estimated to occur in-vivo during ramming (~6 ε/s) using a dropkinson bar or a similar intermediate rate testing system. The properties (i.e., elastic modulus) of horncore bone at in vivo strain rates could be implemented into computational models of bighorn sheep ramming to improve the accuracy of model outputs.

6.3.2. Horncore microdamage and bone remodeling activity

Targeted bone remodeling allows bone tissue to repair microdamage accumulation which makes microcrack toughening (i.e., crack arrest and deflection) particularly effective in osteonal bone tissue [20–22]. With that said, excessive microdamage accumulation can weaken bone and lead to stress fractures and eventual catastrophic failure [23]. In Chapter 2, horncore cortical bone demonstrated relatively high porosity compared to other mammalian cortical bone (typically < 15% [24–28]). Increased horncore cortical porosity may be a result of increased bone resorption related to targeted remodeling activated by microdamage accumulation that occurs during ramming. Furthermore, in Chapter 3, secondary osteons present in velae are indicative of internal bone remodeling that rarely occurs in thinner trabeculae. Velar osteons are expected to provide crack arrest and deflection similar to the toughening mechanisms present in cortical bone tissue. However, the extent to which microdamage accumulation contributes to energy dissipation during ramming remains unclear. It would be interesting to compare the bone properties of horncore cortical and velar bone from samples obtained immediately before and after the rut. Furthermore, common histological techniques could be used to quantify microdamage accumulation [29] and remodeling activity (i.e., resorption vs. refilling activity [30]) in horncore bone tissue. If microdamage accumulation provides a substantial amount of energy dissipation during ramming, then samples collected immediately following the rut would be expected to have higher microcrack density and reduced mechanical properties compared to samples collected before the rut. Conversely, if bone properties are similar before and after rut, that would suggest that the velar bone architecture limits local bone strains to prevent excessive damage accumulation even during impact loading.

6.3.3. Horn-horncore interface attachment

Several attachment mechanisms exist in dermo-epidermal junctions including Sharpey's fibers in bird beaks [17], and the interdigitation of dermal and epidermal lamellae in the equine laminar junction [10,11,13]. In the bighorn sheep horn-horncore interface, Sharpey's fibers anchor the soft-tissue interface to the bone while keratinized interdigitations and surface porosity increase the microscopic contact area between the horn and soft-tissue interface (Chapter 4). The horn side of the interface appears to be the weak link of this interface since this was generally where failure occurred in lap-shear specimens. Thus, it makes sense that the microscopic contact area of the inner horn surface was correlated with lap-shear mechanical properties. With that said, it remains unclear how the soft-tissue interface attaches to the horn. Despite the presence of collagen fibers in and around the horn interdigitations and pores, there was no evidence of collagen fibers penetrating the keratinized tissue like Sharpey's fibers do in bone. Future studies investigating this attachment would benefit from a higher magnification and 3D analysis of the structure. One way to achieve this would be to obtain serial sections using similar microscopy techniques to the ones utilized in this work. This would provide an improved understanding of the 3D morphology of this interface.

6.3.4. Computational modeling

Previous computational models of bighorn sheep ramming were limited by the assumptions of the material properties [31]. Specifically, the horncore bone was assumed to be similar to primate cranial bone and the horn-horncore interface was modeled as a rigid attachment since material properties of horncore bone and the horn-horncore interface were previously unknown. Mechanical properties of horncore bone and the horn-horncore

interface have now been quantified (Chapters 2-4) and can be used to improve existing finite element models of bighorn sheep ramming. Since the elastic modulus had previously been defined for the horncore bone in these models, this value can readily be adjusted to reflect results from this work. Furthermore, the range of values reported here could be used to perform a parametric study to investigate the influence of bone stiffness on energy absorption and brain cavity accelerations during ramming. Parametric studies that alter bone stiffness would be particularly insightful since bone is strain-rate sensitive, and the elastic moduli values measured in this work (Chapters 2 and 3) likely underestimate the elastic modulus of horncore bone at in vivo ramming strain rates (~6 ε/s).

In addition to the improvements in previous models of bighorn sheep ramming, it would also be beneficial to continue exploring how the velar architecture behaves at length scales relevant to the entire horncore. Chapter 5 demonstrated that the velar architecture displays significant size effects and likely does not behave as a continuum material within the limited volume of the horncore. Furthermore, velar bone had lower strain energy density and was less resistant to buckling than trabecular bone in models of small cubes loaded in uniaxial compression. However, it is likely that the organization of the entire velar architecture within the horncore is functionally adapted to the cantilever-like bending experienced during ramming. Future studies should compare the bending performance of velar and trabecular bone architectures at various length scales to determine if the velar bone architecture provides more efficient energy storage when loaded in bending.

6.4. References

[1] H.K. Uhthoff, Z.F.G. Jaworski, Bone loss in response to long-term immobilisation, J Bone Joint Surg. 60-B (1978) 420–429.

[2] Ph. Collet, D. Uebelhart, L. Vico, L. Moro, D. Hartmann, M. Roth, C. Alexandre, Effects of 1- and 6-Month Spaceflight on Bone Mass and Biochemistry in Two Humans, Bone. 20 (1997) 547–551.

[3] S.L. Bass, L. Saxon, R.M. Daly, C.H. Turner, A.G. Robling, E. Seeman, S. Stuckey, The effect of mechanical loading on the size and shape of bone in pre-, peri-, and postpubertal girls: A study in tennis players, Journal of Bone and Mineral Research. 17 (2002) 2274–2280. https://doi.org/10.1359/jbmr.2002.17.12.2274.

[4] E.J. Bassey, S.J. Ramsdale, Increase in femoral bone density in young women following high-impact exercise, Osteoporosis International. 4 (1994) 72–75.

[5] A.E. Goodship, L.E. Lanyon, H. McFie, Functional adaptation of bone to increased stress: An experimental study, Journal of Bone and Joint Surgery. 61 (1979) 539–546.

[6] J. Sanchis-Moysi, C. Dorado, G. Vicente-Rodríguez, L. Milutinovic, G.L. Garces, J.A.L. Calbet, Inter-arm asymmetry in bone mineral content and bone area in postmenopausal recreational tennis players, Maturitas. 48 (2004) 289–298. https://doi.org/10.1016/j.maturitas.2004.03.008.

[7] J.D. Currey, The many adaptations of bone, J Biomech. 36 (2003) 1487–1495. https://doi.org/10.1016/S0021-9290(03)00124-6.

[8] J.D. Currey, Mechanical properties of bone tissues with greatly differing functions, J Biomech. 12 (1979) 313–319. https://doi.org/10.1016/0021-9290(79)90073-3.

[9] J.D. Currey, The Evolution of the Mechanical Properties of Amniote Bone, J Biomech. 20 (1987) 1035–1044.

[10] B. Faramarzi, Morphological and biomechanical properties of equine laminar junction, J Equine Vet Sci. 34 (2014) 589–592. https://doi.org/10.1016/j.jevs.2013.12.007.

[11] C.C. Pollitt, Clinical anatomy and physiology of the normal equine foot, Equine Vet Educ. 4 (1992) 219–224.

[12] C.C. Pollitt, The anatomy and physiology of the hoof wall., Equine Vet Educ. 10 (1998) 318–325.

[13] C.C. Pollitt, S.N. Collins, The suspensory apparatus of the distal phalanx in normal horses, Equine Vet J. 48 (2016) 496–501. https://doi.org/10.1111/evj.12459.

[14] J.E. Douglas, T.L. Biddick, J.J. Thomason, J.C. Jofriet, Stress/strain behaviour of the equine laminar junction, Journal of Experimental Biology. 201 (1998) 2287–2297.

[15] J.J. Thomason, H.L. McClinchey, B. Faramarzi, J.C. Jofriet, Mechanical behavior and quantitative morphology of the equine laminar junction, Anatomical Record -

Part A Discoveries in Molecular, Cellular, and Evolutionary Biology. 283 (2005) 366–379. https://doi.org/10.1002/ar.a.20173.

[16] P. Kochová, K. Witter, R. Cimrman, J. Mezerová, Z. Tonar, A preliminary study into the correlation of stiffness of the laminar junction of the equine hoof with the length density of its secondary lamellae, Equine Vet J. 45 (2013) 170–175. https://doi.org/10.1111/j.2042-3306.2012.00632.x.

[17] A. Genbrugge, D. Adriaens, B. De Kegel, L. Brabant, L. Van Hoorebeke, J. Podos, J. Dirckx, P. Aerts, A. Herrel, Structural tissue organization in the beak of Java and Darwin's finches, J Anat. 221 (2012) 383–393. https://doi.org/10.1111/j.1469-7580.2012.01561.x.

[18] C. van Hemert, C.M. Handel, J.E. Blake, R.M. Swor, T.M. O'Hara, Microanatomy of passerine hard-cornified tissues: Beak and claw structure of the black-capped chickadee (Poecile atricapillus), J Morphol. 273 (2012) 226–240. https://doi.org/10.1002/jmor.11023.

[19] J.H. McElhaney, Dynamic response of bone and muscle tissue., J Appl Physiol. 21 (1966) 1231–1236. https://doi.org/10.1152/jappl.1966.21.4.1231.

[20] D. Vashishth, K.E. Tanner, W. Bonfield, Experimental validation of a microcracking-based toughening mechanism for cortical bone, J Biomech. 36 (2003) 121–124. https://doi.org/10.1016/S0021-9290(02)00319-6.

[21] F.J.O. Brien, D. Taylor, T.C. Lee, The effect of bone microstructure on the initiation and growth of microcracks, Journal of Orthopaedic Research. 23 (2005).

[22] D. Vashishth, J.C. Behiri, W. Bonfield, Crack growth resistance in cortical bone: Concept of microcrack toughening, J Biomech. 30 (1997) 763–769. https://doi.org/10.1016/S0021-9290(97)00029-8.

[23] Z. Seref-Ferlengez, O.D. Kennedy, M.B. Schaffler, Bone microdamage, remodeling and bone fragility: how much damage is too much damage?, Bonekey Rep. 4 (2015) 1–7. https://doi.org/10.1038/bonekey.2015.11.

[24] M.B. Schaffler, D.B. Burr, Stiffness of compact bone: effects of porosity and density, J Biomech. 21 (1988) 13–16.

[25] K.B. Harvey, S.W. Donahue, Bending properties, porosity, and ash fraction of black bear (Ursus americanus) cortical bone are not compromised with aging despite annual periods of disuse, J Biomech. 37 (2004) 1513–1520. https://doi.org/10.1016/j.jbiomech.2004.01.010.

[26] S.J. Wojda, D.R. Weyland, S.K. Gray, M.E. Mcgee-Lawrence, T.D. Drummer, S.W. Donahue, Black bears with longer disuse (hibernation) periods have lower femoral osteon population density and greater mineralization and intracortical porosity, Anatomical Record. 296 (2013) 1148–1153. https://doi.org/10.1002/ar.22720.

[27] T. Landete-Castillejos, J.D. Currey, F. Ceacero, A.J. García, L. Gallego, S. Gomez, Does nutrition affect bone porosity and mineral tissue distribution in deer antlers? The relationship between histology, mechanical properties and mineral

composition, Bone. 50 (2012) 245–254. https://doi.org/10.1016/j.bone.2011.10.026.

[28] J.D. Currey, The Effect of Porosity and Mineral Content on the Young's Modulus of Elasticity of Compact Bone, J Biomech. 21 (1988) 131–139.

[29] D.B. Burr, T. Stafford, Validity of the Bulk-Staining Technique to Separate Artifactual From In Vivo Bone Microdamage, Clin Orthop Relat Res. 260 (1990) 305–308.

[30] M.E. Mcgee, A.J. Maki, S.E. Johnson, O.L. Nelson, C.T. Robbins, S.W. Donahue, Decreased bone turnover with balanced resorption and formation prevent cortical bone loss during disuse (hibernation) in grizzly bears (Ursus arctos horribilis), n.d.

[31] A. Drake, T.L. Haut Donahue, M. Stansloski, K. Fox, B.B. Wheatley, S.W. Donahue, Horn and horn core trabecular bone of bighorn sheep rams absorbs impact energy and reduces brain cavity accelerations during high impact ramming of the skull, Acta Biomater. 44 (2016) 41–50. https://doi.org/10.1016/j.actbio.2016.08.019.

BIBLIOGRAPHY

Abdel-Wahab, A.A., Alam, K. and Silberschmidt, V. v. (2011) 'Analysis of anisotropic viscoelastoplastic properties of cortical bone tissues', *Journal of the Mechanical Behavior of Biomedical Materials*, 4(5), pp. 807–820. Available at: https://doi.org/10.1016/j.jmbbm.2010.10.001.

Ackermans, N.L. *et al.* (2022) 'Evidence of traumatic brain injury in headbutting bovids', *Acta Neuropathologica* [Preprint], (0123456789). Available at: https://doi.org/10.1007/s00401-022-02427-2.

Aguirre, T.G., Fuller, L., *et al.* (2020) 'Bioinspired material architectures from bighorn sheep horncore velar bone for impact loading applications', *Scientific Reports*, 10(1), pp. 1–14. Available at: https://doi.org/10.1038/s41598-020-76021-5.

Aguirre, T.G., Ingrole, A., *et al.* (2020) 'Differing trabecular bone architecture in dinosaurs and mammals contribute to stiffness and limits on bone strain', *PLoS ONE*, 15(8 August), pp. 1–20. Available at: https://doi.org/10.1371/journal.pone.0237042.

Akkus, O., Jepsen, K.J. and Rimnac, C.M. (2000) 'Microstructural aspects of the fracture process in human cortical bone', *Journal of Materials Science*, 35(24), pp. 6065–6074. Available at: https://doi.org/10.1023/A:1026719531300.

Ambrose, C.G. *et al.* (2018) 'Mechanical properties of infant bone', *Bone*, 113(May), pp. 151–160. Available at: https://doi.org/10.1016/j.bone.2018.05.015.

American Society for Testing Materials (2019) 'ASTM D3983-98: Standard Test Method for Measuring Strength and Shear Modulus of Nonrigid Adhesives by the Thick-Adherend Tensile-Lap Specimen', 1(Reapproved), pp. 1–11. Available at: https://doi.org/10.1520/D3983-98R19.2.

ASTM D 1002-05 (2005) 'Standard Test Method for Apparent Shear Strength of Single-Lap-Joint Adhesively Bonded Metal Specimens by Tension Loading (Metal-to-Metal)', *Standards*, 10(Reapproved 2019), pp. 1–5. Available at: https://doi.org/10.1520/D1002-10.on.

ASTM International (2002) 'Standard Test Method for Determination of Modulus of Elasticity for Rigid and Semi- Rigid Plastic Specimens by Controlled Rate of Loading', *ASTM International* [Preprint].

ASTM-D5656-04 (2004) 'Standard Test Method for Thick-Adherend Metal Lap-Shear Joints for Determination of the Stress-Strain Behavior of Adhesives in Shear by Tension Loading', *Annual Book of ASTM Standards*, 10(Reapproved 2017), pp. 1–8. Available at: https://doi.org/10.1520/D5656-10R17.2.

Barak, M.M., Lieberman, D.E. and Hublin, J.J. (2013) 'Of mice, rats and men: Trabecular bone architecture in mammals scales to body mass with negative allometry', *Journal of Structural Biology*, 183(2), pp. 123–131. Available at: https://doi.org/10.1016/j.jsb.2013.04.009.

Barrera, J.W., Le Cabec, A. and Barak, M.M. (2016) 'The orthotropic elastic properties of fibrolamellar bone tissue in juvenile white-tailed deer femora', *Journal of Anatomy*, 229(4), pp. 568–576. Available at: https://doi.org/10.1111/joa.12500.

Bass, S.L. *et al.* (2002) 'The effect of mechanical loading on the size and shape of bone in pre-, peri-, and postpubertal girls: A study in tennis players', *Journal of Bone and Mineral Research*, 17(12), pp. 2274–2280. Available at: https://doi.org/10.1359/jbmr.2002.17.12.2274.

Bassey, E.J. and Ramsdale, S.J. (1994) 'Increase in femoral bone density in young women following high-impact exercise', *Osteoporosis International*, 4(March 1994), pp. 72–75.

Bayraktar, H.H. *et al.* (2004) 'Comparison of the elastic and yield properties of human femoral trabecular and cortical bone tissue', *Journal of Biomechanics*, 37(1), pp. 27–35. Available at: https://doi.org/10.1016/S0021-9290(03)00257-4.

Beresheim, A.C., Pfeiffer, S.K. and Alblas, A. (2018) 'The Influence of Body Size and Bone Mass on Cortical Bone Histomorphometry in Human Ribs', *Anatomical Record*, 301(10), pp. 1788–1796. Available at: https://doi.org/10.1002/ar.23933.

Bergamo, C. (2014) 'Traumatic brain injury and risk of dementia in older veterans: Barnes DE, Kaup A, Kirby KA, et al. Neurology 2014;83:312-9.', *Journal of Emergency Medicine*, 47(5), pp. 617–618. Available at: https://doi.org/10.1016/j.jemermed.2014.09.023.

Bonds, A. and Bonds, A. (2012) 'Standard Guide for Use of Adhesive-Bonded Single Lap-Joint Specimen Test', i(Reapproved 2008), pp. 1–6. Available at: https://doi.org/10.1520/D4896-01R08E01.2.

Bonin, S.J., DeMarco, A.L. and Siegmund, G.P. (2022) 'The Effect of MIPS, Headform Condition, and Impact Orientation on Headform Kinematics Across a Range of Impact Speeds During Oblique Bicycle Helmet Impacts', *Annals of Biomedical Engineering*, 50(7), pp. 860–870. Available at: https://doi.org/10.1007/s10439-022-02961-w.

Bower, J.H. *et al.* (2003) 'Head trauma preceding PD: A case-control study', *Neurology*, 60(10), pp. 1610–1615. Available at: https://doi.org/10.1212/01.WNL.0000068008.78394.2C.

Bragulla, H.H. and Homberger, D.G. (2009) 'Structure and functions of keratin proteins in simple, stratified, keratinized and cornified epithelia', *Journal of Anatomy*, 214(4), pp. 516–559. Available at: https://doi.org/10.1111/j.1469-7580.2009.01066.x.

Brien, F.J.O., Taylor, D. and Lee, T.C. (2005) 'The effect of bone microstructure on the initiation and growth of microcracks', *Journal of Orthopaedic Research*, 23.

Broglio, S.P. *et al.* (2010) 'The Biomechanical Properties of Concussions in High School Football', *Medicine and Science in Sports and Excercise*, 42(11), pp. 2064–2071. Available at: https://doi.org/10.1249/MSS.0b013e3181dd9156.

Brown, T.D. and Ferguson, A.B. (1980) 'Mechanical property distributions in the cancellous bone of the human proximal femur', *Acta Orthopaedica*, 51(1–6), pp. 429–437. Available at: https://doi.org/10.3109/17453678008990819.

Buechner, H.K. (1960) 'The Bighorn Sheep in the United States, Its Past, Present, and Future', *Wildlife Monographs*, 4, pp. 3–174. Available at: https://doi.org/10.1017/CBO9781107415324.004.

Burr, D.B. *et al.* (1985) 'Bone Remodeling in Response to in vivo Fatigue Microdamage', *Journal of Biomechanics*, 18(3), pp. 189–200.

Burr, D.B. *et al.* (1998) 'Does microdamage accumulation affect the mechanical properties of bone?', *Journal of Biomechanics*, 31(4), pp. 337–345. Available at: https://doi.org/10.1016/S0021-9290(98)00016-5.

Burr, D.B., Schaffler, M.B. and Frederickson, R.G. (1988) 'Composition of the cement line and its possible mechanical role as a local interface in human compact bone.', *Journal of biomechanics*, 21(11), pp. 939–945. Available at: https://doi.org/10.1016/0021-9290(88)90132-7.

Burr, D.B. and Stafford, T. (1990) 'Validity of the Bulk-Staining Technique to Separate Artifactual From In Vivo Bone Microdamage', *Clinical Orthopaedics and Related Research*, 260, pp. 305–308.

Burr, D.B. and Turner, C.H. (2001) 'Mechanical Testing Methods', in S.C. Cowin (ed.) *Bone Mechanics Handbook*. Second, pp. 7–6 to 7–24.

Burstein, A.H. *et al.* (1975) 'Contribution of collagen and mineral to the elastic-plastic properties of bone', *The Journal of Bone and Joint Surgery*, 57-A(7), pp. 956–961.

Cappelli, J. *et al.* (2018) 'The bony horncore of the common eland (Taurotragus oryx): composition and mechanical properties of a spiral fighting structure', *Journal of Anatomy*, 232(1), pp. 72–79. Available at: https://doi.org/10.1111/joa.12708.

Cassidy, J.D. *et al.* (2004) 'Incidence, risk factors and prevention of mild traumatic brain injury: Results of the WHO Collaborating Centre Task Force on Mild Traumatic Brain Injury', *Journal of Rehabilitation Medicine, Supplement*, (43), pp. 28–60. Available at: https://doi.org/10.1080/16501960410023732.

Centers for Disease Control and Prevention (2003) 'Report to Congress on Mild Traumatic Brain Injury in the United States: Steps to Prevent a Serious Public Health Problem', *Atlanta, GA: Centers for Disease Control and Prevention* [Preprint].

Centers for Disease Control and Prevention (2015) 'Report to Congress on Traumatic Brain Injury in the United States: Epidemiology and Rehabilitation', *National Center for Injury Prevention and Control; Division of Unitentional Injury Prevention. Atlanta, GA.* [Preprint].

Chambers, T.J. *et al.* (1993) 'Induction of bone formation in rat tail vertebrae by mechanical loading', *Bone and Mineral*, 20, pp. 167–178.

Choi, K. *et al.* (1990) 'The Elastic Moduli of Human Subchondral, Trabecular, and Cortical Bone Tissue and the Size Dependency of Cortical Bone Modulus', *J. Biomechanics*, 23(11), pp. 1103–1113. Available at: https://doi.org/10.1016/0021-9290(90)90003-L.

Choi, K. and Goldstein, S.A. (1992) 'A comparison of the fatigue behavior of human trabecular and cortical bone tissue', *Journal of Biomechanics*, 25(12), pp. 1371–1381. Available at: https://doi.org/10.1016/0021-9290(92)90051-2.

Churches, A.E. and Howlett, D.C.R. (1982) 'Functional Adaptation of Bone in Response to Sinusoidally Varying Controlled Compressive Loading of the Ovine Metacarpus', *Clinical Orthopaedics and Related Research*, 168, pp. 265–280.

Collet, Ph. *et al.* (1997) 'Effects of 1- and 6-Month Spaceflight on Bone Mass and Biochemistry in Two Humans', *Bone*, 20(6), pp. 547–551.

Crowder, C., Heinrich, J. and Stout, S.D. (2012) 'Rib histomorphometry for adult age estimation', *Methods in Molecular Biology*, 915, pp. 109–127. Available at: https://doi.org/10.1007/978-1-61779-977-8_7.

Currey, J.D. (1979) 'Mechanical properties of bone tissues with greatly differing functions', *Journal of Biomechanics*, 12(4), pp. 313–319. Available at: https://doi.org/10.1016/0021-9290(79)90073-3.

Currey, J.D. (1987) 'The Evolution of the Mechanical Properties of Amniote Bone', *Journal of Biomechanics*, 20(11–12), pp. 1035–1044.

Currey, J.D. (1988) 'The Effect of Porosity and Mineral Content on the Young's Modulus of Elasticity of Compact Bone', *Journal of Biomechanics*, 21(2), pp. 131–139.

Currey, J.D. (1999) *What determines the bending strength of compact bone?*

Currey, J.D. (2003) 'The many adaptations of bone', *Journal of Biomechanics*, 36(10), pp. 1487–1495. Available at: https://doi.org/10.1016/S0021-9290(03)00124-6.

Currey, J.D. (2004) 'Tensile yield in compact bone is determined by strain, post-yield behaviour by mineral content', *Journal of Biomechanics*, 37(4), pp. 549–556. Available at: https://doi.org/10.1016/j.jbiomech.2003.08.008.

Currey, J.D. *et al.* (2009) 'The mechanical properties of red deer antler bone when used in fighting', *Journal of Experimental Biology*, 212(24), pp. 3985–3993. Available at: https://doi.org/10.1242/jeb.032292.

Currey, J.D. and Brear, K. (1990) 'Hardness, Young's modulus and yield stress in mammalian mineralized tissues', *Journal of Materials Science: Materials in Medicine*, 1(1), pp. 14–20. Available at: https://doi.org/10.1007/BF00705348.

Currey, J.D., Brear, K. and Zioupos, P. (2019) 'Strain rate dependence of work of fracture tests on bone and similar tissues: Reflections on testing methods and mineral content effects', *Bone*, 128(August), p. 115038. Available at: https://doi.org/10.1016/j.bone.2019.115038.

Currey, J.D. and Butler, G. (1975) 'The mechanical properties of bone tissue in children', *Journal of Bone and Joint Surgery - American Volume*, 57(6), pp. 810–814.

Daneshvar, D.H. *et al.* (2015) 'Post-traumatic neurodegeneration and chronic traumatic encephalopathy', *Molecular and Cellular Neuroscience*, 66, pp. 81–90. Available at: https://doi.org/10.1016/j.mcn.2015.03.007.

Derveni, F. *et al.* (2022) 'Postbuckling behavior and imperfection sensitivity of elastic–plastic periodic plate-lattice materials', *Extreme Mechanics Letters*, 50, p. 101510. Available at: https://doi.org/10.1016/j.eml.2021.101510.

Didehbani, N. *et al.* (2013) 'Depressive symptoms and concussions in aging retired NFL players', *Archives of Clinical Neuropsychology*, 28(5), pp. 418–424. Available at: https://doi.org/10.1093/arclin/act028.

DiGiacomo, G., Tsai, S. and Bottlang, M. (2021) 'Impact Performance Comparison of Advanced Snow Sport Helmets with Dedicated Rotation-Damping Systems', *Annals of Biomedical Engineering*, 49(10), pp. 2805–2813. Available at: https://doi.org/10.1007/s10439-021-02723-0.

Doherty, A.H., Ghalambor, C.K. and Donahue, S.W. (2015) 'Evolutionary physiology of bone: Bone metabolism in changing environments', *Physiology*, 30(1), pp. 17–29. Available at: https://doi.org/10.1152/physiol.00022.2014.

Donahue, S.W. (2018) 'Krogh's principle for musculoskeletal physiology and pathology', *Journal of Musculoskeletal Neuronal Interactions*, 18(3), pp. 284–291.

Donahue, S.W. and Galley, S.A. (2012) 'Microdamage in Bone: Implications for Fracture, Repair, Remodeling, and Adaptation', *Critical Reviews™ in Biomedical Engineering*, 34(3), pp. 215–271. Available at: https://doi.org/10.1615/critrevbiomedeng.v34.i3.20.

Doube, M. *et al.* (2011) 'Trabecular bone scales allometrically in mammals and birds', *Proceedings of the Royal Society B: Biological Sciences*, 278(1721), pp. 3067–3073. Available at: https://doi.org/10.1098/rspb.2011.0069.

Doube, M. *et al.* (2018) 'X-ray microtomography images of trabecular bone from the femoral head and condyle of 18 avian, 72 mammalian and one crocodilian species.' Available at: https://doi.org/10.6084/m9.figshare.7257179.v1.

Douglas, J.E. *et al.* (1998) 'Stress/strain behaviour of the equine laminar junction', *Journal of Experimental Biology*, 201(15), pp. 2287–2297.

Drake, A. *et al.* (2016) 'Horn and horn core trabecular bone of bighorn sheep rams absorbs impact energy and reduces brain cavity accelerations during high impact ramming of the skull', *Acta Biomaterialia*, 44, pp. 41–50. Available at: https://doi.org/10.1016/j.actbio.2016.08.019.

Farah, G., Siwek, D. and Cummings, P. (2018) 'Tau accumulations in the brains of woodpeckers', *PLoS ONE*, 13(2), pp. 1–12. Available at: https://doi.org/10.1371/journal.pone.0191526.

Faramarzi, B. (2014) ‘Morphological and biomechanical properties of equine laminar junction’, *Journal of Equine Veterinary Science*, 34(5), pp. 589–592. Available at: https://doi.org/10.1016/j.jevs.2013.12.007.

Finkbeiner, N.W.B. *et al.* (2016) ‘Knowing what we don’t know: Long-term psychiatric outcomes following adult concussion in sports’, *Canadian Journal of Psychiatry*, 61(5), pp. 270–276. Available at: https://doi.org/10.1177/0706743716644953.

Frank, J.D. *et al.* (2002) ‘Aging and accumulation of microdamage in canine bone’, *Bone*, 30(1), pp. 201–206. Available at: https://doi.org/10.1016/S8756-3282(01)00623-8.

Fuller, L.H. and Donahue, S.W. (2020) ‘Material properties of bighorn sheep (Ovis canadensis) horncore bone with implications for energy absorption during impacts’, *Journal of the Mechanical Behavior of Biomedical Materials*, 114(November 2020), p. 104224. Available at: https://doi.org/10.1016/j.jmbbm.2020.104224.

Gastaldi, D. *et al.* (2020) ‘An experimental procedure to perform mechanical characterization of small-sized bone specimens from thin femoral cortical wall’, *Journal of the Mechanical Behavior of Biomedical Materials*, 112(February), p. 104046. Available at: https://doi.org/10.1016/j.jmbbm.2020.104046.

Geist, V. (1966) ‘Validity of Horn Segment Counts in Aging Bighorn Sheep’, *The Journal of Wildlife Management*, 30(3), pp. 634–635.

Geist, V. (1971) *Mountain Sheep: A Study in Behavior and Evolution*. University of Chicago Press.

Genbrugge, A. *et al.* (2012) ‘Structural tissue organization in the beak of Java and Darwin’s finches’, *Journal of Anatomy*, 221(5), pp. 383–393. Available at: https://doi.org/10.1111/j.1469-7580.2012.01561.x.

Giraud-Guille, M.M. (1988) ‘Twisted plywood architecture of collagen fibrils in human compact bone osteons’, *Calcified Tissue International*, 42, pp. 167–180.

Gocha, T.P. and Agnew, A.M. (2016) ‘Spatial variation in osteon population density at the human femoral midshaft: Histomorphometric adaptations to habitual load environment’, *Journal of Anatomy* [Preprint]. Available at: https://doi.org/10.1111/joa.12433.

Goh, J.C.H., Ang, E.J. and Bose, K. (1989) ‘Effect of preservation medium on the mechanical properties of cat bones’, *Acta Orthopaedica Scandinavica*, 60(4), pp. 465–467. Available at: https://doi.org/10.3109/17453678909149321.

Goodship, A.E., Lanyon, L.E. and McFie, H. (1979) ‘Functional adaptation of bone to increased stress: An experimental study’, *Journal of Bone and Joint Surgery*, 61(4), pp. 539–546.

Guo, X.E. (2001) ‘Mechanical Properties of Cortical Bone and Cancellous Bone Tissue’, in S.C. Cowin (ed.) *Bone Mechanics Handbook*. Second. CRC Press LLC, pp. 10.1-10.23.

Guskiewicz, Kevin M *et al.* (2007) 'Measurement of head impacts in collegiate football players: Relationship between head impact biomechanics and acute clinical outcome after concussion', *Injury Prevention*, 61(6), pp. 1244–1253. Available at: https://doi.org/10.1227/01.NEU.0000280146.37163.79.

Guskiewicz, Kevin M. *et al.* (2007) 'Recurrent concussion and risk of depression in retired professional football players', *Medicine and Science in Sports and Exercise*, 39(6), pp. 903–909. Available at: https://doi.org/10.1249/mss.0b013e3180383da5.

Han, S.H. *et al.* (2009) 'Microscopic age estimation from the anterior cortex of the femur in Korean adults', *Journal of Forensic Sciences*, 54(3), pp. 519–522. Available at: https://doi.org/10.1111/j.1556-4029.2009.01003.x.

Hansen, U. *et al.* (2008) 'The effect of strain rate on the mechanical properties of human cortical bone', *Journal of Biomechanical Engineering*, 130(1), pp. 1–8. Available at: https://doi.org/10.1115/1.2838032.

Harvey, K.B. and Donahue, S.W. (2004) 'Bending properties, porosity, and ash fraction of black bear (Ursus americanus) cortical bone are not compromised with aging despite annual periods of disuse', *Journal of Biomechanics*, 37(10), pp. 1513–1520. Available at: https://doi.org/10.1016/j.jbiomech.2004.01.010.

Havill, L.M. (2004) 'Osteon Remodeling Dynamics in Macaca mulatta: Normal Variation with Regard to Age, Sex, and Skeletal Maturity', *Calcified Tissue International*, 74(1), pp. 95–102. Available at: https://doi.org/10.1007/s00223-003-9038-3.

van Hemert, C. *et al.* (2012) 'Microanatomy of passerine hard-cornified tissues: Beak and claw structure of the black-capped chickadee (Poecile atricapillus)', *Journal of Morphology*, 273(2), pp. 226–240. Available at: https://doi.org/10.1002/jmor.11023.

Huang, W. *et al.* (2017) 'Hierarchical structure and compressive deformation mechanisms of bighorn sheep (Ovis canadensis) horn', *Acta Biomaterialia*, 64, pp. 1–14. Available at: https://doi.org/10.1016/j.actbio.2017.09.043.

Ingrole, A. *et al.* (2021) 'Bioinspired energy absorbing material designs using additive manufacturing', *Journal of the Mechanical Behavior of Biomedical Materials*, 119(February), p. 104518. Available at: https://doi.org/10.1016/j.jmbbm.2021.104518.

Jee, W.S.S. (2001) 'Skeletal Development', in S.C. Cowin (ed.) *Bone Mechanics Handbook*. Second. CRC Press LLC, pp. 24–33.

Johnson, K.L. *et al.* (2017) 'Moisture, anisotropy, stress state, and strain rate effects on bighorn sheep horn keratin mechanical properties', *Acta Biomaterialia*, 48, pp. 300–308. Available at: https://doi.org/10.1016/j.actbio.2016.10.033.

Kalmey, J.K. and Lovejoy, C.O. (2002) 'Collagen Fiber Orientation in the Femoral Necks of Apes and Humans: Do Their Histological Structures Reflect Differences in Locomotor Loading?', *Bone*, 31(2), pp. 327–332.

Kerr, Z.Y. *et al.* (2012) 'Nine-year risk of depression diagnosis increases with increasing self-reported concussions in retired professional football players', *American Journal of Sports Medicine*, 40(10), pp. 2206–2212. Available at: https://doi.org/10.1177/0363546512456193.

Kochová, P. *et al.* (2013) 'A preliminary study into the correlation of stiffness of the laminar junction of the equine hoof with the length density of its secondary lamellae', *Equine Veterinary Journal*, 45(2), pp. 170–175. Available at: https://doi.org/10.1111/j.2042-3306.2012.00632.x.

Krausman, P.R. and Bowyer, R.T. (2003) 'Mountain Sheep (Ovis canadensis and O. dalli)', in G.A. Feldhamer, B.C. Thompson, and J.A. Chapman (eds) *Wild Mammals of North America: Biology, Management, and Conservation*. Second. Baltimore, MD: Johns Hopkins University Press, pp. 1095–1118.

Kuhn, J.L. *et al.* (1989) 'Comparison of the trabecular and cortical tissue moduli from human iliac crests', *Journal of Orthopaedic Research*, 7(6), pp. 876–884. Available at: https://doi.org/10.1002/jor.1100070614.

Landete-Castillejos, T. *et al.* (2012) 'Does nutrition affect bone porosity and mineral tissue distribution in deer antlers? The relationship between histology, mechanical properties and mineral composition', *Bone*, 50(1), pp. 245–254. Available at: https://doi.org/10.1016/j.bone.2011.10.026.

Landis, W.J. and Jacquet, R. (2013) 'Association of calcium and phosphate ions with collagen in the mineralization of vertebrate tissues', *Calcified Tissue International*, 93(4), pp. 329–337. Available at: https://doi.org/10.1007/s00223-013-9725-7.

Lanovaz, J.L., Clayton, H.M. and Watson, L.G. (1998) 'In vitro attenuation of impact shock in equine digits', *Equine Veterinary Journal*, 26, pp. 96–102.

Launey, M.E., Buehler, M.J. and Ritchie, R.O. (2010) *On the mechanistic origins of toughness in bone*, *Annual Review of Materials Research*. Available at: https://doi.org/10.1146/annurev-matsci-070909-104427.

Lee, T.C., Staines, A. and Taylor, D. (2002) 'Bone adaptation to load: Microdamage as a stimulus for bone remodelling', *Journal of Anatomy*, 201(6), pp. 437–446. Available at: https://doi.org/10.1046/j.1469-7580.2002.00123.x.

Lei, J. *et al.* (2020) 'Characterizing Strain Rate-Dependent Mechanical Properties for Bovine Cortical Bones', *Journal of Biomechanical Engineering*, 142(9), pp. 1–8. Available at: https://doi.org/10.1115/1.4046690.

Liu, Y., Luo, D. and Wang, T. (2016) 'Hierarchical Structures of Bone and Bioinspired Bone Tissue Engineering', *Small (Weinheim an der Bergstrasse, Germany)*, 12(34), pp. 4611–4632. Available at: https://doi.org/10.1002/smll.201600626.

Liu, Y.Z. *et al.* (2017) 'A study of woodpecker's pecking process and the impact response of its brain', *International Journal of Impact Engineering*, 108, pp. 263–271. Available at: https://doi.org/10.1016/j.ijimpeng.2017.05.016.

Maity, P. and Tekalur, S.A. (2011) 'Finite element analysis of ramming in Ovis canadensis', *Journal of Biomechanical Engineering*, 133(2), pp. 1–9. Available at: https://doi.org/10.1115/1.4003321.

Maquer, G. *et al.* (2015) 'Bone volume fraction and fabric anisotropy are better determinants of trabecular bone stiffness than other morphological variables', *Journal of Bone and Mineral Research*, 30(6), pp. 1000–1008. Available at: https://doi.org/10.1002/jbmr.2437.

Martin, B. (1992) 'A theory of fatigue damage accumulation and repair in cortical bone.', *Journal of orthopaedic research : official publication of the Orthopaedic Research Society*, 10(6), pp. 818–825. Available at: https://doi.org/10.1002/jor.1100100611.

Martin, R.B. (2002) 'Is all cortical bone remodeling initiated by microdamage?', *Bone*, 30(1), pp. 8–13. Available at: https://doi.org/10.1016/S8756-3282(01)00620-2.

Martin, R.B. (2007) 'Targeted bone remodeling involves BMU steering as well as activation', *Bone*, 40(6), pp. 1574–1580. Available at: https://doi.org/10.1016/j.bone.2007.02.023.

Martin, R.B. *et al.* (2015) 'Material Properties of Cancellous Bone', in *Skeletal Tissue Mechanics*. Second Edition. New York, NY: Springer New York. Available at: https://doi.org/10.1007/978-1-4939-3002-9.

Martin, R.B. and Boardman, D.L. (1993) 'The effects of collagen fiber orientation, porosity, density, and mineralization on bovine cortical bone bending properties', *Journal of Biomechanics*, 26(9), pp. 1047–1054.

Martin, R.B. and Burr, D.B. (1989) *Structure, Function, and Adaptation of Compact Bone*. New York: Raven Press.

Martin, R.B. and Sharkey, N.A. (2001) 'The Mechanical Effects of Preserving Bone', in S.C. Cowin (ed.) *Bone Mechanics Handbook*. Second Edi, pp. 20-6-20–12.

Mason, M.W., Skedros, J.G. and Bloebaum, R.D. (1995) 'Evidence of strain-mode-related cortical adaptation in the diaphysis of the horse radius', *Bone*, 17(3), pp. 229–237. Available at: https://doi.org/10.1016/8756-3282(95)00213-W.

May, P.R.A. *et al.* (1979) 'Woodpecker Drilling Behavior: An Endorsement of the Rotational Theory of Impact Brain Injury', *Archives of Neurology*, 36(6), pp. 370–373. Available at: https://doi.org/10.1001/archneur.1979.00500420080011.

McElhaney, J.H. (1966) 'Dynamic response of bone and muscle tissue.', *Journal of applied physiology*, 21(4), pp. 1231–1236. Available at: https://doi.org/10.1152/jappl.1966.21.4.1231.

Mcgee, M.E. *et al.* (no date) *Decreased bone turnover with balanced resorption and formation prevent cortical bone loss during disuse (hibernation) in grizzly bears (Ursus arctos horribilis)*.

McGee-Lawrence, M.E. *et al.* (2009) 'Six months of disuse during hibernation does not increase intracortical porosity or decrease cortical bone geometry, strength, or mineralization in black bear (Ursus americanus) femurs', *Journal of*

Biomechanics, 42(10), pp. 1378–1383. Available at: https://doi.org/10.1016/j.jbiomech.2008.11.039.

McKee, A.C. and Robinson, M.E. (2014) 'Military-related traumatic brain injury and neurodegeneration', *Alzheimer's and Dementia*, 10(3 SUPPL.), pp. S242–S253. Available at: https://doi.org/10.1016/j.jalz.2014.04.003.

McKittrick, J. *et al.* (2012) 'The structure, functions, and mechanical properties of keratin', *Jom*, 64(4), pp. 449–468. Available at: https://doi.org/10.1007/s11837-012-0302-8.

Meaney, D. and Smith, D. (2012) 'Biomechanics of concussion', *Concussion*, 30(1), pp. 14–27. Available at: https://doi.org/10.1159/000358748.

Meaney, D.F. and Smith, D.H. (2011) 'Biomechanics of Concussion', *Clinics in Sports Medicine*, 30(1), pp. 19–vii. Available at: https://doi.org/10.1016/j.csm.2010.08.009.

Menard, K.P. (1999) 'Dynamic Testing', in *Dynamic Mechanical Analysis: A practical introduction*. CRC Press LLC, pp. 61–89.

Mohsin, S., O'Brien, F.J. and Lee, T.C. (2006) 'Osteonal crack barriers in ovine compact bone', *Journal of Anatomy*, 208(1), pp. 81–89. Available at: https://doi.org/10.1111/j.1469-7580.2006.00509.x.

Morgan, E.F., Unnikrisnan, G.U. and Hussein, A.I. (2018) 'Bone Mechanical Properties in Healthy and Diseased States', *Annual Review of Biomedical Engineering*, 20(1), pp. 119–143. Available at: https://doi.org/10.1146/annurev-bioeng-062117-121139.

Mori, R. *et al.* (2005) 'Preliminary study of histological comparison on the growth patterns of long-bone cortex in young calf, pig, and sheep', *Journal of Veterinary Medical Science*, 67(12), pp. 1223–1229. Available at: https://doi.org/10.1292/jvms.67.1223.

Musy, S.N. *et al.* (2017) 'Not only stiffness, but also yield strength of the trabecular structure determined by non-linear μFE is best predicted by bone volume fraction and fabric tensor', *Journal of the Mechanical Behavior of Biomedical Materials*, 65(September 2016), pp. 808–813. Available at: https://doi.org/10.1016/j.jmbbm.2016.10.004.

Odgaard, A. (1997) 'Three-dimensional methods for quantification of cancellous bone architecture', *Bone*, 20(4), pp. 315–328. Available at: https://doi.org/10.1016/S8756-3282(97)00007-0.

Osborne, D.L. and Curtis, J. (2005) 'A protocol for the staining of cement lines in adult human bone using toluidine blue', *Journal of Histotechnology*, 28(2), pp. 73–79. Available at: https://doi.org/10.1179/his.2005.28.2.73.

Pahr, D.H. and Zysset, P.K. (2008) 'Influence of boundary conditions on computed apparent elastic properties of cancellous bone', *Biomechanics and Modeling in Mechanobiology*, 7(6), pp. 463–476. Available at: https://doi.org/10.1007/s10237-007-0109-7.

Parfitt, A.M. *et al.* (1987) 'Bone histomorphometry: Standardization of nomenclature, symbols, and units: Report of the asbmr histomorphometry nomenclature committee', *Journal of Bone and Mineral Research*, 2(6), pp. 595–610.

Pellman, E.J. *et al.* (2003) 'Concussion in Professional Football: Reconstruction of Game Impacts and Injuries', *Neurosurgery*, 53(4), p. 796. Available at: https://doi.org/10.1227/01.NEU.0000083559.68424.3F.

Phelps, J.B. *et al.* (2000) 'Microstructural heterogeneity and the fracture toughness of bone', *Journal of Biomedical Materials Research*, 51(4), pp. 735–741. Available at: https://doi.org/10.1002/1097-4636(20000915)51:4<735::AID-JBM23>3.0.CO;2-G.

Pocius, A. v. (2002) 'Shear Loading of Adhesive Bonds', in *Adhesion and Adhesives Technology: An Introduction*.

Pollitt, C.C. (1992) 'Clinical anatomy and physiology of the normal equine foot', *Equine Veterinary Education*, 4(5), pp. 219–224.

Pollitt, C.C. (1998) 'The anatomy and physiology of the hoof wall.', *Equine Veterinary Education*, 10(6), pp. 318–325.

Pollitt, C.C. and Collins, S.N. (2016) 'The suspensory apparatus of the distal phalanx in normal horses', *Equine veterinary journal*, 48(4), pp. 496–501. Available at: https://doi.org/10.1111/evj.12459.

Portigliatti Barbos, M., Bianco, P. and Ascenzi, A. (1983) 'Distribution of osteonic and interstitial components in the human femoral shaft with reference to structure, calcification and mechanical properties.', *Acta anatomica*, 115(2), pp. 178–186. Available at: https://doi.org/10.1159/000145688.

Reid, S.A. (1986) 'A study of lamellar oranisation in juvenile and adult human bone', *Anatomy and Embryology*, 174(3), pp. 329–338.

Reilly, D.T. and Burstein, A.H. (1975) 'The elastic and ultimate properties of compact bone tissue.', *Journal of biomechanics*, 8(6), pp. 393–405. Available at: https://doi.org/10.1016/0021-9290(75)90075-5.

Rho, J.Y., Ashman, R.B. and Turner, C.H. (1993) 'Young's Modulus of Trabecular and Cortical Bone Material: Ultrasonic and Microtensile Measurements', *Journal of Biomechanics*, 26(2), pp. 111–119.

Rho, J.Y., Kuhn-Spearing, L. and Zioupos, P. (1998) 'Mechanical properties and the hierarchical structure of bone', *Medical Engineering and Physics*, 20(2), pp. 92–102. Available at: https://doi.org/10.1016/S1350-4533(98)00007-1.

Rubin, C.T. and Lanyon, L.E. (1984a) 'Dynamic strain similarity in vertebrates; an alternative to allometric limb bone scaling', *Journal of Theoretical Biology*, 107, pp. 321–327.

Rubin, C.T. and Lanyon, L.E. (1984b) 'Regulation of bone formation by applied dynamic loads', *The Journal of Bone and Joint Surgery*, 66-A(3), pp. 397–402. Available at: https://archive.org/details/sim_journal-of-bone-and-joint-surgery_1984-03_66-a_3.

Rubin, C.T. and Lanyon, L.E. (1985) ‘Regulation of bone mass by mechanical strain magnitude’, *Calcified Tissue International*, 37, pp. 411–417.

Sanchis-Moysi, J. *et al.* (2004) ‘Inter-arm asymmetry in bone mineral content and bone area in postmenopausal recreational tennis players’, *Maturitas*, 48(3), pp. 289–298. Available at: https://doi.org/10.1016/j.maturitas.2004.03.008.

Schaffler, M.B. and Burr, D.B. (1988) ‘Stiffness of compact bone: effects of porosity and density’, *Journal of Biomechanics*, 21(1), pp. 13–16.

Schaffler, M.B., Burr, D.B. and Frederickson, R.G. (1987) ‘Morphology of the osteonal cement line in human bone.’, *The Anatomical record*, 217(3), pp. 223–228. Available at: https://doi.org/10.1002/ar.1092170302.

Schaffler, M.B., Choi, K. and Milgrom, C. (1995) ‘Aging and matrix microdamage accumulation in human compact bone’, *Bone*, 17(6), pp. 521–525. Available at: https://doi.org/10.1016/8756-3282(95)00370-3.

Sedlin, E.D. (1965) ‘A Rheologic Model for Cortical Bone: A Study of the Physical Properties of Human Femoral Samples’, *Acta Orthopaedica Scandinavica*, 36(sup83), pp. 1–77. Available at: https://doi.org/10.3109/ort.1965.36.suppl-83.01.

Seek, T.W. (2018) *Exploration of Unique Porous Bone Materials for Candidacy in Bioinspired Material Design*. Masters Thesis. Colorado State University.

Seref-Ferlengez, Z., Kennedy, O.D. and Schaffler, M.B. (2015) ‘Bone microdamage, remodeling and bone fragility: how much damage is too much damage?’, *BoneKEy Reports*, 4(December 2014), pp. 1–7. Available at: https://doi.org/10.1038/bonekey.2015.11.

Skedros, J.G. *et al.* (1996) ‘Evidence of structural and material adaptation to specific strain features in cortical bone’, *Anatomical Record*, 246(1), pp. 47–63. Available at: https://doi.org/10.1002/(SICI)1097-0185(199609)246:1<47::AID-AR6>3.0.CO;2-C.

Skedros, J.G. *et al.* (2009) ‘Interpreting cortical bone adaptation and load history by quantifying osteon morphotypes in circularly polarized light images’, *Bone* [Preprint]. Available at: https://doi.org/10.1016/j.bone.2008.10.053.

Skedros, J.G., Hunt, K.J. and Bloebaum, R.D. (2004) ‘Relationships of Loading History and Structural and Material Characteristics of Bone: Development of the Mule Deer Calcaneus’, *Journal of Morphology*, 259(3), pp. 281–307. Available at: https://doi.org/10.1002/jmor.10167.

Sone, J.Y. *et al.* (2017) ‘Helmet efficacy against concussion and traumatic brain injury: a review’, *J Neurosurg*, 126(March), pp. 768–781. Available at: https://doi.org/10.3171/2016.2.JNS151972.

Soons, J. *et al.* (2015) ‘Is beak morphology in Darwin’s finches tuned to loading demands?’, *PLoS ONE*, 10(6). Available at: https://doi.org/10.1371/journal.pone.0129479.

Stettenheim, P.R. (2000) ‘The integumentary morphology of modern birds-an overview’, *American Zoologist*, 40(4), pp. 461–477. Available at: https://doi.org/10.1093/icb/40.4.461.

Thomason, J.J. *et al.* (2005) ‘Mechanical behavior and quantitative morphology of the equine laminar junction’, *Anatomical Record - Part A Discoveries in Molecular, Cellular, and Evolutionary Biology*, 283(2), pp. 366–379. Available at: https://doi.org/10.1002/ar.a.20173.

Tombolato, L. *et al.* (2010) ‘Microstructure, elastic properties and deformation mechanisms of horn keratin’, *Acta Biomaterialia*, 6(2), pp. 319–330. Available at: https://doi.org/10.1016/j.actbio.2009.06.033.

Trim, M.W. *et al.* (2011) ‘The effects of water and microstructure on the mechanical properties of bighorn sheep (Ovis canadensis) horn keratin.’, *Acta biomaterialia*, 7(3), pp. 1228–40. Available at: https://doi.org/10.1016/j.actbio.2010.11.024.

Turner, C.H. (1998) ‘Three rules for bone adaptation to mechanical stimuli’, *Bone*, 23(5), pp. 399–407. Available at: https://doi.org/10.1016/S8756-3282(98)00118-5.

Uhthoff, H.K. and Jaworski, Z.F.G. (1978) ‘Bone loss in response to long-term immobilisation’, *The Journal of Bone and Joint Surgery*, 60-B(3), pp. 420–429.

Vashishth, D., Behiri, J.C. and Bonfield, W. (1997) ‘Crack growth resistance in cortical bone: Concept of microcrack toughening’, *Journal of Biomechanics*, 30(8), pp. 763–769. Available at: https://doi.org/10.1016/S0021-9290(97)00029-8.

Vashishth, D., Tanner, K.E. and Bonfield, W. (2003) ‘Experimental validation of a microcracking-based toughening mechanism for cortical bone’, *Journal of Biomechanics*, 36(1), pp. 121–124. Available at: https://doi.org/10.1016/S0021-9290(02)00319-6.

Wainwright, S.A. *et al.* (1976) ‘Collagen’, in *Mechanical Design in Organisms*. Halsted Press, pp. 81–94.

Wegst, U.G.K. *et al.* (2015) ‘Bioinspired structural materials’, *Nature Materials*, 14(1), pp. 23–36. Available at: https://doi.org/10.1038/nmat4089.

Weiner, S. and Traub, W. (1992) ‘Bone structure: from ångstroms to microns’, *The FASEB Journal*, 6(3), pp. 879–885. Available at: https://doi.org/10.1096/fasebj.6.3.1740237.

Wojda, S.J. *et al.* (2013) ‘Black bears with longer disuse (hibernation) periods have lower femoral osteon population density and greater mineralization and intracortical porosity’, *Anatomical Record*, 296(8), pp. 1148–1153. Available at: https://doi.org/10.1002/ar.22720.

Yamashita, J. *et al.* (2001) ‘The use of dynamic mechanical analysis to assess the viscoelastic properties of human cortical bone’, *Journal of Biomedical Materials Research*, 58(1), pp. 47–53. Available at: https://doi.org/10.1002/1097-4636(2001)58:1<47::AID-JBM70>3.0.CO;2-U.

Yeni, Y.N. *et al.* (1997) ‘The influence of bone morphology on fracture toughness of the human femur and tibia’, *Bone*, 21(5), pp. 453–459. Available at: https://doi.org/10.1016/S8756-3282(97)00173-7.

Yoon, S.H. and Park, S. (2011) ‘A mechanical analysis of woodpecker drumming and its application to shock-absorbing systems’, *Bioinspiration and Biomimetics*, 6(1). Available at: https://doi.org/10.1088/1748-3182/6/1/016003.

Zhang, Y. *et al.* (2018) ‘Microstructure and mechanical properties of different keratinous horns’, *Journal of the Royal Society Interface*, 15(143). Available at: https://doi.org/10.1098/rsif.2018.0093.

Ziv, V. and Weiner, S. (1994) ‘Bone Crystal Sizes: A Comparison of Transmission Electron Microscope and X-Ray Diffraction Line Width Broadening Techniques’, *Connective Tissue Research*, 30(3), pp. 165–175.